



(NASA-CR-184749) APCLLC LIGHTCRAFT PROJECT
(Besselaer Polytechnic Inst.) 166 p
CSCI 22B

N89-18512

Unclas
G3/18 0189651

Apollo

Lightcraft Project



NASA/USRA Advanced Design Program
4th Annual Summer Conference
Kennedy Space Center, Florida
June 13-18, 1988

Apollo

Lightcraft Project

Prepared For:

The NASA/USRA Advanced Design Program
4th Annual Summer Conference
Kennedy SFC, Florida
June 13-17, 1988

Instructor

Professor Leik N. Myrabo
Dept. of Mechanical Engineering, Aeronautical Engineering and Mechanics
Rensselaer Polytechnic Institute, 4004 JEC
Troy, NY 12180-3590
Phone: (518) 276-6545

Editor-in-Chief

Wayne L. Smith
(Teaching Assistant)

Editorial Staff and Major Contributors

Casimer Decusatis, Scott R. Frazier, James L. Garrison, Jr.,
Jonathan S. Meltzer, Marco A. Minucci, Jeffrey P. Moder,
Ciro Morales, Mark T. Mueller, and Jacques C. Richard

Cover Art Credit

Ray Rue, Free-lance Artist, Boston, Massachusetts

Student Participants

Transatmospheric Vehicle Design — Fall, 1987

Angielski, Jeffrey	Kaps, Ronald A.	Sacknoff, Scott M.
Berry, Alan R.	Lieu, James S.	Scharland, Michael J.
Byrnes, Kimberly A.	Meltzer, Jonathan S.	Shea, Elizabeth
Chen, Sammy G.	Minucci, Marco A.	Simon, Jack E.
Culler, Mark F.	Morales, Ciro	Smith, Michael J.
Decusatis, Casimer	Mueller, Mark T.	Superman, Bruce S.
Devoy, Christopher	Pei, James	Weselake, Kenneth
Donato, Rodney J.	Perez, Andrés	Gosden, Andrew
Garrison, James L., Jr.	Perry, Andrew A.	
Higgins, John P.	Podowski, Raphael M.	

Theory of Propulsion — Spring, 1988

Baker, Timothy H.	Hardtmann, Dirk J.	Perez, Andrés
Breckenridge, Rene	King, Kevin L.	Perrie Welsch, Carol
Cody, Greg S.	L'Amoureux, Andrew P.	Robinson, Christopher
Cundiff, Gary A.	Lyle, Robert V., Jr.	Sacknoff, Scott M.
Dondes, Hillary	McComb, Todd M.	Sofge, Charles N.
Dutton, Kevin E.	Meltzer, Jonathan S.	Terzis, Price B
Flynn, Susan E.	Minucci, Marco A.	Vincent, Stefan R.
Garrison, James L., Jr.	Niebanck, Robert D.	Vlcek, Brian L.
Godreau, Julio E.	Niskey, Charles J.	Wojtowicz, Ralph L.

This report was typeset by WCS
using the $L^A_T_E_X$ document
preparation system.

Contents

List of Figures	iv
List of Tables	vii
Abstract	ix
1 Executive Summary	1
1.1 Family of Laser-Boosted Lightcraft	1
1.2 Focus of RPI's Design Project	3
1.3 Apollo Lightcraft Systems Integration	4
1.3.1 Crew Accommodations	4
1.3.2 Landing Gear	4
1.3.3 Receptive Optical Train	6
1.3.4 ERH Thruster: RDWE Mode	6
1.3.5 ERH Thruster: Shroud Lift Mode	10
1.3.6 Scramjet Propulsion Mode	12
1.3.7 MHD-Fanjet Propulsion Mode	12
1.3.8 Aerodynamics of Re-entry	15
1.3.9 Annular Shroud Structural Dynamics	15
1.3.10 Optimal Trajectory Sensitivity Studies	15
1.3.11 Lightcraft Technology Demonstrator (LTD)	15
2 Combined-Cycle Engine Developments	18
2.1 Engine/Vehicle External Geometry	19
2.2 ERH Thruster Refinements	22
2.3 MHD-Fanjet Mode	24
3 Optical Train for Propulsion	32
3.1 Generalized Active Optical Area Analysis	32
3.2 Beam Coherence and Divergence	33

4	Phase Distortion Due to Aero-Optical Phenomena	43
4.1	Introduction	43
4.2	The Apollo Lightcraft Simplified Forebody	44
4.3	Laser Beam Phase Distortion Calculations	45
4.4	The Conical Flowfield Solution	47
4.5	Numerical Results	48
4.6	Conclusions	57
5	Man/Machine Interface	62
5.1	Cabin Layout	62
5.2	Entry/Exit	63
5.3	Video Systems	63
5.4	Avionics	66
6	Flight Control Systems	70
6.1	Ground Orientation	70
6.2	Airborne Flight Control	71
6.3	Orbital Maneuvering and Navigation	75
7	Optical Train for Imaging Applications	79
7.1	Imaging Properties of the Optical System	79
7.2	Electrostatic Cleaning of Optical Surfaces	83
7.3	Protecting the Optical Surfaces	84
8	Optimal Trajectory Analysis	90
8.1	Optimized Propellant Usage	90
8.2	Optimized Energy Usage	93
8.3	Sensitivity Studies	95
8.3.1	Vehicular Drag	95
8.3.2	Laser Wavelength/Atmospheric Attenuation	97
8.3.3	Vehicle Liftoff Weight	98
8.3.4	Maximum Laser Power	98
9	Re-Entry Aerodynamics	104
9.1	Trajectory Analysis	104
9.2	Aerodynamics	108
10	Annular Shroud Structural Dynamics	114
10.1	Introduction	114
10.1.1	Problem Statement	114
10.1.2	Overview of the Analytical Procedure	114
10.1.3	Interpretation of Results	115
10.2	Local Vibration Modes	115
10.3	Global Modes of Vibration	116
10.4	Interpretation of Results	116

10.4.1	Loading Sources	116
10.4.2	Design Options to Avoid Interference with Shroud	118
11	Future Directions	122
A	Details of the Structural Dynamics Analysis	125
A.1	Beam Theory Analysis: Local Modes	125
A.1.1	Basic Equations of Linear Beam Theory	125
A.1.2	Beam Element Cross Sections	125
A.1.3	Location of Centroid and Principle Axes	126
A.1.4	Determination of Moments of Inertia	129
A.1.5	Solution of Beam Equations for Local Modes	130
A.2	Beam Theory Analysis: Global Modes	133
A.2.1	Exact Solution for Vibrations of a Circular Ring	133
A.2.2	Beam Theory Solution for Global Modes	136
B	ERH Thruster Performance	140
C	Lightcraft Technology Demonstrator Loft Lines	150

List of Figures

1.1	Family of Laser Boosted Lightcraft	2
1.2	Ground Based Laser System	5
1.3	Apollo Lightcraft Crew Accommodations	5
1.4	Landing Gear Configuration	7
1.5	Crew Entrance and Egress	7
1.6	Top View of Apollo Lightcraft	8
1.7	Rotary Detonation Wave Engine (RDWE) mode	8
1.8	Apollo Lightcraft Bottom Surface	9
1.9	Shroud Lift Mode ERH Thruster	11
1.10	ERH Operation in Shroud Lift Mode	11
1.11	Scramjet Mode	13
1.12	Adaptive Primary Optics	13
1.13	E-Beam Conductivity Enhancement	14
1.14	Superconducting Magnet Configuration	14
1.15	Re-entry Configurations	16
1.16	Lightcraft Technology Demonstrator	16
2.1	Apollo Lightcraft Configuration	20
2.2	Vehicle Loft Lines	20
2.3	ERH Refresh Mechanisms	23
2.4	RDWE Lateral Refresh	23
2.5	RDWE ERH Thrust Vector Control	25
2.6	Twelve Line Source ERH Thruster	25
2.7	Lateral Refresh Mechanism	26
2.8	Transpiration Cooling During ERH Thruster Mode	26
2.9	MHD Accelerator Using an Electron Beam as a Pre-ionizer	29
2.10	Thrust vs. Mach Number and Seed Factor	29
2.11	Specific Impulse vs. Mach Number and Seed Factor.	31
3.1	Geometry for Fractional Active Area Analysis.	34
3.2	Active Optical Area, $\alpha = 30^\circ$	34
3.3	Active Optical Area, $\alpha = 45^\circ$	36
3.4	Relationship Between Spatial Extent of the Beam and k	36

3.5	Two Beams of Equal Power but Different Phase Profiles	38
3.6	Divergence of the Two Beams	38
3.7	Laser Transmitter vs. Receiver Diameter	40
3.8	Transmitter/Receiver Diameter vs. Range.	40
4.1	Simplified Apollo Lightcraft Forebody (ERH or Scramjet mode) .	46
4.2	Simplified Apollo Lightcraft Forebody (MHD-Fanjet Thruster mode)	46
4.3	Coordinate System	49
4.4	Density Ratio vs. θ for Several Flight Mach Numbers	49
4.5	30° Semi-Apex Angle Cone in Mach 10 Flow	52
4.6	Aero-Optical Coefficient vs. Flight Mach Number in ERH or Scramjet Modes	52
4.7	Aero-Optical Coefficient vs. Flight Mach Number in MHD-Fanjet Mode	53
4.8	Variation of P_I^* Along a Selected Beam (Evaluated Just After the Reflected Beam Has Transversed the Shock Wave)	53
4.9	Variation of P_{II}^* Along a Selected Beam (Evaluated at the Receiving Optics)	55
4.10	Contours of Constant P_{II}^* in the Beam Wavefront	55
4.11	Trajectory-Altitude Profile	56
4.12	Maximum Phase Distortion in the Propulsive Beam vs. Flight Mach Number for a Chosen Trajectory-Altitude Profile	56
4.13	Adaptive Primary Optics for the Apollo Lightcraft	61
5.1	Flight Deck Configuration	64
5.2	Lower Deck Layout	64
5.3	Volume Requirements for Manned Missions	65
5.4	Hatch Configuration	65
5.5	Fiber Optic Camera Locations	67
5.6	Fiber Optic Lens Feed Detail	67
5.7	Flight Crew Station — Side View	68
5.8	Segmented Flat Screen Display System	68
6.1	Tripod Landing Gear Orientation	72
6.2	Thrust Vectoring Control	72
6.3	Thrust Vector Control Through Pressure and Length Variation .	73
6.4	Differential Surface Area Determination	73
6.5	The Apollo Command Module Reaction Control System	77
6.6	Twin Stick Flight Control System	77
7.1	Placement of Video Camera for Imaging Through Optical System	81
7.2	Schematic of Electrostatic Fence	85
7.3	Electrostatic Dust Repulsion System for 30 cm Mirror	85

7.4	Use of the Bow Shock Wave to Deflect Incident Particles from the Primary Optic.	86
8.1	Performance Study — Propellant vs. Laser Energy	96
8.2	Performance Sensitivity to Drag — Propellant Weight	96
8.3	Performance Sensitivity to Aerodynamic Drag — Total Laser Energy	99
8.4	Performance Sensitivity to Lift-Off Weight — Total Laser Energy	99
8.5	Performance Sensitivity to Lift-Off Weight — Propellant Weight	100
8.6	Performance Sensitivity to Laser Power — Propellant Weight . .	100
8.7	Performance Sensitivity to Laser Power — Total Laser Energy .	101
8.8	Performance Sensitivity to Laser Power — Dynamic Pressure . .	101
9.1	Re-entry Configuration	105
9.2	Body Forces During Re-entry	105
9.3	Model for Calculation of Force Coefficients on a Cone	110
9.4	Model for Calculation of Force Coefficients on a Spherical Surface	110
9.5	Effect of Bluntness on L/D ratio for 45° Blunted Cone	112
9.6	Effect of Segment Shape on L/D ratio for 45° Blunted Cone . . .	112
9.7	Effect of Bluntness on L/D ratio for 50° Blunted Cone	113
9.8	Effect of Segment Shape on L/D ratio for 50° Blunted Cone . . .	113
10.1	Flow Chart of Analytical Procedure	117
10.2	Interaction of Environmental Forces on a Transatmospheric Vehicle	117
10.3	ERH Thruster PRF vs. Altitude	119
10.4	ERH Thruster PRF vs. Mach Number	119
10.5	Scramjet PRF vs. Altitude	120
10.6	Scramjet PRF vs. Mach Number	120
A.1	Local Modes of Shroud Vibration	127
A.2	Rectangular Cross Section	127
A.3	Circular Arc Cross Section	131
A.4	Components of the Frequency Equation	134
A.5	Global Modes of Vibration	135

List of Tables

3.1	Change in Fractional Active Area and F	35
3.2	Variation of Atmospheric Density as a Function of Mach Number and Vehicle Forebody Angle.	39
7.1	Resolution Limits for Entire PO	81
7.2	Operating Parameters for Electrostatic Cleaning System	84
7.3	Velocity Change for Incident Particle Contamination as a Func- tion of Mach Number and Shock Wave Semi-Vertex Angle	86
A.1	Section Properties Listing	131
A.2	Material Properties of Graphite-Epoxy	134
A.3	Natural Frequencies for Local Bending	135
A.4	Natural Global Bending Frequencies of the Shroud	138

Abstract

This second year of the NASA/USRA-sponsored Advanced Aeronautical Design effort focused on systems integration and analysis of the "Apollo Lightcraft." This beam-powered, single-stage-to-orbit vehicle is envisioned as the globe-trotting family shuttlecraft of the 21st century. The five person vehicle was inspired largely by the Apollo Command Module, then reconfigured to include a new front seat with dual cockpit controls for the pilot and co-pilot, while still retaining the 3-abreast crew accommodations in the rear seat. Interior arrangement and cargo space is not unlike that of a full-sized American station wagon.

The gross liftoff mass is 5550 kg, of which 500 kg is the payload and 300 kg is the LH_2 propellant. The round trip cost to orbit is projected to be three orders of magnitude lower than the current space shuttle orbiter. The advanced laser-driven "5-speed" combined-cycle engine has "shiftpoints" at Mach 1, 5, 11 and 25+. The Apollo Lightcraft can climb into low Earth orbit in three minutes, or fly to any spot on the globe in less than 45 minutes — for the price of an airline ticket today.

Detailed investigations of the Apollo Lightcraft Project this second year further evolved the propulsion system design, while focusing on the following areas: (1) man/machine interface, (2) flight control systems, (3) power beaming system architecture, (4) re-entry aerodynamics, (5) shroud structural dynamics, and (6) optimal trajectory analysis. The Apollo Lightcraft concept emerged intact after this critical examination, and no technological show-stoppers were uncovered. The principal new findings are documented in this annual report.

Advanced design efforts for the next academic year ('88/'89) will center on a one meter+ diameter spacecraft: the Lightcraft Technology Demonstrator (LTD). Detailed engineering design and analyses, as well as critical proof-of-concept experiments, will be carried out on this small, near-term machine. As presently conceived, the LTD could be constructed using state of the art components derived from existing liquid chemical rocket engine technology, advanced composite materials, and high power laser optics (developed for SDI). Lawrence Livermore National Laboratory intends to boost such a spacecraft, weighing roughly 120 kg, into low Earth orbit using a 25 to 250 MW ground-based laser — in the next 5 years.

Chapter 1

Executive Summary

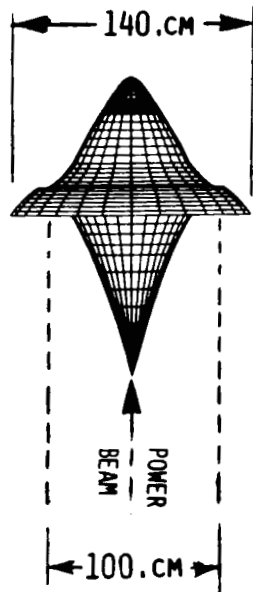
The overall goal for this NASA/USRA-sponsored "Apollo Lightcraft Project" is to develop a revolutionary vehicle technology which can reduce payload transport costs by a factor of 1000 below the Space Shuttle Orbiter. The RPI design team proposes to utilize advanced, highly energetic, beamed-energy sources (laser, microwave) and innovative combined-cycle (airbreathing/rocket) engines to accomplish this goal.

1.1 Family of Laser-Boosted Lightcraft

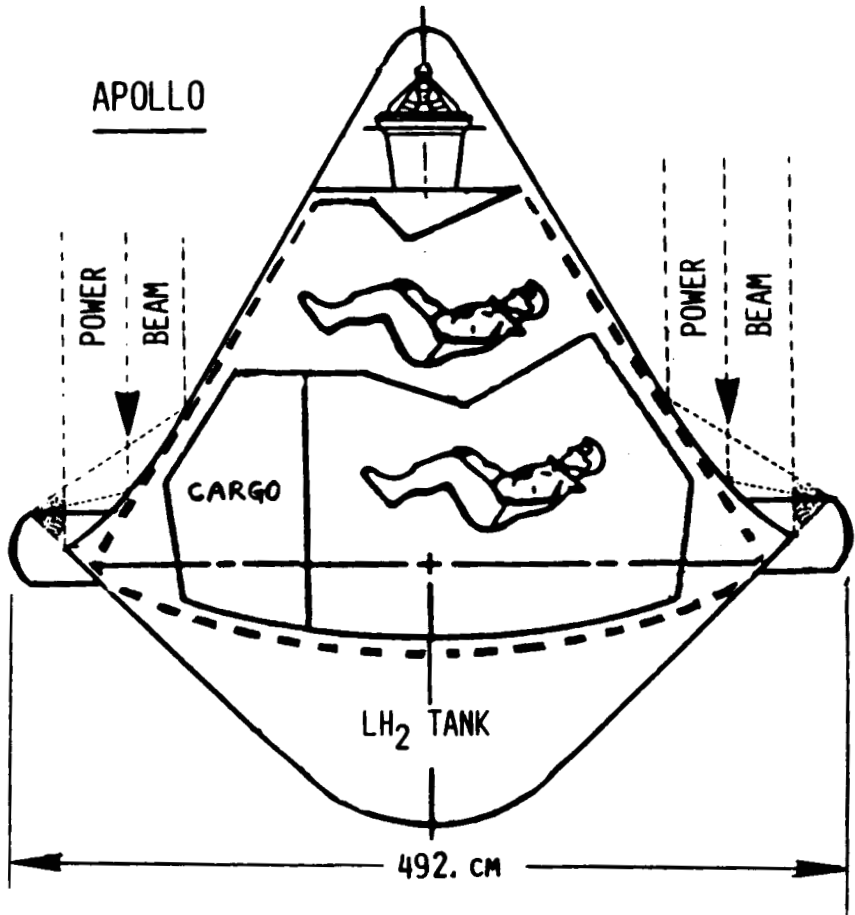
Figure 1.1 shows a family of laser-boosted lightcraft which are likely to trace the development of this new propulsion technology. First to appear will be a small, 1.2 meter diameter, unmanned drone which Lawrence Livermore National Laboratory desires to design, build and boost into orbit within the next five years. This \$2M/year program is now entering its second year. The Lightcraft Technology Demonstrator (LTD) will have a dry launch mass of 120 kg, and be propelled to space with a 25 MW to 250 MW ground-based laser (GBL) placed upon a 3 km altitude mountain site. As portrayed in Fig. 1.2, this powerful laser could be built using existing CO₂ EDL laser technology by assembling 25 to 100 smaller units (of 2.5 MW to 10 MW average power each) into an array. A Chandell-type beam combiner could then be invoked to link the lasers together. Redundant lasers would be built into the system so that inoperative units could be dropped out — with no loss in systems utility.

As presently conceived, the LTD vehicle could be constructed using components derived from current liquid chemical rocket engine technology, advanced composite structures, and high power optics being developed for SDI applications. The one meter diameter laser beam would be delivered directly to the LTD by a 4 meter diameter high power laser telescope (transmitter). The Lightcraft must reach orbital velocity within a maximum range of 800 km from

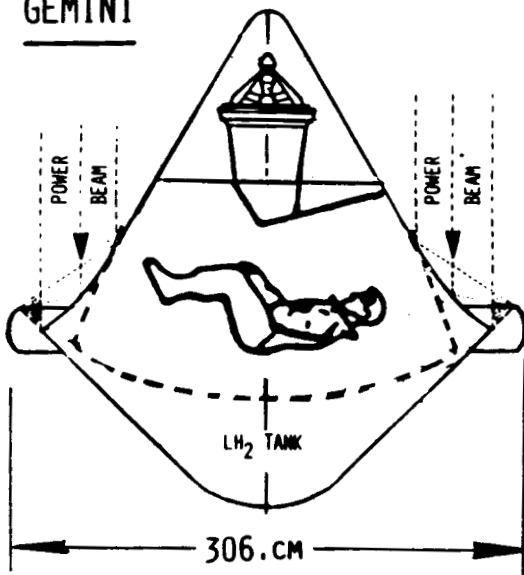
LTD



APOLLO



GEMINI



MERCURY

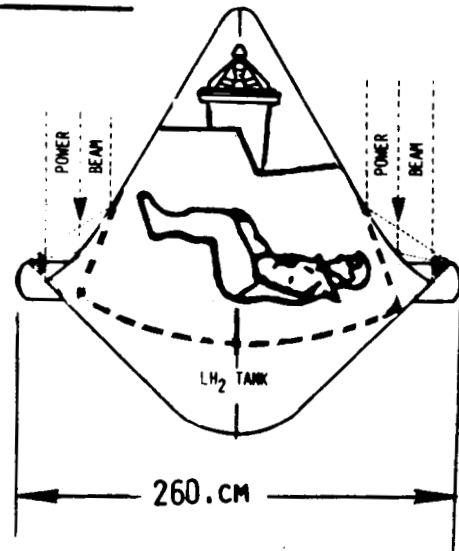


Figure 1.1: Family of Laser-Boosted Lightcraft

the transmitter.

The other three, more advanced, lightcraft in Fig. 1.1 would parallel the early development of U.S. spacecraft, and utilize *orbital* laser power beams. It seems reasonable that since laser propulsion technology will be in its infancy, we must return to the minimum weight/volume approach to spacecraft design. Hence, the one, two, and five person lightcraft are designated Mercury, Gemini, and Apollo, respectively. One may expect the Mercury Lightcraft to be 2.4 m diameter, have a mass of 1300 kg, and require four laser beams to deliver the necessary propulsive power. Each beam would carry the same power as that of the LTD, but be somewhat smaller (e.g., 50 cm) in diameter; this will probably necessitate the application of visible wavelengths to transmit the higher beam powers consumed during the acceleration run to orbit.

A two man, 3 meter diameter, 2700 kg Gemini Lightcraft may require eight such power beams. The 5550 kg, 4.92 m Apollo Lightcraft has been designed for twelve power beams of roughly 75 cm diameter each. In last year's report, 2500 MW was proven to be adequate for the Apollo Lightcraft acceleration run, so each beam must carry about 210 MW.

1.2 Focus of RPI's Design Project

The long range focus of RPI's design project continues to be centered on the Apollo-sized vehicle, since it is destined to become the globe-trotting shuttlecraft for the 21st century family. In the first year of this NASA/USRA-sponsored project, the student team concentrated its efforts on designing a beam-powered, combined-cycle engine that could meet (and exceed) the severe demands of a single-stage-to-orbit mission. This initial effort was successful, producing an engine/vehicle concept that required only a 5-6/people to orbit (~500 kg payload, including space suits) required only \$975 of LH₂ and \$2455 of laser energy. This represents a payload delivery cost of \$3.11/lb, which is a factor of 1000 less than the current STS.

Efforts during the '87/'88 school year were concentrated on the many complex *systems integration* issues involved in the Apollo Lightcraft concept. This detailed investigation evolved the propulsion system to even further detail, while major attention was devoted to the following areas:

1. Man/Machine Interface
2. Flight Control Systems
3. Power Beaming System Architecture
4. Re-entry Aerodynamics
5. Shroud Structural Dynamics, and
6. Optimal Trajectory Analysis

The Apollo Lightcraft survived this critical analysis, and emerged intact. A summary of the principal new findings is presented in the following section.

Design efforts for the next '88/'89 calendar year will center on the Lightcraft Technology Demonstrator (LTD), and associated small scale, proof-of-principle experiments. The LTD is likely to be the first full-scale realization of a single-stage-to-orbit, laser-propelled launch vehicle, having a launch mass of about 300 kg and a dry mass of 120 kg. Once in orbit, the LTD spacecraft will function as an autonomous LEO satellite complete with a fueled attitude control system. Roughly 18 kg is reserved for the sophisticated microcircuitry (i.e., "brain") that controls both laser-launch and satellite functions.

1.3 Apollo Lightcraft Systems Integration

1.3.1 Crew Accommodations

Figure 1.3 portrays the Apollo Lightcraft crew accommodations. The upper cockpit level provides sufficient volume for the pilot and co-pilot, as well as a dual set of controls. This "front seat" cockpit of the Apollo Lightcraft is identical to that of the two place Gemini Lightcraft. Retractable flat display screens, with keyboards, fold up and out of the way, to facilitate entrance and egress. Twin joy sticks are employed for control, like those employed in the Manned Maneuvering Unit (MMU). The lower passenger level (rear seat) is similar to the original Apollo capsule, having three people seated shoulder-to-shoulder. The passenger level would also be provided with flat display screens, since direct viewing of the outside through transparent windows is only possible when the propulsive power beam is shut off. These flat display screens can be linked into a "super vision" system, once the Apollo Lightcraft has finished its acceleration run and the power beam has been cut off, when the vehicle is coasting through space. The "super vision" system uses fiber optic cables, electronic image processing and the display screens to look out the 4.5 meter diameter primary optics. The optical train configuration is similar to the National Multiple Mirror Telescope. Occupants of the Apollo Lightcraft can use this system for a high resolution astronomical observatory, interplanetary laser communications, or for examining promising landing sites from low Earth orbit. For the latter function, this 4.5 m mirror gives a resolution of 6 cm in the visible spectrum.

1.3.2 Landing Gear

A tripod landing gear, with each leg individually actuated, was selected because it is the minimum weight system for a vehicle that can land/take-off vertically, and hover. The gear is conceptually identical to that employed on the Lunar Excursion Module. As indicated in Fig. 1.4, each leg is equipped with a two foot diameter pad which (when fully retracted) becomes an integral part of the re-entry heat shield. Once lowered (i.e., extended), the gear reveals three

ORIGINAL PAGE IS
OF POOR QUALITY

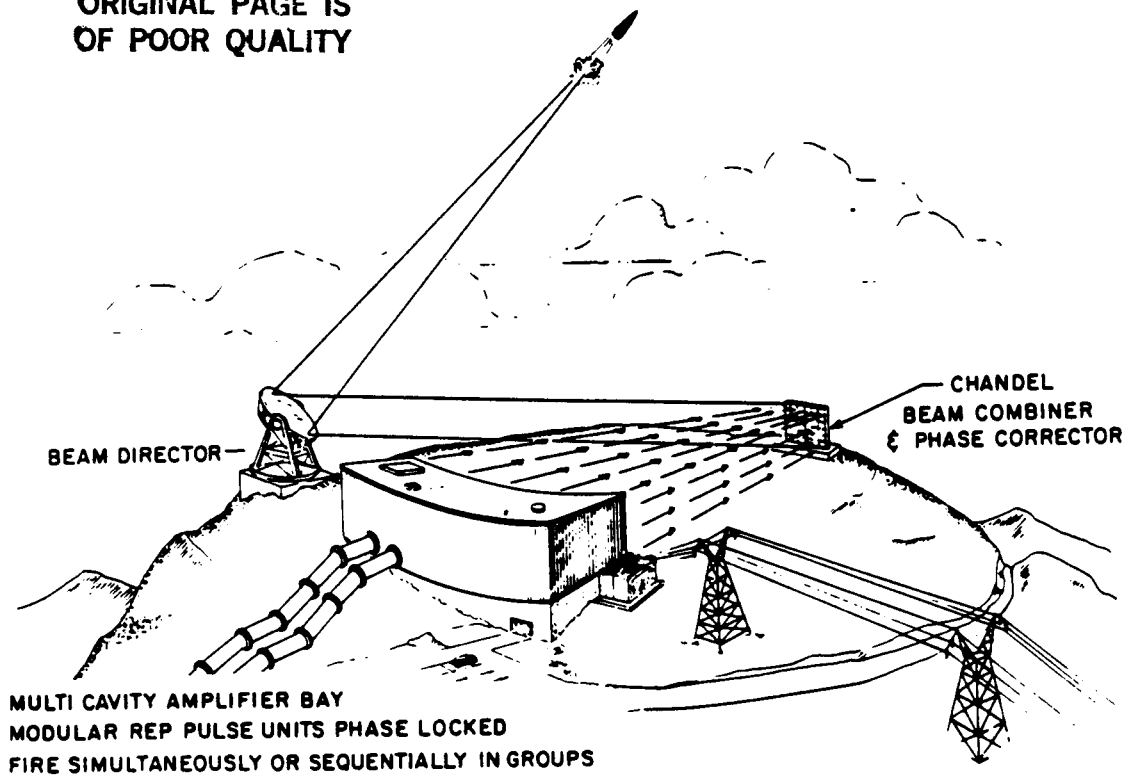


Figure 1.2: Ground Based Laser System
(After Kantrowitz)

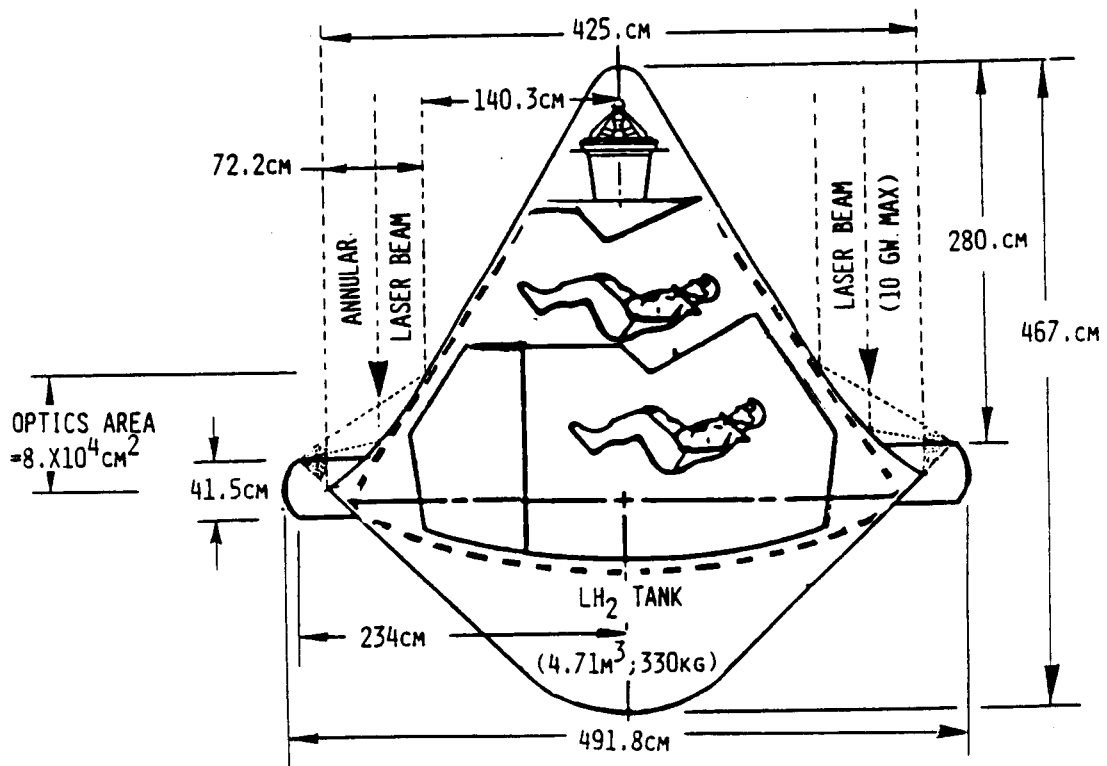


Figure 1.3: Apollo Lightcraft Crew Accommodations

hatches in the pressurized hull. Two are normally used for entrance and egress (as shown in Fig. 1.5), while the other is only employed during emergencies. The two foot diameter opening is probably sufficient for most people, even with space suits. Obviously, larger openings are required to accommodate backpack oxygen systems for extra-vehicular activity (EVA). The entire vehicle kneels for the crew to enter, and in order to point the primary optics precisely at the laser relay satellite.

1.3.3 Receptive Optical Train

Access hatches are placed in the vehicle underbody surface to eliminate the potential for damage to the delicate primary optics (PO) which comprise roughly 50% of the vehicle upper exterior surface area.

Additional measures are required to protect the PO against possible dust and flying insect hazards. Electrostatic repulsion, forced air blowing, and vehicle rotation are potential solutions — possibly used in some combination thereof. Also, since a subsonic “pop-up” maneuver is employed (as described in last year’s report), the potential threat of aerosol and insect impact damage (abrasion, etc.) is minimized when traversing the dense lower atmosphere.

Figure 1.6 presents a top view of the Apollo Lightcraft, indicating the location of the PO surface. During the lift-off phase, the combined-cycle engine operates in a Rotary Detonation Wave Engine (RDWE) mode, as shown in Fig. 1.7. This engine mode is a variation of the External Radiation-Heated (ERH) thruster discussed in last year’s report. Figure 1.8 is a diagram of the vehicle bottom surface showing the location of the secondary and tertiary optics, required in this propulsive mode. Basically, the primary optic is designed to receive pulsed laser beams at only the twelve specific locations given in Fig. 1.6. Each beam is assumed to have a roughly Gaussian intensity distribution, and three detectors (per beam) monitor the laser intensity at the beam’s edge. These detectors are linked to an active feedback system to provide accurate beam pointing and tracking information.

1.3.4 ERH Thruster: RDWE Mode

During the RDWE mode which is used for hover and acceleration to about Mach 1 flight speed, each of the twelve secondary optics condenses the reflected beam onto a tertiary optic — which in turn projects a small 2 cm diameter laser beam across the vehicle lower surface. Through the mechanism of inverse Bremsstrahlung absorption, this laser energy is transferred directly into the air, and creates in the process a high pressure (e.g., 600 atm.) “plasma finger.” Each 80 cm diameter beam is designed to create only one plasma finger.

The RDWE firing sequence can either detonate all twelve fingers simultaneously, or in some predetermined pattern (e.g., fingers 1-2-3-4-5, etc., sequentially, as shown in Fig 1.7). More plasma fingers can be inserted between the

ORIGINAL PAGE IS
OF POOR QUALITY

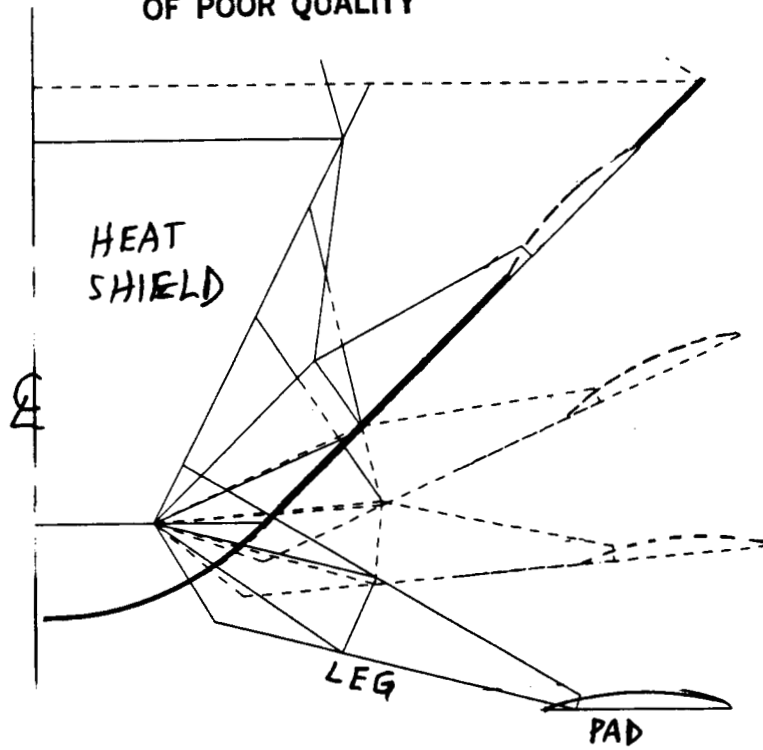


Figure 1.4: Landing Gear Configuration

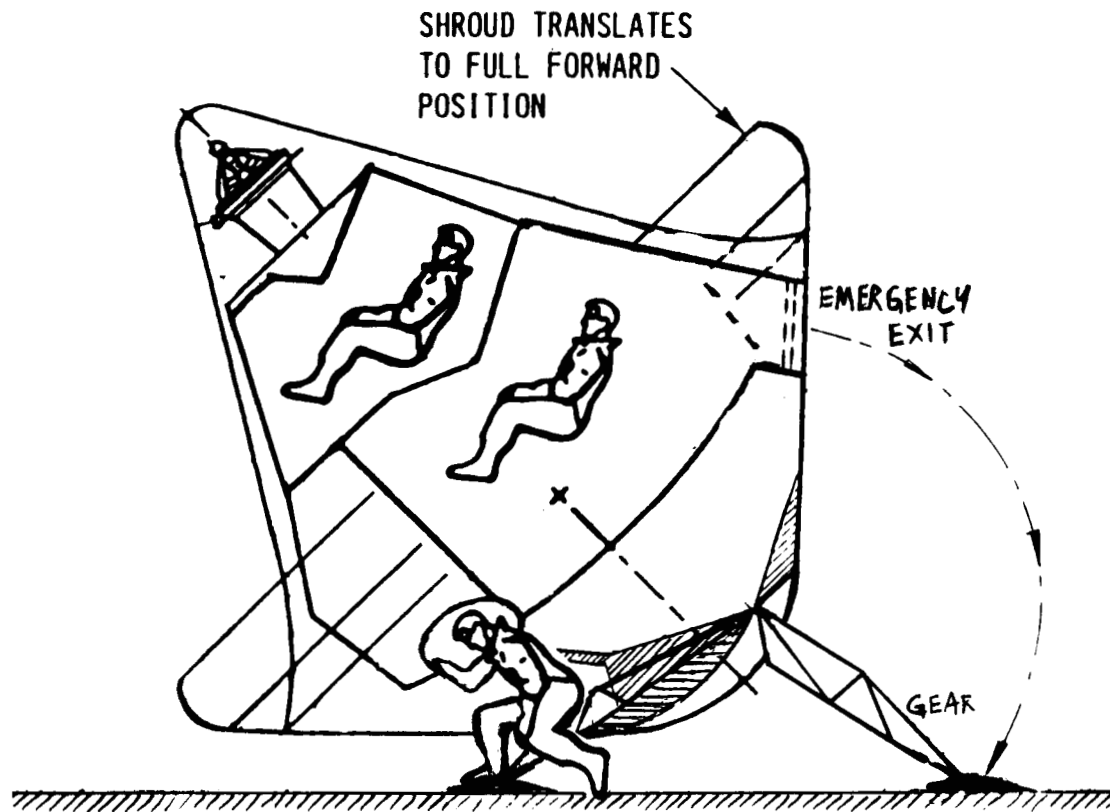


Figure 1.5: Crew Entrance and Egress

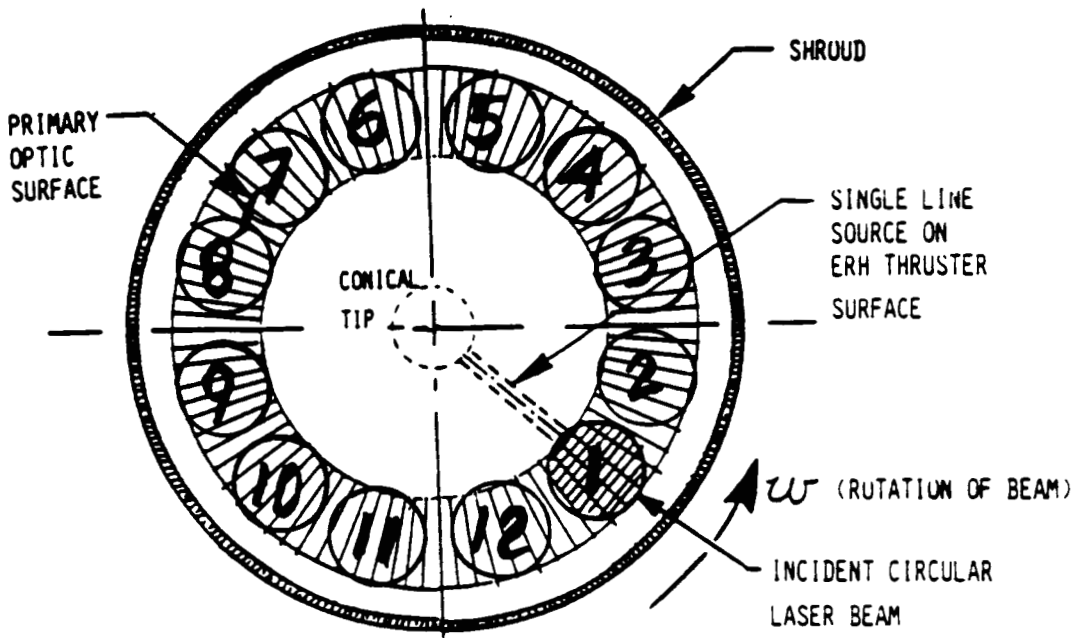


Figure 1.6: Top View of Apollo Lightcraft

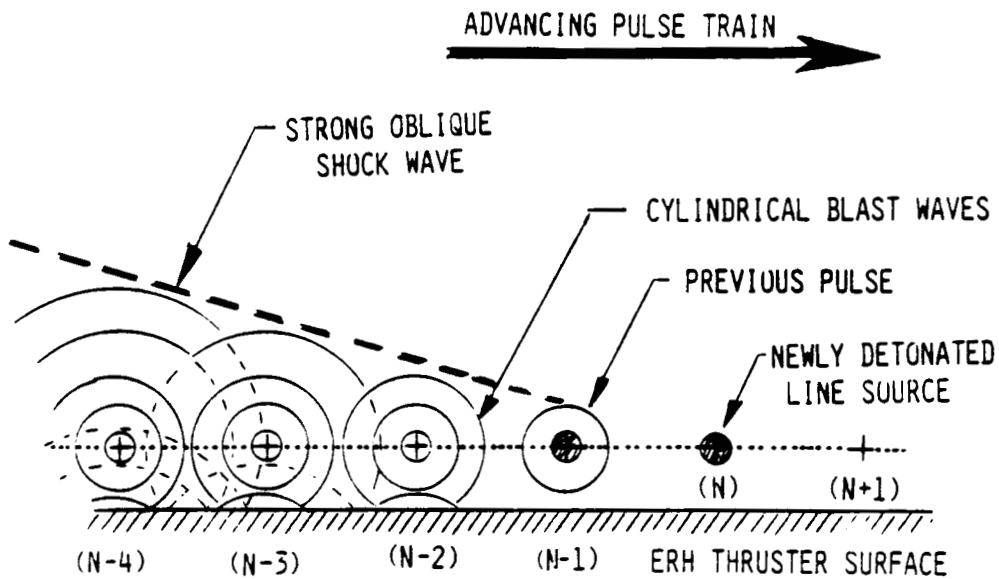


Figure 1.7: Rotary Detonation Wave Engine (RDWE) mode

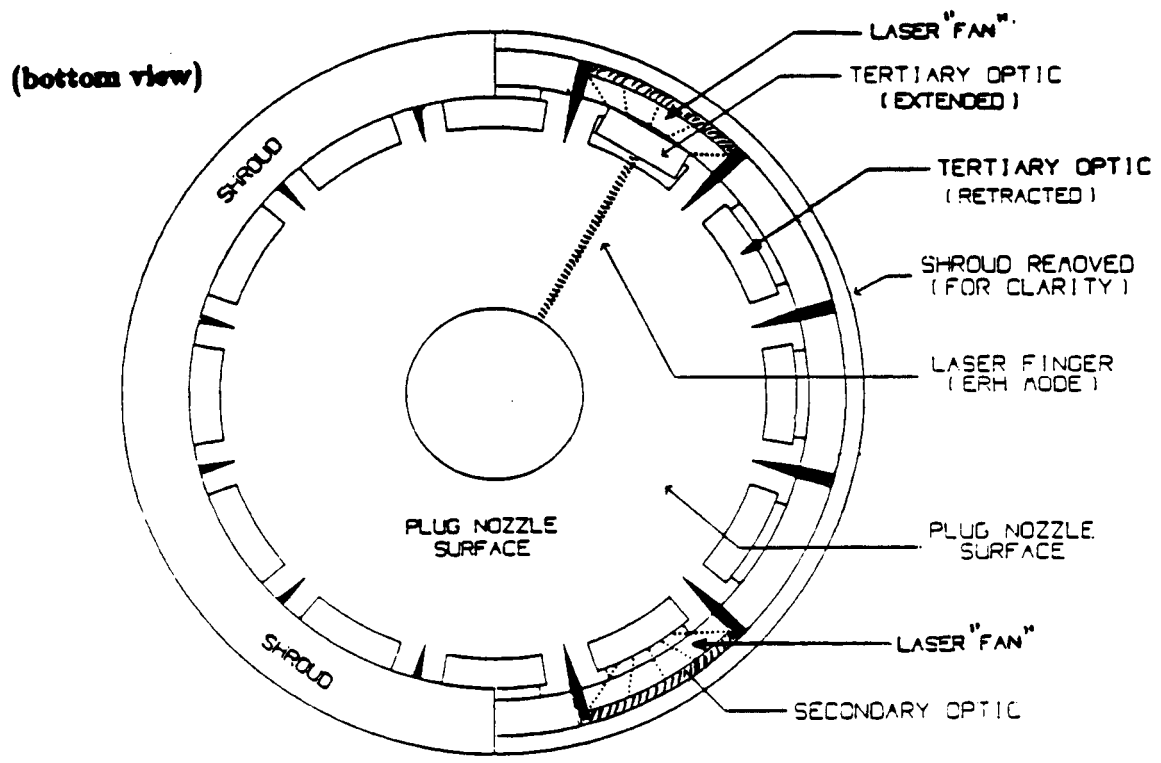
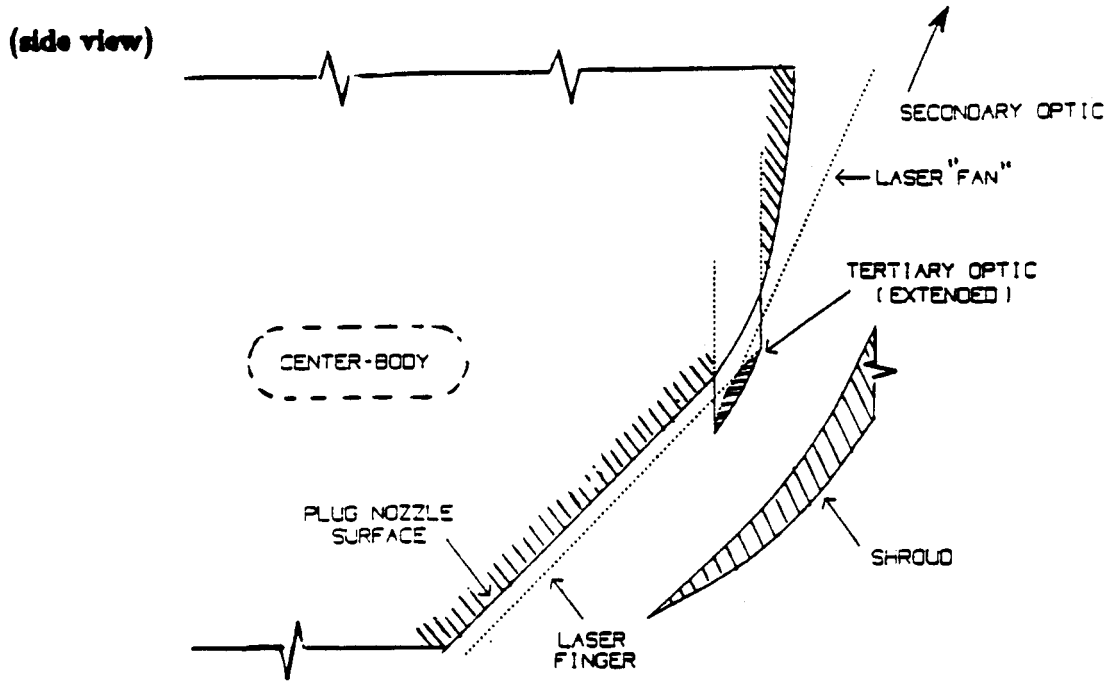


Figure 1.8: Apollo Lightcraft Bottom Surface

fundamental twelve sites (which are tied directly to the receptive optical train) by invoking vehicle rotation. Due to the structural limitations of existing advanced composite materials, maximum rim speeds are not likely to exceed the ambient speed of sound.

During liftoff and acceleration to Mach 1, the generation of excessive noise levels can be prevented by pulsing all twelve plasma fingers simultaneously at *sub-audible rates* (e.g., below 16 Hz), or by operation in the RDWE mode at superaudible frequencies (e.g., > 10 kHz to 20 kHz). Significant noise abatement may also be possible by phased-detonation of the plasma fingers, such that the outgoing sound patterns exactly cancel (i.e., an "electronic muffler").

It is interesting to note that the RDWE mode automatically compresses air into adjacent plasma finger sites, just prior to their detonation. Hence, inherent to the RDWE operation is this "supercharging" function which can provide high thrust levels at liftoff, with zero forward velocity.

Once the vehicle attains a forward velocity of Mach 0.3 to 0.5, the annular shroud finally begins to convect large quantities of fresh, unheated air across the lower center-body ERH thruster surface. However, this particular ERH thruster mode "runs out of steam" at about Mach 3, just as the scramjet mode begins to produce thrust. Accelerating through Mach 3 was perceived as a potential problem in the combined cycle engine proposed for the Apollo Lightcraft.

1.3.5 ERH Thruster: Shroud Lift Mode

To eliminate this potential problem, a second ERH thruster mode was developed. Referred to as the "shroud lift" mode, this mechanism has been analyzed mathematically and proven to give excellent thrust levels from Mach 1.0 up to Mach 6. The new ERH thruster concept which is portrayed in Fig 1.9, will require the inclusion of an annular "super-ignitor array" to the inside shroud surface. This material acts as a self-excited "spark plug" to reduce the time and energy required to ignite an LSD wave at the array surface. Candidate materials are currently being investigated under the LLL sponsored laser propulsion program.

To prepare for engine operation in this mode, the shroud is first shifted aft from position "a" in Fig. 1.10, to position "b." This brings the super-ignitor array into the focus of the primary optics. Next, the pulsed laser beam ignites a 4 cm wide annular LSD (i.e., Laser-Supported Detonation) wave at the super-ignitor array, which resides at a location close to the shroud leading edge. The resulting 600 atm. pressure toroidal plasma bubble then expands against the shroud, generating thrust, as the inlet air blows the bubble aft. When the plasma pressure falls to the local static pressure level, the impulse ends, just before the bubble leaves the shroud trailing edge (see Fig. 1.9). A complete description of the Mach number vs. altitude performance for this new ERH thruster mode is given in Chapter 2.

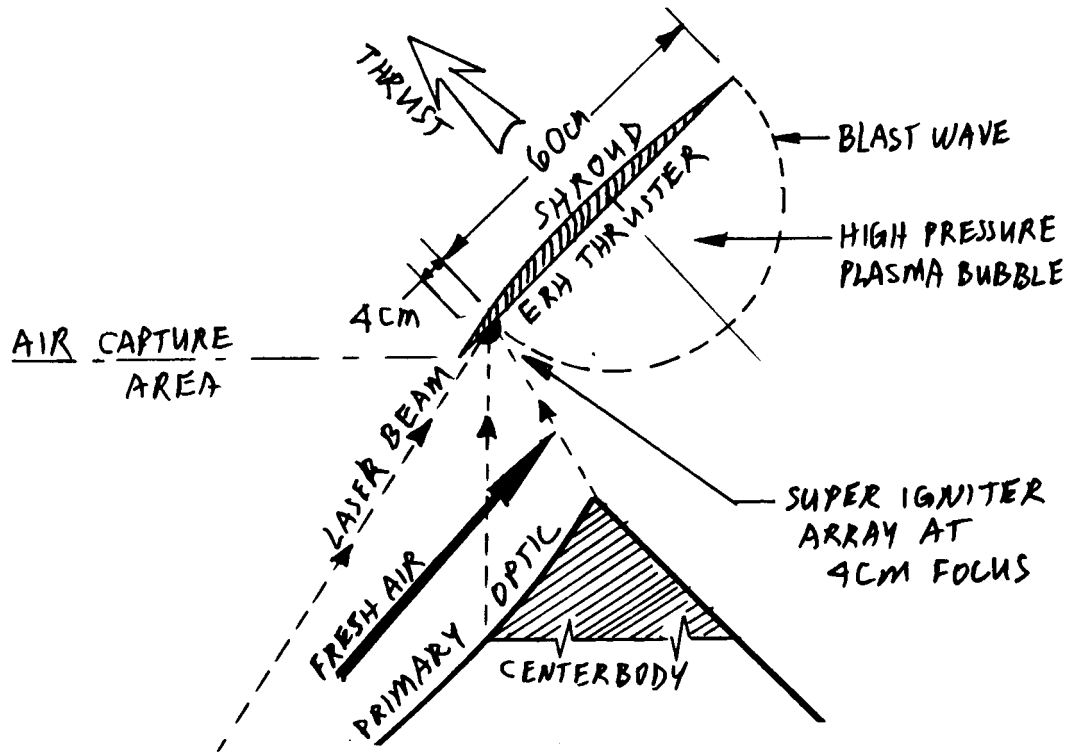


Figure 1.9: Shroud Lift Mode ERH Thruster

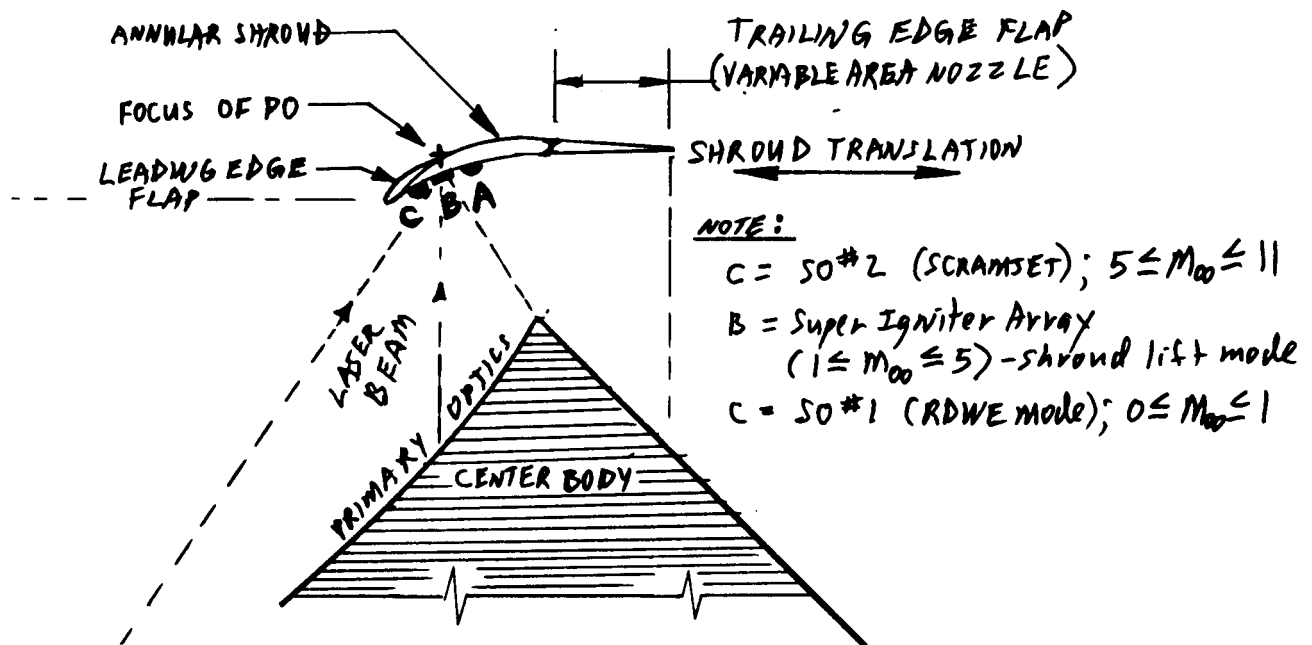


Figure 1.10: Shroud Optical functions vs. translation

1.3.6 Scramjet Propulsion Mode

The complete combined-cycle engine, as presently conceived, is a 5-speed:

1. RDWE thruster,
2. Shroud-Lift ERH thruster,
3. Scramjet,
4. MHD-fanjet, and
5. Rocket.

Shift points are now Mach 1, 5, 11, and 25+. The scramjet mode, with its "planar heater," is pictured in Fig. 1.11, and has not changed in concept from last year's vision.

However, as will be discussed in Chapter 4, it was discovered that significant phase distortions due to aero-optical phenomena will be produced in the laser power beam as it transverses the bow shock wave. These effects are dominant mostly in the lower supersonic flight Mach numbers typical of the ERH thruster mode, and to a lesser extent, in the scramjet and MHD-fanjet modes. As a result, it is now clear that the primary mirror must be an adaptive surface that is actively controlled throughout the acceleration run (see Fig. 1.12). This should present no particular difficulty, especially since these phase distortions are a direct function of flight Mach number, and can be sensed as well as corrected at the vehicle flight platform. Finally, adaptive mirror technology is advancing at a rapid rate under several DOD-sponsored SDI programs.

1.3.7 MHD-Fanjet Propulsion Mode

Two new developments in the MHD-fanjet engine concept bear mentioning. Most importantly, it was noted in the previous NASA/USRA report that some mechanism for augmenting the conductivity of inlet air must be found. Figure 1.13 portrays the most promising solution that could immediately be invoked: a large number (e.g., 24-48) of electron beam accelerators could be mounted within the vehicle forebody, just upstream of the primary optics (see Fig. 1.6). These devices would inject relativistic e-beams (e.g., at 4 MeV) into the compressed inlet air just as it enters the MHD air accelerators. Performance of the MHD accelerators was found to be quite sensitive to air plasma conductivity (e.g., refer to Chapter 2).

Second, it is evident that from studying Fig. 1.14 that the optimum spacing of superconducting magnets for the annular MHD air accelerator may not exactly match the requirements perceived from structural and heat transfer considerations. Perhaps one solution would be to retract every other magnet out of the annular duct flow at flight speeds below Mach 11, when the just produce more drag.

NOTES:

- "PLANAR HEATER" PROMOTES TURBULENT MIXING AND ENABLES EXCEPTIONALLY SHORT SHROUD.
- ≠ PLANAR HEATER IS ACTIVATED BY RP LSD-WAVES.

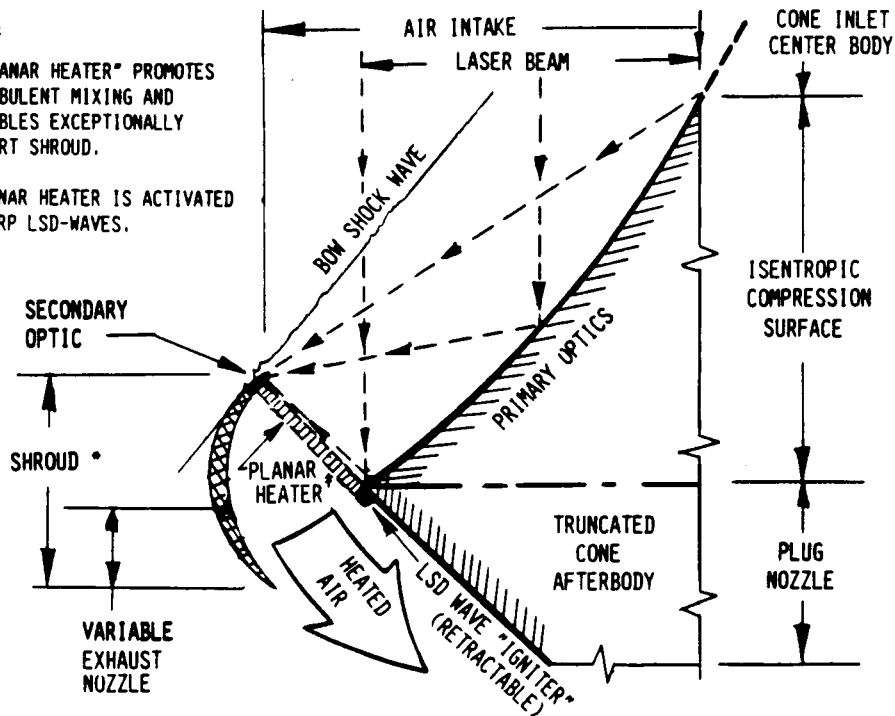


Figure 1.11: Scramjet Mode

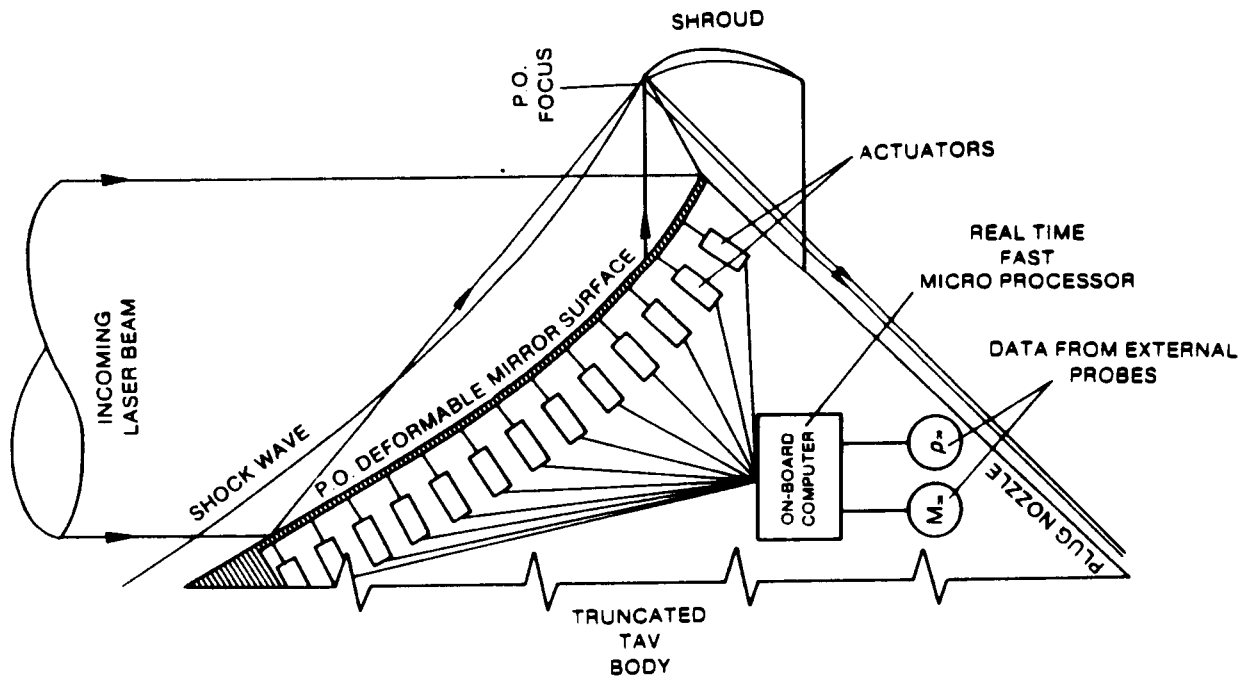
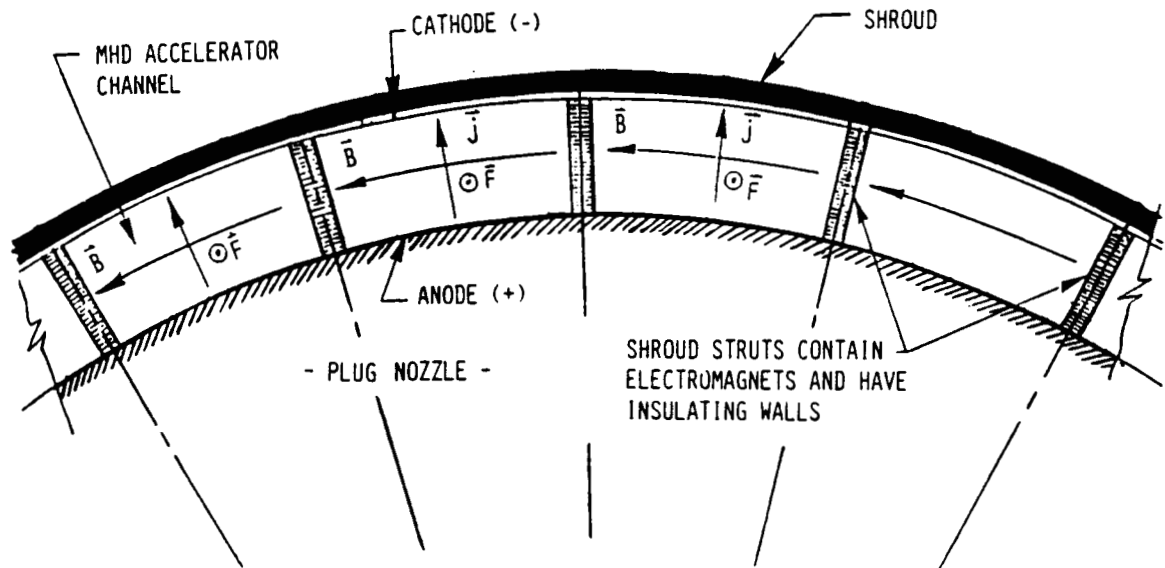
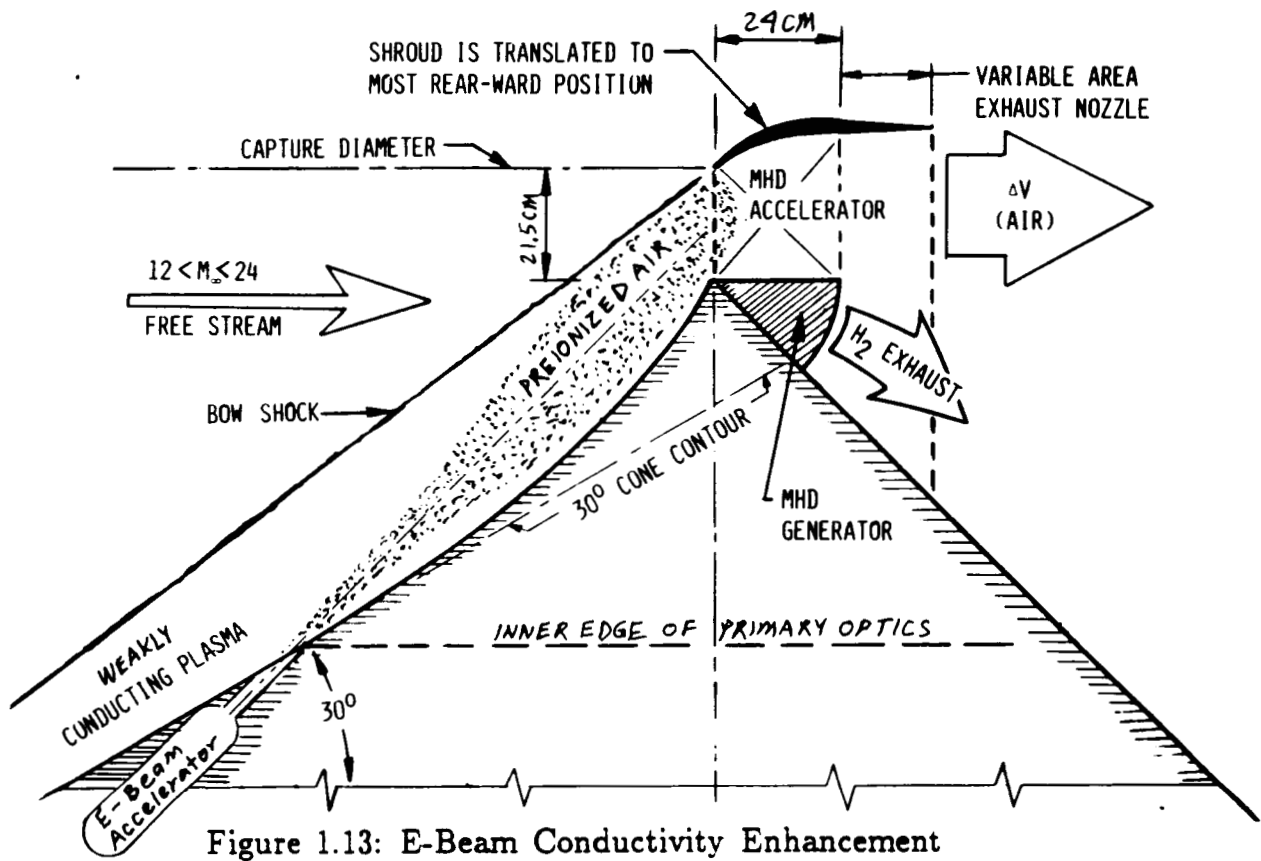


Figure 1.12: Adaptive Primary Optics

ORIGINAL PAGE IS OF POOR QUALITY



Finally, it is fairly obvious that the revolution in low-temperature superconductors will greatly reduce magnet cooling requirements of such advanced hypersonic engines.

1.3.8 Aerodynamics of Re-entry

An examination of the re-entry heat shield contour proposed last year for the Apollo Lightcraft has indicated that a revision might be necessary. Figure 1.15 shows the old 45° half-angle cone in relation with a proposed 50° blunted cone. A larger cone angle and more severe cone truncation may be required to reduce peak acceleration rates to something more in line with human tolerance.

Incidentally, this change will also improve impulse coupling in the RDWE mode, since the thrust vector will be more closely aligned with the vehicle flight axis.

1.3.9 Annular Shroud Structural Dynamics

It is well understood that operation of a pulsed engine at any of the natural frequencies of the engine's structure is undesirable. This could lead to an unstable dynamic situation, where the vibrations induced by the engine pulses would couple with the natural vibration of the structure. This undamped behavior would soon lead to a catastrophic failure of the system. To reduce the risk of this occurring, it is necessary to either avoid engine operation at the natural frequencies, or to pass through these frequencies quickly. In the past year, analyses were carried out to determine the natural frequencies of the Lightcraft's annular shroud. Natural frequencies were determined for both local and global modes of vibration. Of course, since the actual materials and structure of the shroud are not yet determined, these calculations are merely estimates. However, the analytic procedure developed is sound.

1.3.10 Optimal Trajectory Sensitivity Studies

Last year, optimum trajectories were determined for the Apollo Lightcraft following a single relay satellite. To continue the trajectory optimization study, it was necessary to determine how sensitive the optimum trajectories were to changes in some of the trajectory parameters. Such parameters (normally held constant) as vehicle liftoff weight, vehicle drag, and maximum available laser power were examined. The trajectories were found remarkably insensitive to small changes in these operating parameters.

1.3.11 Lightcraft Technology Demonstrator (LTD)

The next year's effort will focus on a detailed analysis of the Lightcraft Technology Demonstrator pictured in Fig. 1.16. This investigation will emphasize

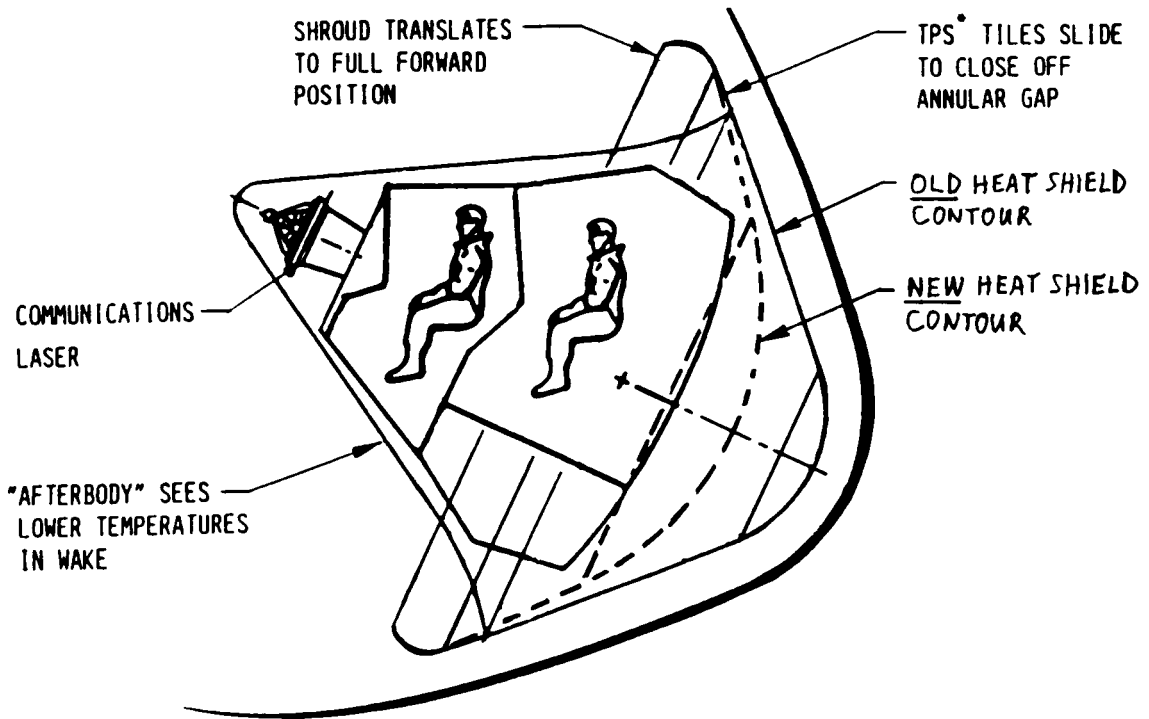


Figure 1.15: Re-entry Configurations

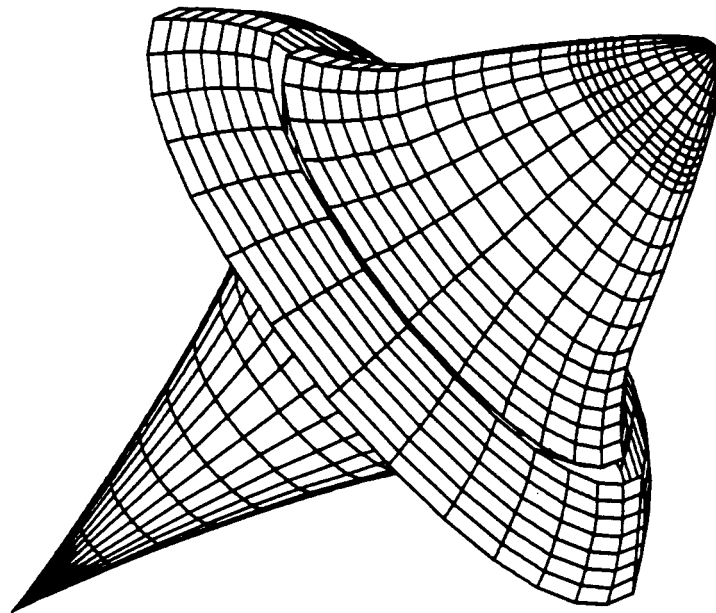


Figure 1.16: Lightcraft Technology Demonstrator

small scale experiments on this near term concept which could be built with existing technology. The LTD's "3-speed" combined-cycle engine is a much simplified version of the Apollo Lightcraft's engine; it eliminates the RDWE and MHD-fanjet propulsion modes.

A major conclusion of this year's study was the following: In order to continue climbing the steep learning curve in laser propulsion technology, emphasis must now switch to detailed engineering analysis of the most elementary propulsion system components, and to critical proof-of-concept experiments. The LTD vehicle provides just this sort of opportunity.

Chapter 2

Combined-Cycle Engine Developments

In this second year of the Apollo Lightcraft Project, much attention has been focused on systems integration of the complex combined-cycle engine. The great range of flight Mach numbers that such advanced airbreathing engines will experience during a transatmospheric flight will require the propulsion system to transition through a series of different thermodynamic cycles — in which each engine mode is optimized for maximum acceleration performance throughout its own relatively narrow Mach number range.

As with any new flight vehicle design effort, the resultant configuration is derived through a series of design compromises, which occur between (often times) conflicting requirements of aerodynamics, propulsion, structures, and payload/mission constraints. In the case of the Apollo Lightcraft, the engine is the entire vehicle; the payload simply occupies the volume dedicated to a large external compression inlet centerbody and the small amount of propellant (e.g., only 5–10% of the gross takeoff weight) is easily contained in the aft external expansion plug nozzle (see Fig. 2.1).

Although this vehicle configuration would appear to simplify the systems integration problem, this is not the case. Since flight propulsive power is delivered by an external energy beam, the receptive optical train places severe constraints on the flight platform geometry, which must be integrated with a large portion of the external vehicle surface. These constraints imply additional concessions to aerodynamics and structural mass fractions. Further, major concessions to vehicle/thruster geometry are demanded by each of the several propulsive modes which comprise the complete combined-cycle engine. Significant weight penalties are associated with the need for variable engine geometries (associated with each engine mode), so these complexities are invoked only when no other reasonable alternatives are available.

In the first year of RPI's Apollo Lightcraft Project, a "straw-man" vehicle configuration was presented, giving fairly specific contours for the external compression inlet centerbody, primary optics, afterbody plug nozzle, and annular shroud. The location of the secondary optics was indicated on several drawings, but the specific manner by which it was to be integrated into the variable geometry shroud — along with all auxiliary functions it must perform — was left largely to the imagination. It was quite apparent that the shroud was one area that required further definition. Another engine related problem was tied to the transition between the ERH thruster and scramjet modes; at Mach 3, the thrust from each mode fell precipitously to zero. These problem areas and others were resolved in the present year's design effort.

Figure 2.2 presents the "old" vehicle contours derived in the first year, along with the "newly refined" contours, which yield significant improvements in overall vehicle performance, for reasons which will become clear shortly. Further evolutions in the overall engine/vehicle optimized geometry can be accomplished only through a rigorous combined theoretical/experimental program that will certainly exceed the scope and resources of this modest NASA/USRA-sponsored program. Therefore, next year's effort will focus on the much simpler, near term engine of the Lightcraft Technology Demonstrator.

This year's combined-cycle engine effort gave special attention to five major areas:

1. Evaluation of engine/vehicle external geometry
 - (a) forebody and afterbody contours
 - (b) further definition of shroud multi-functions
 - (c) integration of receptive optical train
2. ERH thruster refinements
3. MHD-fanjet refinements

The significant accomplishments in each of these areas is described in detail below.

2.1 Engine/Vehicle External Geometry

A number of comments can be made in comparing and contrasting the "old" and "new" engine/vehicle loft lines presented in Fig. 2.2. First to be discussed will be the vehicle lower surface, whose function is now dictated by re-entry aerodynamic heating considerations.

The heat shield geometry was modeled after the GE Mark IV experimental re-entry vehicle, which was not designed for manned operation. Apparently this geometry could give rise to excessive peak re-entry G-levels approaching the

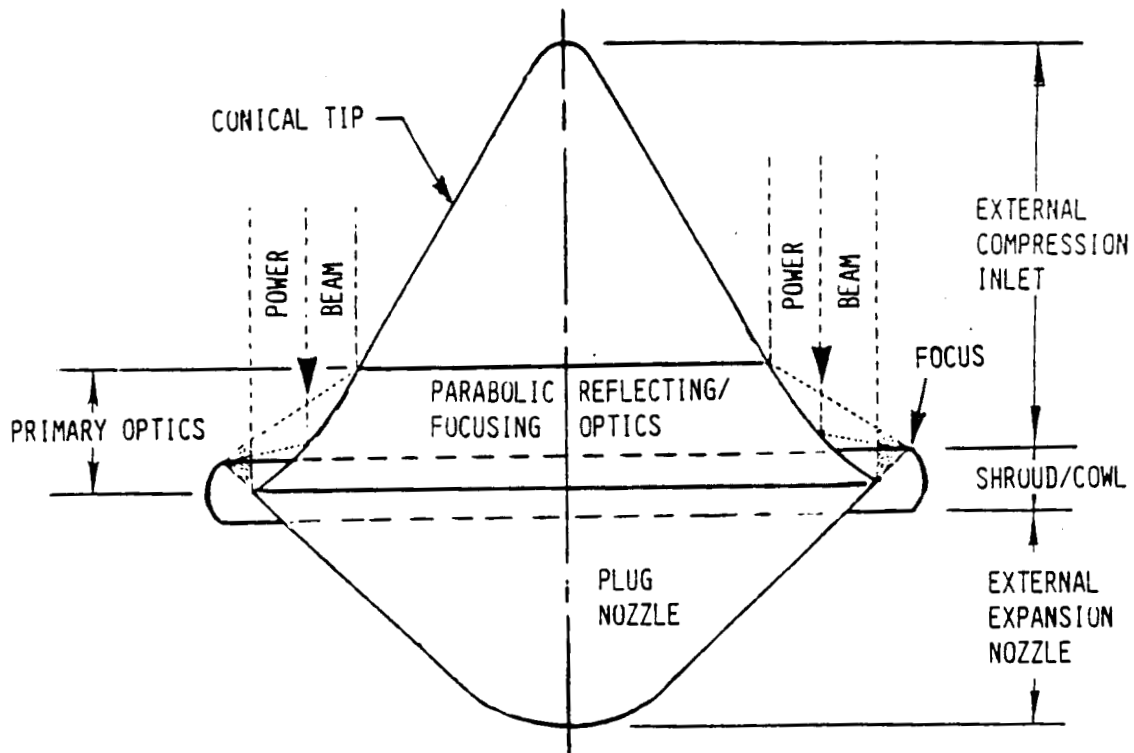


Figure 2.1: General Layout of Engine/Optics/Vehicle Configuration

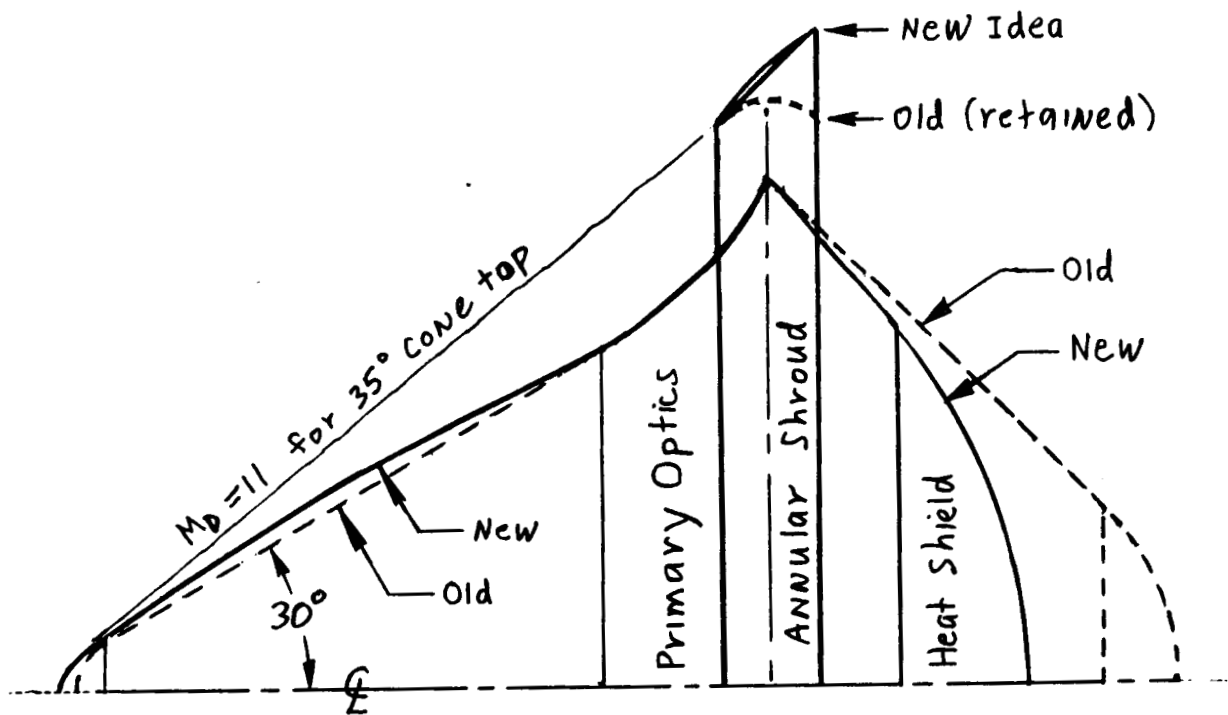


Figure 2.2: Forebody, Afterbody and Shroud Contours

limits of human tolerance. The new, more conservative contour is based on a cone half angle of 50° , and a much larger spherical nose radius almost as large as that used in the original Gemini or Mercury capsules. For Apollo Lightcraft vehicles capable of lunar missions, the lower heat shield geometry may have to match the original Apollo capsule. A major beneficial side effect of such *blunt* heat shields is that the liftoff Rotary Detonation Wave Engine (RDWE) will produce thrust more efficiently; the resultant thrust vector is more closely aligned with the vehicle flight axis.

Note in Fig. 2.2 that two shroud airfoil contours are indicated. As proposed in last year's study, the shroud would have a variable leading edge flap, and a large trailing edge flap that also functions as a variable exit nozzle. This nozzle would comprise the rear half of the shroud and would resemble the variable nozzles used on fighter aircraft today.

For this year's study, the shroud-lift ERH thruster analysis required the shroud to take on the appearance of a 60 cm long, flat-bottomed, circular arc airfoil set at an angle of 45° to the vehicle flight path (see Fig. 2.2). Obviously the shroud cannot assume an infinite variety of contours, but it must satisfy the needs of the ERH thruster, scramjet and MHD-fanjet modes. So far, only fore-aft shroud translation and variable leading/trailing edge flaps have been considered feasible. The final shroud geometry will, of course, be a compromise between several conflicting needs, and continues to be an area where more study is required.

Figure 1.10 shows the optical-related functions that the shroud interior surface must provide — as a function of flight Mach number. Even though the large primary optic will be equipped with electromechanical actuators on its rear surface to control the exact figure contour, the focus of the mirror cannot be changed. Hence, to transition between engine modes which require changing the receptive optical train geometry, the shroud must be translated aft — at the engine "shift points" — to engage different secondary optical (SO) surfaces. For example, in Fig. 1.10, the SO #1 (i.e., point "A") must be at the focus so that the beam can be re-directed to the tertiary optics (TO) (see Figs. 1.6 and 1.8) required for the RDWE ERH thruster mode. The RDWE mode is only used for liftoff and acceleration to Mach 1.

Above Mach 1, the shroud shifts aft to bring the 4 cm long super-ignitor array at point "B" (in Fig. 1.10) into the focus — in order to engage the "shroud lift" ERH thruster mode (refer to Fig. 1.9). This thruster mode accelerates the vehicle to Mach 6. Beyond Mach 6, the shroud shifts aft again to bring point "C" (see Fig. 1.10) into the focus, thereby engaging SO #2 for the scramjet propulsion mode portrayed in Fig. 1.11.

The scramjet mode accelerates the Apollo Lightcraft to a maximum flight Mach number of 11. At this point the shroud translates to its full aft position (see Fig. 1.13) to engage the MHD-fanjet mode, and the primary optics surface is no longer used. In the MHD-fanjet mode, propulsive laser power is brought into the engine through separate high power laser windows.

Throughout each combined-cycle engine mode, the bow shock must be prevented from entering the annular duct. If the shock is swallowed by the annular duct, engine performance will suffer dramatically. As a result, the engine forebody contour had to be altered this year from the (old) blunted 30° half-angle cone to the (new) ogive shape displayed in Fig.2.2. The former contour allowed the bow shock to attach at the shroud lip at a design flight Mach number of 4 (refer to Fig. 8 of Ref. [1]). This was acceptable for the old ERH thruster mode (used until Mach 3), but presented a major problem for the scramjet mode, which operated from Mach 3 to 11.

The new ogive inlet forebody has an effective cone half-angle of about 35° up near the rounded apex; this essentially converts the inlet design Mach number M_D to 11. Beyond Mach 11 (during which the MHD-fanjet operates), the shroud could be either shifted full aft to a new $M_D = 25$ position, or slowly moved aft so that the shock is always attached to the shroud lip.

The performance of any external compression is difficult to analyze analytically (i.e., pressure recovery and capture mass flow rate schedules vs. flight Mach number); e.g., the rate of energy release within the engine is known to greatly effect the amount of air actually entering the inlet. History has shown that experimental testing of such inlets under simulated flight conditions (and input power levels) is the only reliable means of predicting full scale inlet performance.

2.2 ERH Thruster Refinements

The major ERH thruster model refinements have occurred in the area of air refresh mechanisms. Here, "refresh" refers to the process by which fresh, unheated air is forcibly convected into the ERH thruster engine. This process can be likened to the "intake" cycle in a conventional Carnot thermodynamic cycle.

Figure 2.3 shows the three mutually-perpendicular directions in which the site of an LSD-wave heated line source can be refreshed: Lateral, perpendicular, or axial.

For the RDWE mode of the ERH thruster model developed last year, the lateral refresh mode is the most logical. Figure 2.4 illustrates the concept of how a RDWE propulsion system compresses fresh air into the next detonation site. This process can be likened to a supercharging effect. As mentioned earlier, the RDWE variety of ERH thruster can produce significant levels of thrust at zero forward velocity, and is still the most promising engine for acceleration through Mach 1. Incidentally, as will be covered more fully in a later chapter, thrust vector control in the RDWE mode is easily accomplished (see Fig. 2.5).

As illustrated in Fig. 2.6, the Apollo Lightcraft optical train permits a maximum of 12 line sources (i.e., plasma fingers) to be simultaneously pulsed (i.e., ignited), at any given moment. They could also be pulsed one at a time, as illustrated in Fig. 2.6. Several noise abatement procedures are available to the

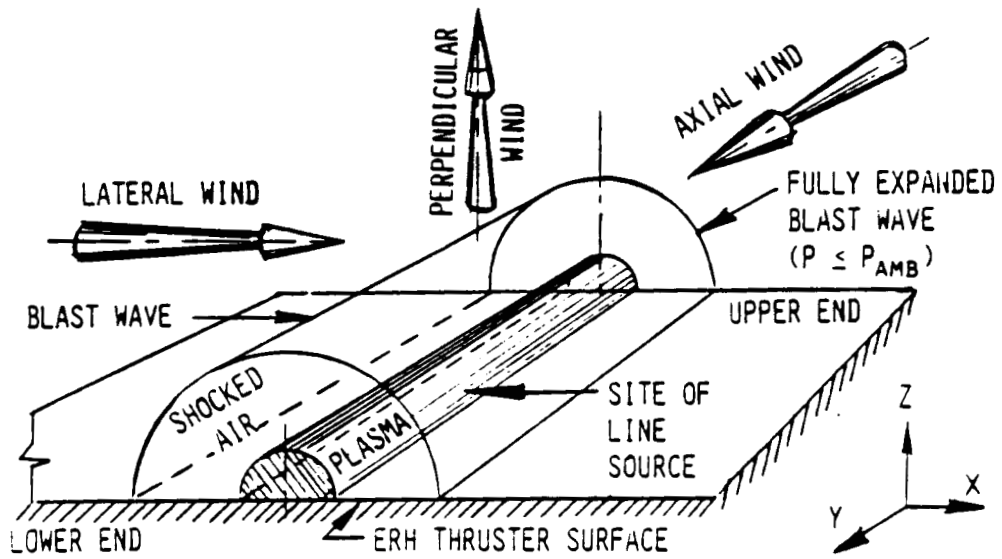
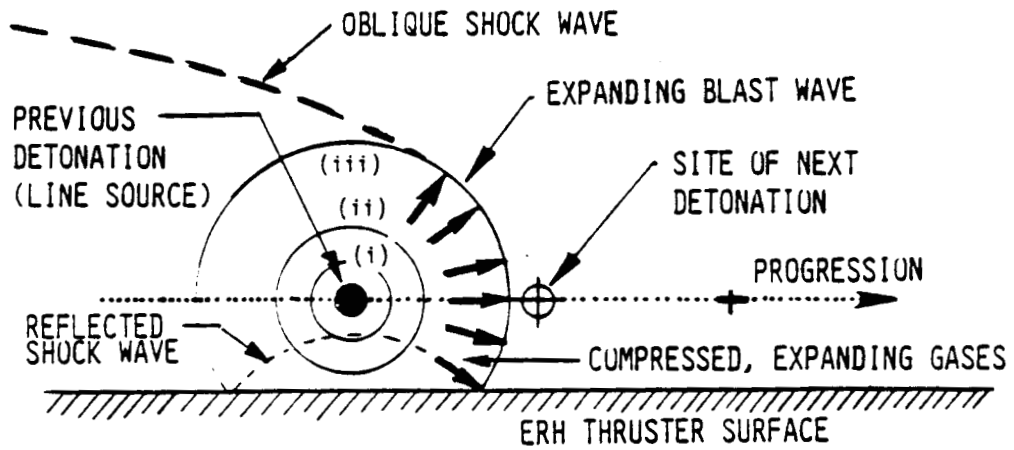


Figure 2.3: Basic ERH Thruster "Refresh" Modes



(BLAST WAVES CONVECT "REFRESH" GASES Laterally)

Figure 2.4: Rotary Detonation Wave Engine (RDWE)

RDWE pulsejet for use at low altitudes in populated regions. During hover and low subsonic flight, all 12 plasma finger could be pulsed at sub-audible frequencies (e.g., below 20 Hz).

During hard acceleration, each finger could be pulsed sequentially around the engine. If the engine/vehicle is also rotated, additional detonation sites could be created between the 12 fundamental sites. With such an approach, the pulsing frequencies could easily exceed 20,000 Hz (which are within the supra-audible region), beyond the limits of normal hearing. Other phased-ignition methods may be employed so that outgoing sound waves exactly cancel — in certain restricted modes of RDWE operation.

Beyond Mach 1, the ERH transitions to the shroud-lift mode portrayed in Fig. 1.9. Since the LSD-wave heated line source forms an annulus inside the shroud, the best mechanism for refresh is still with a lateral wind. As indicated in Fig. 2.7, the refresh wind blows by the shroud in a direction lateral to the ERH thruster surface. The actual 4 cm long surface, where the LSD waves are ignited inside the annular shroud, will probably require active cooling with some sacrificial liquid, as portrayed in Fig. 2.8. This heavily abused surface will be covered with a special super-ignitor array material that will minimize the time and energy expended on igniting the LSD wave. Transpiration cooling will probably be the most successful means of protecting the ignition surface from immediate destruction in the harsh, 600 atm pulsejet environment.

Detailed analytical calculations were performed for the new shroud-lift ERH propulsion mode. The results are presented in Appendix B. Note from the thrust and coupling coefficient plots that this new engine concept gives excellent performance in the flight Mach number range from 0.5 to 6.

2.3 MHD-Fanjet Mode

Last year's analysis of the MHD-fanjet mode indicated that the conductivity of the shock-heated air (i.e., the air passing through the shock formed over the forebody of the vehicle and attached at the shroud) entering the MHD accelerator was too low to obtain significant levels of thrust throughout typical trajectories flown by the Apollo Lightcraft. Flight performance for the MHD-fanjet was generated by assuming a specified level of conductivity enhancement; that is, the conductivity of the air entering the MHD accelerator was assumed to be increased by a specified amount using some conductivity enhancing mechanism. The level of conductivity enhancement required for operation decreases at higher Mach numbers since the temperature of the shock-heated air increases, resulting in an increase in the natural conductivity of the air. In the previous analysis, the level of conductivity enhancement was calculated such that the power required by the MHD accelerator was equal to the total power supplied by the MHD generators (for a given throttle setting). The resulting flight performance was exceptional — specific impulses of 6000 to 18,000 sec and corresponding coupling

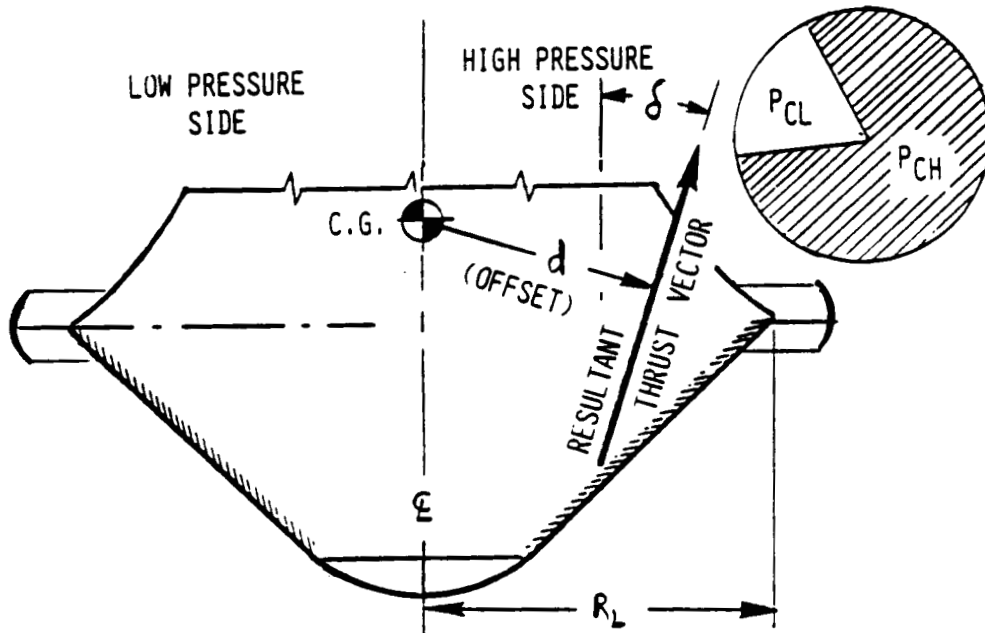


Figure 2.5: Thrust Vector Control Relationships

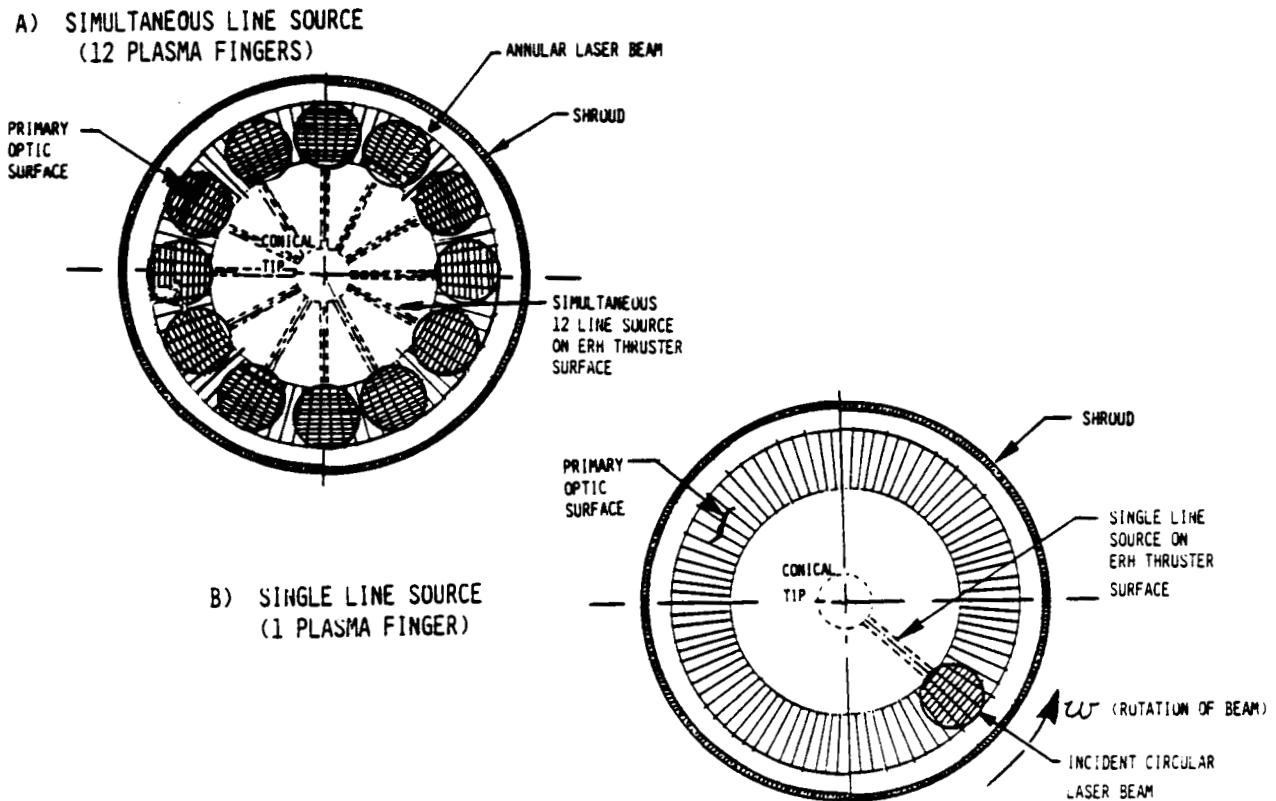


Figure 2.6: Top View of PO Surface Showing Beams and Plasma Fingers

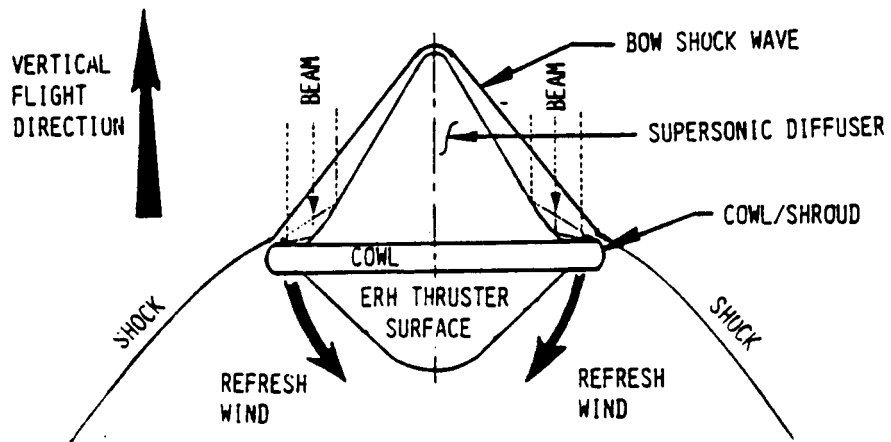


Figure 2.7: Forced Refresh Mode During Supersonic Flight

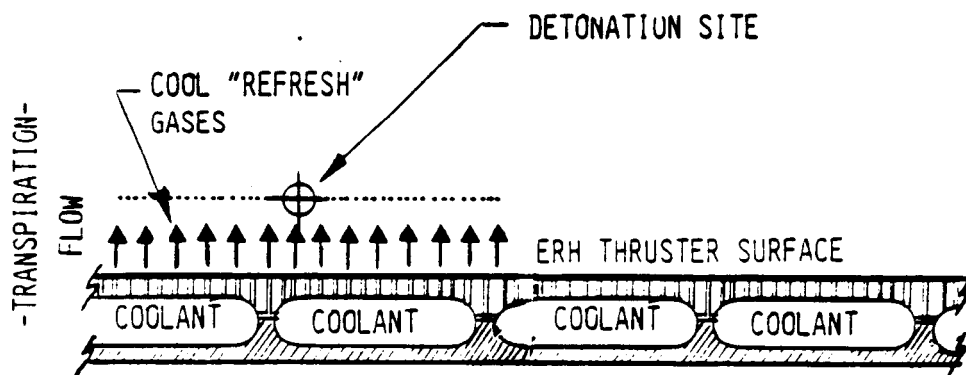


Figure 2.8: Actively Cooled "Super-Igniter-Array"

coefficients of 50 to 120 N/MW - for the flight envelope of the MHD-fanjet mode (100,00 to 250,000 ft. altitude and 11 to 25 flight Mach number).

It has not yet been determined that the levels of conductivity enhancement required for the above performance are obtainable, or that at least some significant levels of conductivity enhancement can be achieved; thus, the primary design challenge for the MHD-fanjet mode is to develop a mechanism for conductivity enhancement. The mechanism must be capable of producing sufficiently large increases in the conductivity of the air entering the MHD accelerator, while also having manageable power and mass requirements. Several mechanisms are currently being considered.

A considerable increase in the conductivity of the air entering the MHD accelerator can be attained by seeding the air (in concentrations of less than 1% per volume) with an easily ionized substance, such as potassium or cesium, at the inlet. Unfortunately, some of the seed particles may condense on the optics; this contamination will decrease the mirror reflectivity, which could result in destructive heating of the mirrors. Although feasible, the optical fouling associated with seeding makes it a poor candidate for a conductivity enhancement mechanism.

Alternatively, the air conductivity can be increased by pre-ionizing the air entering the accelerator. This problem is similar to that encountered in conventional electric discharge gas-flow lasers[2,3,4,5]. Such lasers typically employ one of four methods for pre-ionization:

1. Ultra-violet radiation;
2. Plasma jets;
3. Electron beams;
4. Neutron irradiation.

The electron beam appears to be the most attractive mechanism due to its higher efficiency. In the Apollo Lightcraft, several electron beam sources could be positioned somewhere above the primary optics, continuously firing against the annular inlet of the MHD accelerator. The mechanism is depicted in Fig. 2.9.

Quantitative data on the various mechanisms will require detailed analysis and is not yet available. This will be our primary task for the upcoming year in the design of the MHD-fanjet mode. A preliminary indication of MHD-fanjet performance was initiated by calculating the total thrust τ (i.e., the thrust due to the air accelerated through the MHD accelerator and the high velocity exhaust hydrogen of the MHD generators), the specific impulse,

$$I_{sp}\{\text{sec}\} = \frac{\tau}{\dot{m}_f g}, \quad (2.1)$$

and coupling coefficient

$$C\{N/MW\} = \frac{\tau}{\dot{m}_f Q_L} \quad (2.2)$$

for various levels of conductivity enhancement. The total mass flow rate of the hydrogen through the MHD generators, \dot{m}_f , depends only on the throttle setting *THROT* (i.e., \dot{m}_f equals some fraction of the mass flow rate for 100% throttle, which is the mass flow rate for the HIGH case MHD generator described in last year's report) and the laser energy per unit mass $Q_L = 123.64$ MJ/kg required per generator is assumed constant for various throttle settings. The coupling coefficient is therefore proportional to the specific impulse in the MHD fanjet mode.

Figures 2.10 and 2.11 indicate the effect of changing the Seed Factor, which is defined as the level by which the natural conductivity of the air is increased by one of the above mechanisms. The coupling coefficient $C\{N/MW\}$ may be extracted from Fig. 2.10 by dividing I_{sp} by a factor of 123.64. The figures illustrate that there will be a percentage decrease in τ , I_{sp} , and C corresponding to a percentage decrease in the Seed Factor. The magnitude of the percentage decrease in τ , I_{sp} , and C becomes larger as the flight Mach number increases. However, at the higher Mach numbers, large Seed Factors are not required. The MHD-fanjet performance calculated last year required a Seed Factors ranging from approximately 2800 mhos/m down to 1000 mhos/m for flight Mach numbers going from 11 to 24. If Seed Factors on the order of 1000 mhos/m can be generated by one of the previously discussed mechanisms, performance will not drop drastically from that calculated last year since the percentage decrease in τ , I_{sp} , and C would be on the order of only 25% for Mach numbers below 17 and for Mach numbers above 17, there would be less than a 5% decrease in performance.

Further improvements needed in the analytical model of the MHD accelerator are analogous to those currently occurring in the modelling of the MHD generators. A non-gray gas model for calculating the radiative heat transfer within an MHD generator is currently being formulated. Also, estimates of the power losses associated with eddy current loops formed at the entrance and exit of an MHD generator duct due to the decrease in the applied magnetic field and of power losses due to finite electrode wall segmentation have begun. The MHD accelerator model must also include wall effects eventually. Finally, some attempt to optimize the magnitude of the applied magnetic field in the MHD accelerator to produce maximum velocity increase over the flight envelope should be considered.

References

- [1] Myrabo, L. N. (editor), *Apollo Lightcraft Project*, 1987 report to NASA/USRA Advanced Design Program—Summer Conference.

- [2] Judd, O. P., "An Efficient Electric CO₂ Laser Using Pre-Ionization by UV Radiation," Appl. Phys. Lett., vol. 22, pp. 95-96, Feb. 1973.
- [3] Zaroslov D. Yu., et. al., "Plasma Jet CO₂ Lasers," JETP Lett., vol. 15, pp. 470-472, June 1972.
- [4] Gainsworth, R. K., Mathias, L. E. S. and Cormichael, C. H. H., "Atmospheric Pressure Pulsed CO₂ Laser Utilizing Pre-Ionization by High-Energy Electrons," Appl. Phys. Lett., vol. 19, pp. 506-508, Dec. 1971.
- [5] Ganley, T., Verdeyan, J. T. and Milley, G. H., "Enhancement of CO₂ Laser Power and Efficiency by neutron Irradiation," Appl. Phys. Lett., vol. 18, pp. 568-569, June 1971.

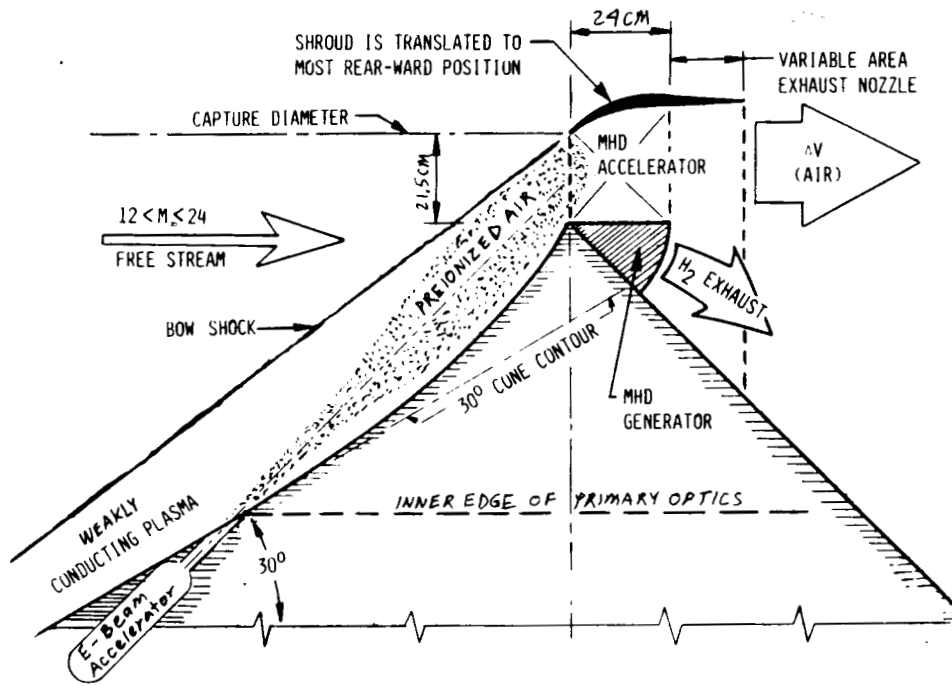


Figure 2.9: MHD Accelerator Using an Electron Beam as a Pre-ionizer

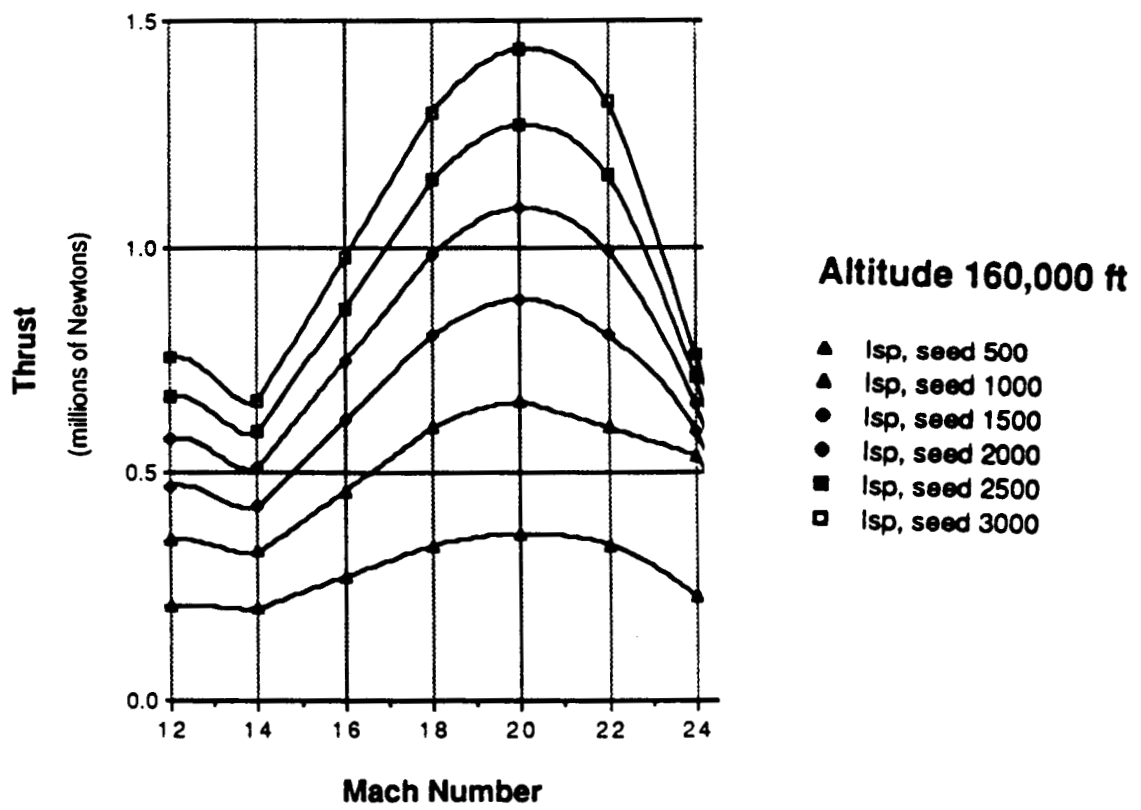


Figure 2.10: Thrust vs. Mach Number and Seed Factor

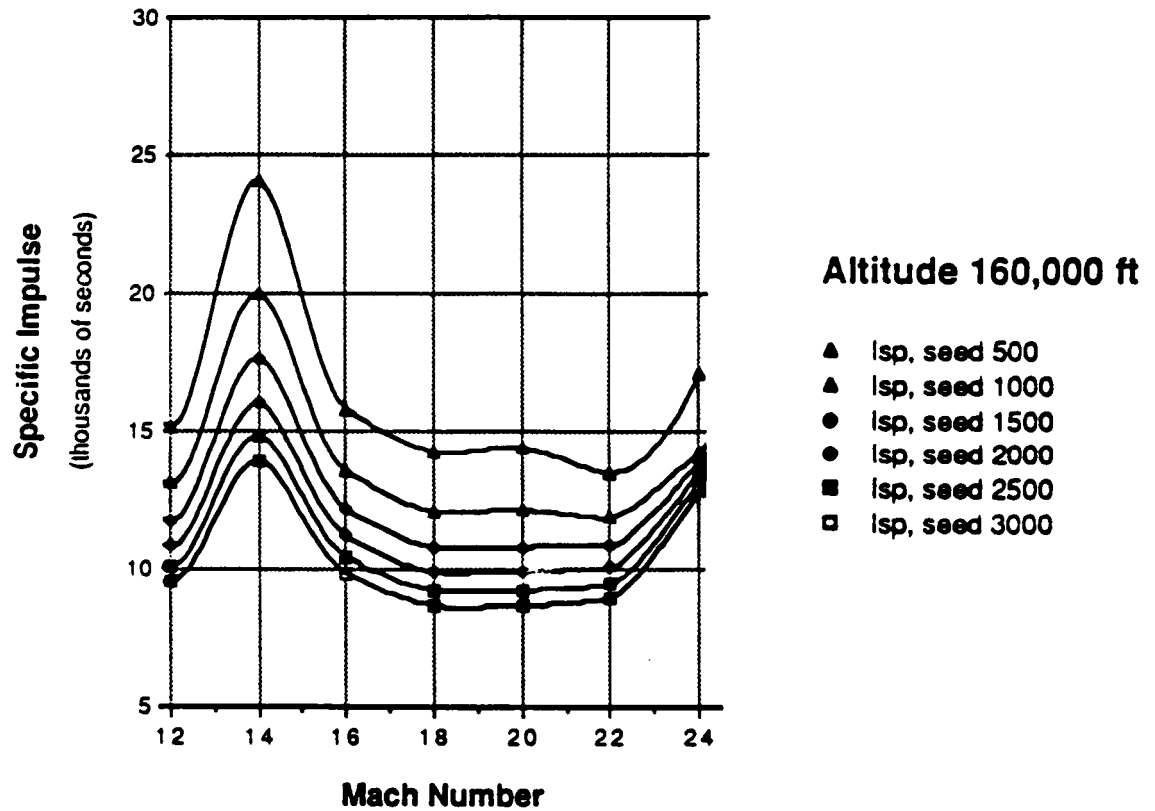


Figure 2.11: Specific Impulse vs. Mach Number and Seed Factor.

Chapter 3

Optical Train for Propulsion

3.1 Generalized Active Optical Area Analysis

The fractional active optical area for the Apollo Lightcraft has been calculated in a previous design report[1]. However, this analysis assumed that the focal point of the primary optic (PO) remains fixed at the shroud tip. In practice, the PO focus should be located slightly behind the secondary optic (SO), so that the fluence does not exceed about 100 J/cm². Fortunately, the earlier design report's calculations may be extended to consider this case.

The basic geometry of the optical train and significant variables for the analysis are defined in Figure 3.1. The original analysis of fractional active area may be found in Ref. [2]; we will merely outline the calculation. Using the variables defined in Figure 3.1, the fractional active area, A , is given by

$$A = \frac{\pi X_i^2 - \pi(X^-)^2}{\pi R^2} \quad (3.1)$$

where R is the radial position of the PO focus. That is, the PO is taken to be a parabolic surface defined by

$$y = \frac{(X - R)^2}{4F} \quad (3.2)$$

The height of the PO focus, F , is defined by

$$F = \frac{R\left(\frac{1}{\tan \Theta} - \frac{1}{\tan \beta}\right) - D}{1 + \frac{1}{\tan^2 \Theta}} \quad (3.3)$$

The previous analysis assumed $D = 0$, that is, the PO focus was located at the shroud tip. We will allow D to vary over the height of the SO (which has been estimated in a previous report). Additionally, we will consider the effect of shifting the PO focus distance, R , further behind the shroud tip.

Determination of the fractional active area also requires the computation of the quantity X^* , given by

$$X^* = R - \frac{2F}{\tan \Theta} \quad (3.4)$$

and X_i , which is the negative root of the equation

$$X_i^2 + \left[-2R - \frac{4F^2}{X} \right] X_i + \left[R^2 - 4F^2 \left(1 - \frac{R}{X} \right) \right] = 0 \quad (3.5)$$

where

$$X = F \tan \alpha. \quad (3.6)$$

As in the earlier analysis, we assume that the conical bow shock remains attached at the cowl lip to minimize spillage drag. Tabulated values of the shock wave angle, β , were taken from Ref. [12] for a given Mach number and forebody angle, Θ . The afterbody angle, α , was taken to be 30° or 45° . The fractional active area as a function of forebody apex half angle for $D = 0.25$ cm is shown in Figures 3.2 and 3.3. A small, non-zero D increases the active area slightly at all Mach numbers.

In addition to vertically repositioning the PO focus, we would like to move it slightly behind the SO by increasing R . The active optical area was calculated for a fairly wide range of R and D ; the results are shown in Table 3.1. Close inspection of Table 3.1 reveals that F increases linearly with R to maintain constant active area.

Based on these results, it should be possible to specify values of R , D and F such that the PO focus is positioned safely behind the SO, without decreasing the active area which was specified for $D = 0$. D should be chosen as half the height of the SO (0.25 cm) while $R \approx 10$ cm behind the SO; this will insure that the SO is not subjected to critical fluence levels. For these values, we calculate a fractional active area of 0.570 and $F = 32.32$ cm.

3.2 Beam Coherence and Divergence

In the following section, we will consider in more detail two specific properties of the power beam which affect the performance of the vehicle's optics. Since we are beaming power over such a long distance (some 36,000 km from a geosynchronous power satellite), the beam will diverge, or spread its cross-sectional area. The vehicle's optical train should account for such divergence. We will derive the basic relationships for beam divergence, following the treatment of Ref. [5].

The spread of a propagating beam may be predicted from the uncertainty relationship between the wave vector, k and the spatial extent of the beam, y , namely [5]:

$$\Delta k \Delta y \geq \frac{1}{2} \quad (3.7)$$

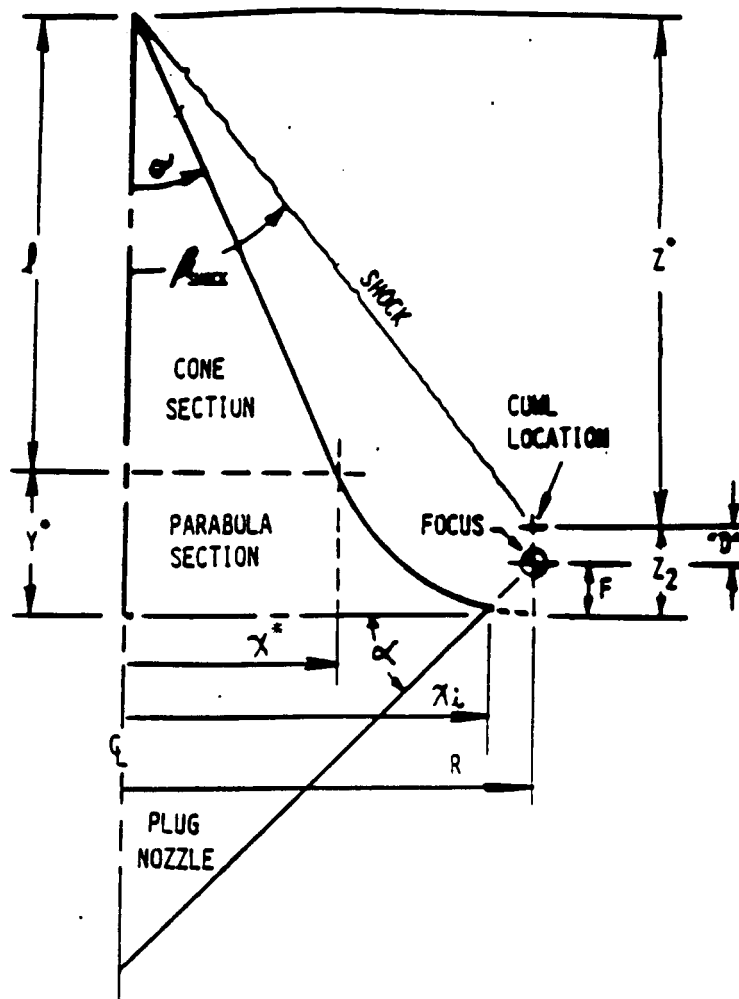


Figure 3.1: Geometry for Fractional Active Area Analysis.

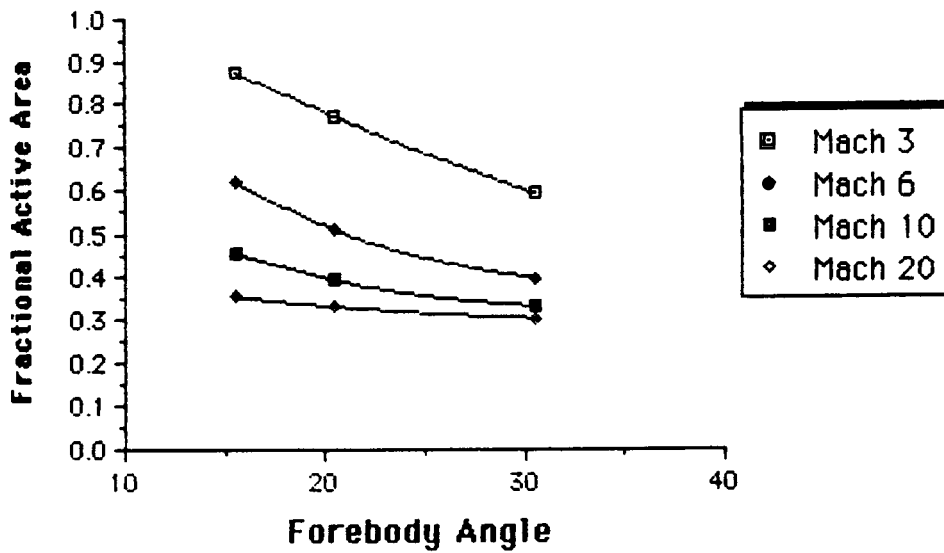


Figure 3.2: Active Optical Area, $\alpha = 30^\circ$

R (cm)	D (cm)	Fractional active area	F (cm)
234	0.25	0.570	30.99
	1.00	0.568	30.81
	2.00	0.565	30.50
	5.00	0.556	29.81
	10.0	0.540	28.56
244	0.25	0.570	32.32
	1.00	0.568	32.10
	2.00	0.565	31.82
	5.00	0.556	31.14
	10.0	0.540	29.88
254	0.25	0.570	33.65
	1.00	0.568	33.47
	2.00	0.565	33.21
	5.00	0.556	32.46
	10.0	0.540	31.21

Table 3.1: Change in Fractional Active Area and F as a Function of R and D

Initially, the beam diameter is limited by the radius of the source aperture or beam waist, w_o . However, in the far field we assume the beam to have a Gaussian profile of the form

$$E(y) = E_o e^{-[y/w_o]^2} \quad (3.8)$$

where it is sufficient to specify the beam profile in one dimension, since the two dimensional problem is symmetric. The beam profile is sketched in Figure 3.4; note that the Gaussian spatial envelope also implies a spread in wave vectors of the form

$$E(k) = \sqrt{\pi} w_o E_o e^{-[\frac{1}{2} k w_o]^2} \quad (3.9)$$

as shown in Figure 3.4. Geometric optics yields a simple relationship for the beam divergence angle,

$$\frac{1}{2} \Theta \approx \frac{\Delta k}{k} \approx \frac{\lambda}{\pi w_o} \quad (3.10)$$

or

$$\Theta \approx \frac{2\lambda}{\pi w_o} \quad (3.11)$$

Note that the divergence angle is a function of wavelength, and that an infinite radius beam does not spread. However, the geometric argument is not exact, and this equation is necessarily an approximation. We can calculate a better estimate by considering the effects of beam coherence.

Consider the two beams represented by Figures 3.5 and 3.6; although they

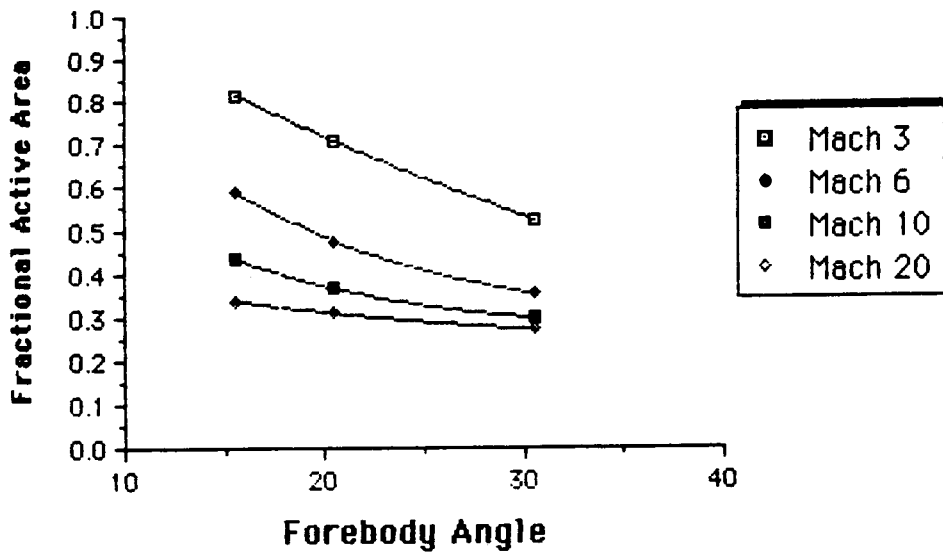


Figure 3.3: Active Optical Area, $\alpha = 45^\circ$

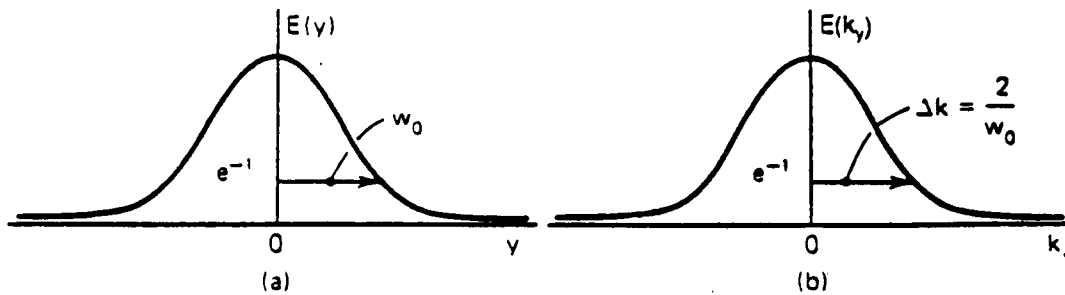


Figure 3.4: Relationship Between (a) Spatial Extent of a beam and (b) Wave Number, k [5].

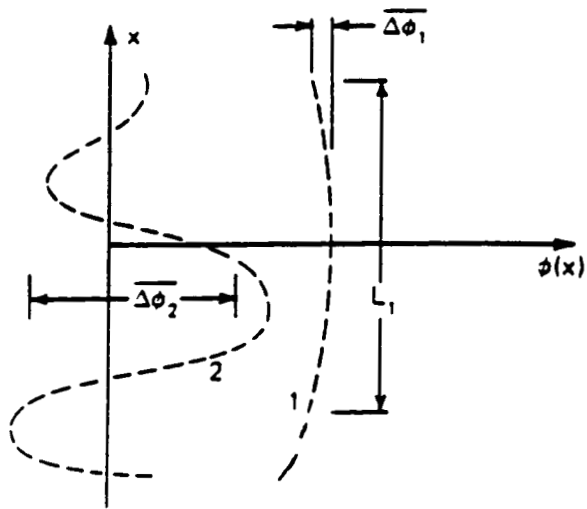


Figure 3.5: Two Beams of Equal Power but Different Phase Profiles [5].

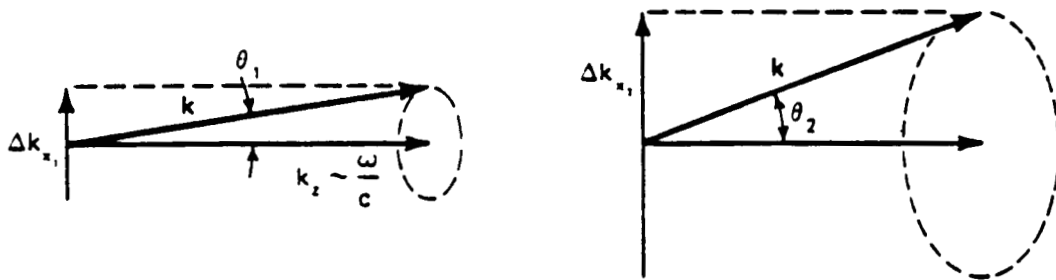


Figure 3.6: Divergence of the Two Beams Shown in Figure 3.5 [5].

have the same initial size, L_1 (and would convey the same power), their phase variation in the transverse direction is considerably different. The first beam has a much smoother phase profile than the second. Since in practice the beam phase always shows some variation (except in the case of an infinite plane wave, as discussed earlier), there must be some component of the wave vector, however small, normal to the propagation direction. The magnitude of this component is well estimated by the mean phase change divided by the beam radius,

$$\Delta k \approx \overline{\Delta\phi}/w_o \quad (3.12)$$

Thus, the wave vector diagrams for the two cases are shown in Figures 3.5 and 3.6. The far field divergence angle can be seen to depend on the phase difference; for small Θ we have

$$\Theta \approx \frac{\Delta k}{k} = \frac{\overline{\Delta\phi}\lambda}{2\pi w_o} \quad (3.13)$$

The beam with the smaller phase variation, or higher coherence, diverges much less. This suggests a highly coherent, phase-locked beam source to minimize beam divergence.

However, a highly coherent source is not the solution to all of our design problems. recall that the beam will be divided into 48 laser "fingers" during ERH thruster mode, which will recombine near the LSD wave ignition point on the vehicle afterbody. Even if only a few laser fingers are generated at once, using a rotating beam, there is still a possibility of interference occurring near the LSD wave ignition point. The resulting interference fringes may not only provide non-uniform generation of LSD waves, but the intensities achieved by constructive interference on the afterbody could be dangerously high, in excess of 5×10^9 W/cm². This presents a classic design conflict; on one hand, a highly coherent beam is desirable to minimize divergence. On the other, we require the ERH laser fingers to be sufficiently incoherent to prohibit interference occurring.

The conflict may be resolved by noting that high coherence is required only until the beam reaches the vehicle. After that point, we would like to induce some degree of spatial phase variation across the beam. The bow shock wave is capable of providing such distortions; it has been shown in a previous section that the beam phase, P , varies according to

$$P \propto \frac{\rho_\infty}{\lambda\rho_{SL}} \int_a^b \left(\frac{\rho_a}{\rho_\infty} \right)_1 - \left(\frac{\rho_a}{\rho_\infty} \right)_2 dS \quad (3.14)$$

where ρ_∞ = Free stream atmospheric density at the vehicle altitude.
 ρ_a = Local density at vehicle surface due to the bow shock wave.
 ρ_{SL} = Atmospheric density at Sea Level.

and the line integral is taken along some distance of the beam path. This expression allows for phase variation between two ray paths, as specified by

Flight Mach Number	ρ_a/ρ_∞	Angle (degrees)	ρ_a/ρ_∞
1.4857	1.8249	30.0	2.0002
1.9274	2.0004	32.5	1.9953
2.6863	2.5280	35.0	1.9822
3.8497	3.3233	37.5	1.9632
5.0109	3.9716	40.0	1.9390
7.8599	4.9511	42.5	1.9090
16.6170	5.8194	45.0	1.8316

Table 3.2: Variation of Atmospheric Density as a Function of Mach Number and Vehicle Forebody Angle.

$(\rho_a/\rho_\infty)_1$ and $(\rho_a/\rho_\infty)_2$. Since the optical phase variation is highly dependent on atmospheric density properties, the phase can be expected to vary significantly during flight (see Table 3.2). Thus, we may use a highly coherent beam source and still achieve sufficient phase distortion at the vehicle to eliminate interference effects.

It is now possible to calculate divergence limits for the beam. Ideally, we would like to design the source such that the maximum divergence still equals the size of the PO. Note that since the far field divergence satisfies the small angle approximation, we have $\Theta \approx r/L$, where r is the beam radius at a distance L from the source. Using this approximation, the beam divergence is commonly expressed in terms of transmitter and receiver diameters, as follows:

$$D_R = 0.9 \frac{\lambda L}{D_T} \quad (3.15)$$

where $D_R =$ received beam diameter, $D_T =$ transmitted beam diameter, and the effect of $\overline{\Delta\phi}$ is neglected for a source without phase locking. A plot of D_R vs. D_T is shown in Figure 3.7 for different laser wavelengths, with $L = 36,000$ km. This figure illustrates once again the property that beam divergence is inversely proportional to the source aperture size, for a given λ and L . In addition, Figure 3.8 illustrates the variation of transmitter and receiver aperture size as a function of range from the source to vehicle.

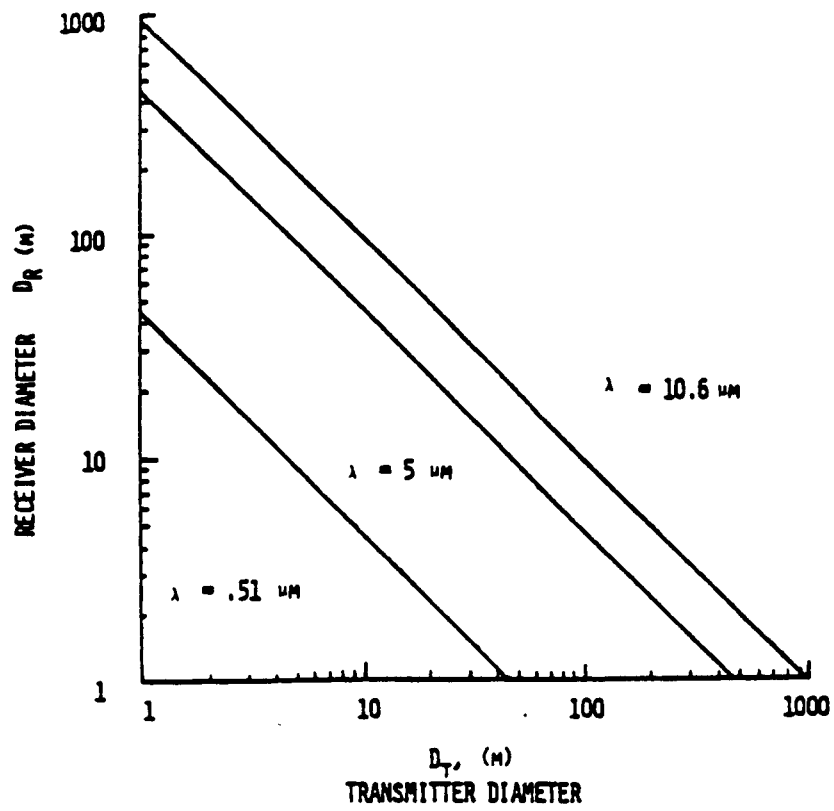


Figure 3.7: Laser Transmitter vs. Receiver Diameter for Path Length = 36,000 km [6].

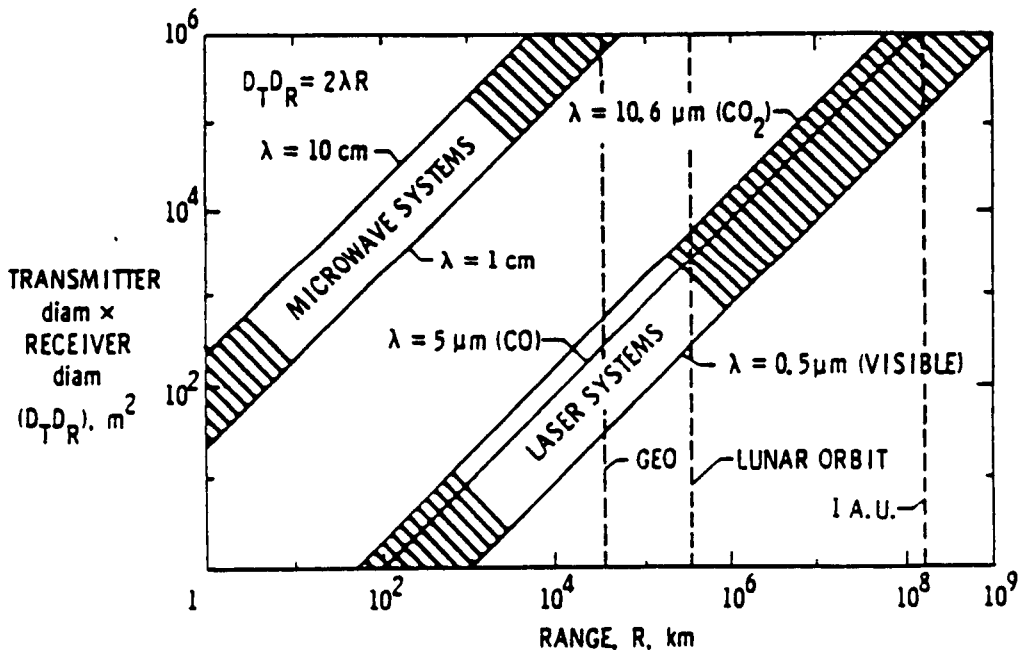


Figure 3.8: Transmitter/Receiver Diameter vs. Range [7].

Nomenclature

A	Fractional active area
D	Distance from cowl tip to primary optic focus
D_R	Received beam diameter
D_T	Transmitted beam diameter
F	Height of the primary optic focus
k	Wave vector
L	Distance from transmission to receiver locations
P	Beam phase
R	Radial position of the primary optic focus
w_o	Source aperture (beam waist)
X_i	Radius to edge of centerbody
X^*	Radial position of the edge of the parabolic surface
y	Spatial extent of the beam, generalized axial coordinate
β	Shock wave angle
$\overline{\Delta\phi}$	Mean phase change
λ	Operating wavelength
ρ	Density
Θ	Forebody semi-vertex angle, beam divergence angle

References

- [1] L. Myrabo et al., "Apollo Lightcraft Project Design Report." NASA/USRA Advanced Design Program, Third Annual Summer Conference, June 1987.
- [2] D. Cross, "Apollo Lightcraft Primary Optic Active Area Analysis," (RPI Library Reserve), 1986.
- [3] Hecht and Zajac, *Optics*. Addison Wesley, NY, 1979.
- [4] A. Bubbenzer, B. Dischler, A. Nyaiesh, "Optical Properties of Amorphous Carbon," Proc. Symposium on Laser Induced Damage in Optical Materials, Boulder, CO, 1981, p 477.
- [5] J. Verdeyen, *Laser Electronics*, Prentice-Hall, (1984).
- [6] D. Humes, "Preliminary Study on the Use of Lasers for Transmission of Power," Proc. Symposium on Space Laser Power Transmission Systems Studies, 1981, p 15.
- [7] P. F. Holloway, L. Bernard Garrett, "Utility of and Technology for a Space Central Power Station," Ibid, p 86.
- [8] Barnoski, *Fundamentals of Optical Fiber Communications*, Academic Press, 1976.

- [9] M. Mitchell Waldrop, "The Mirror Maker," (an interview with Dr. Roger Angel, Univ. Arizona), *Discover*, December 1987, pp 78-87.
- [10] S. Hoenig, "Electrostatic Technology for Control of Dust and Hydrocarbon Vapors in High Power Laser Systems," Proc. Symposium on Laser Induced Damage in Optical Materials, 1981, p 280.
- [11] A. D. Moore, *Electrostatics and its Applications*, McGraw-Hill, NY.
- [12] J. L. Sims, "Tables for Supersonic Flow Around Right Circular Cones at Zero Angle of Attack," NASA Report SP-3004.

Chapter 4

Phase Distortion Due to Aero-Optical Phenomena

The interaction between a propulsive laser beam and the flowfield after the shock wave, generated during the flight of a beam-powered conical-shaped transatmospheric vehicle (TAV), is studied. Although the theoretical model adopted is a simplified one, the results of this study anticipate some of the aero-optical phenomena to be expected during a beamed transatmospheric flight. By considering a propulsive beam operating at $3.8 \mu\text{m}$, phase distortions up to 51.41 wavelengths are reported. The range of flight Mach numbers covered by the present analysis falls between 1.67 and 20. As a major conclusion, considerable beam degradation can be expected only during the beginning of the beamed transatmospheric flight.

4.1 Introduction

The Apollo Lightcraft will have to cross the Earth's atmosphere at supersonic and hypersonic velocities while receiving a very intense laser beam (\sim ten thousand W/cm^2). Before this beam can be taken into the propulsive engines, it must first transverse a conical shock wave, caused by the external compression inlet, across the vehicle forebody. As is well known, a compressible flow over a laser mirror or window causes variations in air density and the index of refraction. These variations introduce a phase shift (or distortion) in the beam. This phase distortion creates optical aberrations in the propulsive beam such as tilting, refocusing, astigmatism and coma. The intensity of these aberrations can be evaluated using the Zernike Polynomial coefficients. These polynomials will be discussed later.

For the sake of simplicity, a few simplifying assumptions are introduced.

These are:

1. The Apollo Lightcraft forebody is assumed to be conical;
2. During the flight, the vehicle angle of attack is set equal to zero;
3. The flow over the mirror (or windows) is assumed to be inviscid;
4. The air behaves as an ideal gas.

The impact of these assumptions on the phase distortion calculations is discussed below.

The work reported here is based on a previous investigation accomplished by A. E. Fuhs on laser turrets[4]. Therefore, the notation adopted in this paper (with regard to phase distortion calculations) will be the same as that of Ref. [4].

4.2 The Apollo Lightcraft Simplified Forebody

The laser power is projected from an orbital relay satellite by twelve cylindrical laser beams equally spaced along the primary optics circumference. Due to the symmetry, just one beam-shockwave interaction needs to be studied.

The performance of the Apollo Lightcraft strongly depends on the laser beam "quality." Furthermore, in the first two thruster modes (ERH and scramjet), the focus position at the secondary optics (shroud) is critical. A slight movement of that focus can drastically alter the TAV trajectory[3]. Even for the last two thruster modes (MHD-fanjet and rocket), if the beam degradation is too high, the coupling coefficient will decrease. As a consequence the global efficiency of the system will also decrease.

Since beam degradation can be predicted by knowing the optical phase distortion distribution over the beam wavefront[4,5], the present analysis is fully justified.

In order to evaluate the beam degradation due to aero-optical phenomena, some simplifications shall be introduced. The isentropic spike-shaped Apollo forebody will be replaced by a conical approximation. This geometry will retain the same original 30° semi-apex angle but will not have the subsequent parabolic section. With this assumption air flow over the forebody will be conical. Therefore, the computed density gradients will be lower than the real ones. This occurs since the simplified flow does not take into account the additional compression introduced by the downstream parabolic section. As it will be seen, the optical phase distortion is proportional to the density gradients crossed by the beam. Hence, the predicted values for beam distortion will be lower than the actual ones.

Another implication of the previous assumption is that the primary optics will be *conical* instead of *parabolic*. As a result there will be no focusing effect in this analysis.

The Apollo Lightcraft simplified forebody indicated with one of the twelve propulsive laser beams is shown in Figures 4.1 and 4.2. Figure 4.1 portrays a simplified version of the ERH and scramjet thruster modes, while Figure 4.2 depicts the simplified situation for the MHD-fanjet mode.

In both the ERH and scramjet thruster modes, it is of interest to evaluate the optical phase distortion at the primary optics focal point. In the simplified problem depicted in Figure 4.1, the problem is approximately equivalent to computing the phase distortion when the reflected beam emerges from the conical wave.

On the other hand, in the MHD-fanjet mode the goal is to calculate the phase distortion distributions developed by the beam at the receiving optics—*inside* the TAV (as seen in Figure 4.2).

Both Figures 4.1 and 4.2 show a cross-section of the vehicle and one of the twelve cylindrical beams in the x - y plane. This plane contains both the TAV axis and the laser beam axis. Note that θ_c stands for the cone semi-apex angle, θ_w is the conical shock wave semi-apex angle, r_o is the distance between the TAV centerline and the laser beam axis, r_i is the distance between a generic ray “ i ” inside the beam and the TAV axis, D is the beam diameter, θ is the polar coordinate and S is a distance along the laser beam. The cylindrical coordinates α and r determine a specific starting ray inside the beam. Finally, M_∞ is the free stream or flight Mach number.

4.3 Laser Beam Phase Distortion Calculations

Although the optical phase distortion can be caused by an external viscous flowfield[4,8], the following calculations will not take into account such viscous flow phenomena. The conical flow field will be assumed to be inviscid. Therefore only the optical phase distortion due to an external inviscid flowfield will be considered in this work.

The phase distortion problem is not only associated with beamed transatmospheric flight; very similar problems are observed in gasdynamic[9] and chemical lasers (ie., flow lasers in general), aerodynamic windows[9,10], and laser turrets[4]. In all of these cases, an optical phase distortion is developed by a laser beam due to density inhomogeneities in the propagation and/or generation media.

The optical phase distortion P can be defined as the difference in the optical path length ΔL between two rays i and j within the laser beam divided by the wavelength of the radiation. So,

$$P = \frac{\Delta}{\lambda} = \frac{L_j - L_i}{\lambda} \quad (4.1)$$

On the other hand, the optical path length L_i for a particular ray i inside

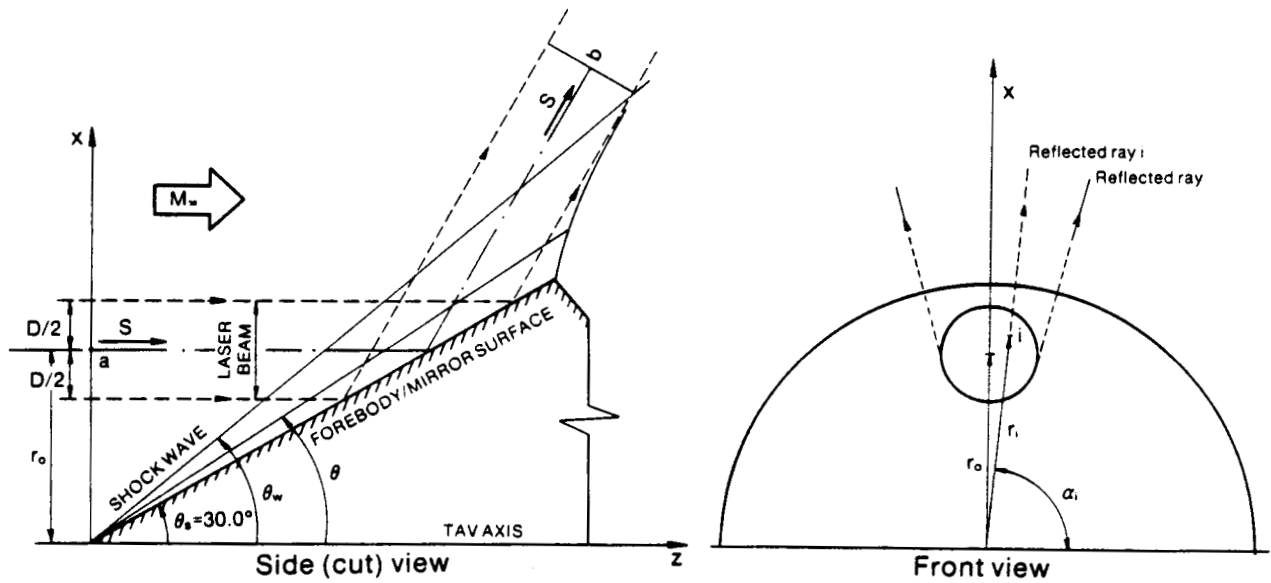


Figure 4.1: Simplified Geometry of the Apollo Lightcraft Forebody in ERH or Scramjet Thruster Mode. Neither the Shroud nor the Plug Nozzle were Represented.

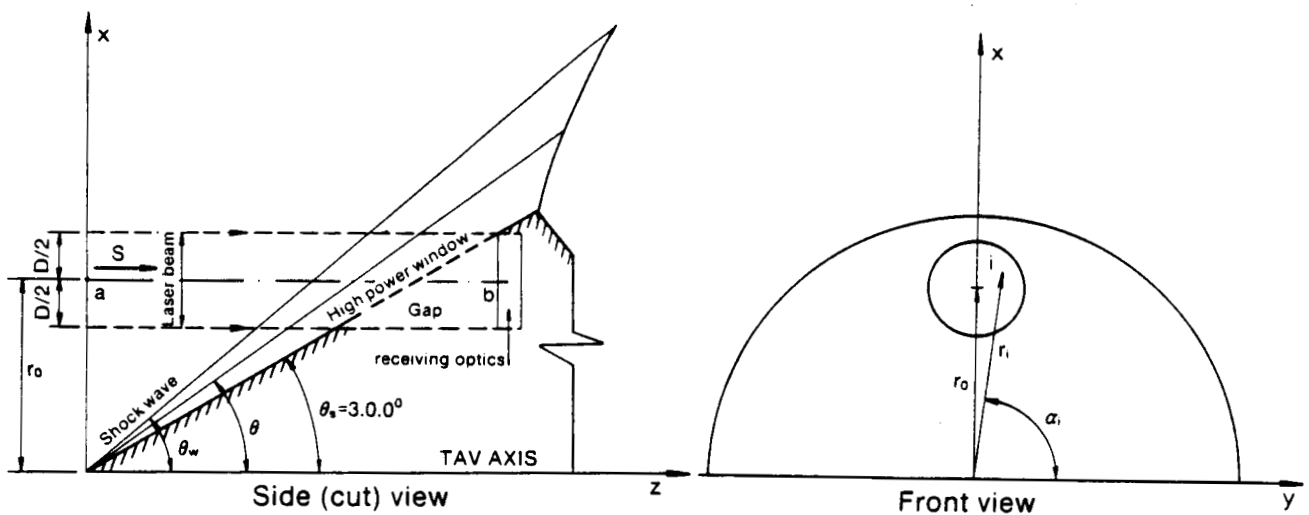


Figure 4.2: Simplified Geometry of the Apollo Lightcraft Forebody in MHD-Fanjet Thruster Mode. Neither the Shroud nor the Plug Nozzle were Represented.

the laser beam is defined as

$$L_i = \int_a^b n(S) dS \quad (4.2)$$

where S is the distance along ray i and the points a and b are positioned on the ray. The index of refraction n is a function of S . As a consequence, Eqn. 4.1 can be written as

$$P = \frac{1}{\lambda} \int_a^b [n(S_j) - n(S_i)] dS \quad (4.3)$$

The local index of refraction n is related to the local gas density ρ by

$$n = 1 + \kappa \frac{\rho}{\rho_\infty} = 1 + \kappa' \left(\frac{\rho_\infty}{\rho_{SL}} \right) \left(\frac{\rho}{\rho_\infty} \right) \quad (4.4)$$

where ρ_∞ is the free stream density at the TAV altitude, and ρ_{SL} is the density at sea level. The constant κ' has an invariant value of approximately 2.3×10^{-4} for infrared radiation. From Eqns. 4.3 and 4.4, one can obtain

$$P = \frac{\kappa' \rho_\infty}{\lambda \rho_{SL}} \int_a^b \left[\left(\frac{\rho}{\rho_\infty} \right)_j - \left(\frac{\rho}{\rho_\infty} \right)_i \right] dS \quad (4.5)$$

The above expression shows a dependence on altitude through the term (ρ_∞/ρ_{SL}) and on the density ratio (ρ/ρ_∞) . The subscripts i and j in the density ratio terms refer to the density ratio along the rays i and j respectively.

4.4 The Conical Flowfield Solution

From Eqn. 4.5, in the previous section, the calculation of the phase distortion encompasses the knowledge of the density ratio (ρ/ρ_∞) . That density ratio can be obtained by solving the Navier-Stokes equations with suitable boundary conditions. These boundary conditions are the TAV forebody geometry and the shock wave. By assuming a conical forebody and isentropic flow behind the shock wave, one can write[11]:

$$\frac{dU}{d\theta} - V = 0 \quad (4.6)$$

$$\frac{dV}{d\theta} - U + \frac{1}{\rho V} \frac{dp}{d\theta} = 0 \quad (4.7)$$

$$\frac{d(\rho V \sin \theta)}{d\theta} + 2\rho U \sin \theta = 0 \quad (4.8)$$

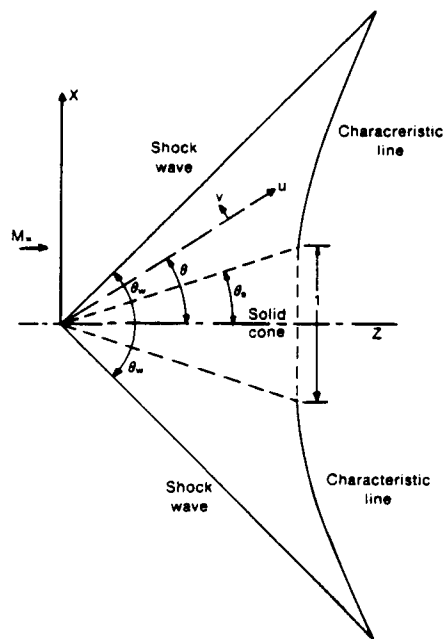


Figure 4.3: Coordinate System[13]

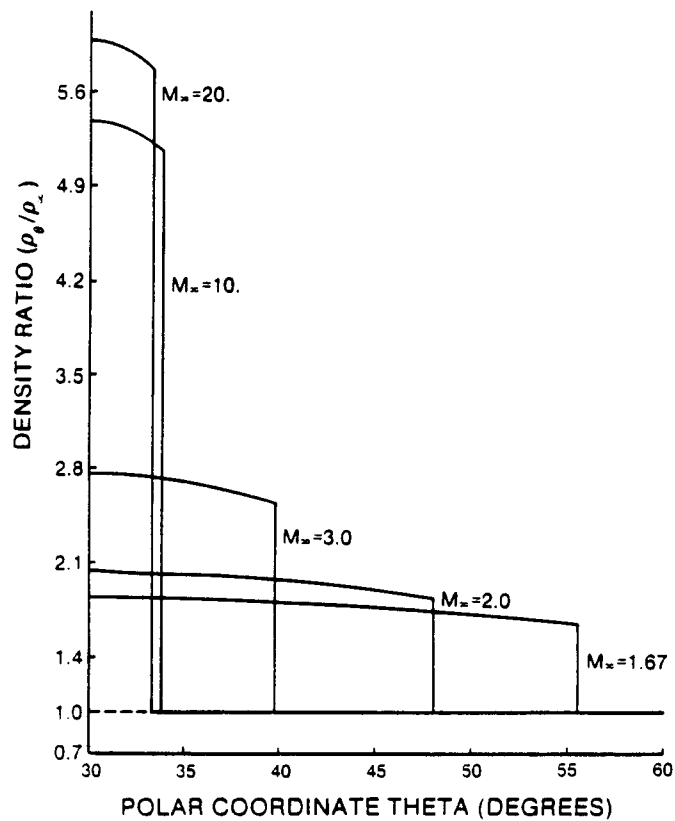


Figure 4.4: Density Ratio vs. θ for Several Flight Mach Numbers

with the following boundary conditions:

$$\text{at } \theta = \theta_s \longrightarrow U = U_s \text{ and } V = 0 \text{ (wall condition)}$$

$$\text{at } \theta = \theta_w \longrightarrow U = U_w \text{ and } V = V_w \text{ (shock condition)}$$

where θ_w , U_w and V_w must satisfy the following relations:

$$\tan \theta_w = \frac{\gamma - 1}{\gamma + 1} \frac{c^2 - U_w^2}{U_w V_w} \quad (4.9)$$

$$M_\infty = \left(\frac{2}{\gamma - 1} \right) \frac{U_w^2}{c^2 \cos^2 \theta_w - U_w^2} \quad (4.10)$$

$$c^2 = U_\infty^2 \left[1 + \frac{2}{\gamma - 1} M_\infty^2 \right] \quad (4.11)$$

where γ is the ratio of specific heats, U and V are the flowfield velocity components in the polar coordinate system, ρ is the local density, p is the local pressure and c is the velocity the fluid would obtain if allowed to expand adiabatically into a vacuum. All the presented variables are shown in Figure 4.3.

Equations 4.6, 4.7 and 4.8 must be solved numerically subject to the boundary conditions indicated above. This task was first accomplished by Kopal[12] and later by Sims[13]. These equations indicate that the flow properties ρ , p and T (absolute temperature) can be written in terms of the polar coordinate θ ; thus, the flow properties are constant over imaginary conical surfaces located between the conical shock wave and the TAV surface. Figure 4.4 shows the density ratio $\rho(\theta)/\rho_\infty$ as a function of θ for several flight Mach numbers.

Figure 4.5 portrays a Schlieren photograph of a 30° semi-apex angle cone undergoing a Mach 10 experiment in a combustion driven Shock Tunnel.

Note that all plots involving the flight Mach number M_∞ start at $M_\infty = 1.67$, since this is the lowest M_∞ which provides an attached conical shock wave for $\theta_s = 30^\circ$.

4.5 Numerical Results

From the preceding section, Eqn. 4.5 can be written as

$$P = \frac{\kappa'}{\lambda} \left(\frac{\rho_\infty}{\rho_{SL}} \right) \int_a^b \left[\left(\frac{\rho(\theta)}{\rho_\infty} \right)_j - \left(\frac{\rho(\theta)}{\rho_\infty} \right)_i \right] dS \quad (4.12)$$

If one assumes that a is located at the incident wave and b is located at the wavefront for which the phase distortion is to be evaluated, the optical phase distortion becomes

$$P = \frac{\kappa'}{\lambda} \left(\frac{\rho_\infty}{\rho_{SL}} \right) \int_0^{S_0} \left[\left(\frac{\rho(\theta)}{\rho_\infty} \right)_j - \left(\frac{\rho(\theta)}{\rho_\infty} \right)_i \right] dS \quad (4.13)$$

where S_o is the distance between the two considered wavefronts, measured along the laser beam axis.

After some geometrical reasoning, one obtains the following:
For the ERH and scramjet thruster modes,

$$P_I = \frac{\kappa' \rho_\infty}{\lambda \rho_{SL}} (r_j - r_i) \left[\frac{1}{\tan \theta_w} - \int_{\theta_w}^{\theta_s} \left(\frac{\rho(\theta)}{\rho_\infty} \right) \frac{d\theta}{\sin^2 \theta} + \int_{\theta_w}^{\theta_s} \left(\frac{\rho(\theta)}{\rho_\infty} \right) \frac{d\theta}{\sin^2(2\theta_s - \theta)} - \frac{1}{\tan(2\theta_s - \theta_w)} \right] \quad (4.14)$$

And for the MHD-fanjet mode,

$$P_{II} = \frac{\kappa' \rho_\infty}{\lambda \rho_{SL}} (r_j - r_i) \left[\frac{1}{\tan \theta_w} - \int_{\theta_w}^{\theta_s} \left(\frac{\rho(\theta)}{\rho_\infty} \right) \frac{d\theta}{\sin^2 \theta} - \left(\frac{\rho_G}{\rho_\infty} \right) \frac{1}{\tan \theta_s} \right] \quad (4.15)$$

where r_i is the distance between ray i and the cone axis measured at the incident wavefront (plane x - y in Figures 4.1 and 4.2) and ρ_G is a reference density, assumed equal to the density at the mirror surface. The use of this reference density comes from the existence of a gap between the receiving optics and the forebody surface. That gap is indicated in Figure 4.2.

Note that the last factors in Eqns. 4.14 and 4.15 are functions of the flight Mach number, cone angle and optical path only. Thus, it is possible to introduce the aero-optical coefficient τ defined by

$$\tau_I = \frac{1}{\tan \theta_w} - \int_{\theta_w}^{\theta_s} \left(\frac{\rho(\theta)}{\rho_\infty} \right) \frac{d\theta}{\sin^2 \theta} + \int_{\theta_w}^{\theta_s} \left(\frac{\rho(\theta)}{\rho_\infty} \right) \frac{d\theta}{\sin^2(2\theta_s - \theta)} - \frac{1}{\tan(2\theta_s - \theta_w)} \quad (4.16)$$

for the ERH and scramjet thruster modes; and by

$$\tau_{II} = \frac{1}{\tan \theta_w} - \int_{\theta_w}^{\theta_s} \left(\frac{\rho(\theta)}{\rho_\infty} \right) \frac{d\theta}{\sin^2 \theta} - \left(\frac{\rho_G}{\rho_\infty} \right) \frac{1}{\tan \theta_s} \quad (4.17)$$

for the MHD-fanjet mode.

As an important result, Eqns. 4.14 and 4.15 can be rewritten as

$$P_I = \frac{\kappa' \rho_\infty}{\lambda \rho_{SL}} (r_j - r_i) \tau_I \quad (4.18)$$

$$P_{II} = \frac{\kappa' \rho_\infty}{\lambda \rho_{SL}} (r_j - r_i) \tau_{II} \quad (4.19)$$

The numerical calculation of τ_I and τ_{II} encompasses the numerical evaluation of the integrals in Eqns. 4.16 and 4.17. In the preceding expressions, subscripts I and II indicate the ERH/scramjet thruster modes and the MHD-fanjet mode, respectively.

Figures 4.6 and 4.7 exhibit the variation of the defined aero-optical coefficients with flight Mach number. In Fig. 4.6 (the ERH/scramjet mode) one sees a tremendous drop of the aero-optical coefficient in the Mach range 1.67 to 4.00. Beyond this point, τ_I remains approximately constant with increasing Mach numbers. This lower limit is indicated in Fig. 4.6.

On the other hand, Figure 4.7 (the MHD-fanjet mode) portrays a different behavior for the aero-optical coefficient, when compared to the previous case. Now τ_{II} increases (in an absolute way) with increasing flight Mach number up to a certain limit – probably attained beyond Mach 24.

The opposite behavior of the aero-optical coefficient observed in Figures 4.6 and 4.7 is associated with the different geometric constraints of the two cases. In the first case, the aero-optical coefficient τ_I is evaluated when the reflected beam crosses the shock wave. This means that τ_I is being evaluated after the laser beam has crossed the supersonic conical flow twice. As a consequence, the distortions introduced by the flow in the beam during its first passage are attenuated during the second passage (ie., after the beam has been reflected by the mirror). The intensity of this attenuation, of course, is a function of the flight Mach, which is introduced in Eqn. 4.16 by the density ratio $\rho(\theta)/\rho_\infty$ and the conical shock angle θ_w .

The aero-optical coefficient τ_{II} in turn is evaluated at the receiving optics inside the Apollo Lightcraft. As a result the propulsive beam crosses the supersonic flow only once, and the optical aberrations introduced during that passage are not counteracted by a second passage.

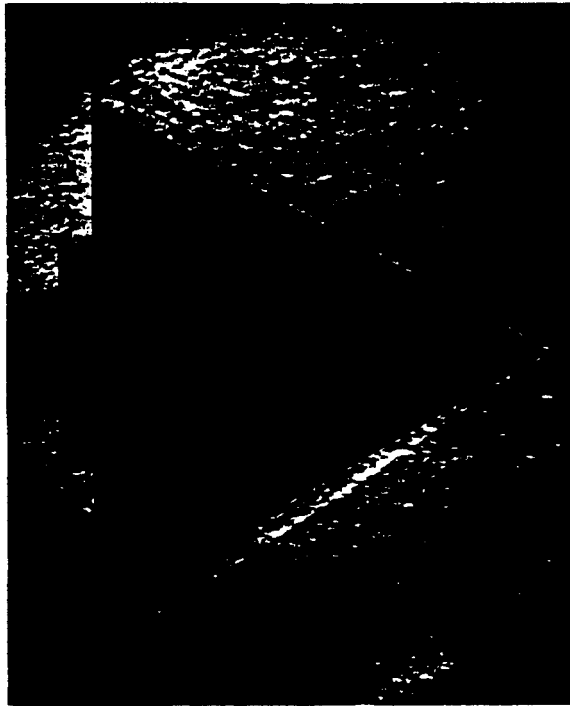
Both the lower and upper limits — observed in Figures 4.6 and 4.7, respectively — are due to the physical upper limit imposed on the density ratio and the shock angle θ_w as the flight Mach number M_∞ tends to infinity.

By choosing the ray starting at the laser beam axis as a reference ray, Eqns. 4.18 and 4.19 can be written as

$$P_I = \frac{\kappa'}{\lambda} \frac{\rho_\infty}{\rho_{SL}} (r - r_0) \tau_I \quad (4.20)$$

$$P_{II} = \frac{\kappa'}{\lambda} \frac{\rho_\infty}{\rho_{SL}} (r - r_0) \tau_{II} \quad (4.21)$$

where r ($r_0 - D/2 < r < r_0 + D/2$) represents the distance between a generic ray starting at $z = \theta$ and the beam axis, and r_0 is the distance between the incident beam axis at $z = 0$ and the cone axis. In order to separate out the altitude and wavelength effects on the optical phase distortion, plots of P_I and P_{II} divided by the factor $(\kappa'/\lambda)(\rho_\infty/\rho_{SL})$ as a function of non-dimensional distance across the beam diameter are portrayed in Figures 4.8 and 4.9 respectively. Let P_I^*



ORIGINAL PAGE IS
OF POOR QUALITY

Figure 4.5: 30° Semi-Apex Angle Cone in Mach 10 Flow (After H. T. Nagamatsu)

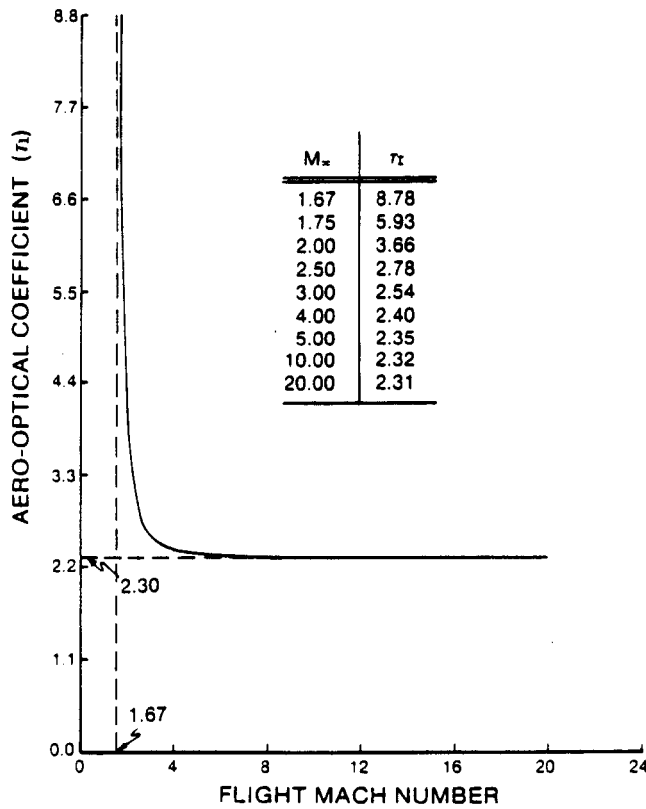


Figure 4.6: Aero-Optical Coefficient vs. Flight Mach Number in ERH or Scramjet Modes

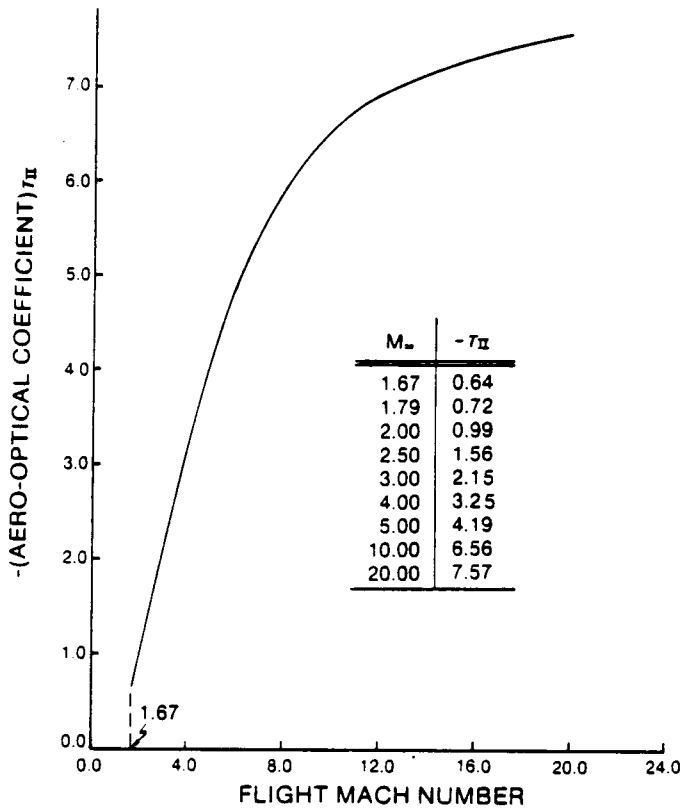


Figure 4.7: Aero-Optical Coefficient vs. Flight Mach Number in MHD-Fanjet Mode

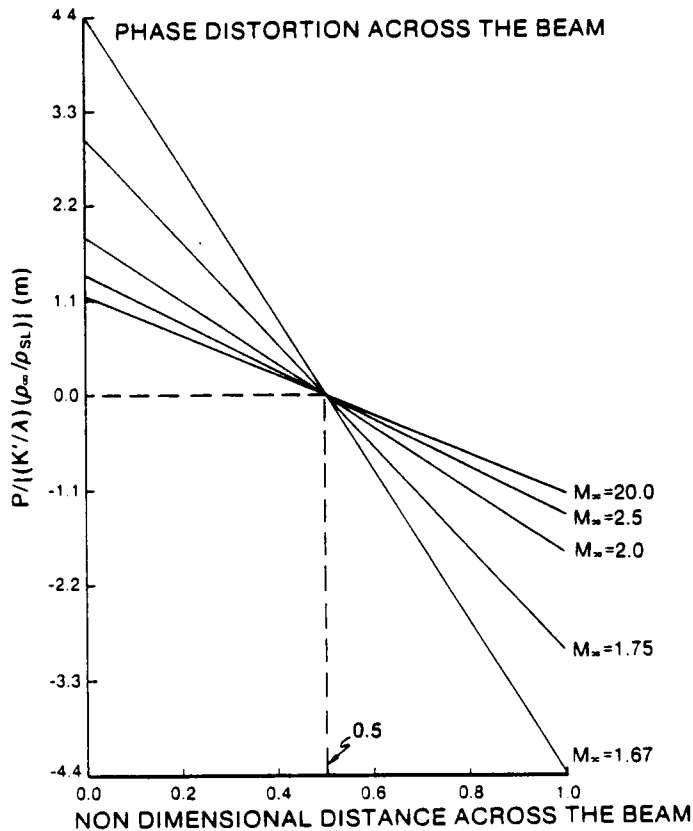


Figure 4.8: Variation of P_I^* Along a Selected Beam (Evaluated Just After the Reflected Beam Has Transversed the Shock Wave)

and P_{II}^* denote values of P_I and P_{II} divided by the factor indicated above. The chosen beam diameter is that defined by the interaction between the x - y plane and the considered laser beam.

Equations 4.20 and 4.21 define the existence of constant phase shift contours inside the beam. If P_{II} , ρ_∞/ρ_{SL} and τ_{II} are held constant, one obtains

$$r - r_0 = \text{constant} \quad (4.22)$$

Equation 4.22 defines a family of concentric circumferences over the plane $z = 0$ with their centers laying at the origin of the x, y, z coordinate system (i.e., at the cone apex). Figure 4.10 shows some maps of constant P_{II}^* contours for three different flight Mach numbers assuming $D = 1.00$ m and $r_0 = 1.65$ m³. Similar results can be obtained for Eqn. 4.20, but due to the conical reflection, the constant P_I^* contours are difficult to represent.

Since the TAV is flying out through the atmosphere, altitude is always increasing, causing the factor ρ_∞/ρ_{SL} to decrease. As a result, a complete evaluation of the phase plane distortion requires a correlation between altitude and flight Mach number. This correlation is provided by a trajectory-altitude profile[3] given in Figure 4.11. A mean value of the "optimized energy" and "optimized weight" Trajectory-Altitude profiles was used. The relationship between the Apollo Lightcraft altitude and the ratio ρ_∞/ρ_{SL} was found using a standard atmosphere model[14].

By using the above considerations and the following values for D , r_0 , κ' and λ

$$\begin{array}{ll} D = 1.00 \text{ m} & r_0 = 1.65 \text{ m} \\ \kappa' = 2.3 \times 10^{-4} & \lambda = 3.8 \mu\text{m} \end{array}$$

The maximum absolute value of the optical phase distortion (occurring at the studied wavefront) is plotted against the flight Mach number in Figure 4.12.

Figure 4.12 takes into account not only the altitude change, but also the change of propulsion modes. The discontinuity observed at Mach 10 represents the transition from the scramjet mode to the MHD-fanjet mode.

A major conclusion indicated in Figure 4.12 is that the aero-optical phenomena will introduce considerable aberrations in the propulsive beam only during the beginning of the transatmospheric flight (i.e., at low altitudes). These aberrations can be obtained from the computed phase distortion distribution and the Zernike Polynomials[4,5,7].

The optical distortion distribution over an aperture of radius $D/2$ can be written in terms of the Zernike Polynomials as follows:

$$P = \sum_{j=1}^{10} A_j F_j \quad (4.23)$$

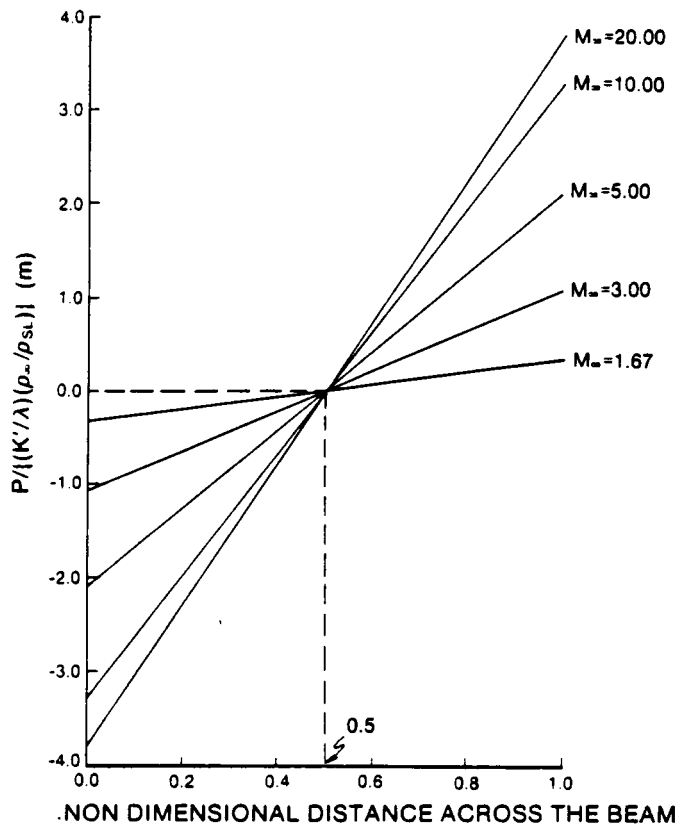


Figure 4.9: Variation of P_{II}^* Along a Selected Beam (Evaluated at the Receiving Optics)

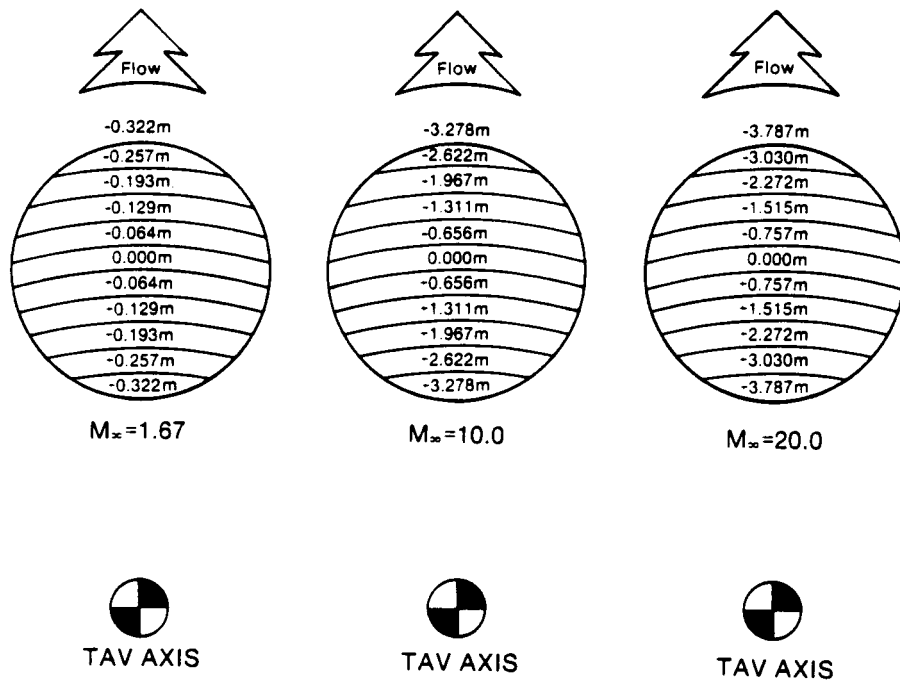


Figure 4.10: Contours of Constant P_{II}^* in the Beam Wavefront Located at the Receiving Optics. Three Different Mach Numbers are Portrayed

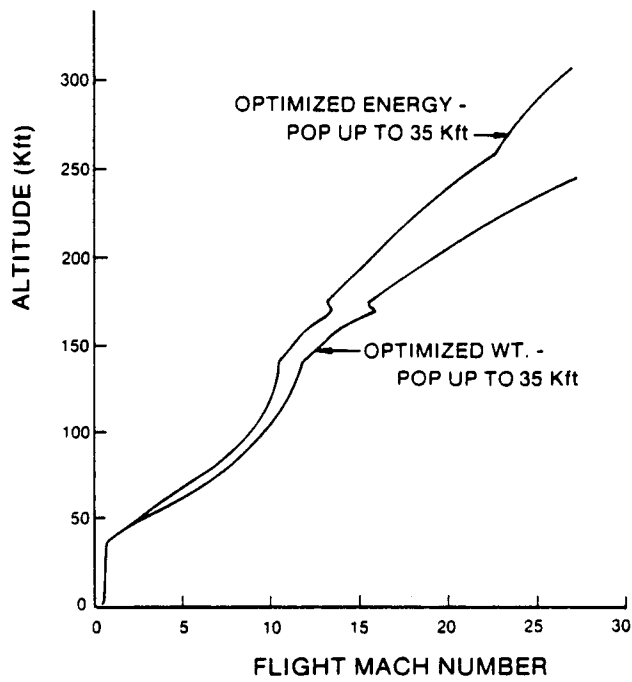


Figure 4.11: Trajectory-Altitude Profile

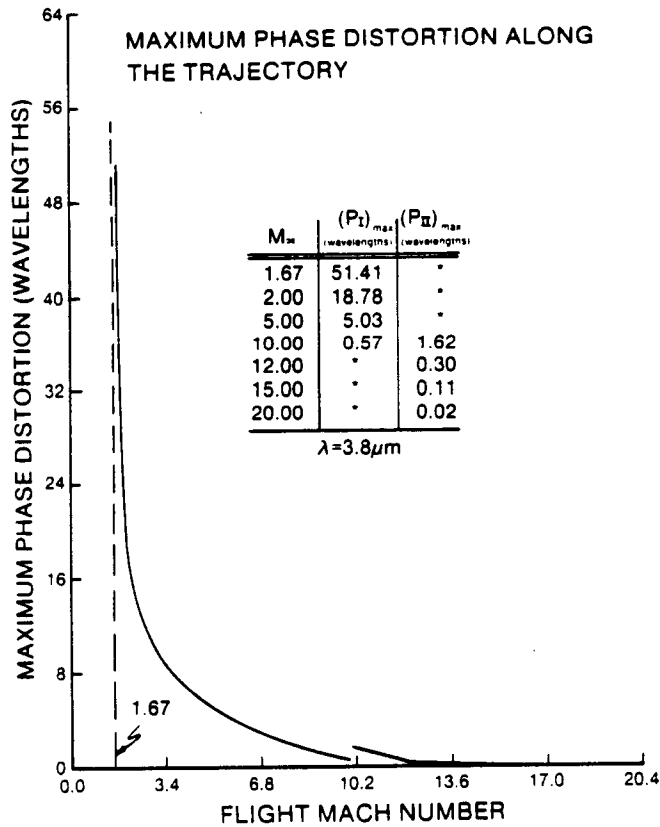


Figure 4.12: Maximum Phase Distortion in the Propulsive Beam vs. Flight Mach Number for a Chosen Trajectory-Altitude Profile

where

$$0 \leq r' \leq \frac{D}{2} \quad (4.24)$$

$$F_1 = \left(\frac{4}{\pi D^2}\right)^{1/2} \quad (\text{uniform phase shift}) \quad (4.25)$$

$$F_2 = \left(\frac{64}{\pi D^4}\right)^{1/2} x' \quad (\text{tilt}) \quad (4.26)$$

$$F_3 = \left(\frac{64}{\pi D^4}\right)^{1/2} y' \quad (\text{tilt}) \quad (4.27)$$

$$F_4 = \left(\frac{768}{\pi D^6}\right)^{1/2} \left(x^{1/2} + y^{1/2} - \frac{1}{8}D^2\right) \quad (\text{refocus}) \quad (4.28)$$

$$F_5 = \left(\frac{384}{\pi D^6}\right)^{1/2} \left(x^{1/2} - y^{1/2}\right) \quad (\text{astigmatism}) \quad (4.29)$$

$$F_6 = \left(\frac{1536}{\pi D^6}\right)^{1/2} (x'y') \quad (\text{astigmatism}) \quad (4.30)$$

$$F_7 = \left(\frac{2048}{\pi D^8}\right)^{1/2} \left(x'^3 - 3x'y'^2\right) \quad (\text{coma}) \quad (4.31)$$

$$F_8 = \left(\frac{2048}{\pi D^8}\right)^{1/2} \left(y'^3 - 3y'x'^2\right) \quad (\text{coma}) \quad (4.32)$$

$$F_9 = \left(\frac{2048}{\pi D^8}\right)^{1/2} \left(3x'^2 + 3y'^2 - \frac{1}{2}D^2\right) x' \quad (\text{coma}) \quad (4.33)$$

$$F_{10} = \left(\frac{2048}{\pi D^8}\right)^{1/2} \left(3x'^2 + 3y'^2 - \frac{1}{2}D^2\right) y' \quad (\text{coma}) \quad (4.34)$$

$$x' = r' \cos \theta' \quad (4.35)$$

$$y' = r' \sin \theta' \quad (4.36)$$

$$A_j = \int_0^{2\pi} \int_0^{\frac{D}{2}} P(r', \theta') F_j(r', \theta) r' dr' d\theta'. \quad (4.37)$$

The quantities r' and θ' are cylindrical coordinates at the beam cross-section and A_j are coefficients which indicate the magnitude of each aberration[7].

Consequently, the intensity of each aberration can be evaluated by substituting Eqn. 4.20 or 4.21 into Eqn. 4.37. These intensities can be used in the design of an adaptive optics system to compensate the aberrations.

Figure 4.13 portrays a sketch of an adaptive primary optics for the Apollo Lightcraft. In this figure we can see the actuator underneath the mirror surface. The actuators are controlled by an onboard high speed computer. This computer evaluates the intensity of the aberrations developed across the beam and generates a counter-action by deforming the mirror surface. The entire system (computer and actuators) must respond quickly enough to accommodate the altitude and flight Mach numbers changes.

4.6 Conclusions

A very simple analysis of optical distortions in a propulsive laser beam due to a conical supersonic flowfield over a mirror/window was performed. From this analysis one can expect considerable aberrations in a $3.8 \mu\text{m}$ propulsive laser beam during the beginning of the low altitude portion of the transatmospheric flight. As the TAV climbs to higher altitudes where the ambient density decreases, the optical phase distortion due to aero-optical phenomena is minimized.

Although the results indicate useful trends, the reader must keep in mind that the analysis ignores such important considerations as real gas effects, actual Apollo forebody geometry, viscous effects, etc. These effects can possibly increase the predicted phase distortion values, even in regions where it can now be neglected (e.g., during the MHD-fanjet mode).

By using Zernike polynomial, the intensity of the optical aberrations can be calculated; therefore a vehicle-based adaptive optics system can be designed to partially overcome the aberrations.

As a final conclusion, the present work attempts to give a rough prediction of the aero-optical phenomena to be expected during Apollo Lightcraft transatmospheric flights. Further investigations should be made in order to develop more realistic models for the aero-optical phenomena. Both theoretical and experimental investigations in this area will certainly open new perspectives for the "future of flight."

Nomenclature

c	Limiting Velocity due to expansion into vacuum
D	Propulsive laser beam diameter
L	Optical path length
M	Mach number
n	Index of refraction
p	Pressure
P	Optical phase distortion
r	Polar coordinate at x - y plane, with origin at tip of cone
r',θ'	Polar coordinates at the incoming beam shadow in x - y plane, with origin at the center of the beam shadow
S	Distance measured along the laser beam, with origin at the intersection the incoming laser beam and the x - y plane
T	Absolute temperature
U	Velocity along conical ray line
V	Velocity normal to conical ray line
x,y,z	Cartesian coordinate axes, with origin at the tip of cone; z -axis = cone axis
x',y'	Cartesian coordinate axes at the incoming laser beam shadow in x - y plane with origin at the center of the beam shadow
γ	Ratio of specific heats
θ	Conical ray angle, from cone axis
κ	Gladstone-Dale constant for the infrared region
λ	Wavelength
ρ	Air density
τ	Aero-optical coefficient

Subscripts

G	Indicates values at the gap between the TAV forebody surface and the receiving optic
i,j	Denote values at two arbitrary rays i and j inside the laser beam
o	Indicates reference values
s	Refers to values at the cone surface
w	Refers to values at the shock wave surface
I	Denotes the ERH and Scramjet Thruster modes
II	Denotes the MHD fanjet mode
∞	Indicates free stream conditions
θ	Indicates dependence on the conical ray angle, θ

Superscripts

*	Indicates quantity is divided by $(\kappa'/\lambda)(\rho_\infty/\rho_{SL})$
---	---

References

- [1] Willinski, M. I., "Beamed Electromagnetic Power as a Propulsion Energy Source," American Rocket Society Journal, Vol. 29, Aug. 1958, pp. 601-603.

- [2] Fisher, A. "Beam-Power Plane" *Popular Science*, Vol. 232, No. 1, Jan. 1988, pp. 62-65.
- [3] Myrabo, L. N., et al, *Apollo Lightcraft Project*, NASA/USRA Advanced Design Program, 3rd Annual Summer Conference, Washington, D.C., June 1987.
- [4] Fuhs, A. E., Fuhs, S. E., "Optical Phase Distortion Due to Compressible Flow Over Laser Turrets," *Progress in Astronautics and Aeronautics*, Vol. 80, 1982, pp. 101-137.
- [5] Born, M. and Wolf, E., *Principles of Optics*, Pergamon Press, New York, 1964.
- [6] Myrabo, L. N., et al, "Advanced Energy Conversion Concept for Beamed-Energy Propulsion," Final Technical Report, AFOSR-84- 0361, Aug. 1987.
- [7] Hogge, C. B. and Butts, R. R., "Frequency Spectra for the Geometric Representation of Wavefront Distortions due to Atmospheric Turbulence," *IEEE Transactions on Antennas and Propagation*, Vol. AP- 24, 1976, pp. 144-154.
- [8] Fuhs, A. E., "Potential Flow: Nonlinear Compressible Flow," Lecture 3B, Short Course on Laser Aerodynamics, presented April 11-22, 1977, at Air Force Weapons Laboratory, Kirtland Air Force Base, NM.
- [9] Anderson, J. D., Jr., *Gasdynamic Lasers: an Introduction*, Academic Press, 1976.
- [10] Parmentier, E. M., Greenbert, R. A., "Supersonic Flow Aerodynamic Windows for High-power Lasers," *AIAA Journal*, Vol. 11, 1973, p. 943.
- [11] Liepman, H. W., Roshko, A., *Elements of Gas Dynamics*, Wiley, 1957.
- [12] Kopal, Z., "Tables of Supersonic Flow Around Yawing Cones," M.I.T., Dept. of Electrical Engr., 1947.
- [13] Sims, J. L., "Tables for Supersonic Flow Around Right Circular Cones at Zero Angle of Attack." NASA SP-3004, 1963.
- [14] U.S. Standard Atmosphere, 1962.

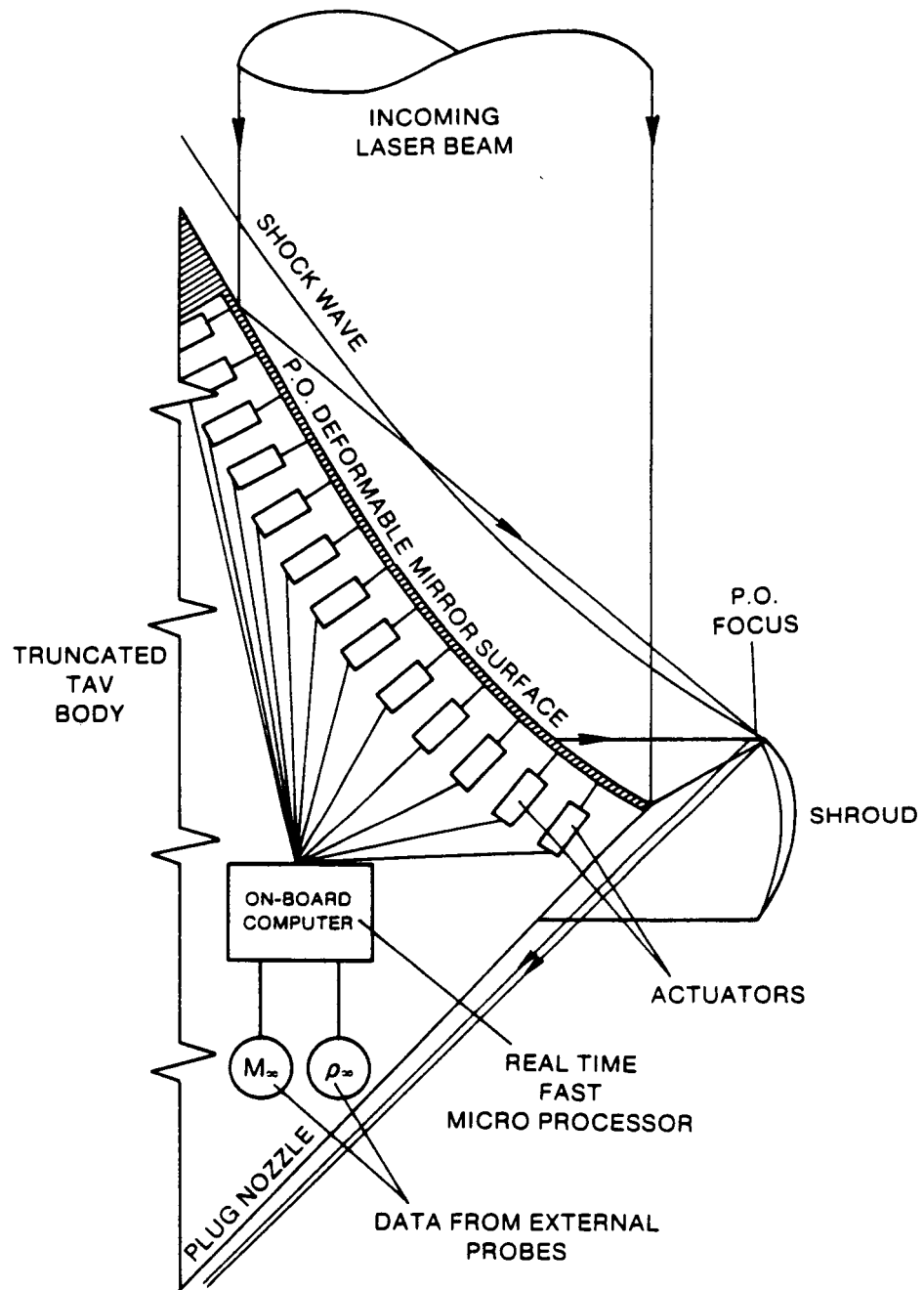


Figure 4.13: Adaptive Primary Optics for the Apollo Lightcraft

Chapter 5

Man/Machine Interface

This chapter on flight crew systems will concentrate on the actual working environment of the Apollo Lightcraft. We will not, however, be dealing with environmental control. That topic will be researched at a later time. The topics covered are as follows; cabin layout, entry/exit of the Lightcraft, video systems, and avionics. The key to interior design of the Apollo Lightcraft was ergonomics. Due to limited space, and the relatively short periods of time people will be in the Lightcraft, ease of use of the entire system is essential.

5.1 Cabin Layout

The Apollo Lightcraft design requires adequate room for a five man crew on missions lasting no more than one or two days. To fit five crew members in the current design, a two deck system was utilized. This two deck configuration has been modified from previous reports[6]. This was mandated by the removal of a third superfluous hatch on the flight deck, and making it an emergency exit on the lower deck. The two man flight crew (pilot and copilot/navigator) would be positioned above the passengers/crew with access to all flight controls and monitors. Figure 5.1 shows the flight deck configuration. The lower deck will consist of three acceleration couches located side by side, with access to all hatches and cargo. Underneath the center seat is an emergency hatch which can be accessed by folding back the seat.

Many seating variations were examined, but the side-by-side arrangement provided maximum comfort for the passengers. A triangular seating arrangement was found to have optimum space utilization, and a star arrangement would provide the easiest entry/exit ability. The side-by-side arrangement, although more difficult to on- and off-load; would allow the passengers to see and talk to each other, is psychologically more beneficial to the well being of the occupants, and will reduce feelings of claustrophobia and isolation. Figure 5.2

shows the lower deck layout, and position of entry/exit hatches.

Needless to say, it is a tight fit for all five crewmembers. According to NASA data[9], as shown in Figure 5.3, for one to two day missions, a minimum of 50 ft³ per man is required. This is the same volume provided by the Lightcraft, per man. This will eventually restrict Lightcraft mission durations to two days.

5.2 Entry/Exit

The simplest way to provide entry and exit for the crew is by providing access to the landing gear bays. Any inconsistency in the surface of the upper hull could potentially absorb enough of the power beam to prove disastrous[7]. Entry/exit must be provided for, and be equally accessible to all crewmembers. Without jeopardizing the structural integrity of the Lightcraft, hatches in the landing gear bays were seen as the most acceptable solution.

As seen in Figure 5.4, circular pressure hatches will open inward. It would be difficult and costly to make the landing gear bays airtight, thus environmental integrity will be maintained through the interior hatches. In addition, these hatches open inward, so that when pressurized, the hatches will remain airtight regardless of a mechanical or electrical failure.

Since the Lightcraft is to be a next generation transportation vehicle and not an exploratory vessel, EVA capability for the crew is not a high priority. No airlocks are provided, and the hatches can only be opened to space by hand in an emergency only after the interior has depressurized. This provides an added safety measure as the Lightcraft environment cannot be exposed to space unless done so manually and intentionally.

For docking with orbital platforms, it is assumed that a pressurized docking bay will exist on the destination. The upper Lightcraft hull and shroud are too delicate for conventional nose docking. Further, the only exits are the lower gear bay hatches, and they are difficult to access with a gantry or docking module due to the necessary extension of the landing gear. Because of the relatively small size of the Lightcraft, this assumption appears reasonable.

To further facilitate entry and exit, the Lightcraft will have the ability to "lean" forward to a point where the gear bays will have greater exposure. The landing gear will have the capability of individual extension, providing the means to lean to one side. The relative "slant" of the Lightcraft crew decks will also help the crewmembers crawl into their respective acceleration couches.

5.3 Video Systems

Due to the intensity of energy carried by the power beam, windows could not possibly be used in the Lightcraft design[7]. However, for some portions of the mission, some exterior views must be provided. A video system able to provide views in many directions is needed. This can easily be achieved using flexible

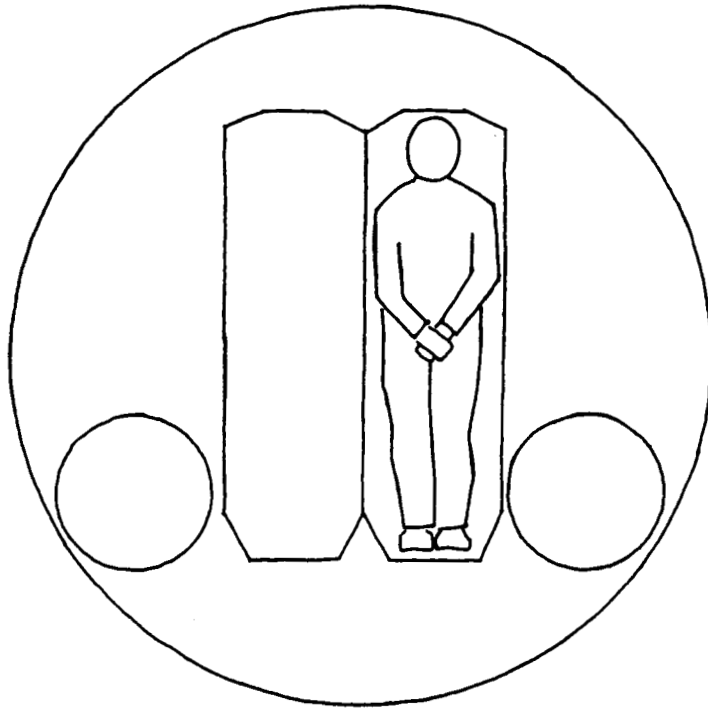


Figure 5.1: Flight Deck Configuration

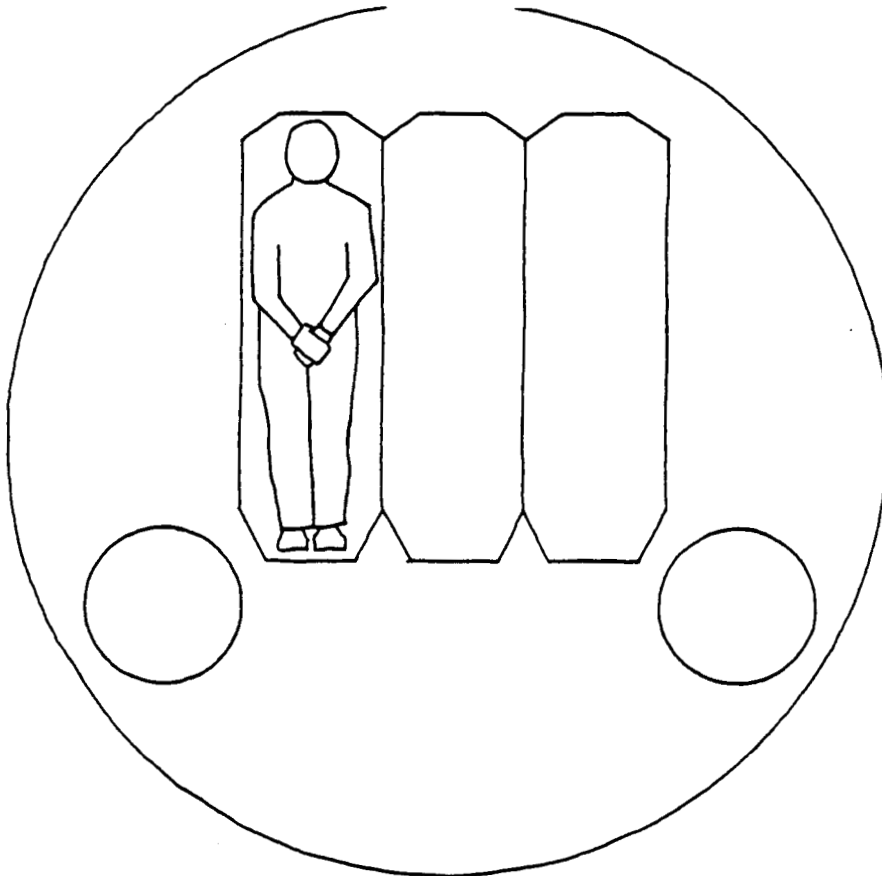
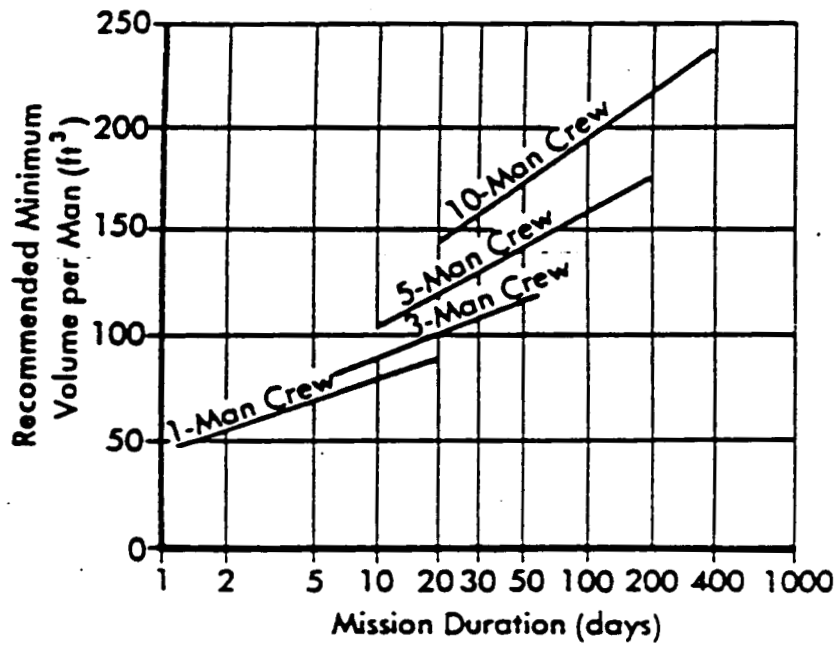


Figure 5.2: Lower Deck Layout



Volume requirements.

From: Web, Paul, M.D. "Bioastronautics Databook", NASA SP-3006, 1964

Figure 5.3: Volume Requirements for Manned Missions

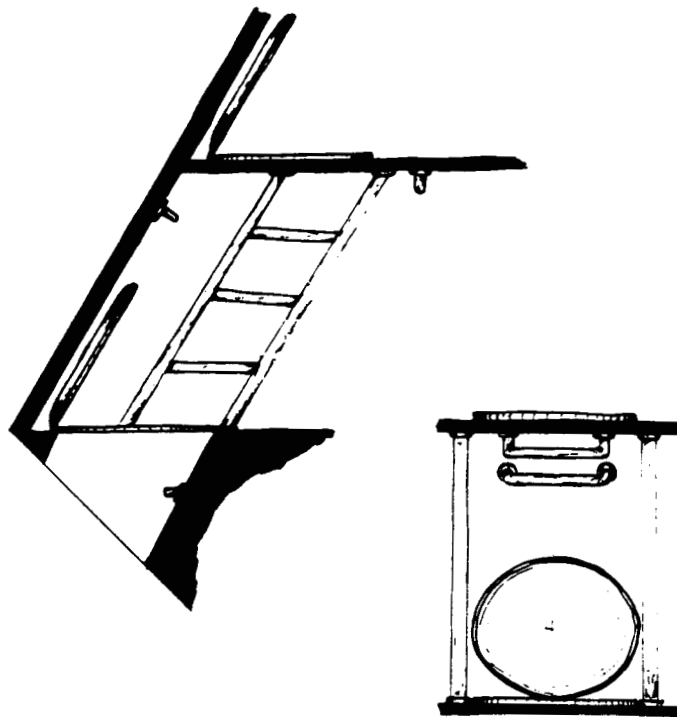


Figure 5.4: Hatch Configuration

fiber optics, similar to those used by doctors to look inside the human body, located on the vehicle. Integration of remote views from satellites or control facilities will also facilitate the acquisition of external views.

Figure 5.5 shows the placement of four fiber optic cameras, located at 90° positions around the shroud. Figure 5.6 is a detail of the shroud camera. The cameras will be shielded when not in use, and be able to rotate through 360° on the y-axis, and 90° on the z-axis. This provides nearly complete coverage around the Lightcraft. The system is further augmented with a nose camera for critical docking maneuvers.

All camera feeds will be sent to the visual processor section of the onboard flight computer. This system will control all cameras, as well as provide the flight crew with the needed view on the display system. This will allow the creation of a real time "virtual" external view[5]. Remote camera feeds from the power satellite will also augment view representation and data display. The flight crew can access any view or data, at any time, so long as it does not conflict with camera survivability. Also, in emergency situations, the computer will provide only the specific information and view needed for the flight crew, in order to reduce distraction at critical times.

Information and exterior views will be displayed on a segmented color flat-screen on the flight deck. All screen segments will be stowable. Recesses in the upper portion of the deck will store the screens when folded to the "up" position. Figure 5.7 shows a side view of a flight crew station. All panel and control sections will fold up to provide greater room for entry, exit, or any other activity.

With computer control over each segment, the flight computer can display specific information on each; or provide an integrated mosaic. The flight crew can further augment any data displayed. The final view will look similar to that of a HUD (Heads Up Display) used by modern fighters superimposed on an exterior view (Figure 5.8)[3].

5.4 Avionics

The avionics of the Lightcraft will take maximum advantage of the visual processor. The system is flexible to the flight crews' needs, and will use the flight computer as an extra crewmember. At any point during a mission, almost any data or information can be displayed at the command of the flight crew. There are also set display functions, such as take-off mode, docking mode, or landing mode. Emergency displays will be pre-programmed in the event of mishap. The computer will determine the type of emergency, and will display an emergency procedure list as well as the data needed to resolve the problem.

Informational overload is a significant concern for the flight crew[8]. When the level of information simplification is increased, the quantity of information that can be absorbed also increases. Through examining informational displays

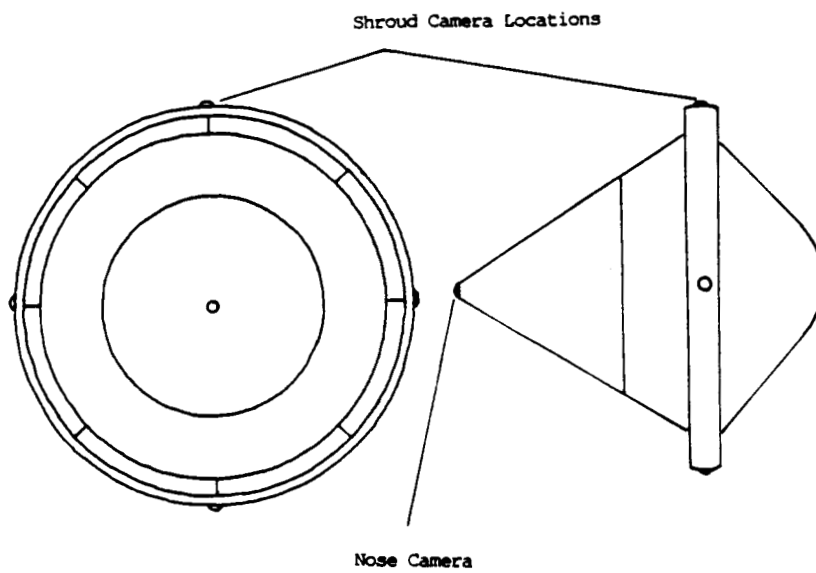


Figure 5.5: Fiber Optic Camera Locations

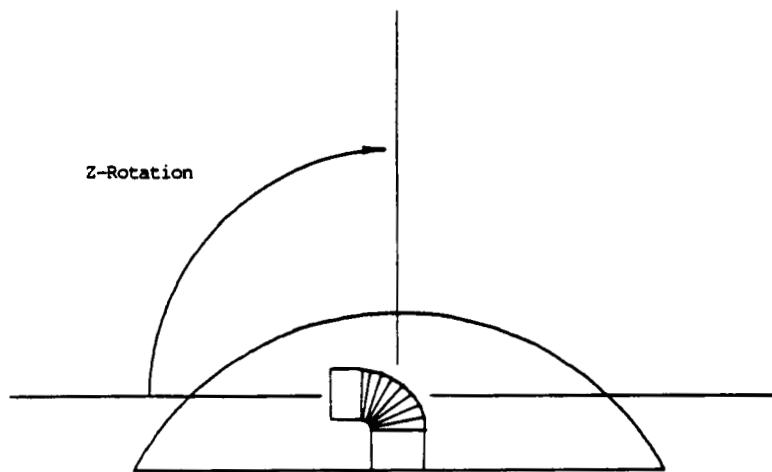


Figure 5.6: Fiber Optic Lens Feed Detail

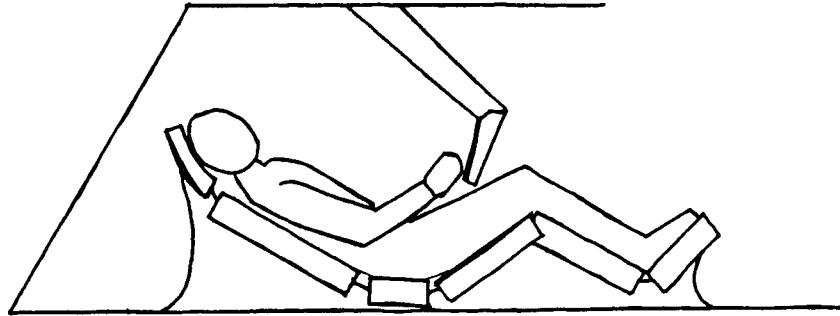


Figure 5.7: Flight Crew Station—Side View

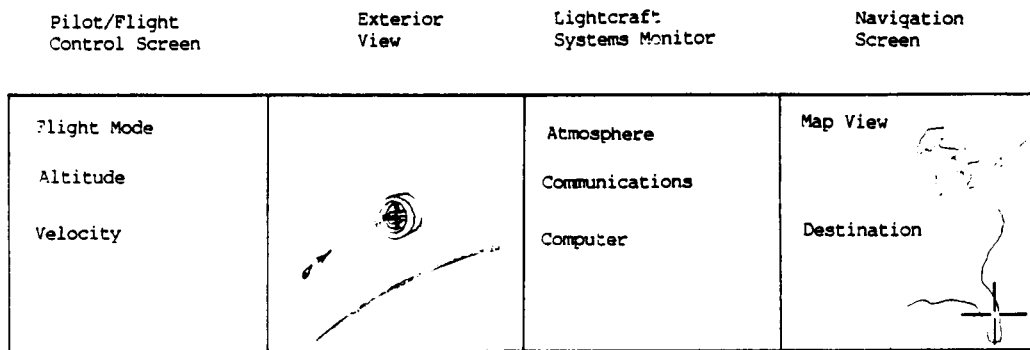


Figure 5.8: Segmented Flat Screen Display System

on modern fighters such as the F/A-18 Hornet, it was found that flight data needs to be grouped according to the systems being used and the portion of mission. It was also determined that flight data needs to be presented graphically, as graphical information can be absorbed and retained better than pure numbers or analog gauges[3]. Although the flight crew can augment the displays to their needs, the computer will be programmed to dedicate specific information to specific screen segments. One segment will be dedicated to engine performance and system operation, another will display navigational data, etc. Figure 5.8 shows some examples of the screen display overlay concept. In addition, manually controlled checklists on touchscreens will insure the completion of any pre-flight and mission critical tasks.

References

- [1] Experimental Aircraft Association, *Oshkosh '87 Sport Aviation Showcase*, 1987 edition.
- [2] Gatland, Kenneth, *Space Technology: a Comprehensive Encyclopedia of Space Exploration*, Crown Publishers, New York, 1984.
- [3] Gunston, Bill and Mike Spick, *Modern Air Combat, the Aircraft, Tactics and Weapons Employed in Aerial Warfare Today*, Crescent Books, New York, 1983.
- [4] Joels, Kerry M. and Gregory P. Kennedy, *The Space Shuttle Operator's Manual*, Ballentine Books, New York, 1982.
- [5] Lockheed Georgia Corporation, "Advanced Concepts, Flight Station Simulation," 1986.
- [6] Myrabo, Leik and others, *Apollo Lightcraft Project*, Rensselaer Polytechnic Institute, 1987.
- [7] Myrabo, Leik and Dean Ing, *The Future of Flight*, Baen Publishing, New York, 1985.
- [8] Taylor, Richard L., *Instrument Flying*, Macmillan Publishing Co. New York, 1986.
- [9] Web, Paul M.D., "Bioastronautics Databook," NASA SP-3006, 1964

Chapter 6

Flight Control Systems

This chapter deals with the problem of controlling the direction of travel of the Apollo Lightcraft in all of its flight modes. Because of the revolutionary propulsion system used, a system of differentially applied thrust was used to control the direction of travel of the Lightcraft while in the atmosphere. Prior to takeoff, an initial angle of launch can be obtained through adjustment of the tripod landing gear. During atmospheric powered flight, thrust applied differentially on the lower hull surface provides directional control. Finally, in the non-powered modes of flight, such as orbital maneuvers and unpowered re-entry, a traditional reaction jet system is used. These three systems allow for full control over the Lightcraft trajectory at all times. Although most of the control over the Lightcraft will be handled by the onboard flight computer, the flight crew will be provided control inputs and positive control over certain parts of the flight regime.

6.1 Ground Orientation

In order to obtain positive beam acquisition from orbiting power relay satellites, the Lightcraft will have to be able to adjust its initial beam contact angle on its own. Since no satellite can be expected to be directly overhead at any given moment, and the maximum incident angle of the power beam is within 3° , flexibility in Lightcraft orientation is the best solution. This system requires little more than extra flexibility in individual landing gear extension.

Because of the need to orient the incident angle of the Lightcraft on the ground, a tripod landing gear system is used (Figure 6.1). Each gear leg is capable of individual extension, and through computer control allows precise alignment on the power beam. In an emergency situation, the gear can still be hand cranked into landing configuration. This part of the control system will be computer controlled through a feedback loop with the power satellite's

communication beam. This beam will provide information on the exact location of the satellite, and will allow the computer to modify its orientation for optimal alignment.

In addition to beam acquisition, the landing gear will be pre-programmed for entry/exit configuration. This will "lean" the Lightcraft to provide easier means of getting on and off the vehicle, as explained in Chapter 5.

6.2 Airborne Flight Control

Atmospheric flight control under powered conditions requires modification of the propulsive sequence of the thrust pulses. There are no aerodynamic surfaces capable of positive attitude control of the Lightcraft in the powered flight modes. Also, reaction jets are inefficient for attitude control in the atmosphere. Thus, a system for controlling the *thrust* of the Lightcraft was developed.

The system developed controls the thrust differential applied to each section of the Lightcraft hull during the initial ERH (External Radiation Heating) thruster mode of engine operation[6]. This is done through varying the length and frequency of beam pulses to each section of the hull. Figure 6.2 illustrates this thrust vector control theory. The Lightcraft hull will have a section exposed to a higher relative pressure.. This will induce a moment around the center of gravity of the Lightcraft, and thus change its attitude. With this scheme, there is a shift in the thrust vector. Since the propulsion system of the Lightcraft is segmented, control of each thrust segment will easily provide the necessary attitude and thrust vector control.

The controlling parameters are the pressures, P_{cl} and P_{ch} , and the wedge angle, θ_l . Variation of these parameters will provide the necessary moment. In order to simplify calculations, the following assumptions were made: first, pressure will be applied almost uniformly over the surface of the hull from the ERH blast wave. Second, the rate at which specific segments of the propulsive system are activated can be varied. And third, the focus of the laser beam can be moved along the hull surface to change the length of the propulsive segments. Note that in Figure 6.3 the initial ERH thruster mode is shown; however, this mode of control can be used for all the segmented power modes of the Apollo Lightcraft.

Approximations for the moment arms upon which this thrust differential will act were determined for three of the engine modes: initial ERH mode, scramjet, and MHD fanjet mode. For the initial ERH mode, a value of 1.959 ft was obtained. For scramjet and MHD fanjet, values of 0.717 ft and 7.324 ft were determined respectively. Differences between modes are incurred from the number and shape of segments each propulsive mode uses, and their respective moment arms.

The differential area of the hull this thrust acts upon is, with reference to Figure 6.4, modeled as a trapezoid:

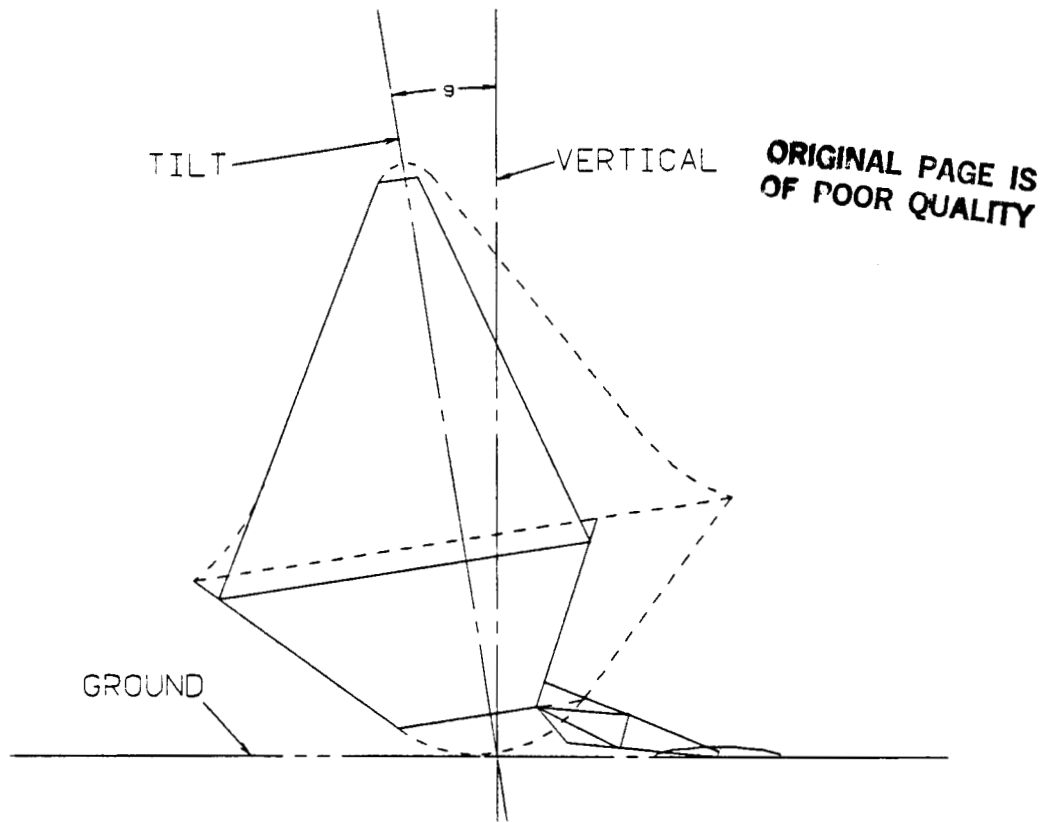


Figure 6.1: Tripod Landing Gear Orientation

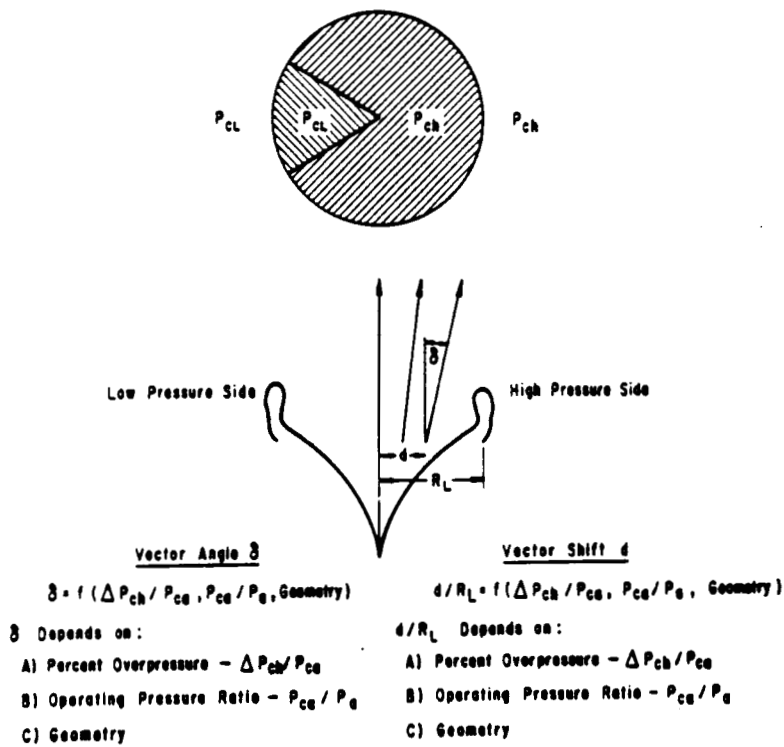


Figure 6.2: Thrust Vectoring Control

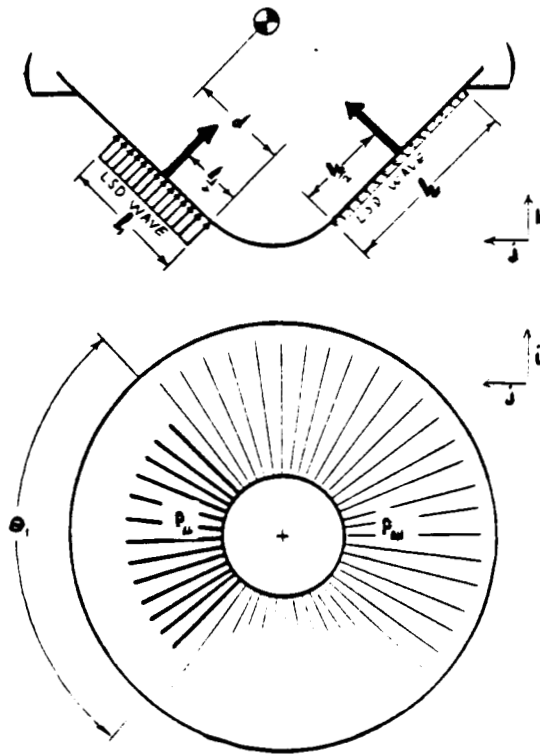


Figure 6.3: Thrust Vector Control Through Pressure and Length Variation

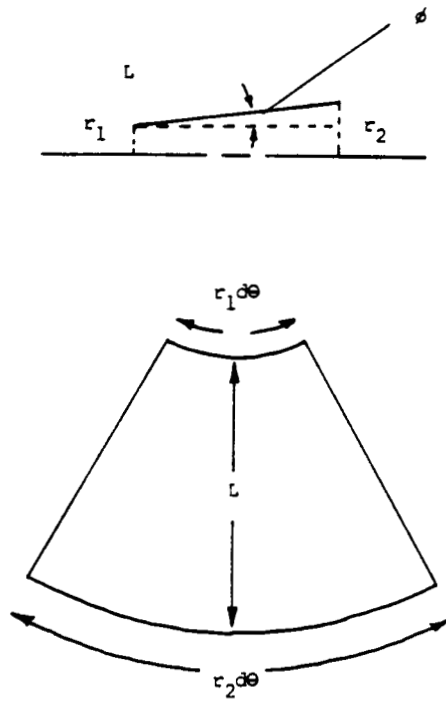


Figure 6.4: Differential Surface Area Determination

$$A_{TRAP} = h \left(\frac{1}{2}b_1 + b_2 \right) \quad (6.1)$$

$$dA = L \left(\frac{1}{2}b_1 + b_2 \right) d\theta \quad (6.2)$$

$$L_L = r_2 - r_1 \quad (6.3)$$

$$L \sin \phi = r_2 - r_1 \quad (6.4)$$

$$L = \frac{r_2 - r_1}{\sin \phi} \quad (6.5)$$

Therefore, for a fixed L ,

$$dA = \frac{(r_2 - r_1)(r_1 + r_2)}{2 \sin \phi} d\theta = \frac{r_2^2 - r_1^2}{2 \sin \phi} d\theta \quad (6.6)$$

Thus, for the situation illustrated in Figure 6.3, the following thrust differential is described:

$$dT = PL_1 \left(r_1 + \frac{L_1}{2} \sin \phi \right) d\theta \left[-\cos \phi (\cos \theta \hat{i} + \sin \theta \hat{j}) + \sin \phi \hat{k} \right] \quad (6.7)$$

where all factors correspond to those in Figures 6.2 through 6.4. The differential area upon which dT is based is illustrated in Figure 6.4.

Integrating over this differential area gives the equations for the thrust magnitude for each hull segment. Adding the two equations gives the overall thrust magnitude as shown below:

$$T_1 = 2P_d L_2 \left(r_1 + \frac{L_2}{2} \sin \phi \right) \sin \phi \left[-\cot \phi \sin \frac{\theta_1}{2} \hat{j} + \frac{\theta_1}{2} \hat{k} \right] \quad (6.8)$$

$$T_2 = 2P_{ch} L_L \left(r_1 + \frac{L_L}{2} \sin \phi \right) \sin \phi \left[\cot \phi \sin \frac{\theta_1}{2} \hat{j} + \left(\pi - \frac{\theta_1}{2} \right) \hat{k} \right] \quad (6.9)$$

$$\begin{aligned} T_T &= T_1 + T_2 = \\ &2 \sin \phi \left[P_{ch} L_L \left(r_1 + \frac{L_L}{2} \sin \phi \right) - P_d L_2 \left(r_1 + \frac{L_2}{2} \sin \phi \right) \right] \cot \phi \sin \frac{\theta_1}{2} \hat{j} \\ &+ \left[P_{ch} L_L \left(r_1 + \frac{L_L}{2} \sin \phi \right) \left(\pi - \frac{\theta_1}{2} \right) + P_d L_2 \left(r_1 + \frac{L_2}{2} \sin \phi \right) \frac{\theta_1}{2} \right] \hat{k} \end{aligned} \quad (6.10)$$

This uneven application of thrust through the center of gravity naturally results in a moment applied to the Lightcraft. The equations are derived in a like manner, and are presented here:

$$dM = \left(d - \frac{L}{2} \right) PL_1 \left(r_1 + \frac{L_1}{2} \sin \phi \right) d\theta \left[-\sin \theta \hat{i} + \cos \theta \hat{j} \right] \quad (6.11)$$

$$M_1 = -2P_d \left(d - \frac{L_1}{2} \right) L_2 \left(r_1 + \frac{L_2}{2} \sin \phi \right) \sin \frac{\theta_1}{2} \hat{i} \quad (6.12)$$

$$M_2 = +2P_{ch}(d - \frac{L_1}{2})L_2(r_1 + \frac{L_2}{2} \sin \phi) \sin \frac{\theta_1}{2} \hat{i} \quad (6.13)$$

$$M_T = M_1 + M_2 = 2 \left[P_{ch}(d - \frac{L_L}{2}) - P_{cl}(d - \frac{L_1}{2}) \right] [L_2(r_1 - \frac{L_2}{2} \sin \phi)] \sin \frac{\theta_1}{2} \hat{i} \quad (6.14)$$

Since the pressure areas, length of propulsive segments, and relative pressure magnitudes can all be varied, this provides ample means for refined Lightcraft control during the powered flight phases. The estimated maximum moment which can be induced upon the Lightcraft is 130,000 ft-lbs. Through computer simulation, it was determined that the maximum moment required to compensate for aiming error, and course correction, was only 13,000 ft-lbs.

Equations and approximations for the advanced ERH thruster, scramjet and MHD fanjet modes can be similarly obtained, by substituting engine mode data and moment arm computations. The advanced ERH thruster mode is similar to the scramjet for all practical computational purposes.

This system for attitude and course control is more than adequate and exceeds the requirement by an order of magnitude.

6.3 Orbital Maneuvering and Navigation

While in orbit, the Lightcraft will not utilize beamed propulsion. An orbital maneuvering system will have to be carried along. Orbital maneuvering is a delicate task requiring precise applications of thrust to move the Lightcraft to its desired orbital destination. The Lightcraft will have to be capable of roll, pitch, yaw, and translation on all three axes. Celestial and inertial navigation systems will be required for accurate maneuvering[9].

This is the flight mode in which the crew will be in total control. Although provisions will be made for computer controlled orbital maneuver, the flight crew will have the capability to override at any point, and assume positive Lightcraft control. The Lightcraft crew will need to control the Lightcraft for orbital docking, orbital change, and orientation for an Apollo style re-entry. The system utilized to control the Lightcraft will be a series of reaction jets, similar to the original Apollo[7].

This orbital maneuver system will consist of two parts; first, the navigational sensors, and second, the actuators. The navigational sensors will consist of an inertial navigation system, similar to that used on the Space Shuttle, use of Navstar or the military GPS (Global Positioning System) satellite links, and celestial navigation.

The inertial navigation system uses a system of gyroscopes and accelerometers to sense changes in orientation and velocity. This system is currently being used successfully by the military, and by the Shuttle. Its accuracy and dependability is increasing with the use of ring laser gyros. Navstar or the GPS

would be the easiest and most reliable method of orbital navigation. This system could be used alone if not for the chance of electrical failure on either the satellites or the Lightcraft, or failure of the transmission/reception equipment. Finally, celestial navigation offers the most accurate and reliable method for navigation. Sailors have used the stars for navigation for thousands of years. A simple sextant linked to the onboard navigational computer could provide navigational information. The only disadvantage to this system is that it is slow and tedious. A combination of all three would provide maximum reliability, safety, and accuracy. All three navigational systems would then be fed into the flight computer, and rechecked frequently in a feedback loop with the previous navigational input.

The reaction jet system would be similar to that used on the original Apollo design, as illustrated in Figure 6.5. The reaction jets will use a pressurized hydrogen bleed from the main Lightcraft fuel tank, or pressurized nitrogen. Nitrogen appears to be the system of choice. Although a sacrifice in payload must be made, liquid nitrogen is cheap, extremely easy to handle, and safer. There should be sufficient fuel left from launch to provide for all orbital maneuver if the hydrogen system is used. Additional RCS (Reaction Control System) pods will have to be stowed in the lower hull underneath the movable TPS (Thermal Protection System).

When in orbit, the Lightcraft would enter re-entry configuration, and the RCS pods would be deployed. Prior to actual re-entry, the RCS pods would be retracted, and thermal doors would be closed to protect them. Roll, pitch, and yaw, as well as translational commands, would be sent through the flight computer, and the respective control jets would be activated. Control jet activation algorithms will be similar to the Apollo command/service module command set[8].

Commands could be issued from a pre-programmed flight path in the computer, or a twin stick controller used by the pilot. The twin stick system is similar to the one used on the MMU (Manned Maneuvering Unit) on the Shuttle. This system offers the most ease of use and flexibility for flight control. The pilot can maneuver following flight cues from the computer, or fly "seat of the pants." The hand controls are illustrated in Figure 6.6.

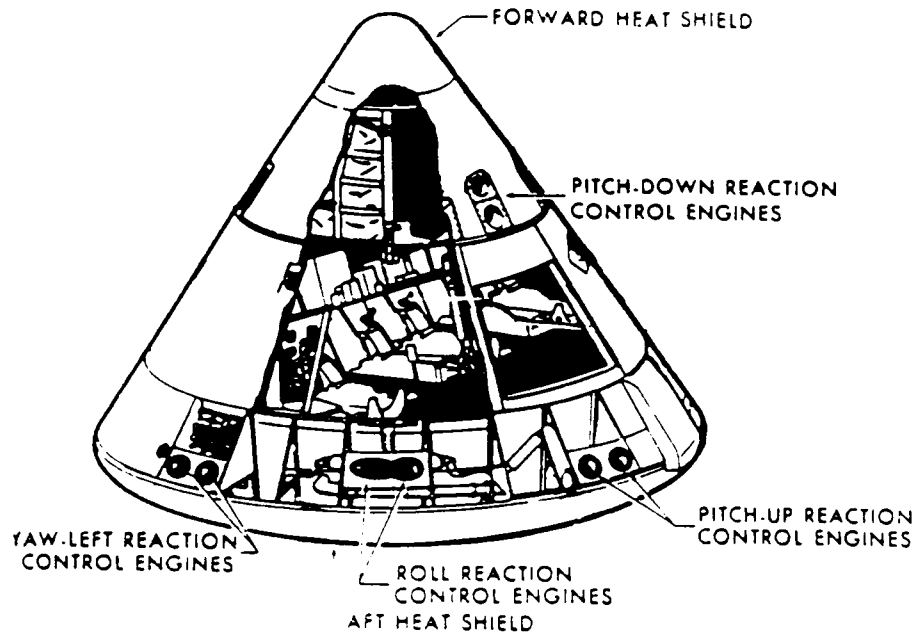


Figure 6.5: The Apollo Command Module Reaction Control System [7]

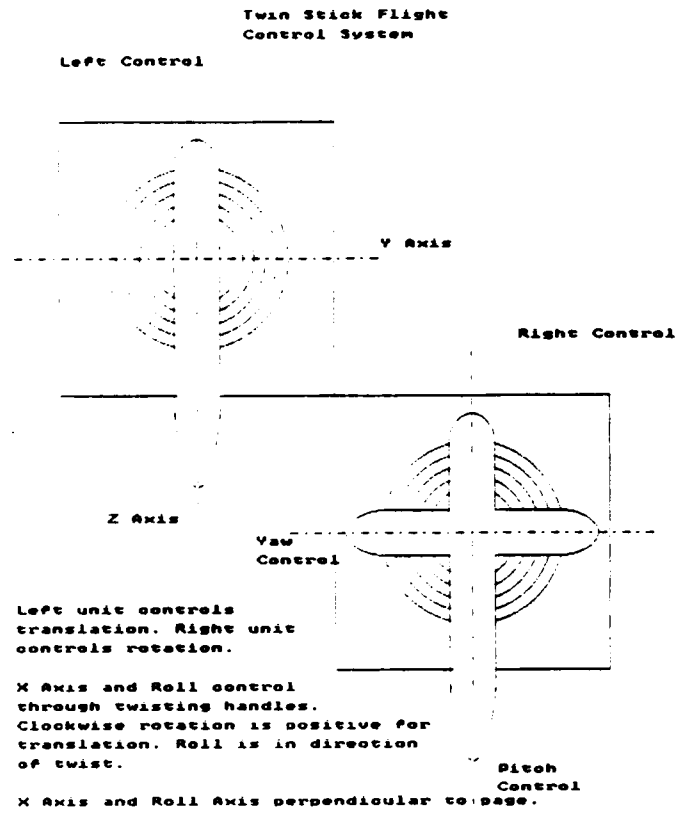


Figure 6.6: Twin Stick Flight Control System

Nomenclature

A	Area of hull segment acted upon by the blast wave
L_1	Length of low pressure segment
L_2	Length of high pressure segment
M_T	Total moment on Lightcraft
P_{cl}	Low pressure segment magnitude
P_{ch}	High pressure segment magnitude
r_1	Low pressure segment lower radius
r_2	Low pressure segment upper radius
T_T	Total thrust acting on hull
ϕ	Cone angle of the lower hull
θ_1	Arc of low pressure segment

References

- [1] Graham, A. R., "NASA Plug Nozzle Handbook", Contract NAS 9-3748, General Electric Co. for the New York State Atomic and Space Development Authority.
- [2] Kaplan, Marshall H. *Modern Spacecraft Dynamics and Control*. New York: Wiley, 1976.
- [3] Myrabo, L. N. and others, "Advanced Energy Conversion Concept For Beamed-Energy Propulsion," Contract RPI-5-24170, Rensselaer Polytechnic Institute for the Air Force Office of Scientific Research, 1987.
- [4] Myrabo, L. N. and others, *Apollo Lightcraft Project*, Rensselaer Polytechnic Institute for the NASA/USRA Advanced Design Program, 1987.
- [5] NASA Report #N68-20449, "Guidance, Flight Mechanics, and Trajectory Optimization," Vol. VIII: Boost Guidance.
- [6] Myrabo, L. and Ing, D. *The Future of Flight*, Baen Publishing, New York, 1985.
- [7] Brooks, C. and Ertdel, I., *The Apollo Spacecraft, a Chronology. Volume III*. NASA, Washington D.C. 1976.
- [8] Greensite, A. *Analysis and Design of Space Vehicle Flight Control Systems*, Spartan Books, New York, 1970, pp 197-236.
- [9] Stearns, E. *Navigation and Guidance in Space*, Prentice Hall, Inc. New Jersey, 1963, pp 82-91, 110-113.

Chapter 7

Optical Train for Imaging Applications

7.1 Imaging Properties of the Optical System

It has been suggested that the optical system of the Apollo Lightcraft could also function as a telescope system. In other words, when the power beam is not operating (if the vehicle is at rest or coasting) it would be possible to "look through" the optical system from inside the vehicle. Since the mirrors are of large diameter and diffraction-limited quality, such a system should be capable of high quality imaging over long distances. For example, it might be possible to inspect the power satellites from the ground before launch, or view the vehicle's destination from a coasting position in low orbit. In addition, since the mirrors are highly reflective not only in the visible but also in the infrared and microwave bands, the system has potential applications as a laser or microwave communications antenna. The following chapter represents an analysis of the system's imaging capabilities in the visible, microwave and infrared regions.

The resolution limits of an imaging system may be determined from the Rayleigh criteria[3], which determines the minimum angular separation, $\Delta\Theta$ between two points which can just be resolved by the system,

$$\Delta\Theta = 1.22 \frac{\lambda}{D} \quad (7.1)$$

where λ is the operating wavelength and D is the system's input aperture diameter. The quantity $1/\Delta\Theta$ is referred to as the resolving power of the system. The Rayleigh criteria may also be expressed in terms of the minimum distance between two points which can just be resolved at a distance l ,

$$d(l) = 1.22 \frac{\lambda l}{D} \quad (7.2)$$

This quantity is taken to be a measure of the system's resolution limits when it is evaluated at $l = f$, the focal length of the system.

Another important property is the numerical aperture of the system, which may be defined by[3]:

$$N.A. = \frac{D}{2f} \quad (7.3)$$

The numerical aperture squared is a measure of the light gathering power of a system. We will also use the f -number, or $f/\#$, of the system, defined by

$$f/\# = \frac{f}{D} \quad (7.4)$$

This is expressed as a single number, so that $f/\# = 3$ is written as $f/3$. The system's $f/\#$ determines the amount of light which reaches the final image plane. For this reason, the reciprocal of the $f/\#$ is known as the relative aperture of the system; thus, a smaller $f/\#$ allows more light to reach the final image. If the image is recorded on either photographic film or an electronic detector, the $f/\#$ squared is a measure of exposure time; for this reason, it is also referred to as the speed of the system. Thus, smaller $f/\#$'s also imply higher speeds. Finally, it seems reasonable that the speed should be related to the light gathering power of the system, and in fact

$$f/\# = \frac{1}{2}(N.A.). \quad (7.5)$$

Having defined the properties of interest, we may now proceed with an evaluation of the Lightcraft optical system. It should be possible to use the entire primary optic (PO) as the light gathering mirror of our optical system. Images from each segment of the PO could be combined (in a manner to be discussed shortly) to generate a single image; this would increase the effective diameter of the entrance pupil to 144.4 cm! The system is now characterized by a $N.A.$ of 2.315, and $f/\# = 0.216^1$. There is a corresponding increase in resolution as well, as given by Table 7.1. Thus, the imaging system performs extremely well! However, note that if the imaging system is to be used in flight, then the fine details of the image will be blurred by any mechanical vibration or flight turbulence in excess of $d(l)$. In flight, then, the minimum resolution distance will be limited not by the optics but by vibrations within the optical supports. In addition, the optical system could only be used for imaging during subsonic flight, when the conical bow shock wave is not present. This shock wave represents a plane of extreme optical phase distortion, which hopelessly distorts the image.

It would be possible to combine images from different segments of the PO using multiple cameras, as illustrated in Figure 7.1. The images from each camera are combined electronically by an on-board computer; segmented mirrors have already been used successfully in ground-based telescopes[3]. In this

¹By comparison, we may consider a typical high quality camera system[3]; a $N.A.$ on the order of 1 is considered quite good for a wide-angle lens, and an $f/1$ lens is very fast.

	Wavelength				units
	400 nm	700 nm	10.6 μm	1.0 cm	
$\Delta\Theta$	3.38×10^{-7}	5.90×10^{-7}	8.95×10^{-6}	8.48×10^{-2}	radians
$d(f)$	1.05×10^{-7}	1.89×10^{-7}	2.80×10^{-6}	2.64×10^{-2}	meters
$d(36,000 \text{ km})$	12.16	21.29	322.41	3.04×10^6	meters
$d(360 \text{ km})$	0.122	0.213	3.22	3.04×10^4	meters
$d(180 \text{ km})$	0.061	0.106	1.61	1.52×10^4	meters

Table 7.1: Resolution Limits for Entire PO

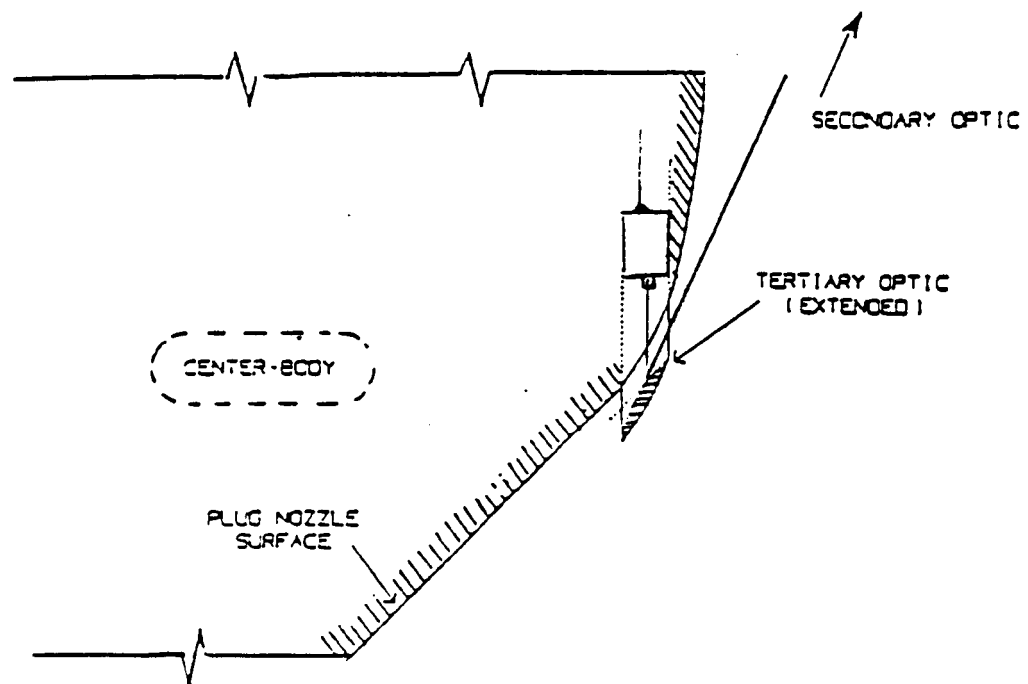


Figure 7.1: Placement of Video Camera for Imaging Through Optical System

design, the camera is enclosed in the afterbody and receives an image reflected from each tertiary optic (TO). It would not be necessary to use every TO; a dozen cameras, symmetrically spaced, could provide a sufficient image. We note that the concept of using several mirrors to simulate a single large diameter mirror has been demonstrated previously in the Multiple Mirror Telescope and the National New Technology Telescope[9].

However, it may be possible to eliminate the need for multiple cameras. A single-mode optical fiber is capable of transmitting high quality images from the image plane[8]. In addition, a coherent² fiber bundle is capable of covering a large area of the image. It is thus possible to replace the cameras with coherent, single-mode fiber bundles to receive the image from the TO; the various signals could be channeled directly to a central computer processor/detector located in the cockpit. Thus, a single, large detector array could replace twelve cameras and their associated electronics. Optical fibers are also relatively inexpensive, so that more than twelve TO links could be used to generate a higher quality image. The optical fibers are also immune to external electromagnetic interference, unlike the twelve separate cameras proposed earlier. Thus, a fiber optic system could produce an image free of noise due to electronic interference at the detector.

There is one final concern to be addressed in the optical system, namely spherical aberration. This can be expected to be the dominant form of aberration in the system, resulting from the annular, parabolic PO. Since the secondary optic (SO) is also annular, most of the spherical aberration induced by the PO will be corrected at the SO. We also note, however, that if the optical fiber design is utilized, the fiber bundles can be made to act as a field flattener to correct for aberrations. This is accomplished by polishing the ends of the fiber bundle into a rigid contour, or mosaic[1]. These mosaics can be ground to match the wavefront contour at their input, and to match the profile of the detector plane at their output. Thus, the fiber optic channel itself can be designed to correct spherical aberration in the image. An imaging system using fiber optics could also be useful for inspecting the optical train for dirty optical surfaces or damage to the mirrors. Recall that a coherent fiber bundle is used to observe the image; the single-mode fibers within this bundle typically have a diameter of 5 microns. Since the focal spot at the TO is expected to be 1 cm in diameter, the bundle would be composed of 4×10^6 individual fibers. (Bundles approaching this size are commonly used in communications systems). In practice, a somewhat smaller number of fibers would probably be used to allow for nonuniform packing and a thin layer of cladding between the fibers.

This system could be used to inspect the optical surfaces for flaws; each 5 micron diameter fiber can view an area of 50 microns diameter on the SO, or 500 microns diameter on the PO. Thus, by visual inspection alone it would be

²Note that in fiber optics terminology, "coherent" refers to a fiber bundle whose components terminate at the same plane.

possible to detect flaws of this size or greater on the SO and PO. If any defects were found, they could be illuminated by shifting one end of the fiber bundle from the detector to an array of laser diodes. Each diode could illuminate one of the single-mode fibers making up the bundle. By activating the correct diode, it would be possible to shine light through the system to illuminate the defects, which could then be easily located and repaired.

7.2 Electrostatic Cleaning of Optical Surfaces

As noted in last year's report, the receptive optical surfaces of the Apollo Lightcraft must be kept free of dust particles and other surface contamination. Since the optics are fabricated to very high surface tolerances, it is impractical to clean them with any form of chemical or abrasive glass cleaning fluids. It has been suggested that a flexible plastic shield could be extruded to protect the optics when the vehicle is at rest. However, dust particles would also accumulate on this shield, causing high dust concentrations in the area when the shield is removed. Ideally, we would require some method for removing dust from the area around the optics, without making physical contact with the optical surfaces.

Electrostatic dust precipitators have the potential to clean optical surfaces in this manner; in fact, this technology is currently used to create dust-free environments in electric power generating plants and laboratory clean rooms[11]. Recent studies have also applied electrostatic repulsion systems to clean high-energy laser mirrors and large telescope objectives without obstructing the optical path[10]. This report will review the basic concept of electrostatic cleaning technology, as well as proposing a system for the Apollo Lightcraft.

The basic principles of electrostatic cleaning are illustrated by the electrostatic fence shown in Figure 7.2. A high voltage (on the order of 15 kV) is applied to an array of needle-like conductors; the field at the needle tip is high enough to initiate a localized corona discharge. This generates a large number of electrons, which interact with the surrounding air to produce ozone. The negatively charged oxygen molecules are drawn to an area of lower potential, thus generating an "electric wind" that diverts incoming particles. Note that uncharged air is free to flow through the system. This mechanism of dust repulsion is known as field charging; it is most effective for particles in excess of 100 microns diameter[11]. The ionized oxygen molecules serve an additional purpose, since they charge incoming dust particles; the charged dust is then repulsed by the electrostatic field in the region. As the charged dust is repelled, it collides with other incoming dust which may in turn induce a charge on more incident dust particles. This secondary repulsion mechanism is known as diffusion charging, and is most efficient for submicron diameter particles.

The arrangement in Figure 7.2 causes the dust to deposit on a grounded screen rather than the protected surface. However, the technology has been

investigated for removing dust from an area, rather than causing deposition on another surface[10]. Figure 7.3 illustrates a non-contact system for cleaning 30 cm diameter laser mirrors without obstructing the optical path; this system was developed under a U.S. Air Force contract and published in Ref. [10]. In this case, the electric wind is made to flow over the surface from all sides; dust particles are swept away from the surrounding area, and will not deposit near the mirror. The design was determined experimentally, since there is no theory to predict parameters such as the optimum needle spacing, needle length, or screen opening dimensions. It may also be able to protect mirrors from out-gassing of materials in space, desorption of water from the vehicle structure, or micrometeorites.

Information from Ref. [10] indicates that this design should scale fairly well to different sized mirrors. It has also been shown [10] that the corona discharge produces no detectable radio frequency noise over the 54-160 kHz AM band and the 88-108 MHz FM band; thus, operation of this system should not interfere with the Lightcraft communication systems or on board electronics. Based on this, we propose an electrostatic cleaning system for the Apollo Lightcraft, with operating parameters as shown in Table 7.2.

7.3 Protecting the Optical Surfaces

Note that the conical bow shock wave acts to protect the PO by slowing down incident particles and tending to sweep them away from the PO mirror. The effect is illustrated in Figure 7.4, which shows a particle of mass m being swept towards the PO with free-stream velocity V_∞ . As the particle transverses the shock wave and nears the vehicle surface, it is slowed to a velocity V_δ . The ratio V_δ/V_∞ was calculated numerically for a given Mach number and shock wave semi-vertex angle, β . Some typical values are given in Table 7.3. Note from this table that the velocity change is greatest at low Mach numbers; this

All calculations done for Apollo Lightcraft scale,
assuming needle spacing and height as given in [10].

	Area to be cleaned (cm ²)	Size of needle array (cm)	Required voltage (kVolts)
Mirror shown in Figure 7.3	706.85	15.0	17.0
Primary Optic	8×10^4	159.57	180.85
Secondary Optic	106.67	5.83	6.61
Tertiary Optic ^a	2.25	0.84	0.95

^aEach TO to be cleaned individually

Table 7.2: Operating Parameters for Electrostatic Cleaning System

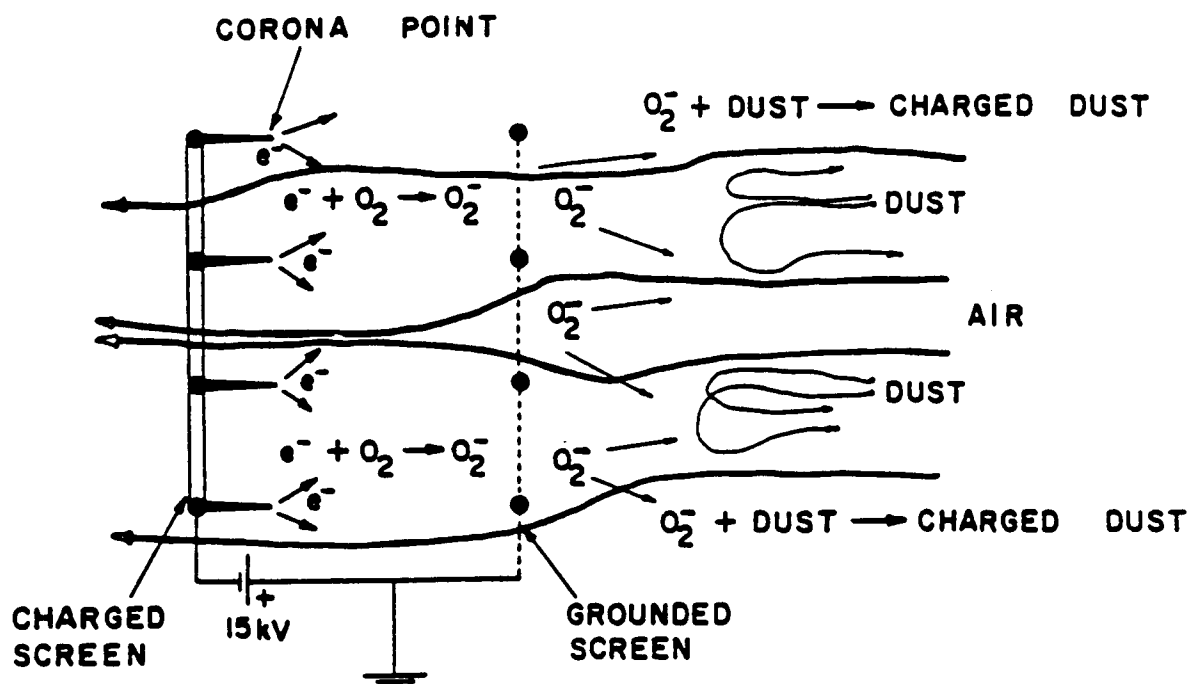


Figure 7.2: Schematic of Electrostatic Fence to Reject Dust and Admit Air[11].

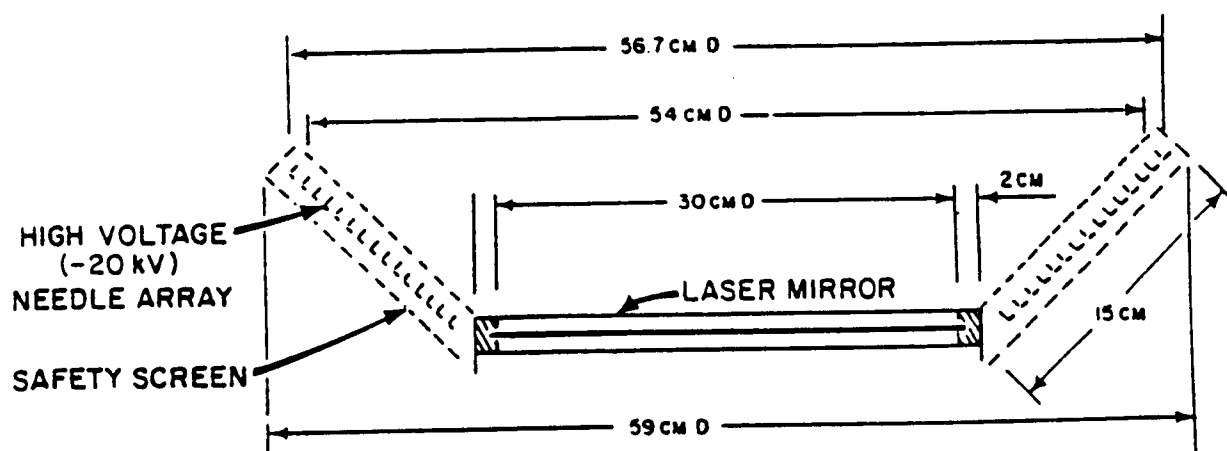


Figure 7.3: Schematic Drawing of Electrostatic Dust Repulsion System for 30 cm Mirror[10].

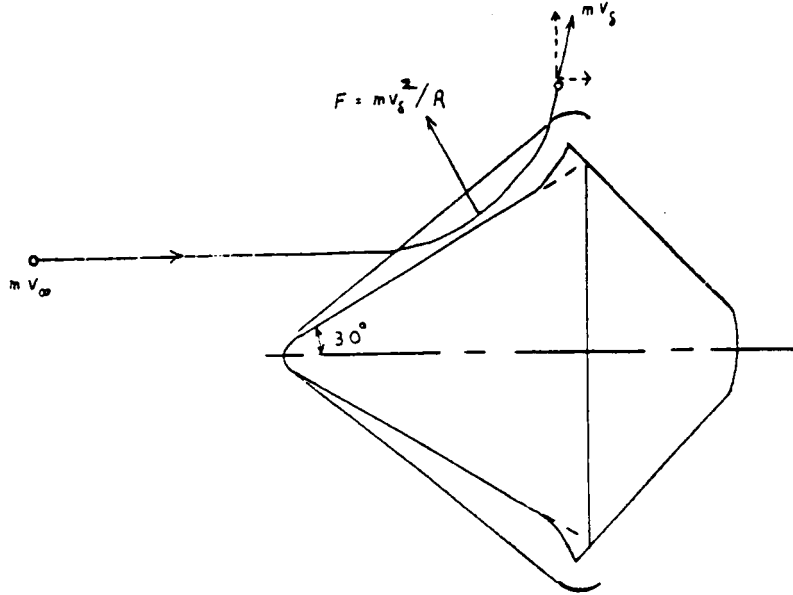


Figure 7.4: Use of the Bow Shock Wave to Deflect Incident Particles from the Primary Optic.

M_∞	β , (degrees)	V_0/V_∞
1.1382	68.259	0.8226
1.5144	44.559	0.8879
1.9541	34.620	0.9086
2.5787	27.854	0.9241
3.0217	25.163	0.9310
4.5910	20.639	0.9443
6.5012	18.665	0.9511
8.7125	17.724	0.9546
16.855	16.805	0.9582

Table 7.3: Velocity Change for Incident Particle Contamination as a Function of Mach Number and Shock Wave Semi-Vertex Angle

is also where the possible particle contamination is highest. Also, the values in Table 7.3 are actually underestimates, since they assume a purely conical forebody and do not account for the additional effects of the craft's parabolic forebody.

Under this approximation, it is possible to estimate the maximum velocity of an incident particle which will still be deflected. The particle's initial momentum is mV_∞ ; assuming it follows the streamlines as shown in Figure 7.4, it will be acted upon by a centripetal force given by

$$F = \frac{mV_\delta^2}{R} \quad (7.6)$$

where R is the radius of curvature of the PO surface ($R = 62.54 \text{ cm}$). The deflected particle emerges with momentum mV_δ . Assuming a 30° forebody semi-vertex angle, we may calculate by conservation of momentum components:

change in momentum = (centripetal force) \times (interaction time)

$$\begin{aligned} m(V_\infty - V_\delta \cos 30^\circ) &= \frac{m}{R} V_\delta^2 t \cos 60^\circ \\ m(V_\delta - V_\delta \sin 30^\circ) &= \frac{m}{R} V_\delta^2 t \sin 60^\circ \end{aligned} \quad (7.7)$$

where t represents the time required for the interaction; we estimate t to be on the order of 10^{-4} sec, the beam pulse rate. Solving Equation 7.7 simultaneously,

$$\begin{aligned} V_\delta &= \frac{R \sin 30^\circ}{t \sin 60^\circ} = 3,611 \text{ m/s} \\ V_\infty &= V_\delta (\cos 30^\circ + \frac{V_\delta t}{R} \cos 60^\circ) = 4,170 \text{ m/s} \end{aligned} \quad (7.8)$$

Thus, the forebody geometry (R and the semi-vertex angle) determines the maximum velocity of an incident particle which can still be deflected from the PO. Particles exceeding this velocity may strike and damage the PO. Note that this effect is not present when the craft leaves the atmosphere, so micrometeorites travelling at speeds of up to 2 million cm/sec are still a potential problem. A rugged dielectric coating, such as a 400–600 Å thick layer of synthetic diamondlike carbon, could also be applied to protect the optics. These coatings are transparent from 0.35 to 50 μm wavelength[4], and exhibit both high bond strength and good thermal properties. Such materials would also be well suited for MHD Fanjet windows.

Nomenclature

D	Input aperture diameter
$d(l)$	Minimum distance between two points that can be resolved at a distance l
f	Focal length
$f/\#$	f -number
m	Particle mass
M_∞	Free stream Mach number
$N.A.$	Numerical aperture
PO	Primary Optic
R	Primary optic radius of curvature
SO	Secondary Optic
t	Required interaction time
TO	Tertiary Optic
V_δ	Particle velocity near the vehicle surface
V_∞	Free stream velocity
β	Shock wave semi-vertex angle
$\Delta\Theta$	Minimum resolvable angular separation
λ	Operating wavelength

References

- [1] L. Myrabo et al., "Apollo Lightcraft Project Design Report." NASA/USRA Advanced Design Program, Third Annual Summer Conference, June 1987.
- [2] D. Cross, "Apollo Lightcraft Primary Optic Active Area Analysis," (RPI Library Reserve), 1986.
- [3] Hecht and Zajac, *Optics*. Addison Wesley, NY, 1979.
- [4] A. Bubenzer, B. Dischler, A. Nyaiesh, "Optical Properties of Amorphous Carbon," Proc. Symposium on Laser Induced Damage in Optical Materials, Boulder, CO, 1981, p 477.
- [5] J. Verdeyen, *Laser Electronics*, Prentice-Hall, (1984).
- [6] D. Humes, "Preliminary Study on the Use of Lasers for Transmission of Power," Proc. Symposium on Space Laser Power Transmission Systems Studies, 1981, p 15.
- [7] P. F. Holloway, L. Bernard Garrett, "Utility of and Technology for a Space Central Power Station," Ibid, p 86.
- [8] Barnoski, *Fundamentals of Optical Fiber Communications*, Academic Press, 1976.
- [9] M. Mitchell Waldrop, "The Mirror Maker," (an interview with Dr. Roger Angel, Univ. Arizona), *Discover*, December 1987, pp 78-87.

- [10] S. Hoenig, "Electrostatic Technology for Control of Dust and Hydrocarbon Vapors in High Power Laser Systems," Proc. Symposium on Laser Induced Damage in Optical Materials, 1981, p 280.
- [11] A. D. Moore, *Electrostatics and its Applications*, McGraw-Hill, NY.
- [12] J. L. Sims, "Tables for Supersonic Flow Around Right Circular Cones at Zero Angle of Attack," NASA Report SP-3004.

Chapter 8

Optimal Trajectory Analysis

The analysis of an air-breathing launch vehicle's trajectory capabilities is of paramount importance. Not only must the vehicle be capable of achieving orbit, but it must be able to do so in an cost-efficient manner. The Apollo Lightcraft's trajectory analysis was carried out with the help of a software tool, SORT (for *Simulation and Optimization of Rocket Trajectories, Version IV*)[3]. This program will optimize orbital trajectories through iteration, yielding a trajectory which satisfied the constraints placed upon it (i.e., minimize energy usage, propellant mass, etc.). The analysis was carried out through repeated trajectory simulations followed by examination and integration of the results[1]. Last year's report demonstrated the optimum propellant usage trajectory and the optimum energy usage trajectory. These have been further investigated, and sensitivity studies have been performed to determine the affect of changes in the operating parameters of the Lightcraft.

8.1 Optimized Propellant Usage

The reason for minimizing propellant weight for a launch vehicle is that more of the liftoff mass can be *payload*. Since delivering payload to orbit is the desired effect, reducing the total propellant fraction makes the craft "mass efficient."

Many computer simulations were run to explore trajectories that minimize total propellant use. As the other important vehicle parameters and models "firmed up," it became evident that the envisioned craft could fly to orbit using only very small propellant fractions (5-10 percent) of the gross liftoff weight. The SORT program was used to find the optimum trajectory—given a fixed set of inputs like pop-up altitude, maximum laser power available, and of course weights, aerodynamics, etc. The program iterated on the desired position of the relay satellite when the Apollo Lightcraft begins to pitch over and accelerate. It is interesting to note that the final propellant values were quite similar between

cases with different pop-up altitudes and laser powers. This is because SORT iterates to find a trajectory path that minimizes propellant use. If inputs that affect the early portion of the trajectory ($M < 10$) are changed, the iterator will select a pitch profile that optimizes the flight path through the MHD fanjet region, even though the early segment is different.

If it is known before the launch that the vehicle has extra propellant available, this information can be utilized in a number of ways. If nothing else is changed, the vehicle will simply have greater capability for achieving a nominal insertion—in the event of any system malfunctions, or abort scenarios. The extra propellant could be used to make up for “in-flight” problems that would reduce performance. Of course, some propellant must already be allotted for system dispersions, and this simply *adds* to the amount available for these dispersions. A second option for utilizing excess propellant margin is to change the trajectory to a different profile which is less optimal than the baseline trajectory. This could improve abort performance, where large system failures or dispersions create the need for an unusual maneuver; or it might be used to simply relieve structural or aerodynamic stress. The final option is to increase payload weight. This obviously requires that the excess performance capability is recognized with sufficient time before flight to modify the payload and/or cargo hold. This latter solution reaps the greatest tangible gain to the system, since payload delivery is the purpose of launch vehicles.

If the vehicle is “still on the drawing board,” as the Apollo Lightcraft is, this data can be utilized to change the vehicle configuration; matching the payload capability with the propellant requirements. The desired payload for the Apollo Lightcraft is transferring five astronauts to low Earth orbit. The external profile of the Apollo Lightcraft was selected largely on the basis of aerodynamic and engine considerations, rather than propellant requirements. Approximately 4.7 m^3 of internal volume was set aside for tankage, which will hold about 730 pounds (330 kg) of liquid hydrogen. If the mission can be completed using 330 kg, then the current configuration is feasible. Boosting to orbit using only 6 percent of the liftoff weight as propellant would be truly revolutionary. Much effort in the trajectory analysis study was expended attempting to verify that this kind of performance is possible with these recently developed engine models.

The two engine modes that obviously affect propellant usage are the MHD fanjet and the rocket. These laser-energized engines have very high specific impulses. The analysis assumed a rocket performance that is at the upper end of theoretical possibilities (i.e., 1500–2000 sec), although certainly *not* the maximum possible value. However, the MHD fanjet performance values are very close to the theoretical limit. Actual hardware using this engine cycle might have considerably lower performance. The trajectory analysis used these optimistic values to find the *potential* of these kinds of engines. If further analysis shows that actual hardware could only get *one-half* of this performance, overall vehicle performance would still be revolutionary.

When allotting the available propellant for an ascent trajectory, a few other

parameters must be considered. Some fuel must be reserved for the de-orbit rocket burn. Although the descent trajectory has not been evaluated, it was assumed that a 330 ft/s (100 m/s) velocity decrease would lower perigee enough for a successful re-entry. This requires that about 60 pounds of liquid hydrogen must be set aside for de-orbit.

Allocations must also be made for the unusable propellant and a flight performance reserve. The unusable propellant is the liquid (or gaseous) hydrogen which cannot be captured by the fuel pump inlet, as well as that propellant trapped in the fuel lines between the pump and the engine when the inlet runs dry. The space shuttle main propulsion system (MPS) has an unusable residual under one percent. However, a much smaller tank and plumbing system would probably dictate a larger percentage for the Apollo Lightcraft. If 2.0% is used, this yields 14 lbm of unusable hydrogen in the tanks and plumbing of the fuel system.

Finally, some reserve must be maintained for system dispersions. These dispersions include off-nominal engine performance, propellant loading uncertainties, guidance and flight control biases and disturbances, as well as wind and atmospheric variations. All of these factors can reduce performance. Evaluation of this reserve is a highly complicated statistical process which assigns probabilities to various dispersions and failures. These are then averaged together to find the flight performance reserve for the desired amount of protection (2 or 3 standard deviations, etc.). This evaluation is highly dependent on the chosen hardware, launch procedures, etc.; which are currently undefined for the Apollo Lightcraft. If one percent is tentatively selected for this value (the space shuttle MPS reserves about 0.35%), this removes another 7 lbm from that available for nominal flight planning.

The trajectory results consistently showed propellant usage around 650 lbm when using the optimistic MHD generator and fanjet models. Adding up all of the propellant sub-divisions for our optimistic case would require a liftoff hydrogen loading of 735 lbm (333 kg), which is very close to the amount that can fit in the limited volume of the current lightcraft design. Using a more moderate MHD fanjet performance, the propellant weight would have to be increased to about 1250 pounds. Although this volume of propellant would not fit inside the current vehicle airframe, it represents a liftoff propellant fraction under 10 percent. This is still spectacular compared to chemical rockets. In order to deliver the 11,600 lbm lightcraft (empty) to orbit with current chemical rocket technology (assuming the same insertion mass fractions as the STS), 155,000 lbm of propellant would be required. Even when compared with the conservative MHD fanjet case, this represents a propellant reduction of 2 orders of magnitude.

In part, this disparity can be explained by looking at the "rocket equation," given as:

$$\frac{m_i}{m_f} = e^{\Delta v / I_{sp} g} \quad (8.1)$$

where m_i is the initial vehicle mass, m_f is the "burn out" mass, I_{sp} is the engine specific impulse, g is the acceleration due to gravity, and Δv is the fixed velocity increment. The above equation neglects drag and gravity losses which are quite important in orbital launch trajectories, but illustrates that the driving term is an exponential.

If the Apollo Lightcraft were to generate a 33,000 ft/s velocity change for its mass fraction (this value accounts for some gravity and aerodynamic losses), the net average specific impulse is almost 19,000 seconds. This very high specific impulse is achieved because, up until Mach 11 or so, no propellant whatsoever is expended (The average specific impulse for the MHD and rocket modes is around 8000 seconds). Even though the average specific impulse is about 50 times higher than the chemical rockets, the mass usage is about 250 times lower. This is due to an exponential effect that heavily penalizes "low" specific impulse engines.

Obviously, a vehicle like the Apollo Lightcraft can reach orbit with much lower propellant requirements than a vehicle using chemical propulsion. This is important because it greatly reduces the size of the launch vehicle. The lower amount of propellant also reduces the risk of explosion since the vehicle is not a tenuous mass of separated chemical reactants. In fact, a vehicle similar to the Apollo Lightcraft could use *water* instead of hydrogen for propellant (although with reduced specific impulse), since the propellant provides none of the energy to accelerate itself. All of the energy comes from the laser source. The mass is required only as an accelerated reaction mass in the rocket mode, and as an expendable working fluid for the conversion of laser energy to electricity during the MHD fanjet mode. The propulsion system concept for this type of vehicle is undoubtedly revolutionary. However, reducing the propellant usage is not the only important parameter to consider when evaluating these launch trajectories. The total amount of laser energy consumed in propelling the vehicle to orbit is also important.

8.2 Optimized Energy Usage

In a chemical engine, the energy used by the vehicle is intrinsically related to the fuel (and oxidizer) used during the mission/trajectory. For laser energized vehicles, this is not the case. The energy used and propellant expended are not directly linked. The energy cost of the flight may be a significant portion of the launch costs and will probably exceed the propellant costs. The laser energy and propellant are linked indirectly by that fact that an obviously inefficient trajectory will cost both extra propellant and extra energy. However, there are maneuvers that save energy, but do not change the propellant usage significantly. Considering this, a brief study was performed to evaluate energy use.

Changes in the early part of the trajectory when using the ERH thruster and scramjet do not directly affect the propellant usage, but will change the laser energy required for this segment of flight. As discussed in last year's report,

the pop-up maneuver is a significant energy saver; since it avoids flying through the lower atmosphere at high speed. In fact, to save energy in this segment of the flight, the SORT program wants to "loft" the trajectory quite a bit. Flying as high as possible reduces vehicle drag. Of course, the air-breathing engines only work well when the air flow is in a certain range. Too little airflow causes propulsive efficiency to drop, and too much can dilute the mass specific energy addition so much that the inlet losses are not recovered. Therefore, climbing out steeply early in the trajectory, to reduce the drag losses, can penalize the later engine modes because they must operate at higher than optimal altitudes.

When the basic framework of the trajectory is left intact and the SORT program iterates to minimize total energy required for the ascent, the result is very close to the optimized weight case. The optimized energy trajectory uses 538 GW-sec of laser energy (149,560 kW-hr) compared to 547 GW-sec for the optimized propellant case. In order to save 9 GW-sec of energy, expenditure of an additional 25 pounds of liquid hydrogen is required. The fact that these two different optimization concepts yield nearly identical results indicates that energy use and propellant consumption are indirectly linked. The total trajectory-averaged coupling coefficient seems to decrease fairly parallel to the averaged specific impulse for these trajectories. This is not an intuitive result, but net averaged values of coupling coefficient and specific impulse do depend on trajectory losses. These air-breathing trajectories generally indicate that flying a trajectory with lower *net* coupling coefficients will also result in a reduced net specific impulse.

However, the coupling coefficient of the rocket mode is greater than the MHD fanjet at high altitudes and Mach numbers. Therefore, additional energy could be saved by using the rocket in place of the fanjet late in the trajectory, but with a drastic cut in specific impulse (6,000 to 2,000 seconds). So if, near the end of the fanjet phase, the rocket is used to complete the apogee insertion, some energy could be saved. This scenario was simulated and the program iterated to find the minimum energy case. Unfortunately, the minimum energy solution required that the rocket turn on fairly early in the fanjet phase (where the effective coupling coefficients cross each other). This solution used so much propellant that it seriously violated the assumptions used to determine the liftoff weight. Often, the required propellant was 2 or 3 times as much as the baseline case, which would significantly change the vehicle liftoff weight and internal volume of the craft. Therefore, an analysis was performed that evaluated the energy versus propellant tradeoff, while still fairly close to the optimized propellant solution. Figure 8.1 shows how the propellant usage increases with reductions in laser energy, when the rocket is turned on progressively earlier in the trajectory. The optimized energy case that did not use the early rocket burn is also indicated on this plot.

During the vehicle design process, it is necessary to investigate the inherent cost trade-offs when exchanging energy for propellant. Accurate values for the laser energy cost would be required for this analysis, and that would be difficult

to project. The laser energy cost would be a direct function of the number of vehicles in operation, number of relay satellites, laser duty cycles, and the space power grid infra-structure. That analysis is beyond the scope of the present design effort, and Figure 8.1 is shown simply to illustrate the range of possibilities to be considered for this type of vehicle.

8.3 Sensitivity Studies

When the performance analysis for any vehicle begins, it is appropriate to systematically vary some of the vehicle parameters (i.e., ones that are usually assumed fixed in the optimizing analysis) to determine if that analysis leans heavily on any particular input or assumption. For example, vehicle drag might be changed 10% to see how drastically this affects the ascent trajectory. This process determines the sensitivity of the trajectory performance to slight changes in vehicle parameters. This is useful when beginning studies on configuration changes, and gives early indications of potential vehicle problems. Key parameters chosen for the present study are vehicle drag, total vehicle weight, laser wavelength/atmospheric attenuation, and maximum laser power. The baseline case had a pop-up maneuver to 35,000 feet, maximum time-average laser power of 2.8 GW, a laser wavelength of 3.5 microns, and a laser relay satellite with an altitude of 150 nautical miles.

8.3.1 Vehicular Drag

Since the vehicle drag was a large trajectory driver that led to developing the pop-up maneuver, this seemed like a good place to start. The entire drag coefficient curve was scaled up or down, and the program recomputed the optimized weight solution. Figures 8.2 and 8.3 show the change in propellant weight and laser energy (respectively) as the drag coefficient was changed. Note that these curves are very flat, indicating that changes in drag coefficient do not affect vehicle performance very much. This is a surprising result considering how much drag affected the "off-the-deck" trajectories. The reason for this is that the pop-up maneuver has reduced the aerodynamic losses during the trajectory to a comparatively small effect on the performance. The dynamic pressures are now fairly small and the drag coefficients during most of the flight are *very* low. A 30% increase on a very small number (0.06) is still a small number (0.078). Notice that the curve does indicate a progressively steepening performance penalty as the drag increases. This suggests that as long as the drag coefficient during the scramjet and the MHD fanjet modes stays at or below 0.08 to 0.10, the performance of the vehicle is not significantly affected. Also note that increasing the drag 30% is precisely equivalent to increasing the wetted surface area 30% and leaving the drag coefficient alone. Therefore, this study has effectively determined the effects of aerodynamic shape *and* size on

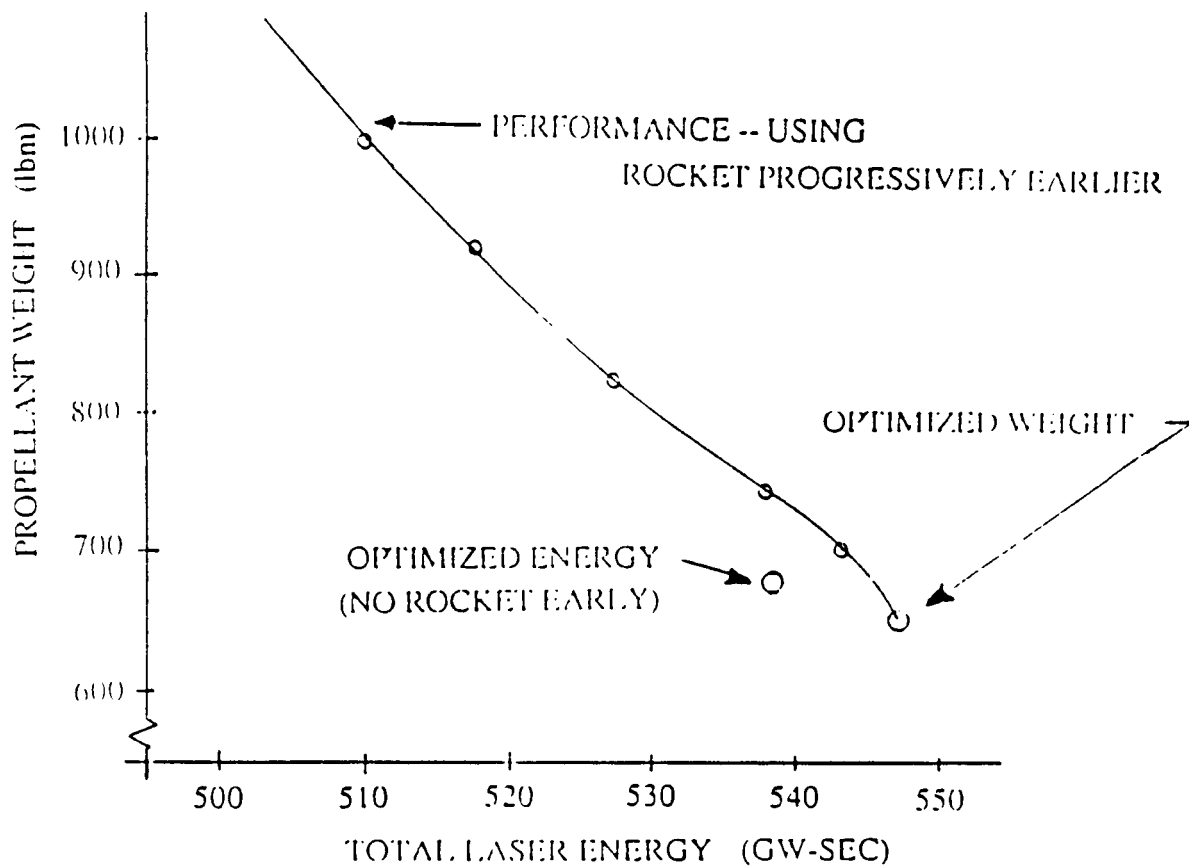


Figure 8.1: Performance Study—Propellant vs. Laser Energy

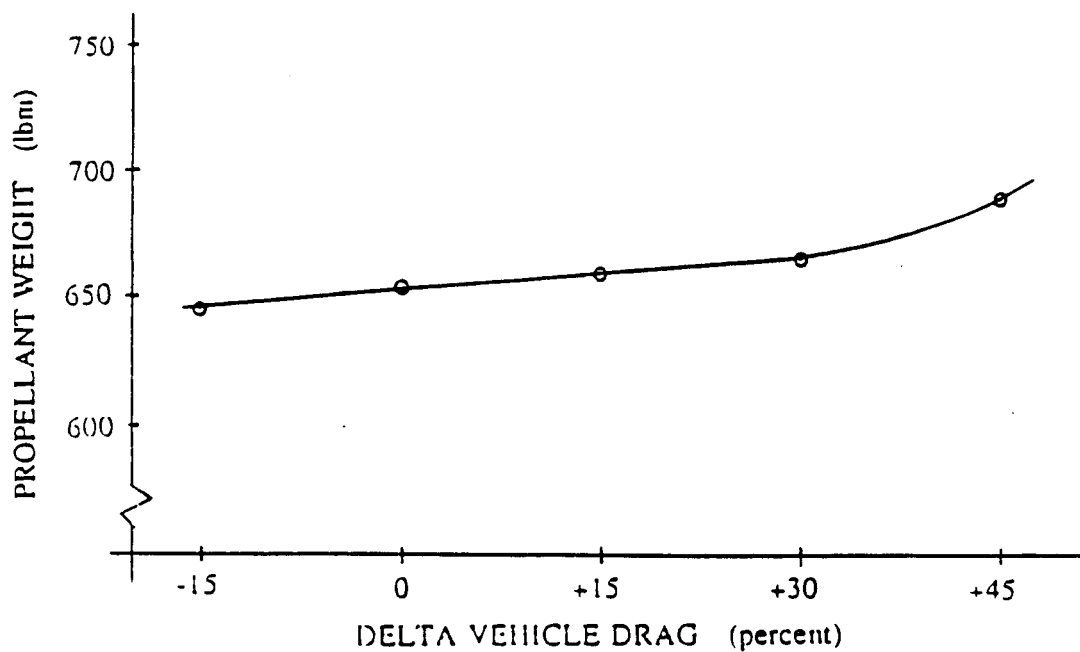


Figure 8.2: Performance Sensitivity to Aerodynamic Drag—Propellant Weight

vehicle performance.

8.3.2 Laser Wavelength/Atmospheric Attenuation

The choice of laser wavelength and the associated atmospheric attenuation has been generally neglected in the preceding discussion. Wavelength selection would normally be driven by the laser intensities desired upon the craft's primary optics, and the type of lasers available. High intensities will obviously yield more power collected per receiver optical area; also, the intensity threshold for plasma ignition on the optics increases with shorter wavelengths. However, atmospheric attenuation generally increases as the wavelengths get shorter in the infrared, visible and ultraviolet electromagnetic spectrum[6]. The atmospheric attenuation actually has many peaks and troughs (i.e., windows) throughout the entire electromagnetic spectrum. The spectrum around the visible band has the largest capability of delivering the power densities needed for the Apollo Lightcraft. Light generation in this spectral region is associated with lasers (rather than say masers for microwaves). Selection of a particular laser device may determine what wavelength of light can be produced. In theory, free electron lasers can be designed to produce almost any frequency, within a certain band, and therefore, the available range of wavelengths was assumed to be a spectrum rather than a few selected points. Free electron lasers also offer promise of very high conversion efficiencies (20-50%).

The atmospheric attenuation losses associated with these lightcraft trajectories has been greatly reduced by the pop-up maneuver. Since only very low powers are needed in the low atmosphere (where attenuation is the greatest), the transmission losses are very small for most of the current trajectories. Almost all simulations used attenuation data for 3.5 micron light, which is an intermediate value in the possible spectrum (i.e., 10.6 to 0.34 μm). The attenuation of the energy leaving the laser is only about 2 GW-sec of the entire 547 GW-sec delivered to the vehicle. If the wavelength is shortened to 0.34 microns (ultraviolet), the losses increase to 36 GW-sec. Attenuation losses rapidly build up at shorter wavelengths than this. At about 0.3 microns, attenuation is near 100%, and atmospheric transmission becomes untenable. Using laser energy at 0.34 microns, the craft could receive 10 GW of energy on the current optic size (8 m^2). This was the original maximum design condition for the vehicle, but as the trajectory analysis has shown, there is no need for such high powers on this sized craft. The use of lower power requirements, and the pop-up maneuver, have reduced the laser attenuation to a small role among the performance drivers.

8.3.3 Vehicle Liftoff Weight

Another potential change that could occur in the design process is a reevaluation of the current weight estimates. The question arises then, how critical is weight to the trajectory analysis that has been completed so far? Figures 8.4 and 8.5

show how lightcraft energy and propellant usage are affected by variations in the liftoff weight. The effect is significant, but fairly linear. Propellant weight increases roughly "one to one" with the liftoff weight; i.e., the craft delivers 10% more weight to orbit for 10% more propellant. The only reason this is possible is because the very large specific impulses keep the propellant fraction so low. This type of trade-off is entirely foreign to chemically-powered vehicles. For the space shuttle, a 100 pound increase in inert (non-propellant) liftoff weight requires an additional 1400 pounds of propellant to deliver it. The fact that the Apollo Lightcraft has such linear propellant requirements indicates that these types of vehicles might be successfully scaled up to much larger configurations (and payloads). The major problem remaining will be the difficulties in scaling up the laser power to go with the increased vehicle size.

8.3.4 Maximum Laser Power

The final sensitivity study addresses changing the engine "power setting" during flight. For simplicity, the power setting was set at a fixed value for all of the trajectory—following the ERH thruster mode. Clearly, this will *not* be optimal, but to allow "throttling" in a first cut analysis would incredibly compound the problem. Since a nearly infinite number of possibilities exist, where would one start? Sometime in the future, when the optimal characteristics of lightcraft trajectories are more clearly defined, the first clues on how to optimally throttle such a craft might also become apparent.

It became evident early in the analysis that maximum power (10 GW) flights were not efficient. Subsequently, power was decreased slowly until it reached approximately 3 GW. The lightcraft could still fly at lower power settings, but the trajectories were more constrained. In other words, finding a successful trajectory at the low power settings became increasingly difficult; hence, most of the analysis used 2.8 GW of laser power. Even though there were indications that performance could be improved somewhat at lower powers, it constrained the solutions so severely that it would limit the scope of the analysis if power settings too low were used early in the analysis. After the other parameters were investigated, the power issue was revisited.

Figures 8.6, 8.7, and 8.8 illustrate what happens as the power is varied. The propellant weight does not change very much. Since most of the early analysis focused on this, it only seemed appropriate to reduce the power setting (and hence the laser size) until it seemed to affect the difficulty in finding a good solution. The energy plot (Figure 8.7) shows that decreasing the power, and therefore thrust, actually *saves* energy. There are two reasons for this. The first is, as power is reduced, the coupling coefficient of the MHD fanjet gets better because the propulsive efficiency increases. The second reason is shown in Figure 8.8. The dynamic pressure increases considerably as the power setting increases. This again verifies the decision to reduce drag with power reduction and the pop-up maneuver.

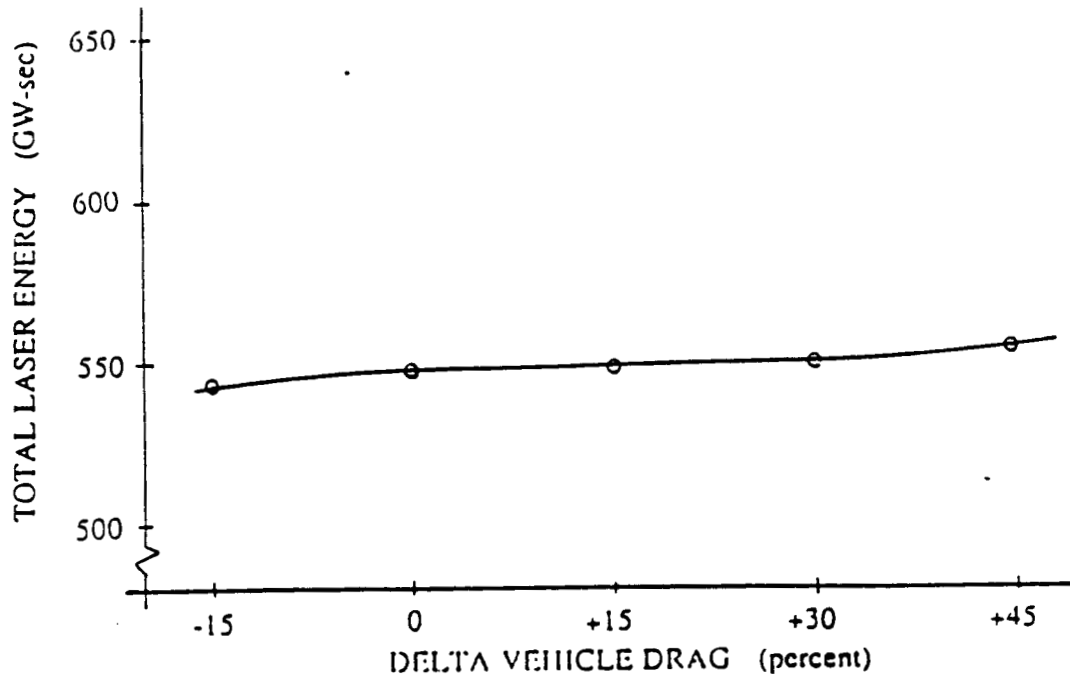


Figure 8.3: Performance Sensitivity to Aerodynamic Drag—Total Laser Energy

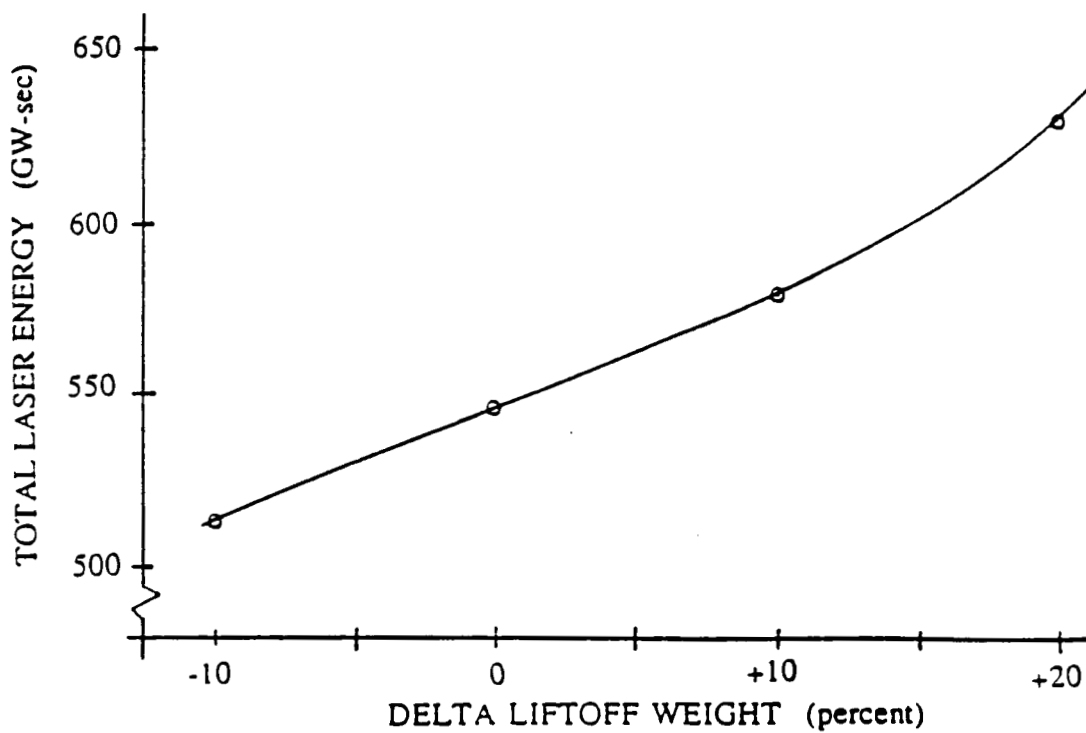


Figure 8.4: Performance Sensitivity to Lift-Off Weight—Total Laser Energy

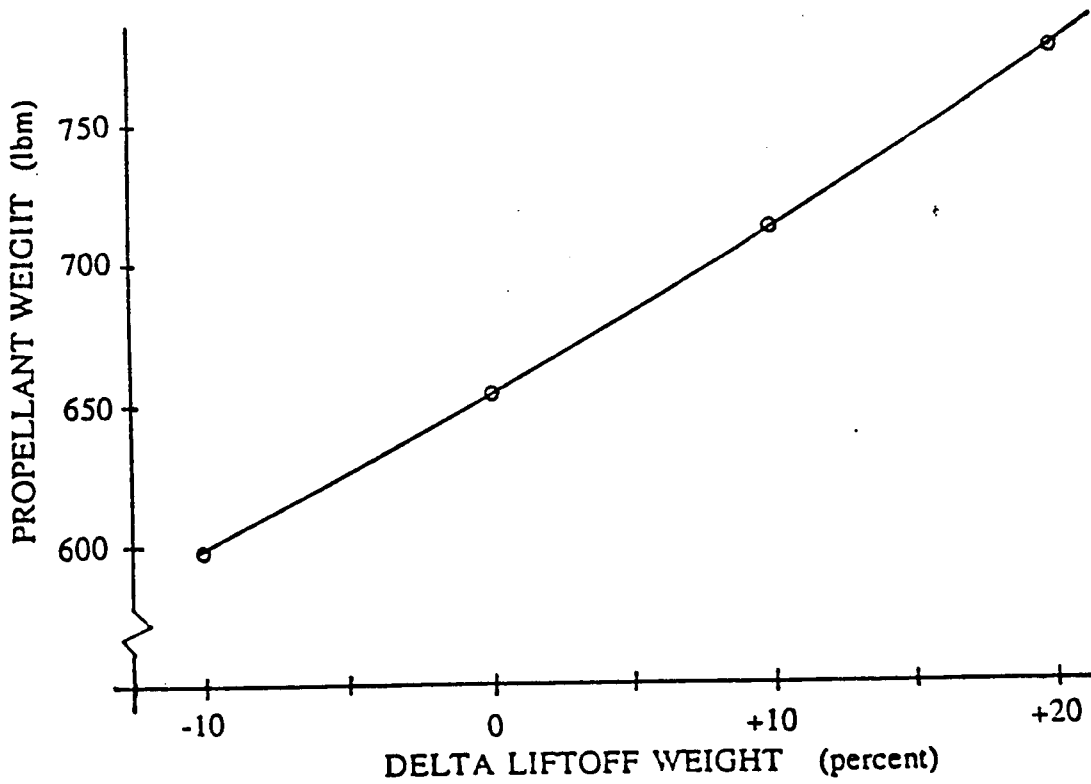


Figure 8.5: Performance Sensitivity to Lift-Off Weight—Propellant Weight

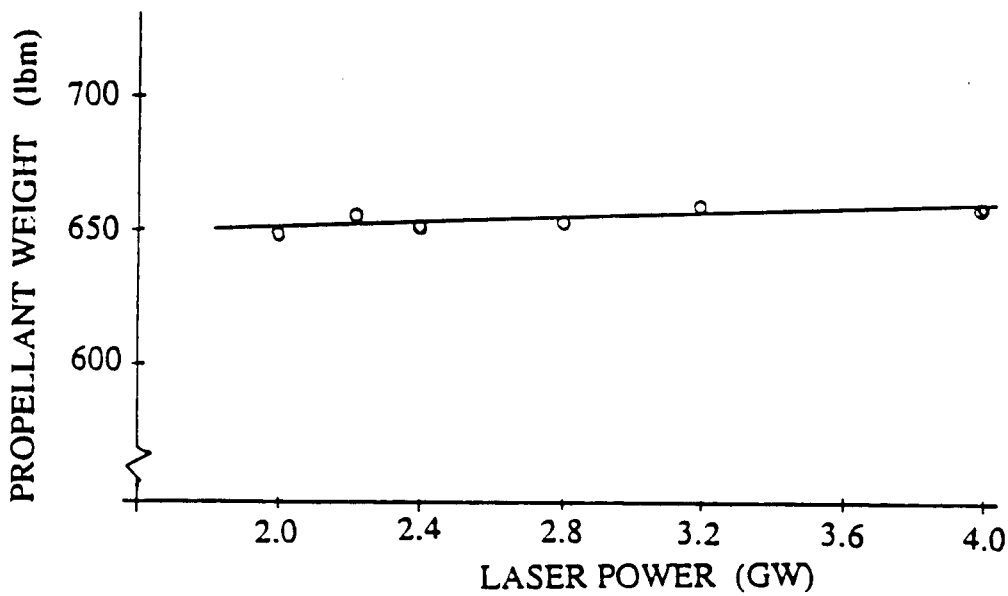


Figure 8.6: Performance Sensitivity to Laser Power—Propellant Weight

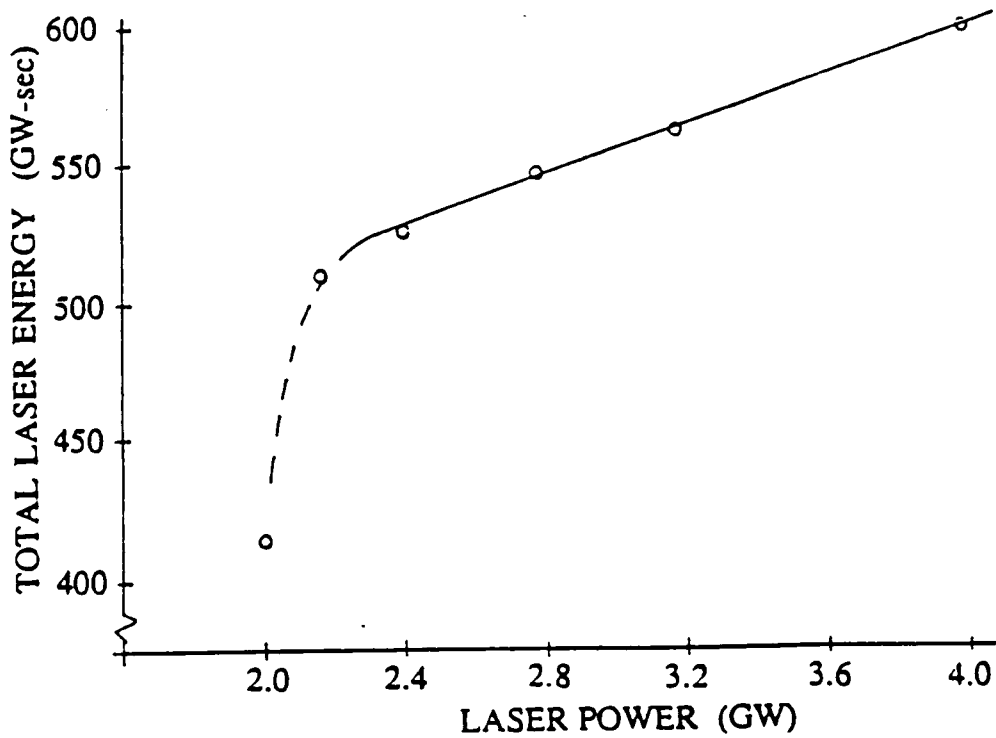


Figure 8.7: Performance Sensitivity to Laser Power—Total Laser Energy

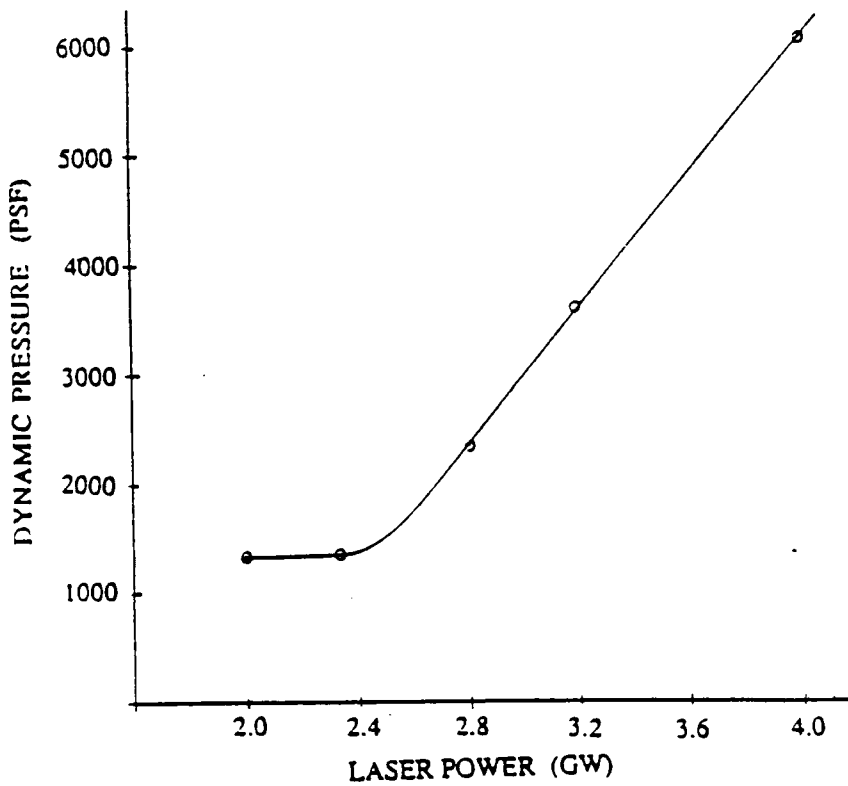


Figure 8.8: Performance Sensitivity to Laser Power—Dynamic Pressure

Some low power cases near the borderline of possibility indicate that significant reductions in total laser energy might be possible as the power settings drop near 2 Gigawatts (See Figure 8.7). The reason for this seems to be that the propulsive efficiency of the MHD fanjet increases quite a bit right before the thrust goes negative. Some simulated trajectories operating in this regime indicated energy savings as high as 25%. The MHD fanjet uses about two thirds of the total laser energy of the flight due to the necessarily lower coupling coefficients for the higher Mach numbers, so the coupling coefficient in this engine mode will be the primary driver for total energy cost. However, it is very difficult to get a trajectory that performs sufficiently well in the scramjet mode (where the drag is higher at the lower altitudes) at these power settings. The scramjet performance is so low at these very low power settings that the vehicle does not reach orbit before the satellite "disappears" over the horizon. Another parameter could be varied to improve that situation. If the laser relay satellite altitude is raised, the vehicle will pitch over slower, giving the vehicle more time to accelerate in the scramjet mode. This issue will require further study because one is looking for successful solutions near the "ragged edge" where the trajectories either fail altogether or exhibit excellent energy performance.

References

- [1] Frazier, S. R., "Trajectory Analysis of a Laser-Energized Transatmospheric Vehicle," Master's Thesis, Rensselaer Polytechnic Institute, Troy, NY, August 1987.
- [2] Bate, R. R., Mueller, D. D., and White, J., *Fundamentals of Astrodynamics*, Dover Publishing Co., NY 1979.
- [3] Berning, M., "Version IV User's Guide for the Simulation and Optimization of Rocket Trajectories Program," McDonnell Douglas Astronautics Co., Houston, TX, Transmittal Memo No. 1.2-TM-FM86028-53, Dec. 1985.
- [4] Bush, W. B., "Magnetohydrodynamic—Hypersonic Flow Past a Blunt Body," *Journal of Aerospace Science*, Nov. 1958.
- [5] Drake, J. H., "Optimal Isothermal Acceleration of a Plasma with Constant Magnetic Field," Lockheed Missile and Space Co., Palo Alto, CS, *AIAA Journal*, Vol 1, No. 9, 1963.
- [6] Elterman, L., "UV, Visible, and IR Attenuation for Altitudes to 50 km—1968," Report No. AFCRL-68-0153, Optical Physics Laboratory, Air Force Cambridge Research Laboratories, L. G. Hanscom Field, Bedford, MA, April 1968.
- [7] Hill, P., and Peterson, C., *Mechanics and Thermodynamics of Propulsion*, Addison Wesley Publishing, 1965.

- [8] McCormick, B. W., *Aerodynamics, Aeronautics, and Flight Mechanics*, John Wiley and Sons, New York, NY, 1979.
- [9] Moder, J. P., Blandino, J. S., Frazier, S. R., Myrabo, L. N. of Rensselaer Polytechnic Institute, Troy, NY, and Rosa, R. J., of Montana State Univ., Bozeman, MT, "Laser Energized MHD Generator for Hypersonic Electric Air-Turborockets," AIAA/SAE/ASME/ASEE 23rd Joint Propulsion Conference, 1987.
- [10] Myrabo, L. N. (editor), *Apollo Lightcraft Project*, 1987 report to NASA/USRA Advanced Design Program—Summer Conference.
- [11] Myrabo, L. N., Ing, D., *Future of Flight*, Baen Enterprises, New York, NY 1985.
- [12] Nyberg, G. A., Hill, S. C., Mitty, T. J., Lidke, K., and Poulin, S., "Performance Analysis of a Laser-Powered SSTO Shuttlecraft," RPI, Troy, NY, Feb. 1987.
- [13] Patch, R. W., "Thermodynamic Properties and Theoretical Rocket Performance of Hydrogen—100,000 K and 1.01325×10^8 N/m²," NASA Report SP-3069.
- [14] Razier, Yu., P., *Laser Induced Discharge Phenomena*, Consultants Bureau, New York, NY 1977.
- [15] Resler, E. L., and Sheer, W. R., "The Prospects for Magneto-Aerodynamics," *Journal of the Aeronautical Sciences*, April 1968.
- [16] Rosa, R. J., *Magnetohydrodynamic Energy Conversion*, McGraw-Hill, NY, 1968.
- [17] Yos, J., "Revised Transport Properties for High Temperature Air and its Components," Avco Systems Division, Lowell, MA, Technical Report, Nov 28, 1967.

Chapter 9

Re-Entry Aerodynamics

9.1 Trajectory Analysis

The initial configuration for the afterbody of the Apollo Lightcraft was designed to fit the requirements of the ERH thruster mode. Little attention was given to satisfying the restrictions of manned re-entry. Realizing the significance of addressing these concerns, analyses were begun to determine what the restrictions were, how well the current configuration met these restrictions, and how the configuration should be redesigned to better satisfy these requirements.

For manned re-entry, the overriding restrictions arise from two areas: human tolerance to accelerations, and vehicle aerodynamic heating. For initial purposes, only the acceleration (or aerodynamic load factor) problem was addressed. While peak load factors may reach values as high as 10 g's for very short durations, it is desirable to restrict operation over the majority of the trajectory to 4 g's or less.

Initially, only conceptual attention had been given to the vehicle configuration during re-entry. It was assumed that the shroud would translate to the fully forward position and be integrated into the heat shield. The heat shield would cover the entire afterbody of the vehicle. The resulting afterbody configuration would be a blunted 45° cone with a base diameter equal to that of the maximum diameter of the shroud. This configuration is shown in Fig. 9.1.

To find out how well this configuration met the applied restrictions, it became necessary to solve the point-mass equations of motion for a spherical, non-rotating Earth. These equations, describing the vehicle's acceleration and flight path angle, are derived from a study of the forces acting on the vehicle, as presented in Fig. 9.2.

The equation for the acceleration may be written as,

$$\frac{dV}{dt} = g \sin \gamma - \frac{D}{m} \quad (9.1)$$

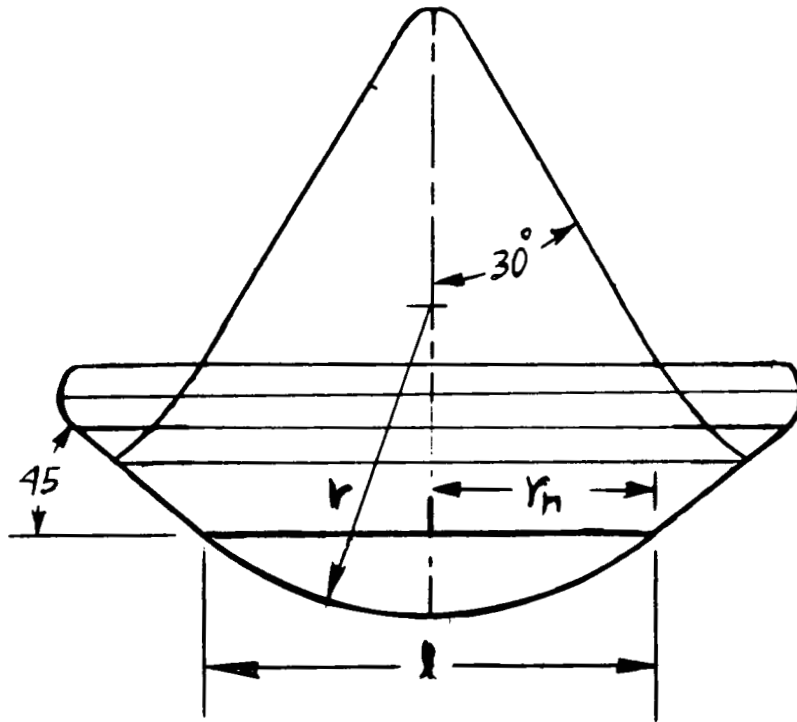


Figure 9.1: Re-entry Configuration

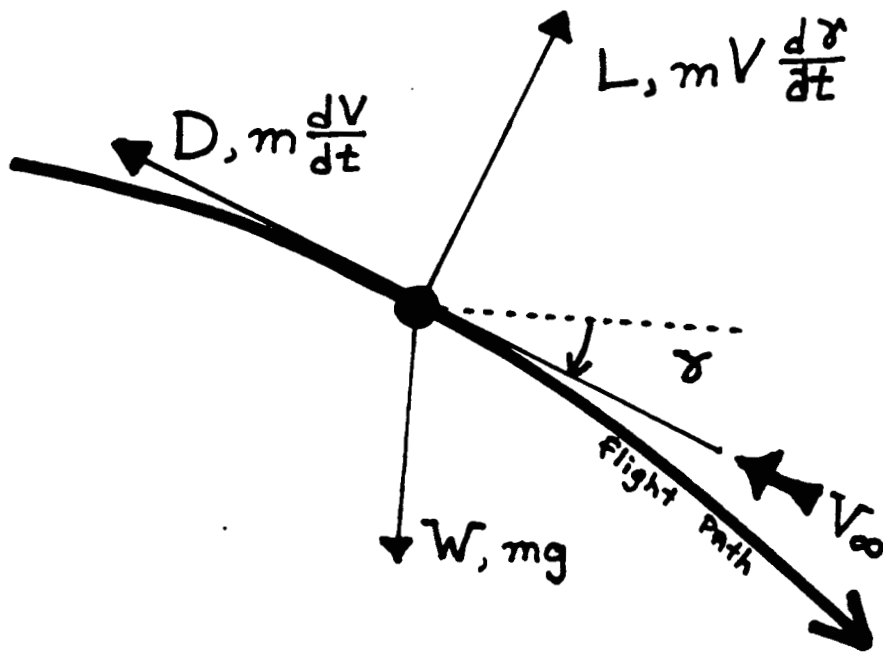


Figure 9.2: Body Forces During Re-entry

or in terms of the drag as,

$$\frac{dV}{dt} = g \sin \gamma - \rho \frac{V^2 C_D S}{2m} \quad (9.2)$$

For convenience the ballistic factor may be introduced as,

$$BF = \frac{mg}{C_D S} \quad (9.3)$$

which results in the expression

$$\frac{dV}{dt} = g \sin \gamma - \rho \frac{gV^2}{2BF} \quad (9.4)$$

For purposes of performing calculations, it is desirable to express the acceleration in terms of the change in velocity with respect to altitude. Applying the chain rule,

$$\frac{dV}{dt} = \frac{dV}{dz} \frac{dz}{dt} \quad (9.5)$$

where $\frac{dz}{dt}$ is simply the vertical component of velocity

$$\frac{dz}{dt} = -V \sin \gamma \quad (9.6)$$

Therefore, the change in velocity with respect to altitude becomes,

$$\frac{dV}{dz} = \frac{\rho g V}{2BF \sin \gamma} - \frac{g}{V} \quad (9.7)$$

Similarly, the change in flight path angle with respect to time is given by

$$\frac{d\gamma}{dt} = \frac{g \cos \gamma}{V} - \frac{L}{mV} - \frac{V \cos \gamma}{R + z} \quad (9.8)$$

which leads to the expression

$$V \left(\frac{d\gamma}{dt} + \frac{d\theta}{dt} \right) = g \cos \gamma - \frac{\rho g V}{2BF} \frac{L}{D} \quad (9.9)$$

where the $\frac{d\theta}{dt}$ term includes the effects of curvature

$$\frac{d\theta}{dt} = \frac{\rho g}{2BF} \frac{L}{D} - \frac{g}{V^2 \tan \gamma} \quad (9.10)$$

However, since $\frac{d\theta}{dt} \ll 1$, its effects may be neglected. Applying the chain rule, the change in flight path angle with respect to altitude becomes

$$\frac{d\gamma}{dz} = \frac{\rho g}{2BF \sin \gamma} \frac{L}{D} - \frac{g}{V^2 \tan \gamma} \quad (9.11)$$

Finally, the load factor or deceleration in g's is given as

$$G = \rho \frac{V^2 S}{2W} \sqrt{C_L^2 + C_D^2} \quad (9.12)$$

Together Eqns. 9.7 and 9.11 represent the coupled non-linear equations governing re-entry motion. A computer code was developed to solve these equations numerically using a simple Euler method. The 1959 ARDC Model Atmosphere was used to provide the altitude-density profile. The aerodynamic coefficients, which are functions of the vehicle's configuration and orientation, are obtained as discussed in Section 9.2. The mission requirements for the Apollo Lightcraft specify that the vehicle be capable of operating on orbital and sub-orbital trajectories. This specifies the upper limit of the entrance velocity as escape velocity, approximately 26,000 ft/s.

Since the vehicle has no inherent lift-to-drag ratio, the first case tested was ballistic, or non-lifting, re-entry. Variations in both the entrance angle and velocity were tested to study the affect on the deceleration profile. Variations resulted in changes in the magnitude but not the location of the peak loading. While in all cases the deceleration profiles proved unacceptable, the investigation revealed that the entry angle was limited to very shallow angles, 5° or less. Further, exceedingly high decelerations at all but very low sub-orbital velocities indicate that the vehicle must incorporate lift into its trajectory.

As an initial investigation of lifting re-entries, the simplest case of constant L/D ratios was investigated. Results followed those outlined by Loh[2] for moderate L/D ratios and shallow angles of inclination, with the vehicle exhibiting an oscillatory or skipping behavior.

With the introduction of a variable L/D ratio the analysis increases in complexity. Depending on how much lift, and at what location it is applied, solutions will vary. While at this time variable L/D trajectories have yet to be investigated, a brief discussion of the analysis is included. Extensive work on variable L/D ratio flight has been conducted by Loh[2] to obtain both approximate and analytical solutions. Solutions cited include flight at constant deceleration or load factor, constant heat input, constant equilibrium temperature, constant rate of descent and constant flight path angle. By applying these solutions to certain portions of the trajectory, such as the high speed entry portion, or the region of critical heating or loading, reductions in the maximum values can be obtained.

Numerical solutions for the required L/D program are possible by applying optimization techniques such as calculus of variations or gradient methods such as the "steepest descent" procedure outlined by Bryson, et. al.[1]. These procedures usually require that several initial conditions, such as altitude, entry angle and velocity, be specified; as well as some stopping condition such as a final altitude. In addition, constraints such as an acceleration tolerance rate may be placed upon the problem. A payoff quantity, such as minimum total heat input, and a nominal (reference) trajectory, are also specified. Calcula-

tions proceed by making corrections to the nominal trajectory based upon the boundary conditions and restrictions.

Future studies plan to investigate both the solutions provided by Loh and the optimization techniques presented by Bryson. In addition, the analysis will be extended to include aerodynamic heating and vehicle stability considerations.

9.2 Aerodynamics

As discussed in the previous section, in order to solve the equations of motion it is necessary to obtain expressions for the aerodynamic force coefficients. During the majority of the trajectory, the vehicle will be traveling in the hypersonic regime (taken to be $M > 4$). In this region the forces are dominated by pressure effects, with viscous and other effects representing only about ten percent of the total. Noting this, the flow may be approximated as inviscid, and Newtonian Impact Theory can be used to obtain theoretical predictions of the force coefficients.

As discussed by Regan[3], Newtonian Impact Theory assumes that the component of momentum normal to the surface of the body is converted to a pressure acting on the body, while the tangential component remains conserved. The resulting pressure is related to the magnitude of the normal velocity and may be written as,

$$(p - p_\infty) = \rho_\infty V_n^2 = \rho_\infty (\mathbf{V} \cdot \mathbf{n})^2 \quad (9.13)$$

The force acting on the elemental area can be written in vector form as

$$d\mathbf{F} = (p - p_\infty) \mathbf{n} da \quad (9.14)$$

Neglecting the side force and integrating over the area exposed to the flow, expressions for the axial and normal force coefficients are obtained as follows,

$$C_A = \frac{2}{\rho_\infty V_\infty^2 S} \int \int (\mathbf{V} \cdot \mathbf{n})^2 (\mathbf{n} \cdot \mathbf{i}) da \quad (9.15)$$

$$C_N = \frac{2}{\rho_\infty V_\infty^2 S} \int \int (\mathbf{V} \cdot \mathbf{n})^2 (\mathbf{n} \cdot \mathbf{j}) da \quad (9.16)$$

It is important to note that for regions not exposed to the flow (shadow regions), Newtonian Theory predicts the pressure and force to be zero.

As shown in Figure 9.1, the vehicle re-entry configuration is composed of a 30° conical forebody and a blunted 45° conical afterbody. If the vehicle orientation is limited to deflection angles less than the afterbody cone angle, the entire forebody will lie in a shadow region of the flow approaching the afterbody. Since Newtonian theory predicts zero force in shadow regions, the forebody may be neglected in the analysis.

The force coefficients for the blunt configuration are calculated by examining the individual contributions of the cone frustrum and spherical portions.

Equation 9.15 and 9.16 are used to calculate the force coefficients for the cone as shown in Fig. 9.3.

$$C_{A.C} = 2 \sin^2 \theta + \sin^2 \gamma (1 - 3 \sin^2 \theta) \quad (9.17)$$

Similarly, the normal force coefficient for the cone is defined to be

$$C_{N.C} = 2 \cos^2 \theta \sin \gamma \cos \alpha \quad (9.18)$$

Blunting is achieved by adding a spherical nose with a chord length equal to the diameter at the truncation point of the cone frustrum. If the entire segment is to remain exposed to the flow, an upper limit to l/r ratio is established by the tangents formed by the sides of the cone at the point of truncation. Thus, the case of maximum nose roundness is given by the addition of a tangent segment at the point of truncation. Specifying the truncation point, or the segment chord length, and the l/r ratio establishes the arc angle as defined by

$$\sigma = \sin^{-1} \frac{r_n}{r} \quad (9.19)$$

Applying Eqns. 9.15 and 9.16 to the model of the spherical segment shown in Fig. 9.4, yields expressions for the axial and normal force coefficients.

$$C_{A.S} = -\cos^2 \alpha (\cos^4 \sigma - 1) + \frac{1}{2} \sin^2 \alpha \sin^4 \sigma \quad (9.20)$$

$$C_{N.S} = \sin \alpha \cos \alpha \sin^4 \sigma \quad (9.21)$$

The lift and drag coefficients may be calculated from the axial and normal force coefficients

$$C_D = C_A \cos \alpha + C_N \sin \alpha \quad (9.22)$$

$$C_L = C_N \cos \alpha - C_A \sin \alpha \quad (9.23)$$

Applying these relations, the lift and drag coefficients for the cone and the spherical segment are given as

$$C_{D.C} = [2 \sin^2 \theta + \sin^2 \alpha (1 - 3 \sin^2 \theta)] \cos \alpha + [2 \cos^2 \theta \sin \alpha \cos \alpha] \sin \alpha \quad (9.24)$$

$$C_{L.C} = [2 \sin^2 \theta + \sin^2 \alpha (1 - 3 \sin^2 \theta)] \sin \alpha - [2 \cos^2 \theta \sin \alpha \cos \alpha] \cos \alpha \quad (9.25)$$

$$C_{D.S} = \left[-\cos^2 \alpha (\cos^4 \sigma - 1) + \frac{1}{2} \sin^2 \alpha \sin^4 \sigma \right] \cos \alpha + [\sin \alpha \cos \alpha \sin^4 \sigma] \sin \alpha \quad (9.26)$$

$$C_{L.S} = \left[-\cos^2 \alpha (\cos^4 \sigma - 1) + \frac{1}{2} \sin^2 \alpha \sin^4 \sigma \right] \sin \alpha - [\sin \alpha \cos \alpha \sin^4 \sigma] \cos \alpha \quad (9.27)$$

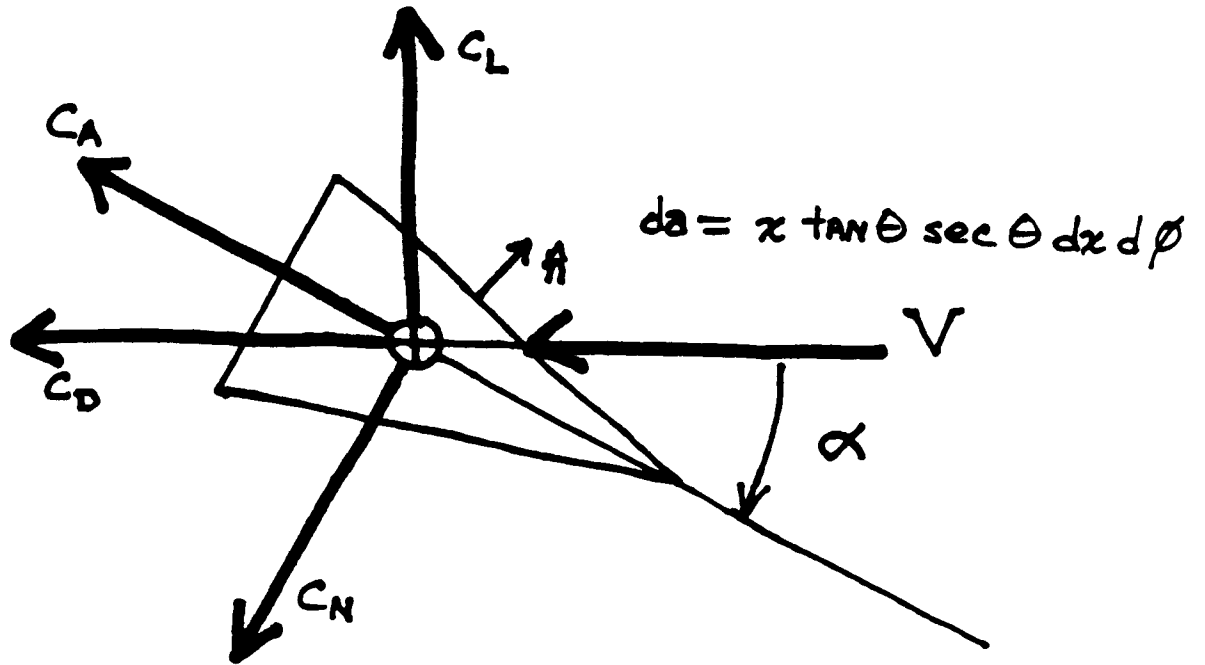


Figure 9.3: Model for Calculation of Force Coefficients on a Cone

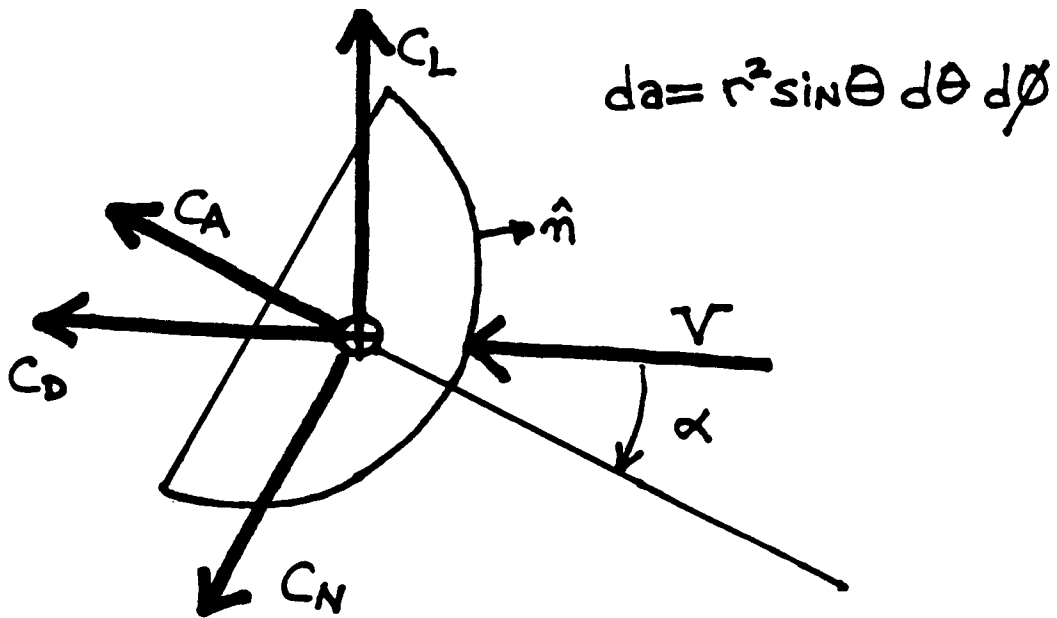


Figure 9.4: Model for Calculation of Force Coefficients on a Spherical Surface

The complete configuration may be evaluated as the sum of the individual components referenced to the same base area.

$$C_D = C_{D.C} \left[1 - \left(\frac{r_n}{r_B} \right)^2 \right] + C_{D.S} \left(\frac{r_n}{r_B} \right)^2 \quad (9.28)$$

$$C_L = C_{L.C} \left[1 - \left(\frac{r_n}{r_B} \right)^2 \right] + C_{L.S} \left(\frac{r_n}{r_B} \right)^2 \quad (9.29)$$

Cones of 45° and 50° were tested at four truncation locations for the cases of a tangent spherical nose and an l/r ratio of 0.1. Raising the truncation point allows the effect of increasing bluntness to be studied. While individually, both the lift and drag coefficients decrease, the lift-to-drag ratio is seen to increase.

results are presented in Fig. 9.5 for a 45° cone and Fig. 9.7 for a 50° cone.

A comparison of the spherical segment shape reveals that as the l/r ratio decreases, making the shape less round, both lift and drag coefficients decrease; this results in a decrease in the L/D ratio.

Finally, by comparing results of Figs. 9.5–9.8, increasing the cone angle can be seen to increase the values of both aerodynamic coefficients.

A comparison of the effectiveness of different vehicle configurations can be made by using the aerodynamic information to run the trajectory simulation. At this time, complete results for all the configurations discussed have yet to be obtained. While a redesign of the re-entry configuration cannot be recommended yet, it is expected that the resulting configuration will show an increase in bluntness due to the favorable increase in L/D ratios yielded by such a move.

References

- [1] Bryson, A., et. al., "Determination of the Lift or Drag Program that minimizes Re-entry Heating with Acceleration or Range Constraints Using a Steepest Descent Computation Procedure," IAS Paper No. 61-6, Jan, 1961.
- [2] Loh, W. H. T., *Re-entry and Planetary Entry Physics and Technology*, Springer Verlag, NY, 1968.
- [3] Regan, Frank, J., *Re-entry Vehicle Dynamics*, AIAA, NY 1984.
- [4] Truitt, R. W., *Hypersonic Aerodynamics*, The Ronald Press Company, New York, 1959.
- [5] Allens, H. J., and Eggars, A. J., "A Study of the Motion and Aerodynamic Heating of Missiles Entering the Earth's Atmosphere at High Supersonic Speeds," NASA TN 4047, 1957.

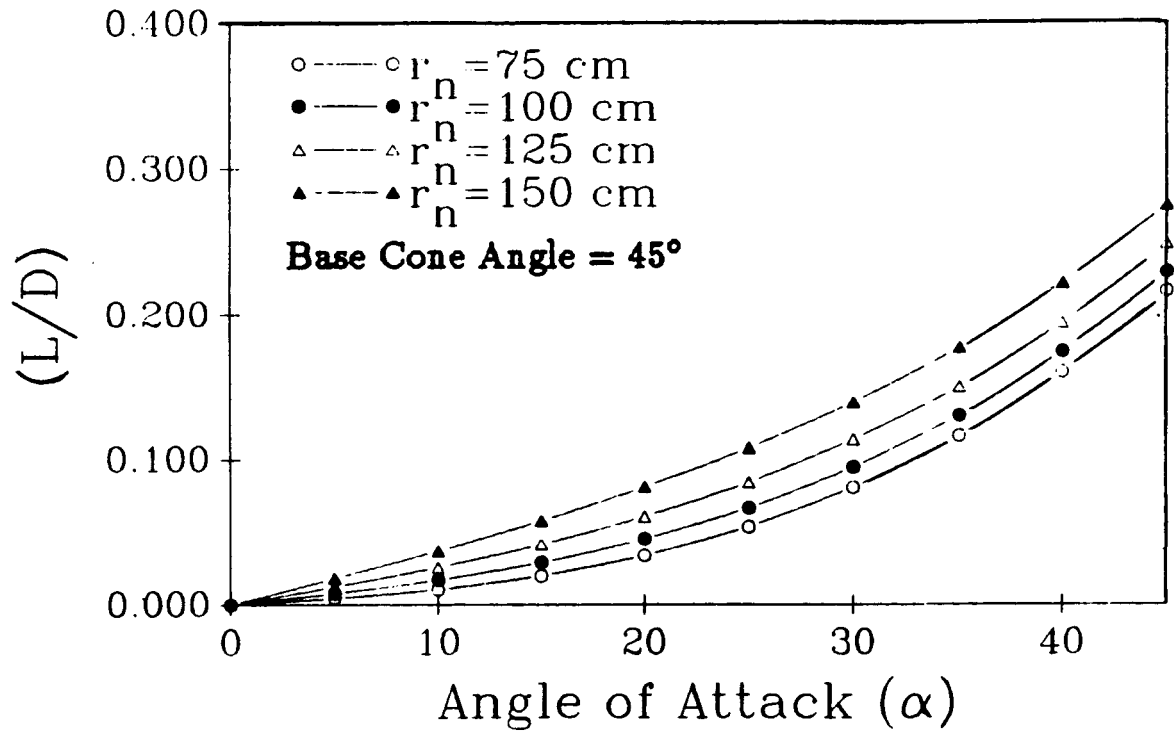


Figure 9.5: Effect of Bluntness on L/D ratio for 45° Blunted Cone

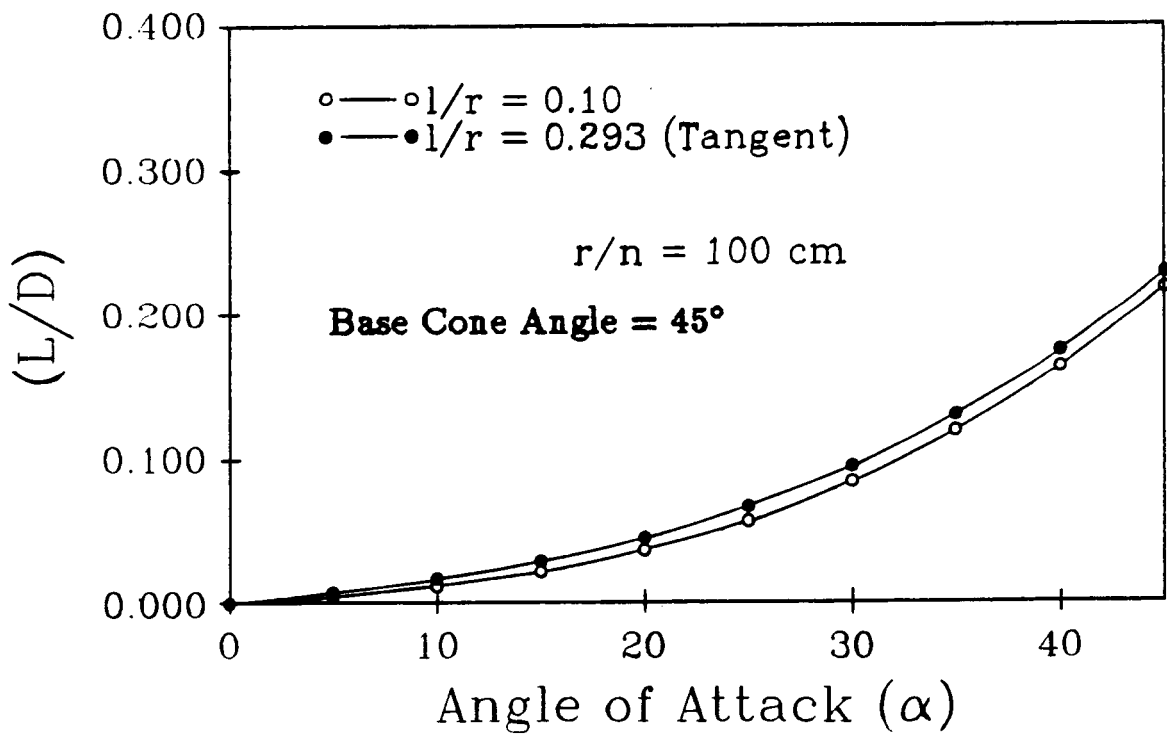


Figure 9.6: Effect of Segment Shape on L/D ratio for 45° Blunted Cone

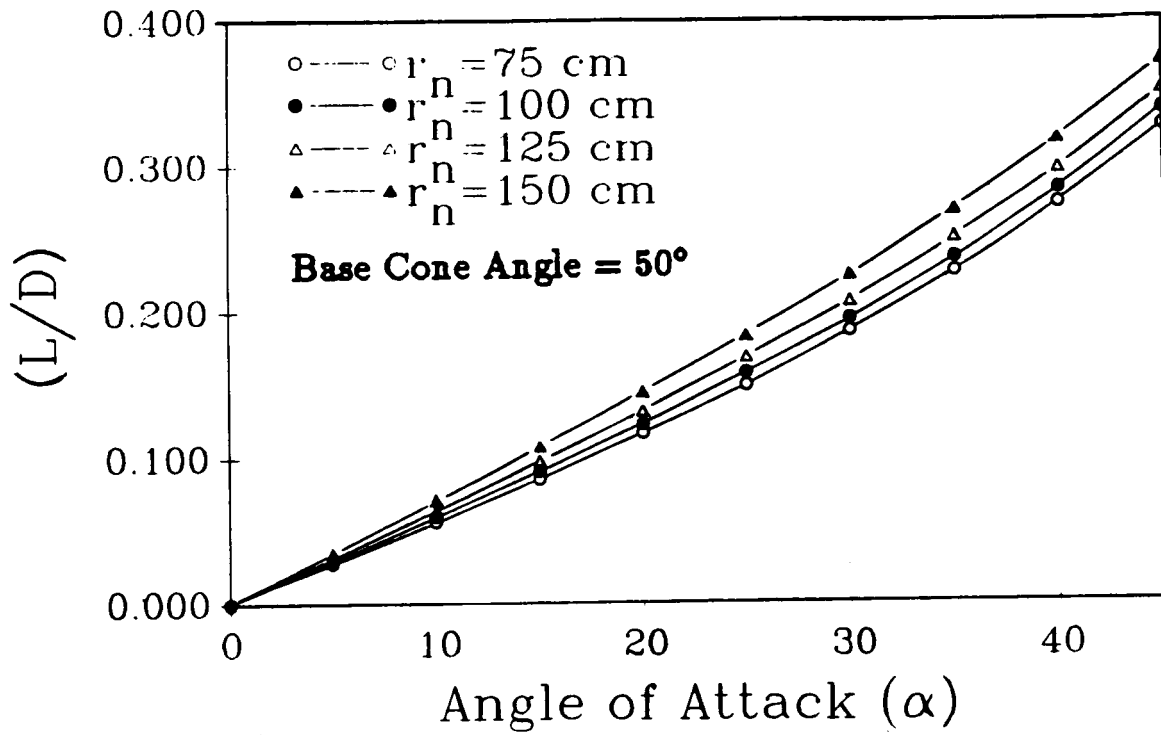


Figure 9.7: Effect of Bluntness on L/D ratio for 50° Blunted Cone

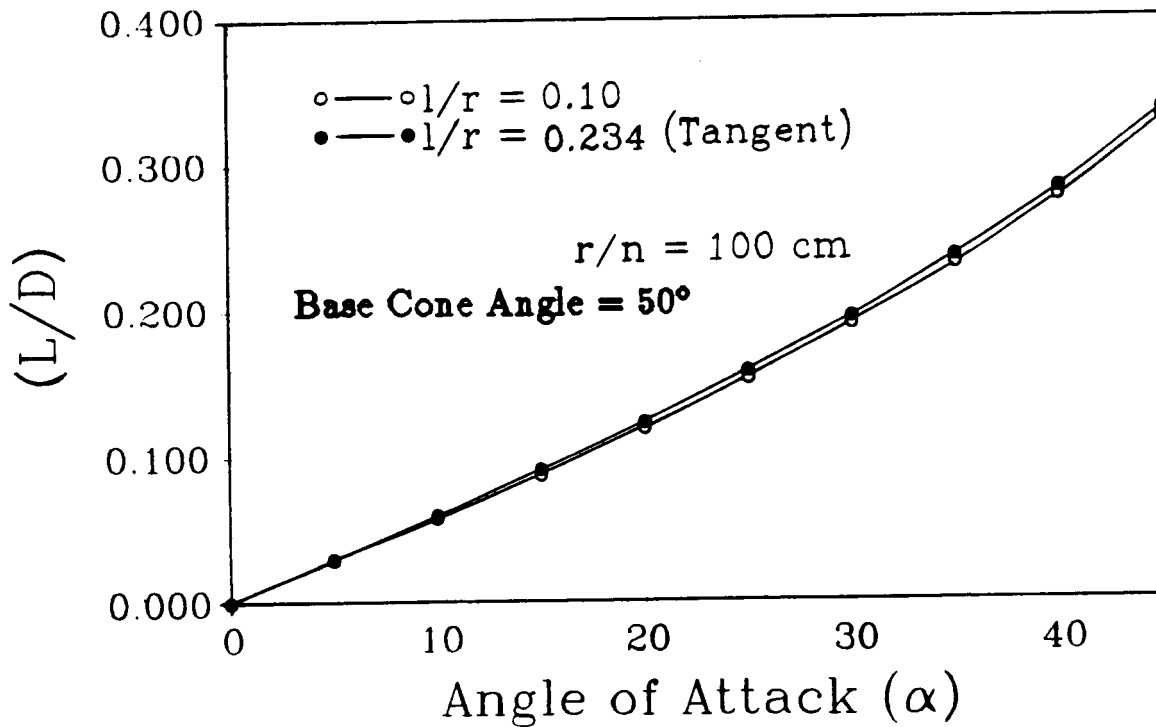


Figure 9.8: Effect of Segment Shape on L/D ratio for 50° Blunted Cone

Chapter 10

Annular Shroud Structural Dynamics

10.1 Introduction

10.1.1 Problem Statement

Analysis was conducted to determine the natural frequencies of the Apollo Lightcraft's annular shroud. This element of the vehicle's design was focused upon because of the unique and critical structural problems which it poses. Not only is the shroud an integral component in the operation of the laser energized engine, but it also imposes the most demanding material and structural specifications.

The shroud presented analytical and design problems which have had no precedent in aerospace engineering to date¹, so an innovative computational procedure had to be devised to arrive at the preliminary structural dynamic data presented herein.

10.1.2 Overview of the Analytical Procedure

This analytical work began with the assumption that the shroud can be modeled as a series of rigid beam elements connecting the twelve supporting struts. This assumption reduces a complex mathematical exercise (or a finite element model of questionable accuracy) to a problem in elementary beam theory. In this model, however, only the local vibration modes of each bay could have been produced. To observe the effects of global modes, a revised beam theory analysis was conducted under the same model of rigid, straight beams between the struts.

¹The closest problem in aerospace engineering is that of the hypersonic inlet, such as on the SR-71 Blackbird. Vibration theory for an annular ring was first developed by Euler for the analysis of bells.

The revised analysis utilized modified boundary conditions, consistent with the series of possible global mode shapes. This set of global modal frequencies was also compared to an "exact" analytical prediction derived under an entirely different set of assumptions.

10.1.3 Interpretation of Results

For insight into the effect that the existence of these frequencies would have on the design and performance of the Apollo Lightcraft, pulse repetition frequency (PRF) data was compiled for both the external radiation heated (ERH) thruster and the scramjet engine modes. This data gives the required pulse frequency of the laser propulsion system and hence, the frequencies of the dominant forcing function imposing a load on the shroud. Aeroelastic and thermal loading were not considered because it is believed that these represent higher-order effects to be included in a more detailed analysis at some later date. Figure 10.1 shows a flow chart representation of the analytical procedure used to determine this information as well as possible routes to be taken in the future.

10.2 Local Vibration Modes

The analytical procedure followed to determine the local vibration modes is outlined in detail in Appendix A. Several points can be made as to the relative accuracy of these computations. First, it should be noted that using a more realistic, unsymmetrical cross-section with a set of principle axes located acutely off-center required a large amount of computational time and mathematical effort. This complicated cross-section, however, gave frequency values that were very close, as shown in Figure A.1.5, to those predicted from the use of a simple rectangular shape. Examination of Equations A.37 and A.38 can give an explanation for why this is so. The section properties (E and I) lie inside of the square root; therefore, they influence the frequency to a lower order than parameters such as k and L . Since the effort has already been expended in generating section properties for the circular arc cross-sections; however, they will be used exclusively for the remainder of this work.

Having noted these facts, one can assume for future analyses that improvement of this accuracy will not necessarily lie in computing better section properties, but in such things as taking the curvature of the beam into account, or more complex boundary conditions. In an advanced analysis, it may be safe to assume a rectangular cross-section and devote most of the computational work towards taking the aforementioned affects into account.

Another point that should be raised is that no attention was paid to torsional vibrations, mainly due to the computational complexity which it would entail. Intuitively, short (aspect ratio 5.33) beams that are fixed at either end should be very stiff. It was generally assumed that torsional natural frequencies would

be high enough so as not to come into play in the range of frequencies that were considered here. This is one area in which future analytical work is needed, however.

The internal structure of the shroud was not considered at all, mainly due to the lack of any substantial data on the subject. Again, because this is a section property, and because the shroud is so thin, the assumption of a solid cross-section was adequate for this analysis. Along the same lines, the averaged modulus of the carbon-epoxy may not be very accurate, since anisotropic properties of composite laminates would probably be present in any design of the shroud, since such properties could prove to have desirable effects.

10.3 Global Modes of Vibration

The analytical procedure for the determination of the global vibration modes is detailed in Appendix A. Essentially, the same statements on the accuracy and assumptions made for the local modal analysis can be applied to the preceding work on global modes. One important point should be mentioned here, however; the use of Love's equations for a circular ring of circular cross-section predicted the frequencies within 10% of what was found from the beam theory analysis. This should be taken as an indication that this theory is valid. A deviation this small is impressive when one considers that the two analytical procedures were based upon widely different assumptions, either of which could be considered questionable. The exact theory required that the shroud be represented as a continuous annulus having a circular cross-section (mathematically, of different radii in the x - and y -bending directions) while beam theory required that this ring be broken into straight segments with a more accurate cross-section.

10.4 Interpretation of Results

10.4.1 Loading Sources

Once the natural frequencies of the shroud are found, the next step in the design process is to find the frequencies of loading that the structure will be subjected to. A large number of forces act upon a vehicle during a transatmospheric trajectory; a comprehensive summary of them and their interaction is shown in Figure 10.2[6]. For this work only the most dominant force, that of the propulsion system, will be considered. Data giving the PRF for maximum engine efficiency were obtained from last year's report.

ERH Thruster Vibrations

The data for the PRF needed to be maintained for maximum efficiency in the ERH Thruster mode is plotted as a function of altitude in Figure 10.3, and as

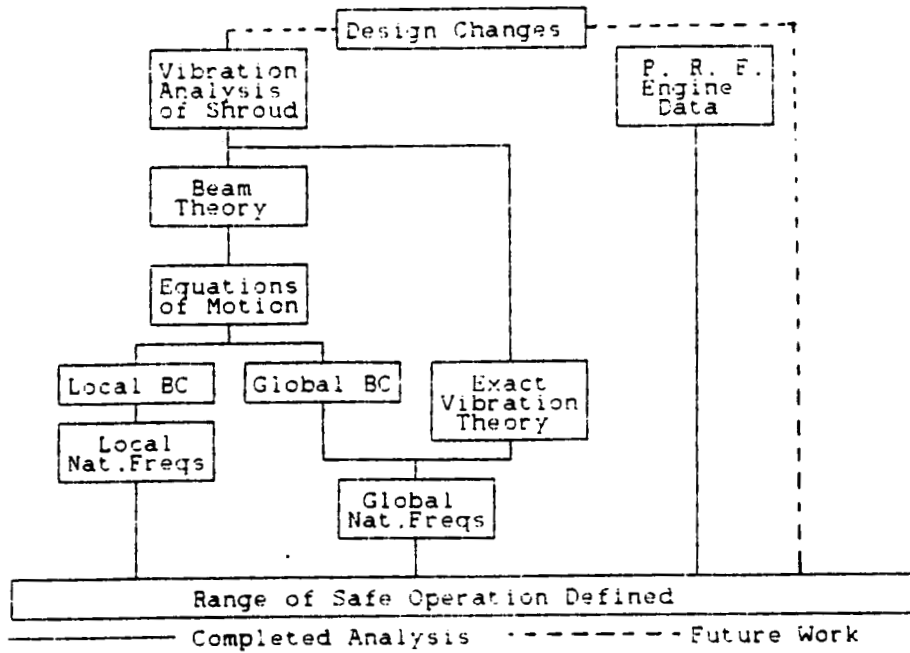


Figure 10.1: Flow Chart of Analytical Procedure

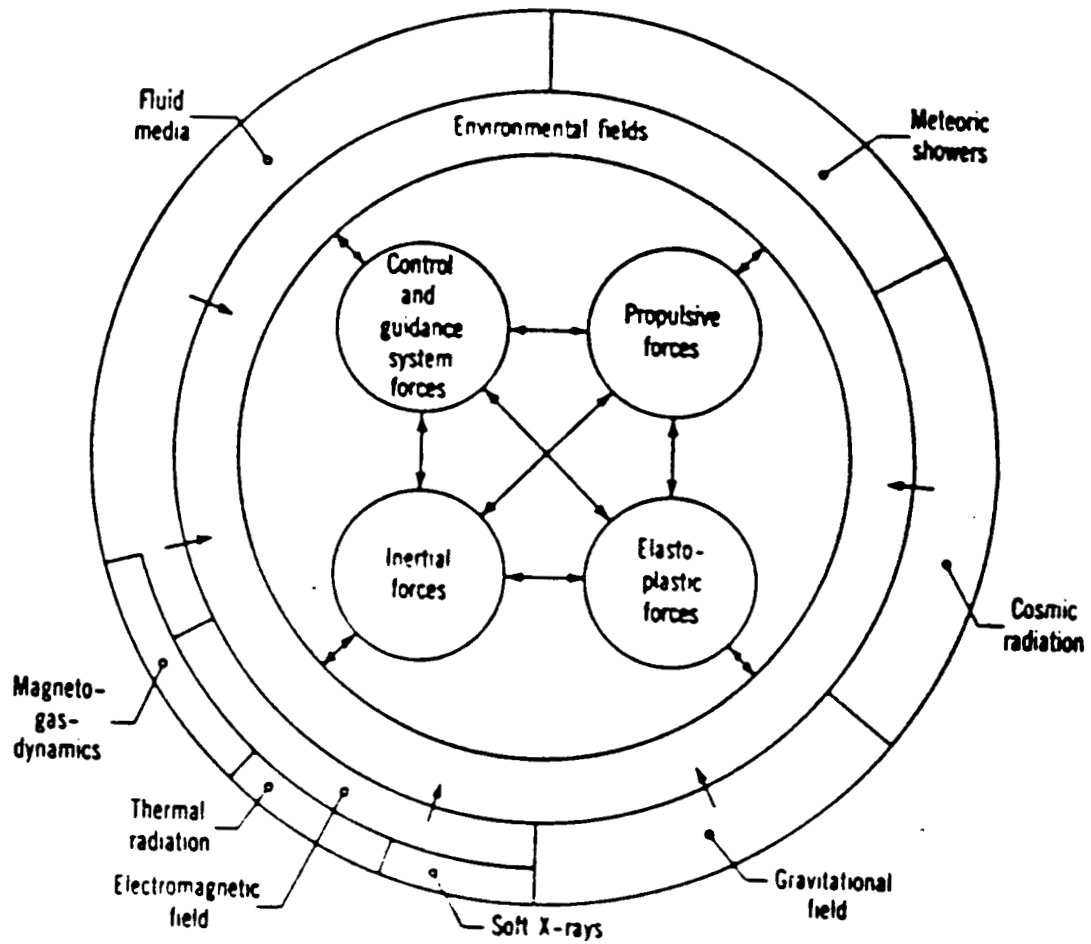


Figure 10.2: Interaction of Environmental Forces on a Transatmospheric Vehicle

a function of Mach number in Figure 10.4. Natural frequencies are drawn on these graphs to indicate areas that should be avoided in the operation of the engine.

Scramjet Mode Vibrations

The PRF data obtained for the scramjet mode is plotted as a function of altitude in Figure 10.5 and as a function of Mach number in Figure 10.6. The natural frequencies determined in this work are also indicated.

10.4.2 Design Options to Avoid Interference with Shroud

Examination of Figures 10.3, 10.4, 10.5, and 10.6 shows that many modes of engine operation do create pulse repetition frequencies that coincide with the natural frequencies of the annular shroud. It is not clear as to how it might be possible to operate the engine so as to avoid these PRFs without sacrificing performance. Another problem that can be noted is that a large quantity of these vibrations occur within the audible spectrum. This is not desirable for a source of oscillation as powerful as these engine modes.

A few possible remedies to these problems are suggested. First, it may be possible to construct the interior of the shroud so as to change its section properties or give it better damping properties. It might be possible to make use of the anisotropic properties of composite laminates in this manner. Another idea that seems novel now, but will probably become the norm before the time-frame scheduled for construction of the Apollo Lightcraft, is the utilization of active controls. To control aircraft flutter, many ideas have been proposed in recent years that rely on extremely fast and accurate digital computers to apply small signals to an aircraft's control surfaces to damp out unwanted oscillations. The X-29 research aircraft is the most visible application of this technology. It may be possible to apply similar control algorithms to control surfaces around the Apollo Lightcraft shroud that serve to dampen vibrations generated by the engine's pulse frequencies.

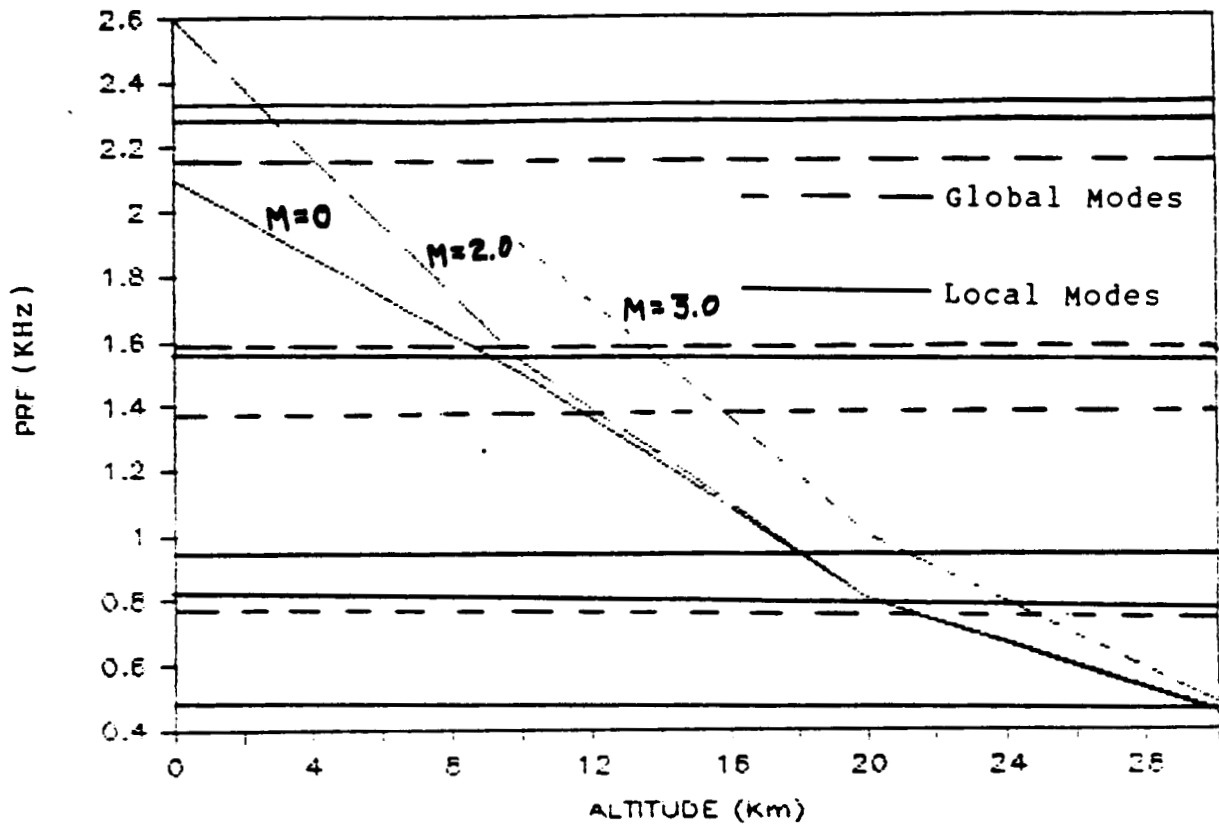


Figure 10.3: ERH Thruster PRF vs. Altitude

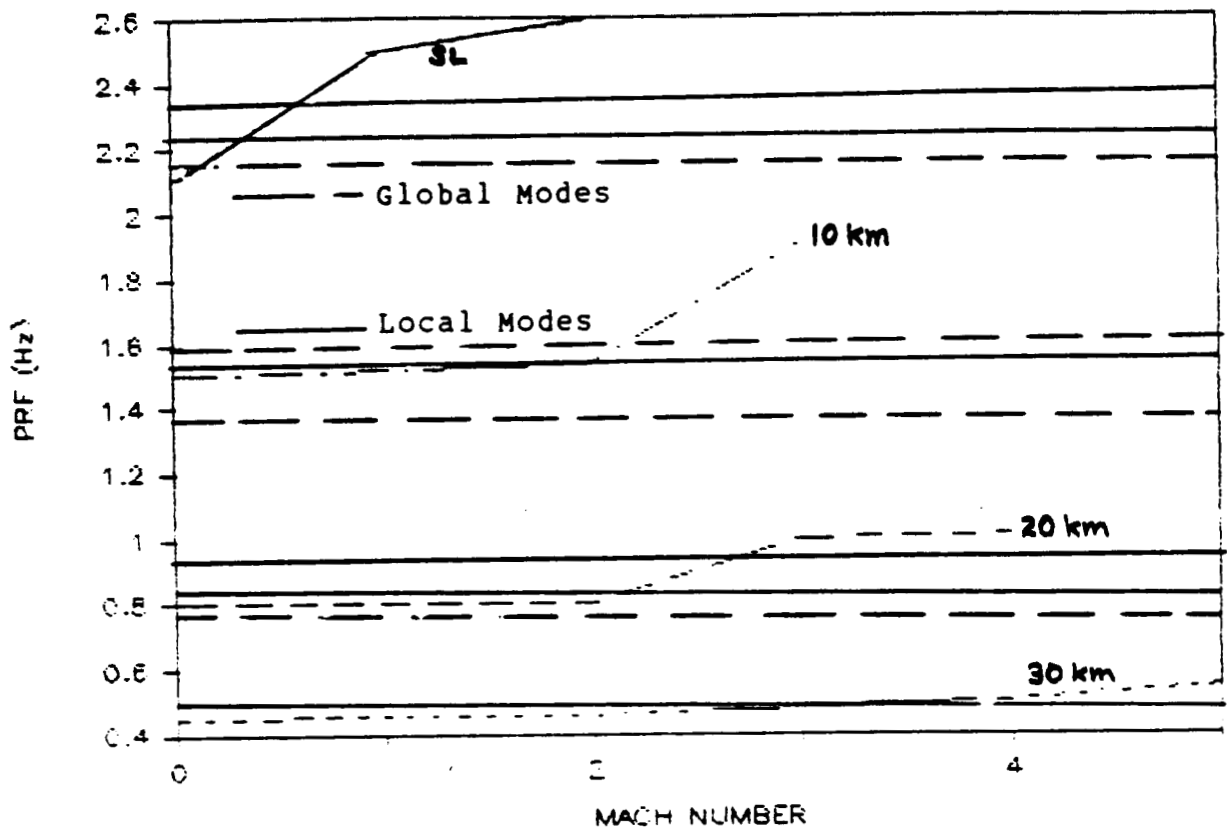


Figure 10.4: ERH Thruster PRF vs. Mach Number

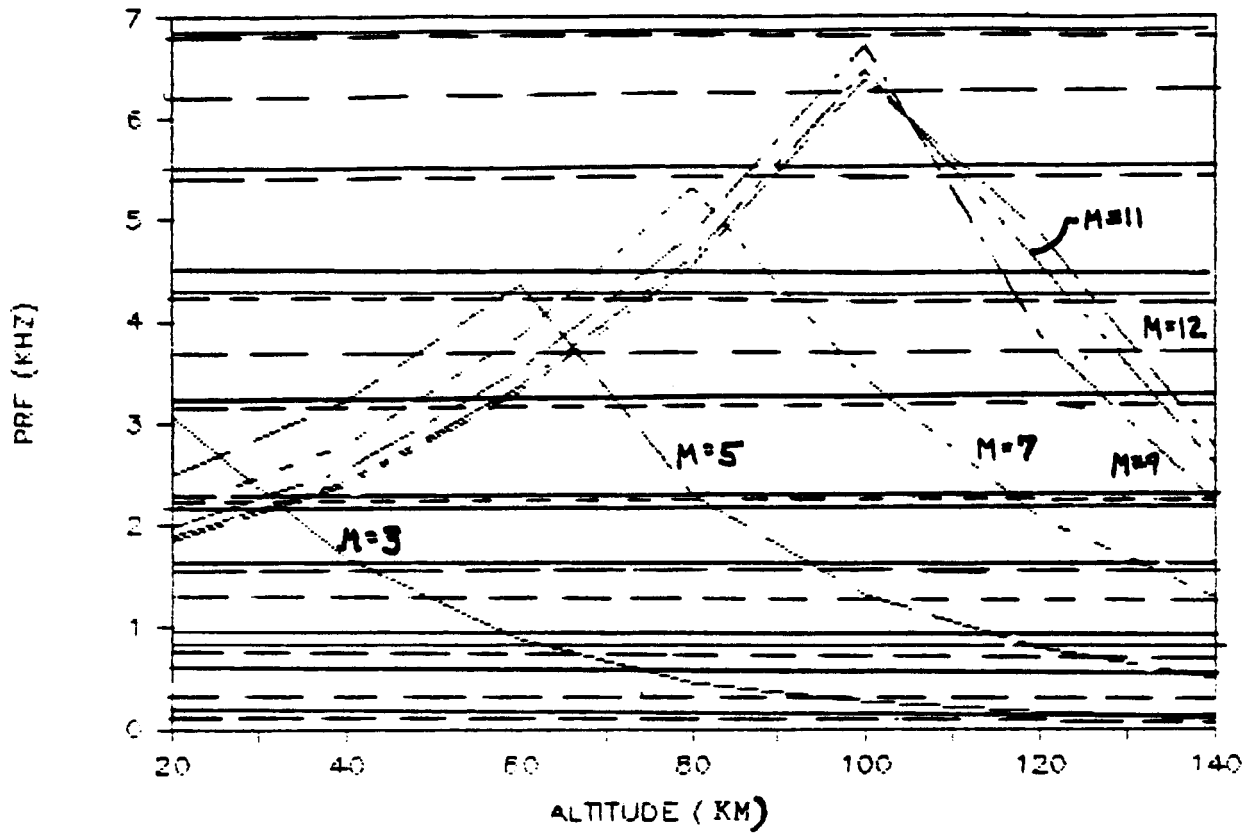


Figure 10.5: Scramjet PRF vs. Altitude

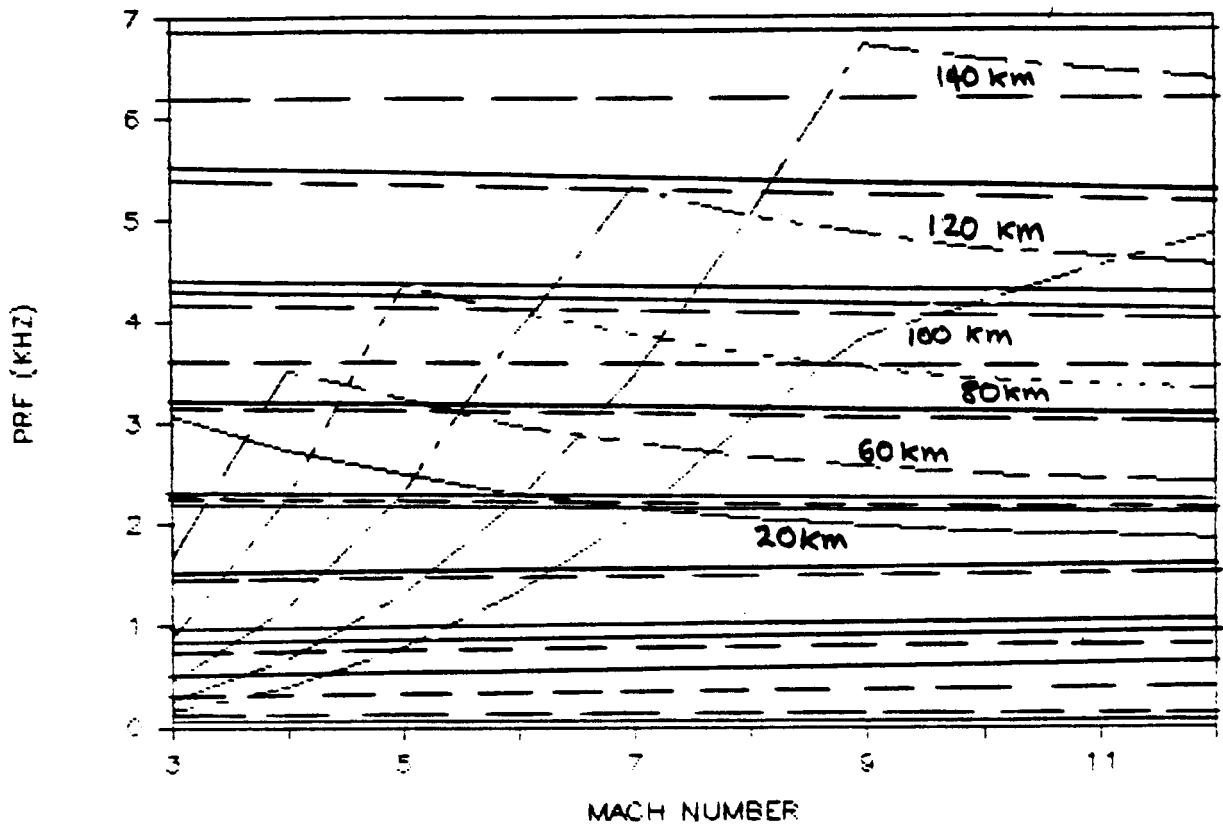


Figure 10.6: Scramjet PRF vs. Mach Number

References

- [1] T. Hehl, *Composite Shell Vibration—A Case Study*, Unpublished Work.
- [2] O. A. Bauchau, lecture notes from *Theory of Structures*, Spring 1987.
- [3] F. P. Beer and E. R. Johnston, *Mechanics of Materials*, McGraw-Hill Book Company, 1981.
- [4] S. W. Tsai and H. T. Hahn, *Introduction to Composite Materials*, Technomic Publishing, 1980.
- [5] A. E. H. Love, *A Treatise on the Mathematical Theory of Elasticity*, Dover Publications, 1944, pp 452-3.
- [6] Ashley and Bisplinghoff, *Principles of Aeroelasticity*, Dover Publications, 1969.

Chapter 11

Future Directions

As mentioned in the Executive Summary, next year's effort will focus on theoretical and experimental investigations into the Lightcraft Technology Demonstrator (LTD). The LTD's propulsion system is a much simplified version of the Apollo Lightcraft's combined-cycle engine, and has just three modes of operation:

1. Shroud Lift ERH Thruster Mode ($0.3 < M_\infty < 5.5$)
2. Scramjet ($5.5 < M_\infty < 11$)
3. Rocket ($11 < M_\infty < 25^+$)

The LTD will be launched from a 3 km mountain peak with a steam cannon — at a velocity of 100 m/s (i.e., Mach 0.3). This eliminates the need for the RDWE, a variety of ERH thruster which can produce thrust at *zero* forward velocity. Beyond Mach 11, the LTD leaves the atmosphere as a laser-heated rocket, using LN_2 as propellant. About 180 kg of propellant will be required to place the LTD vehicle into low Earth orbit. Of this, 5–10% is expended to cool the primary optics during the shroud-lift ERH thruster and scramjet modes; this coolant is dumped overboard immediately after use. About 80% of the propellant is consumed in the rocket mode. The remaining 10–15% evaporates into the gaseous state, pressurizes the tank, and is later used for attitude control of the satellite, once in orbit.

This change in focus is necessary to continue climbing the steep learning curve in laser propulsion technology. Emphasis must now shift to critical proof-of-concept experiments, and detailed engineering design/analysis of the most rudimentary propulsion components.

Theoretical investigations into the LTD machine will be focused on the following. Detailed structural analysis and design of the spacecraft will be performed using finite element computer codes. The dynamic response of the

shroud to pulsed thruster operation will be studied. Candidate structural materials include ceramic carbon and kevlar composites, aircraft quality aluminum, titanium and stainless steel. The primary optic is likely to be made of aluminum, regeneratively cooled with LN₂. The LN₂ tank will be constructed of filament wound kevlar and carbon fiber, with an inner aluminum vapor barrier. The shroud will be constructed of high temperature carbon or ceramic composite material. The entire conical inlet forebody will be covered with the blacktile thermal protection system used on the STS orbiter. The LN₂ tank will also serve as the principal frame for the entire spacecraft. All interconnecting structure will be lightweight carbon fiber. The annular shroud leading edges, radial support struts and inner ERH thruster surface will be actively cooled with LN₂. Propellant/coolant delivery will be accomplished by pressurizing the storage tank. Methods for fabricating all vehicle components will be identified. Sources of existing components (e.g., the spherical propellant tanks) will be located.

External aerodynamics of the vehicle will be studied using three-dimensional (3-D) computational fluid dynamics (CFD) codes such as PHOENICS. ERH thruster and pulsed rocket physics will be explored with the aid of 2-D CFD blast wave codes, to be obtained from NRL. The existing 1-D scramjet code will be improved to include high temperature real gas effects, using a code supplied by NASA Lewis Research Center. The effects of repetitively pulsed LSD-wave heating in the scramjet mode will also be studied.

Experimental investigations of the LTD spacecraft will explore both vehicle aerodynamics and combined-cycle engine propulsion performance. Existing RPI transonic, supersonic, and hypersonic test facilities will be employed with small scale models.

The RPI hypersonic shock tunnel is currently in operation under the supervision of Professor H. T. Nagamatsu. A five inch diameter model of the LTD vehicle will be mounted at the end of a support sting and tested throughout a wide flight speed range from Mach 4 to 12. The shock tunnel will exactly mimic the real flight conditions of air velocity, temperature and pressure. Pressure taps and heat transfer gauges will be distributed over the LTD model surface to provide important information on the flow around the vehicle during transatmospheric flight. Strain gauges located within the sting will output data concerning drag and lift produced during non-zero pitch angles. Schlieren pictures will enable flow visualization, and aid in the design of the inlet forebody. The conical bow shock must be prevented from being swallowed into the annular inlet beyond Mach 12.

The RPI shock-tunnel could also be used to measure data concerning the LTD scramjet mode performance. The tunnel test section is large enough to mount a 22 cm wide section of the full-scale annular scramjet engine. This 2-D model is about 1/15th of the shroud circumference, subtending an angle of 24 degrees. Propulsive laser power can be delivered into the test section through a high power laser window; alternatively, an electric discharge could be used to simulate pulsed laser energy deposition. Pulse energies in the range of 500 J to

2 kJ will be needed, with pulse durations of 0.1 to 1.0 μ sec.

The existing RPI transonic blow-down tunnel can easily be employed to gather ERH thruster performance data using the same 2-D, 22 cm engine segment, and the laser or electric power sources. The Lumonics #622 CO₂ laser modules generate 500 J at 1 μ sec and would be ideal for these experiments. Efforts will be made to locate one to four of these units, and to inquire as to their availability on a loan basis from NASA or DOD or DOE sources. The Lumonics #622 laser has a square output aperture measuring roughly 20 cm \times 20 cm, and exactly matches the requirement of this 2-D engine segment. Also, it should be noted that air enters the shroud at roughly Mach 1 throughout most of the ERH thruster operational range.

Finally, again using a 1/15th scale segment of the annular combined-cycle engine, performance data on the pulsed laser-heated N₂ rocket mode can be gathered. The transonic blow-down tunnel exhausts into an evacuated dump tank, so simulated back pressures typical of 150 kft to 350 kft could easily be simulated. Nitrogen propellant can be delivered to the rocket engine injector plate (a porous metal surface) by a tank of pressurized N₂. As with the ERH thruster experiment, laser power can be focused into the engine by reflecting the laser beam off the rear primary optical surface, which also compromises the vehicle afterbody. Alternatively, a pulsed electric discharge can be used to simulate power injection.

Appendix A

Details of the Structural Dynamics Analysis

A.1 Beam Theory Analysis: Local Modes

A.1.1 Basic Equations of Linear Beam Theory

The first idea of applying elementary beam theory to the Apollo Lightcraft shroud vibration problem was presented by T. Hehl[1]. In that work, the essential concepts used here were proposed; however, several assumptions and solution techniques used by Hehl were not found to be valid in the present analysis.

Basic differential equations of beam vibration are derived from the equating the elastic force of the beam deflection with the inertial (D'Alembert) force of motion. For a straight beam aligned as in Figure A.1, these equations are written in general form for translational motion in the x and y directions as[2]:

$$\frac{d^2}{dz^2} \left(I_{xx} \frac{d^2 u}{dz^2} \right) + \frac{d^2}{dz^2} \left(I_{xy} \frac{d^2 v}{dz^2} \right) = \frac{m}{E} \frac{d^2 u}{dt^2} \quad (\text{A.1})$$

$$\frac{d^2}{dz^2} \left(I_{xy} \frac{d^2 u}{dz^2} \right) + \frac{d^2}{dz^2} \left(I_{yy} \frac{d^2 v}{dz^2} \right) = \frac{m}{E} \frac{d^2 v}{dt^2} \quad (\text{A.2})$$

A.1.2 Beam Element Cross Sections

The first step taken toward simplifying these equations for the purposes which that are intended to be used in this work was to use beam sections having a constant cross sectional shape and which are, for now, assumed to be solid. Immediately, this will make the terms I_{xx} , I_{yy} , and I_{xy} constants and allow them to be moved outside the derivatives.

The two solid beam cross sections which were considered are shown in Figures A.2 and A.3. Figure A.2 shows a simple rectangular cross section similar to that used in the previous work. The dimensions chosen for this rectangular shape were taken as the maximum width of the proposed shroud and the height from the variable area exhaust nozzle to the top of the shroud. The contribution of the variable area exhaust nozzle cross section is not included in computation of the flexural rigidities of the beam because it is assumed that this component would not contribute any structural strength or stiffness to the shroud. Cross sectional area representing the nozzle is included in computing the mass distribution along the shroud, however. The actual dimensions of the shroud were obtained from last year's report.

A more accurate cross section is also used, which resembles the real shroud with about the highest degree of accuracy obtainable based upon the preliminary design data. This cross section (shown in Figure A.3) models the shroud as the cusp formed by two circles, the innermost having a radius equal to the focal length of the secondary optics and located so as to place the focal point upon the LSD wave "ignitors" around the spacecraft. With the data provided in Figure A.3, the outer and inner surface shapes can be described by the following equations (all lengths in meters):

$$x_{outer} = 0.1403 + \sqrt{0.05779 - y^2} \quad (A.3)$$

$$x_{inner} = \sqrt{0.1116 - y^2}. \quad (A.4)$$

A.1.3 Location of Centroid and Principle Axes

To simplify Equations A.1 and A.2 it is necessary to use a system of axes which has its origin at the centroid of the cross-section in question and an orientation defined by principle axes of bending. By placing the origin at the centroid, the coupling between bending and twisting is eliminated, an implicit assumption in the statement of Equations A.1 and A.2. Use of the principle axes eliminates bending coupling between x and y directions, in effect making $I_{xy} = 0$. Re-orienting the coordinate system in this manner (and distinguishing it as the x' and y' directions) reduces Equations A.1 and A.2 to the following:

$$\frac{d^4 u}{dz^4} + \frac{EI_{xx}}{m} \frac{d^2 u}{dt^2} = 0 \quad (A.5)$$

$$\frac{d^4 v}{dz^4} + \frac{EI_{yy}}{m} \frac{d^2 v}{dt^2} = 0 \quad (A.6)$$

These fourth order differential equations are the equations of motion for uncoupled bending in the principle axes directions. Note that torsional motion of the beam is not considered since it is believed to have too high a frequency to be important.

Beam Theory Approx.

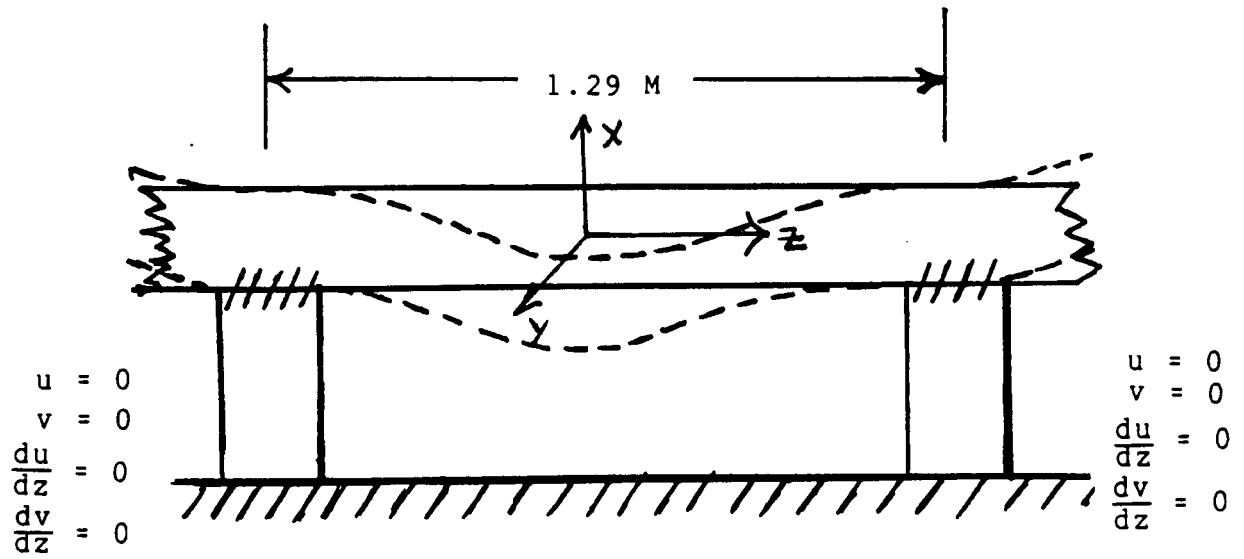


Figure A.1: Local Modes of Vibration of the Apollo Lightcraft Shroud

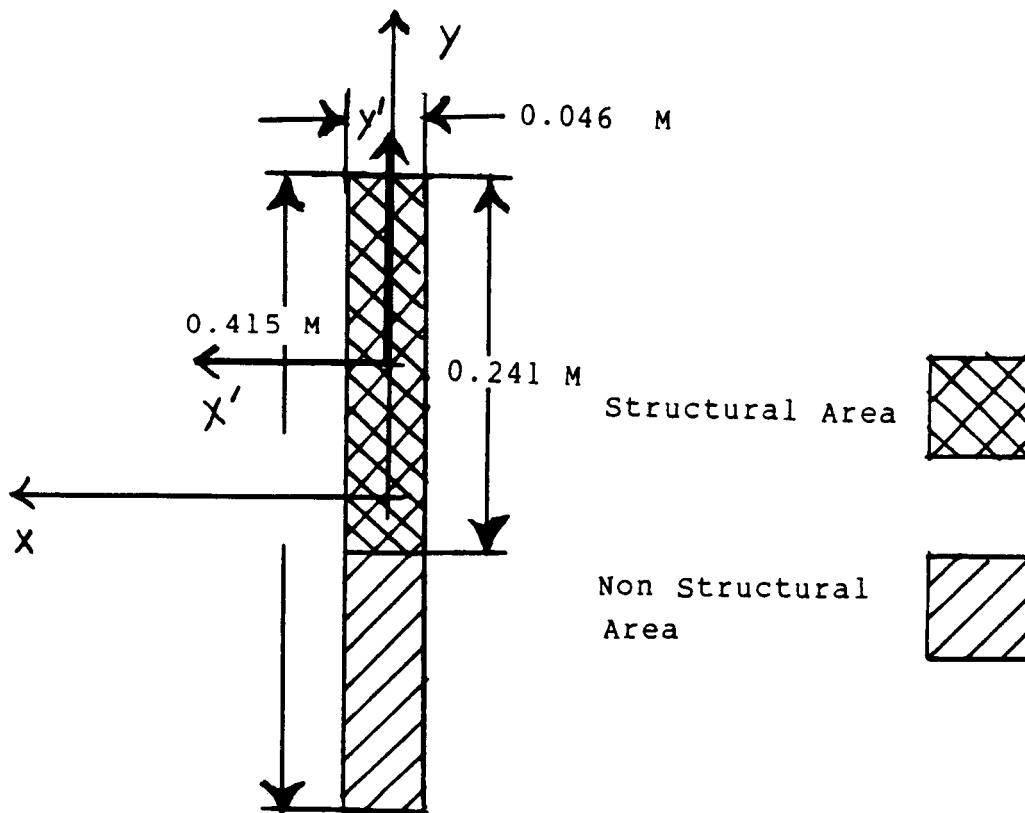


Figure A.2: Rectangular Cross Section

Rectangular Cross Section

Utilizing Equations A.5 and A.6 first requires that the x' - y' coordinate system be defined. For the rectangular cross section, symmetry will define the (x_o, y_o) coordinates of the centroid as (0.0, 0.08755) meters and the principle axes will be aligned with those of the (x, y) coordinate system. Putting this in mathematical form gives the following transformation:

$$x' = x \text{ meters} \quad (\text{A.7})$$

$$y' = y - 0.08755 \text{ meters.} \quad (\text{A.8})$$

Circular Arc Cross Section

For the circular cross section, the centroid must be found from its defining equations[3]

$$x_o = \frac{\int_{A_s} x dA}{A_s} \quad (\text{A.9})$$

$$y_o = \frac{\int_{A_s} y dA}{A_s} \quad (\text{A.10})$$

The area of this cross section was determined by integration as in Equation A.11.

$$A_s = \int_{-0.0325}^{0.2076} [0.1403 + 0.05779 - y^2 - 0.1116 - y^2] dy \quad (\text{A.11})$$

Solving this yields $A_s = 0.00877 \text{ m}^2$. Substitution of Equations A.3 and A.4 into the centroid definitions (A.9 and A.10) gives the following:

$$x_o = \frac{1}{A_s} \int_{-0.0325}^{0.2076} \int_{0.1116-y^2}^{0.1403+\sqrt{0.05779-y^2}} x dx dy \quad (\text{A.12})$$

$$y_o = \frac{1}{A_s} \int_{-0.0325}^{0.2076} \int_{0.1116-y^2}^{0.1403+\sqrt{0.05779-y^2}} y dx dy \quad (\text{A.13})$$

These can both be integrated analytically to give (x_o, y_o) for the circular arc cross-section to be (0.34, 0.067) meters.

Defining the principle axes requires finding the orientation of a coordinate system placed at the centroid which will make $I_{xy} = 0$. This new coordinate system (x', y') would be rotated by an angle α with respect to the (x, y) system as shown in Figure 10.1. Rotation as such would produce the following set of transformation equations for (x', y') :

$$x' = (x - x_o) \cos \alpha - (y - y_o) \sin \alpha \quad (\text{A.14})$$

$$y' = (x - x_o) \sin \alpha - (y - y_o) \cos \alpha. \quad (\text{A.15})$$

To determine the required rotation angle, α , the above set of equations must be substituted into the definition of I_{xy} :

$$I_{xy} = \int_{A_o} x'y' dA \quad (\text{A.16})$$

Making this substitution, setting the resulting integral equal to zero, and factoring out similar terms involving trigonometric functions of α gives the following equation:

$$\begin{aligned} & \cos \alpha \sin \alpha \int_{-0.0325}^{0.2076} \int_{\sqrt{0.1116-y^2}}^{0.1403+\sqrt{0.05779-y^2}} [(x-x_o)^2 - (y-y_o)^2] dx dy + \\ & [\cos^2 \alpha - \sin^2 \alpha] \int_{-0.0325}^{0.2076} \int_{\sqrt{0.1116-y^2}}^{0.1403+\sqrt{0.05779-y^2}} (x-x_o)(y-y_o) dx dy \\ & = 0 \end{aligned} \quad (\text{A.17})$$

These two double integrals were evaluated numerically, reducing Equation A.17 to an implicit expression for α which was solved iteratively to get a rotation angle of $\alpha = -17.4^\circ$. Substituting these numerical results into Equations A.14 and A.15 results in a transformation from (x, y) coordinates to the principle axes (x', y') :

$$x' = -0.3444 + 0.9542x + 0.2990y \quad (\text{A.18})$$

$$y' = 0.0378 - 0.2990x + 0.9542y \quad (\text{A.19})$$

for the circular arc cross section. The locations of both sets (x, y) and (x', y') are shown on the cross sections in Figures A.2 and A.3.

A.1.4 Determination of Moments of Inertia

Rectangular Cross Section

For a rectangular cross section, like the one used in this analysis, the moments of inertia for bending in the x' and y' directions are [3]:

$$I_{xx} = \frac{1}{12} ht^3 \quad (\text{A.20})$$

$$I_{yy} = \frac{1}{12} h^3 t \quad (\text{A.21})$$

This yields $I_{xx} = 2.0 \times 10^{-6} \text{ m}^4$ and $I_{yy} = 53.5 \times 10^{-6} \text{ m}^4$.

Circular Arc Cross Section

For the circular arc cross-section, the moments of inertia must be found by directly integrating the definitions:

$$I_{xx} = \int_{A_o} x'^2 dA \quad (\text{A.22})$$

$$I_{yy} = \int_{A_0} y'^2 dA \quad (\text{A.23})$$

Substitution of the transformation Equations A.18 and A.19 into these integrals yields the following set of integrals:

$$I_{xx} = \int_{-0.0325}^{0.2076} \int_{0.1116-y^2}^{0.1403+\sqrt{0.05779-y^2}} [-0.3444 - 0.9542x + 0.2990y]^2 dx dy \quad (\text{A.24})$$

$$I_{yy} = \int_{-0.0325}^{0.2076} \int_{0.1116-y^2}^{0.1403+\sqrt{0.05779-y^2}} [0.0378 - 0.2990x + 0.9542y]^2 dx dy \quad (\text{A.25})$$

Numerical evaluation of these yields the following values for the moments of inertia: $I_{xx} = 1.62 \times 10^{-6} \text{ m}^4$ and $I_{yy} = 35.96 \times 10^{-6} \text{ m}^4$. These section properties are tabulated in Table A.1.4.

A.1.5 Solution of Beam Equations for Local Modes

Having obtained the section properties, Equations A.5 and A.6 can be used to determine the natural frequencies of each beam element between two of the supporting struts. The first assumption to be made for this calculation, beyond that allowing the applicability of basic straight beam theory to this problem, is that the beam elements representing sections of the shroud between adjacent supporting struts can be modeled as being fixed rigidly to the struts. This means that the beam sections are isolated from each other. With this assumption stated, the four boundary conditions needed to solve the dynamical equation of beam motion in the x -direction (Equation A.5) are: $u = 0$ and $\frac{du}{dz} = 0$ at $z = 0$; $u = 0$ and $\frac{du}{dz} = 0$ at $z = L$. In the y -direction a similar set of boundary conditions can be specified: $v = 0$ and $\frac{dv}{dz} = 0$ at $z = 0$; $v = 0$ and $\frac{dv}{dz} = 0$ at $z = L$ for use with Equation A.6. Figure A.1 shows the physical meaning of these statements in terms of the geometry of the shroud.

To make the mathematics less cumbersome, Equations A.5 and A.6 can be written in terms of the dimensionless parameters $\delta = \frac{z}{L}$ and $\tau = \sqrt{EI_{xx}/mL^4}t$. With the derivatives taken with respect to these variables, the set of equations reduces to:

$$\frac{d^4u}{d\delta^4} + \frac{d^2u}{d\tau^2} = 0 \quad (\text{A.26})$$

$$\frac{d^4v}{d\delta^4} + \frac{d^2v}{d\tau^2} = 0. \quad (\text{A.27})$$

Since we are only interested in the natural frequencies of harmonic motions that would satisfy the above set of equations, a periodic solution can be assumed of the form:

$$u = u'(\delta) e^{i\Omega\tau} \quad (\text{A.28})$$

$$v = v'(\delta) e^{i\Omega\tau} \quad (\text{A.29})$$

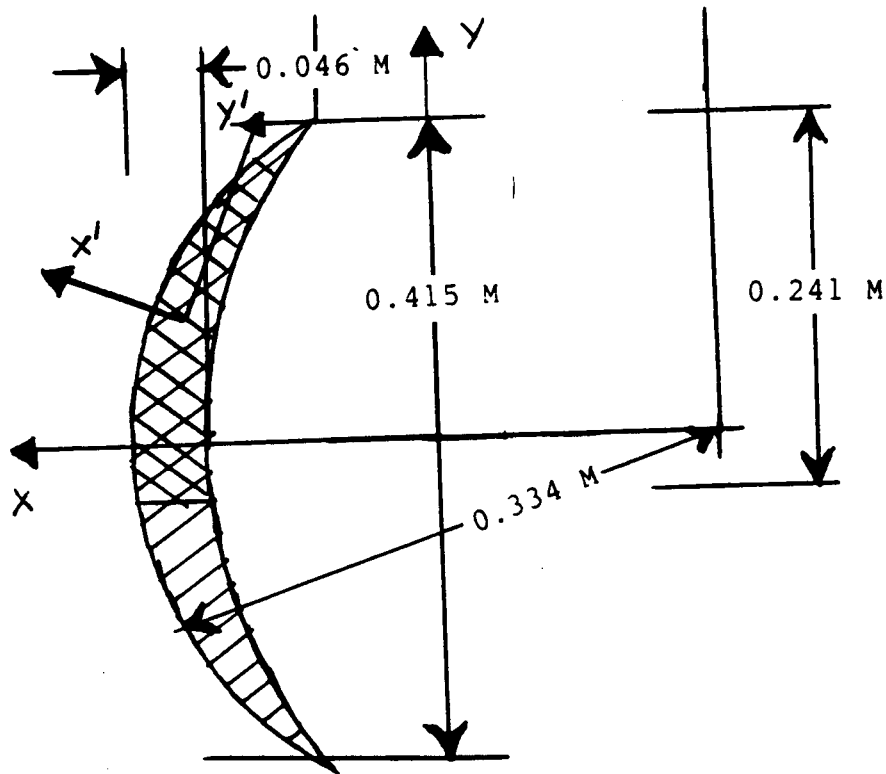


Figure A.3: Circular Arc Cross Section

	Rectangular Cross Sect.	Circular Arc Cross Sect.
Centroid x_0 (m) y_0 (m)	0.0 0.08755	0.34 0.067
Principle Axis Orient- ation(deg)	0.0	17.4
Moments of Inertia I_{xx} (m ⁴) I_{yy} (m ⁴)	2.0×10^{-6} 53.5×10^{-6}	1.62×10^{-6} 35.9×10^{-6}
Structural Section Area (m ²)	0.0114	0.0088
Total Geo. Section Area	0.0193	0.0145

Table A.1: Section Properties Listing

where Ω is a normalized natural frequency in radians/second. For the purposes of this analysis, the frequencies will be expressed in cycles/second (Hz) through the transformation

$$f_n = \frac{\Omega_n}{2\pi} \sqrt{\frac{EI_{xx}}{mL^4}} \quad (\text{A.30})$$

Substituting the separated forms of the solution above into the differential equations and making the change of variables: $k^4 = \Omega^2$, the following set of fourth-order, linear ordinary differential equations is obtained:

$$\frac{d^4 u'}{d\delta^4} - k^4 u' = 0 \quad (\text{A.31})$$

$$\frac{d^4 v'}{d\delta^4} - k^4 v' = 0. \quad (\text{A.32})$$

The solution to linear differential equations like those above is known to be exponential in nature. The characteristic polynomials of these equations would be of the form $r^4 = k^4$, giving roots of $\pm k$ and $\pm ik$. For simplicity, this exponential solution can be written in terms of trigonometric and hyperbolic functions such as:

$$u'(\delta) = C_1 \cos(k\delta) + C_2 \sin(k\delta) + C_3 \cosh(k\delta) + C_4 \sinh(k\delta) \quad (\text{A.33})$$

$$v'(\delta) = C_1 \cos(k\delta) + C_2 \sin(k\delta) + C_3 \cosh(k\delta) + C_4 \sinh(k\delta). \quad (\text{A.34})$$

Applying the fixed-beam boundary conditions to this general solution produces the following:

$$\begin{aligned} u'(0) &= 0 : \\ v'(0) &= 0 : \quad C_1 + C_3 = 0 \\ \frac{du'}{d\delta}(0) &= 0 : \\ \frac{dv'}{d\delta}(0) &= 0 : \quad C_2 + C_4 = 0 \\ u'(1) &= 0 : \\ v'(1) &= 0 : \quad C_1(\cos k - \cosh k) + C_2(\sin k - \sinh k) = 0 \\ \frac{du'}{d\delta}(1) &= 0 : \\ \frac{dv'}{d\delta}(1) &= 0 : \quad C_1(\sin k + \sinh k) + C_2(\cosh k - \cos k) = 0 \end{aligned} \quad (\text{A.35})$$

Non-trivial solutions would only exist if the determinant of the coefficient matrix were zero. This condition gives the following equation for the frequency parameter k (eigenvalues):

$$1 - \cosh(k) \cos(k) = 0. \quad (\text{A.36})$$

This implicit expression for k can only be solved exactly by iteration. A very accurate approximation to this solution, however, can be found by noting that as k increases, $\cosh k$ gets larger exponentially. A value of k which satisfies

this equation must produce $\cos k$ on the same order of magnitude as $1/\cosh k$. The graph of $\cos k$ and $1/\cosh k$ shown in Figure A.4 reveals that $1/\cosh k$ approaches zero very quickly, so a good approximation of k can be taken from the roots of $\cos k = 0$. Mathematically, this condition is that $k_n = \frac{1}{2}\pi(2n + 1)$. Tests with smaller k values indicate that this approximation is accurate within three significant figures, well above the precision of this analysis as a whole. It should be noted that the accuracy of this approximation would increase with increasing k .

Combining this information, the natural frequencies of the Apollo Lightcraft shroud in local vibration modes can be expressed as:

$$f_{xn} = (2n + 1)^2 \frac{\pi}{8} \sqrt{\frac{EI_{xx}}{mL^4}} \quad (\text{A.37})$$

$$f_{yn} = (2n + 1)^2 \frac{\pi}{8} \sqrt{\frac{EI_{yy}}{mL^4}} \quad (\text{A.38})$$

A viable material for the construction of this shroud is some form of carbon-fiber composite. To get a representative set of material properties for such a material, those of T300/5208 Graphite-Epoxy (a common aerospace material) were used. These material properties are listed in Table A.1.5[4].

Utilizing these material properties in conjunction with the section properties determined earlier, Equations A.37 and A.38 can be used to generate the necessary frequencies for each integer value of n . The mass per unit length, m , was found by multiplying the density of T300/5208 by the total geometric area, consistent with the assumption that the entire cross-section (including the nozzle) would contribute to the mass distribution. The graphite-epoxy composite, being an anisotropic lamina, has widely different values for moduli in the longitudinal and transverse directions. To take into account the assumption that the complete structural plates of these laminates would have plies oriented at many different angles to allow the final component to act as if it were isotropic, an "averaged" value for the Young's modulus of 95 GPa is used[1]. A tabulated listing of the calculated natural frequencies is given in Table A.1.5.

A.2 Beam Theory Analysis: Global Modes

A.2.1 Exact Solution for Vibrations of a Circular Ring

Consideration of Figure A.5 will demonstrate the possibility of the existence of global vibration modes between the individual sections of the shroud. For a first approximation to these frequencies, an equation derived by A. E. H. Love for the vibration of a circular ring with N nodal points[5] will be used. This expression for flexural vibrations in the plane of the ring (the x directions used

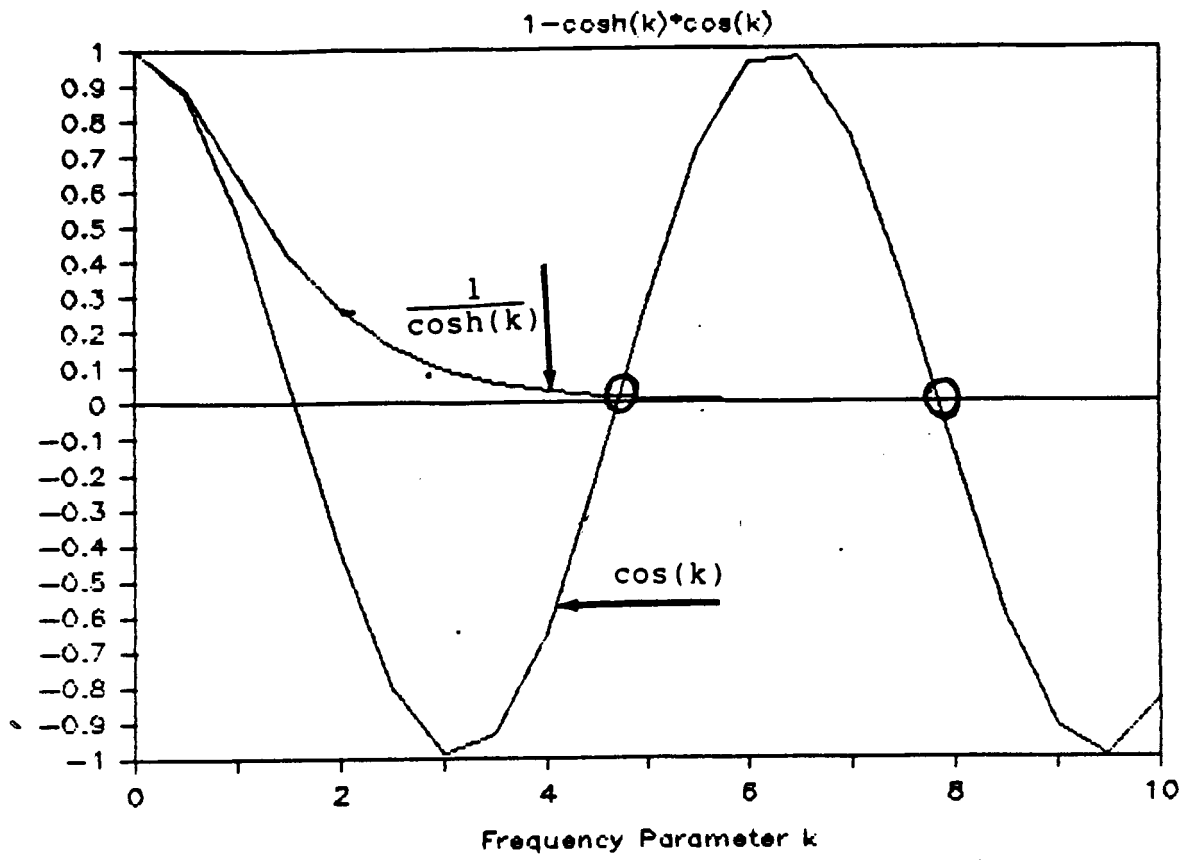


Figure A.4: Components of the Frequency Equation

Property	Value
Young's Mod. E_x (GPa) E_y (GPa)	181 10.3
Poisson's Ratio σ	0.28
Shear Mod. G (GPa)	7.17
Density (Kg/m^3)	1900

Table A.2: Material Properties of Graphite-Epoxy

ORIGINAL PAGE IS
OF POOR QUALITY

Mode No.	Rectangular Sect.		Circular Arc Sect.	
	x' Bend.	y' Bend.	x' Bend.	y' Bend.
1	0.17	0.89	0.17	0.82
2	0.46	2.44	0.48	2.26
3	0.91	4.79	0.94	4.43
4	1.50	7.90	1.55	7.34
5	2.24	11.81	2.24	10.96
6	3.12	16.49	3.22	15.30
7	4.16	21.96	4.32	20.38
8	5.34	28.20	5.55	26.17
9	6.67	35.23	6.93	32.69
10	8.15	43.03	8.46	39.93
11	9.77	51.62	10.15	47.90
12	11.55	60.99	11.99	56.60
13	13.47	71.14	13.99	66.00
14	15.54	82.07	16.14	76.16
15	17.76	93.78	18.44	87.02
16	20.12	106.27	20.90	98.62
17	22.63	119.54	23.51	110.93
18	25.29	133.59	26.27	123.97

Table A.3: Natural Frequencies for Local Bending of the Apollo Lightcraft Shroud (kHz)

Beam Theory Approx.

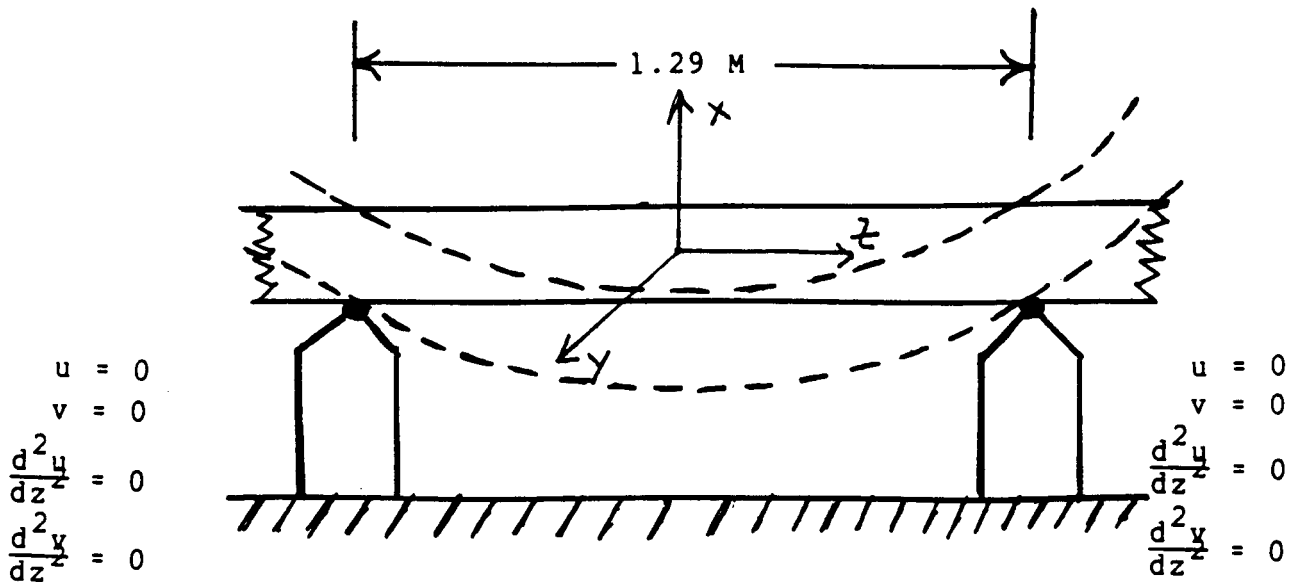


Figure A.5: Global Modes of Vibration of the Apollo Lightcraft Shroud

here) can be written as

$$f^2 = \frac{Er^4}{16\pi mR^4} \frac{N^2(N^2 - 1)^2}{N^2 + 1} \quad (\text{A.39})$$

Flexural vibrations out of the plane of the ring (the y direction for the shroud) have frequencies found from the relation

$$f^2 = \frac{Er^4}{16\pi mR^4} \frac{N^2(N^2 - 1)^2}{N^2 + 1 + \sigma} \quad (\text{A.40})$$

In this equation, it is assumed that the ring has a circular cross-section of radius r . The ring itself has a radius of R . For a first approximation to the results for the shroud, a radius corresponding to a circular cross-section having the same I_{xx} as the shroud cross-section would be used for in-plane (x) bending. Similarly, for out-of-plane bending (y -direction), a radius giving a circular cross-section of moment of inertia I_{yy} would be used. The moment of inertia around any line passing through the center of a circular cross-section is given by

$$I = \frac{\pi}{4} r^4 \quad (\text{A.41})$$

Using this expression with $I_{xx} = 1.62 \times 10^{-6} \text{ m}^4$ and $I_{yy} = 35.6 \times 10^{-6} \text{ m}^4$ yields $r_x = 0.0379 \text{ m}$ and $r_y = 0.0822 \text{ m}$.

The boundary condition for these global modes is that a nodal point occurs at each of the twelve connections with struts around the shroud. This requirement means that the number of wavelengths allowed on the circular ring must be a multiple of 6. In mathematical terms, this implies the substitution of $N = 6n$ into Equations A.39 and A.40 to yield

$$f_{xn}^2 = 2916 \frac{Er_x^4}{\pi R^4} \frac{n^2(n^2 - 1)^2}{36n^2 + 1} \quad (\text{A.42})$$

$$f_{yn}^2 = 2916 \frac{Er_y^4}{\pi R^4} \frac{n^2(n^2 - 1)^2}{36n^2 + 1 + \sigma} \quad (\text{A.43})$$

A.2.2 Beam Theory Solution for Global Modes

In the same manner as for the local vibration modes, the global modes can be found by considering the segment of the shroud between any two of the twelve struts to be a straight beam. The only change in this theory would be that the boundary conditions for a fixed end could no longer be applied, since excitation of global modes requires interaction between the beam segments. Examination of Figure A.5, however, indicates that another boundary condition can be found from the fact that each of the nodes must be an inflection point for the deformed shroud structure; therefore, there must be zero curvature at each end of each segment. The condition of no motion at the end points is retained.

Mathematically, this set of boundary conditions can be written as: $u(0) = 0$ and $\frac{d^2 u}{dz^2}(0) = 0$; $u(L) = 0$ and $\frac{d^2 u}{dz^2}(L) = 0$; $v(0) = 0$ and $\frac{d^2 v}{dz^2}(0) = 0$; $v(L) = 0$ and $\frac{d^2 v}{dz^2}(L) = 0$. Applying these new constraints to the general solution of the beam equation (Equation A.33 and A.34) yields the following set of equations:

$$\begin{aligned}
 u'(0) &= 0 : \\
 v'(0) &= 0 : \quad C_1 + C_3 = 0 \\
 \frac{d^2 u'}{dz^2}(0) &= 0 : \\
 \frac{d^2 v'}{dz^2}(0) &= 0 : \quad C_1 - C_3 = 0 \qquad C_1 = 0 \text{ and } C_3 = 0 \\
 u'(L) &= 0 : \\
 v'(L) &= 0 : \quad C_4 \sinh k + C_2 \sin k = 0 \\
 \frac{du'}{dz}(L) &= 0 : \\
 \frac{dv'}{dz}(L) &= 0 : \quad C_4 \sinh k - C_2 \sin k = 0
 \end{aligned} \tag{A.44}$$

Taking the determinant of the last set of equations to be zero, as was done for the local modes, yields the frequency equation:

$$\sinh k \sin k = 0 \tag{A.45}$$

Solutions to this equation will be either the roots of $\sinh k = 0$ (the trivial solution of $k = 0$), or the roots of $\sin k = 0$, which is well known to be: $k_n = n\pi$. Combining this with the other parameters needed to dimensionalize the frequency, an expression for the x and y bending natural frequencies of the global modes can be given as

$$f_{xn} = \frac{n\pi}{4} \sqrt{\frac{EI_{xx}}{mL^4}} \tag{A.46}$$

$$f_{yn} = \frac{n\pi}{4} \sqrt{\frac{EI_{yy}}{mL^4}} \tag{A.47}$$

The numerical results are presented in Table A.2.2.

ORIGINAL PAGE IS
OF POOR QUALITY

3.3 Natural Global Bending Frequencies of the Apollo
Lightcraft Shroud.

Mode No.	Circular Ring		Beam Theory		% Deviation	
	x Bend	y Bend	x Bend	y Bend	x	y
1	0.08	0.38	0.08	0.36	6.1	5.7
2	0.34	1.59	0.31	1.45	9.3	9.1
3	0.76	3.59	0.69	3.26	9.8	9.7
4	1.36	6.40	1.23	5.79	10.0	10.0
5	2.13	10.01	1.92	9.05	10.2	10.1
6	3.07	14.42	2.77	13.03	10.2	10.1
7	4.17	19.63	3.77	17.73	10.2	10.1
8	5.45	25.64	4.92	23.16	10.2	10.2
9	6.90	32.46	6.23	29.31	10.2	10.2
10	8.52	40.08	7.69	36.19	10.3	10.2
11	10.31	48.50	9.30	43.79	10.3	10.2
12	12.27	57.72	11.07	52.12	10.3	10.2
13	14.40	67.74	12.99	61.16	10.3	10.2
14	16.70	78.57	15.07	70.93	10.3	10.2

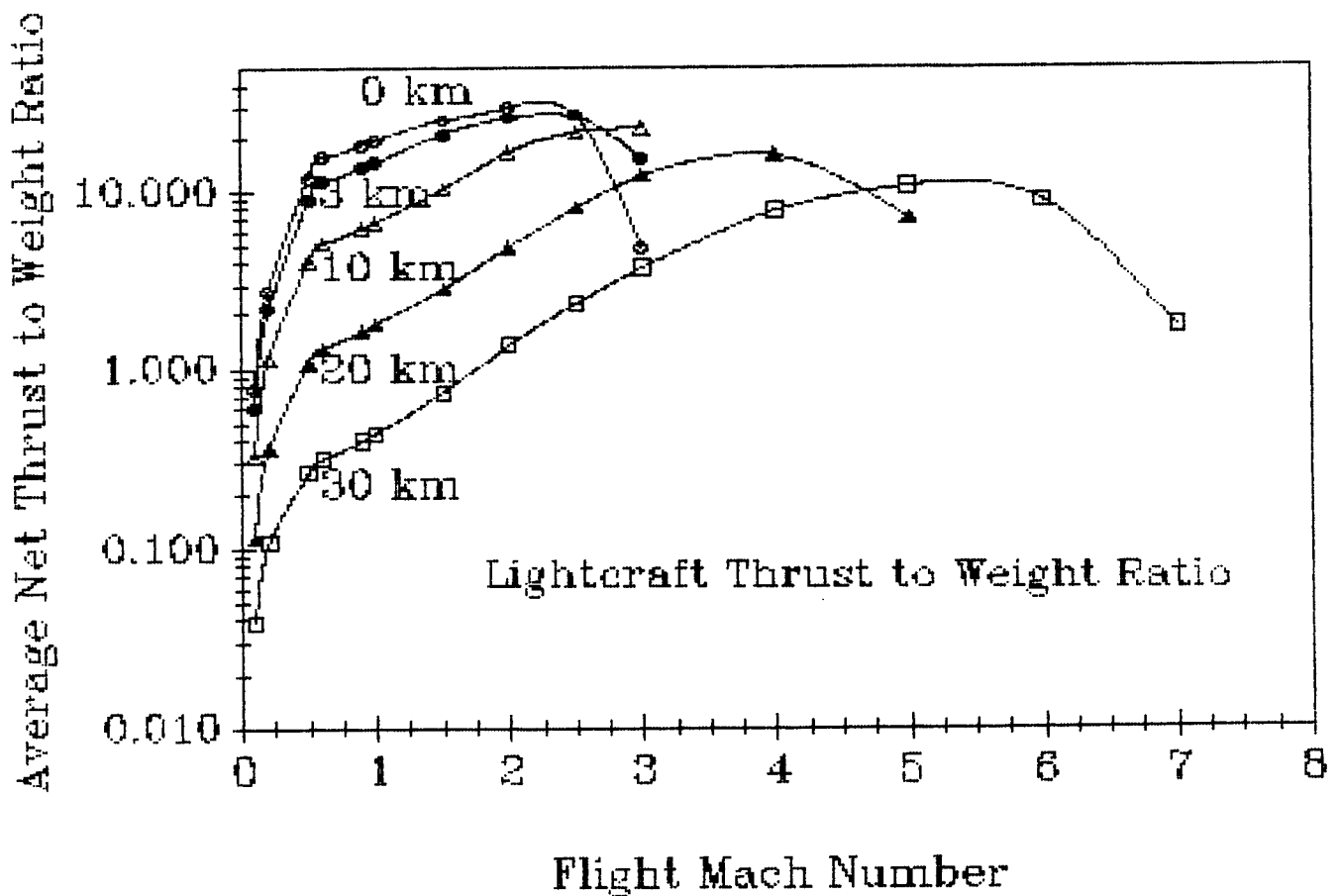
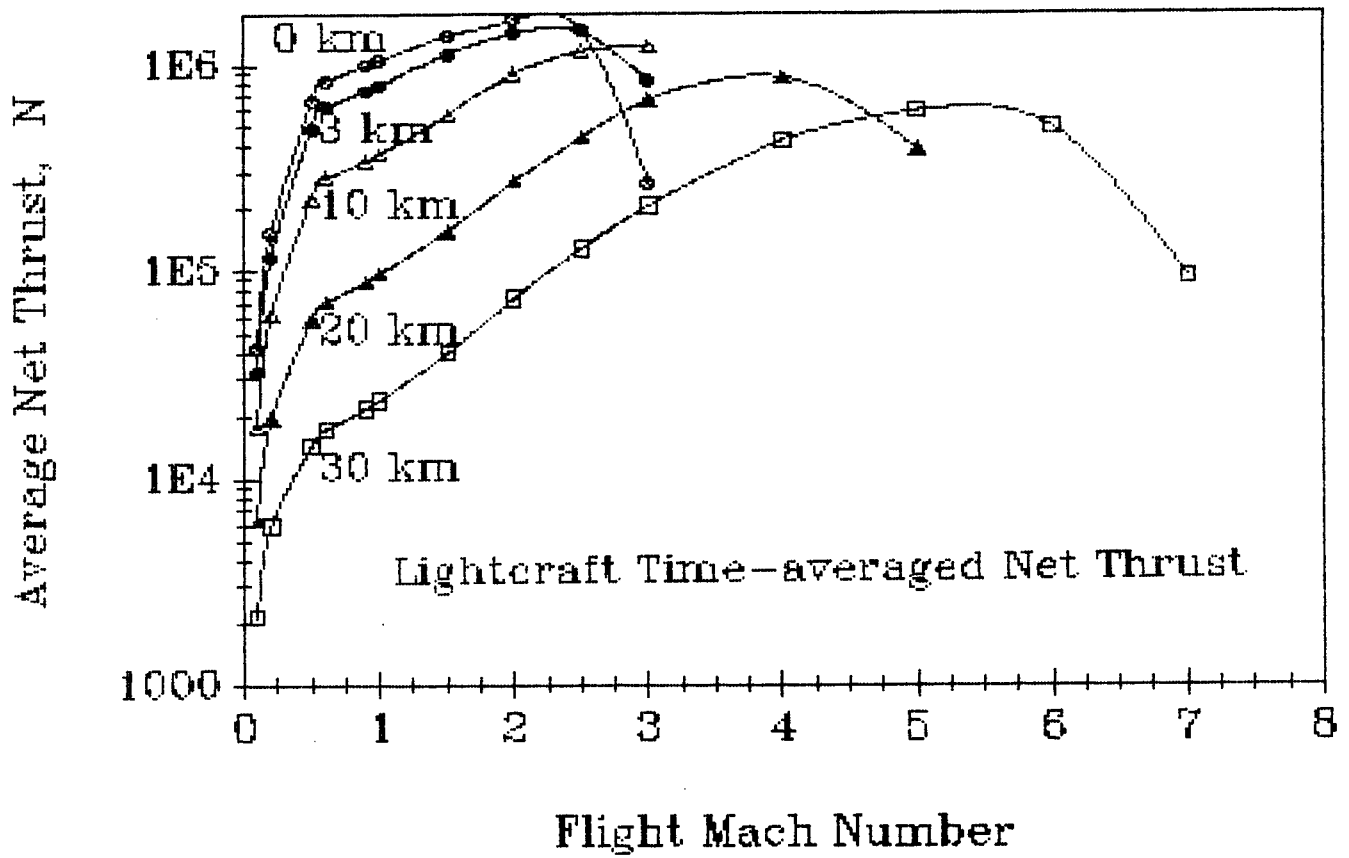
Table A.4: Natural Global Bending Frequencies of the Apollo Lightcraft Shroud

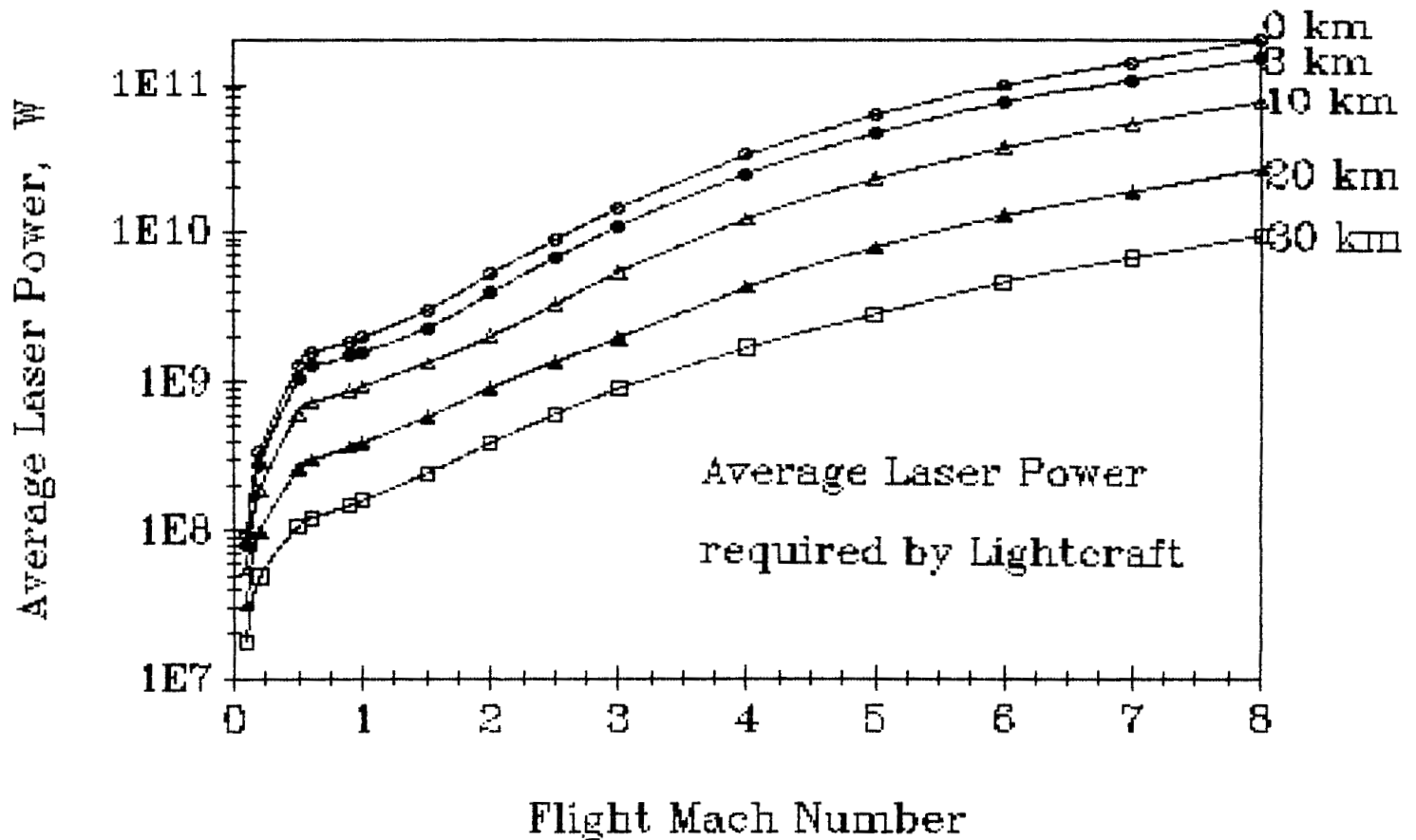
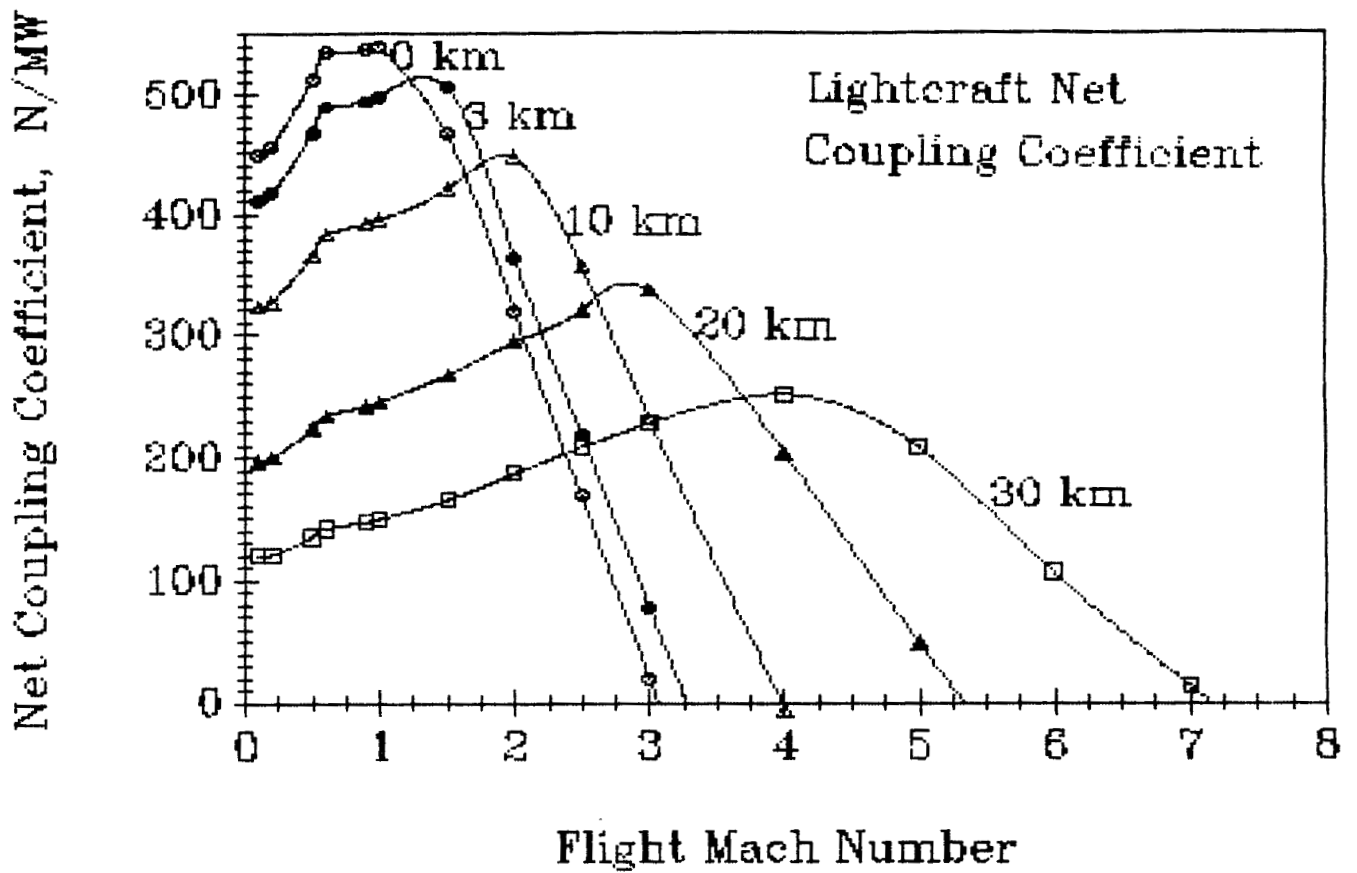
References

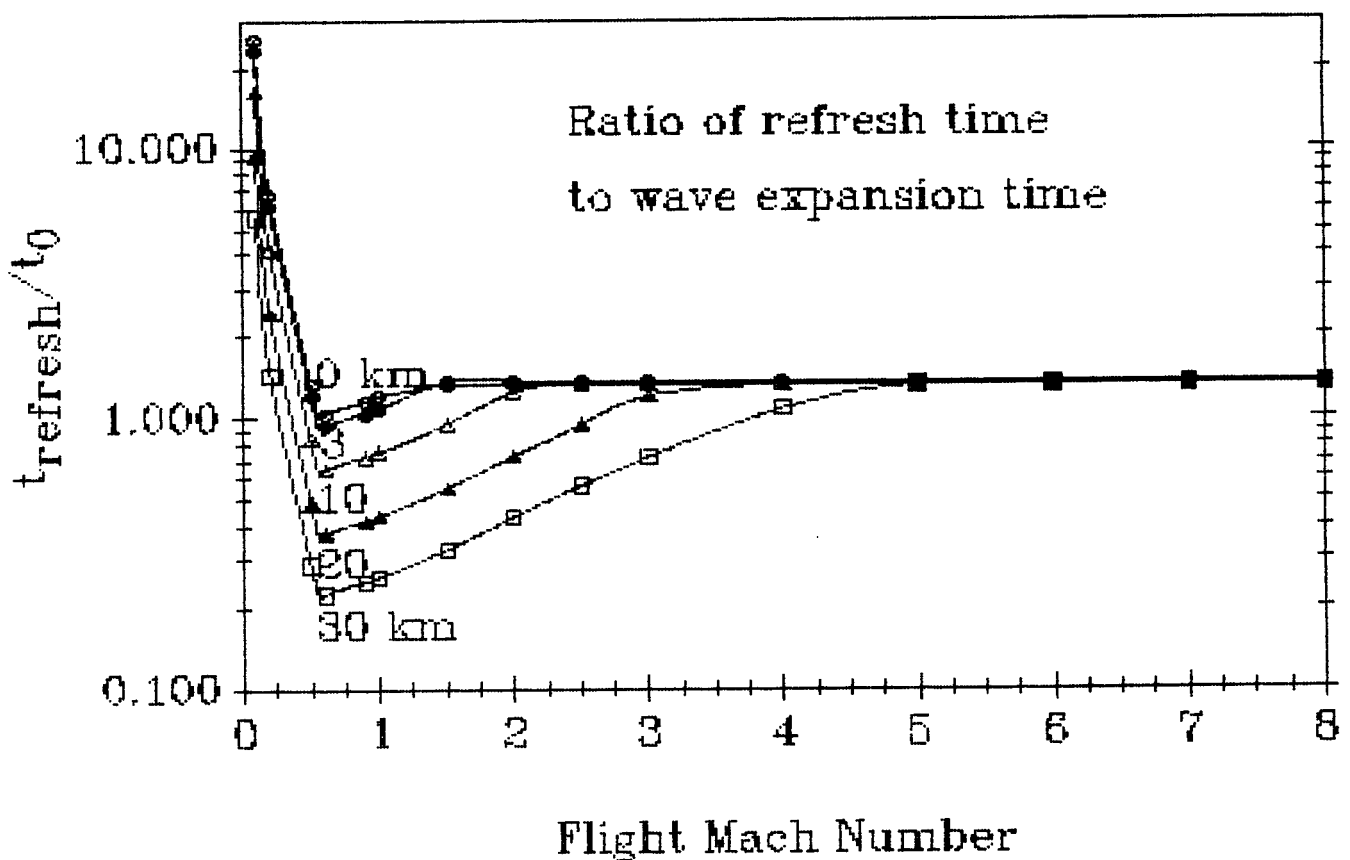
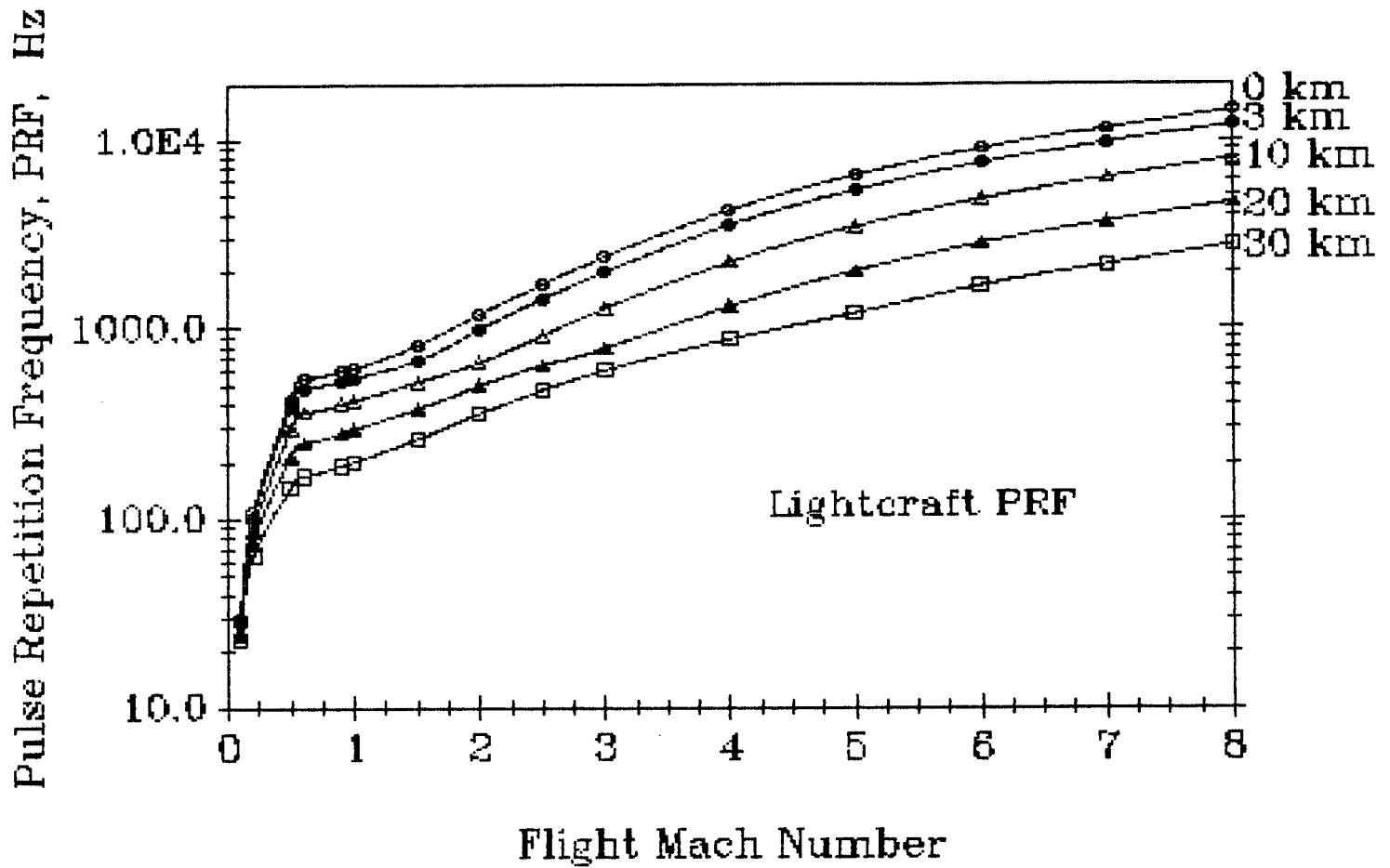
- [1] T. Hehl, *Composite Shell Vibration—A Case Study*, Unpublished Work.
- [2] O. A. Bauchau, lecture notes from *Theory of Structures*, Spring 1987.
- [3] F. P. Beer and E. R. Johnston, *Mechanics of Materials*, McGraw-Hill Book Company, 1981.
- [4] S. W. Tsai and H. T. Hahn, *Introduction to Composite Materials*, Technomic Publishing, 1980.
- [5] A. E. H. Love, *A Treatise on the Mathematical Theory of Elasticity*, Dover Publications, 1944, pp 452-3.
- [6] Ashley and Bisplinghoff, *Principles of Aeroelasticity*, Dover Publications, 1969.

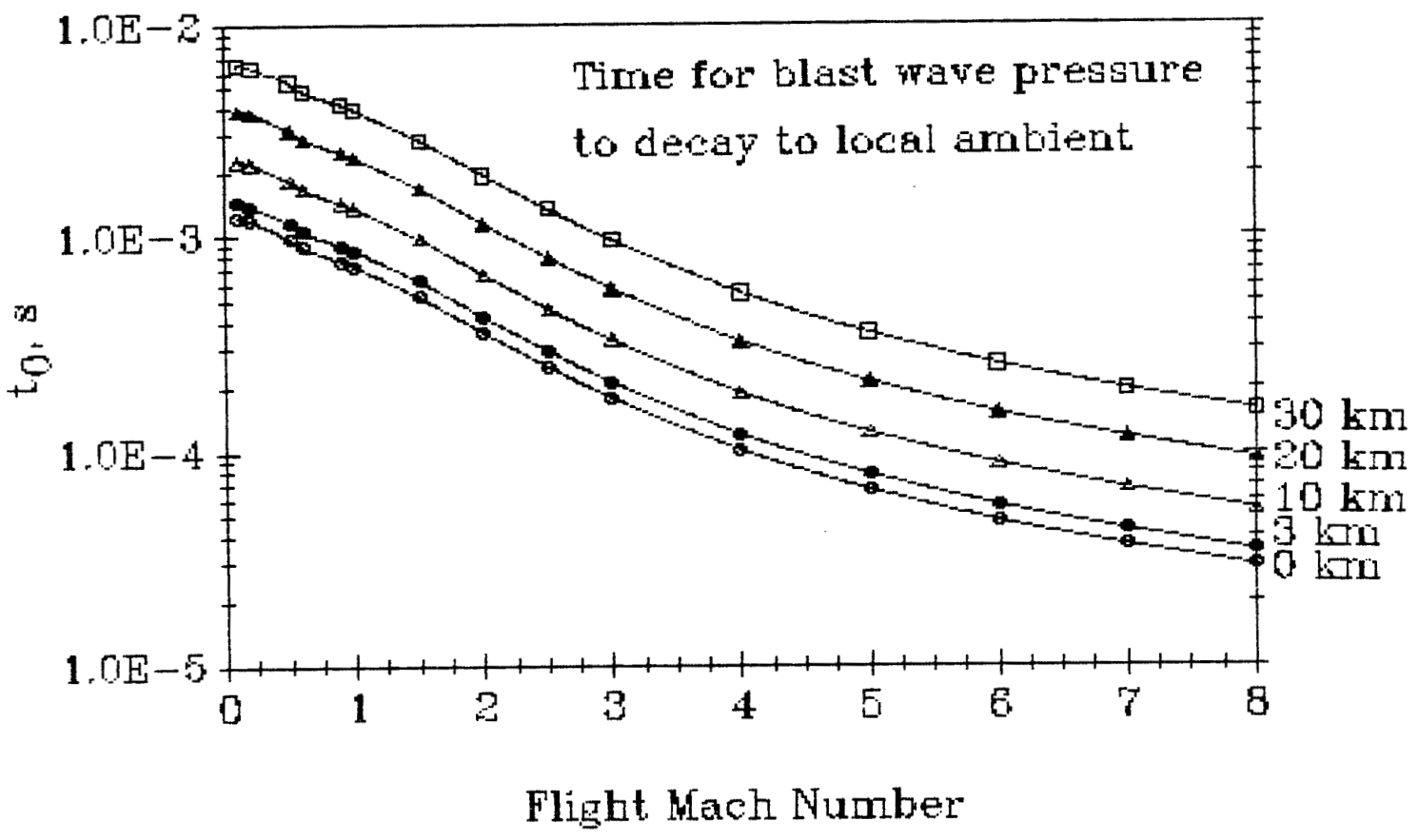
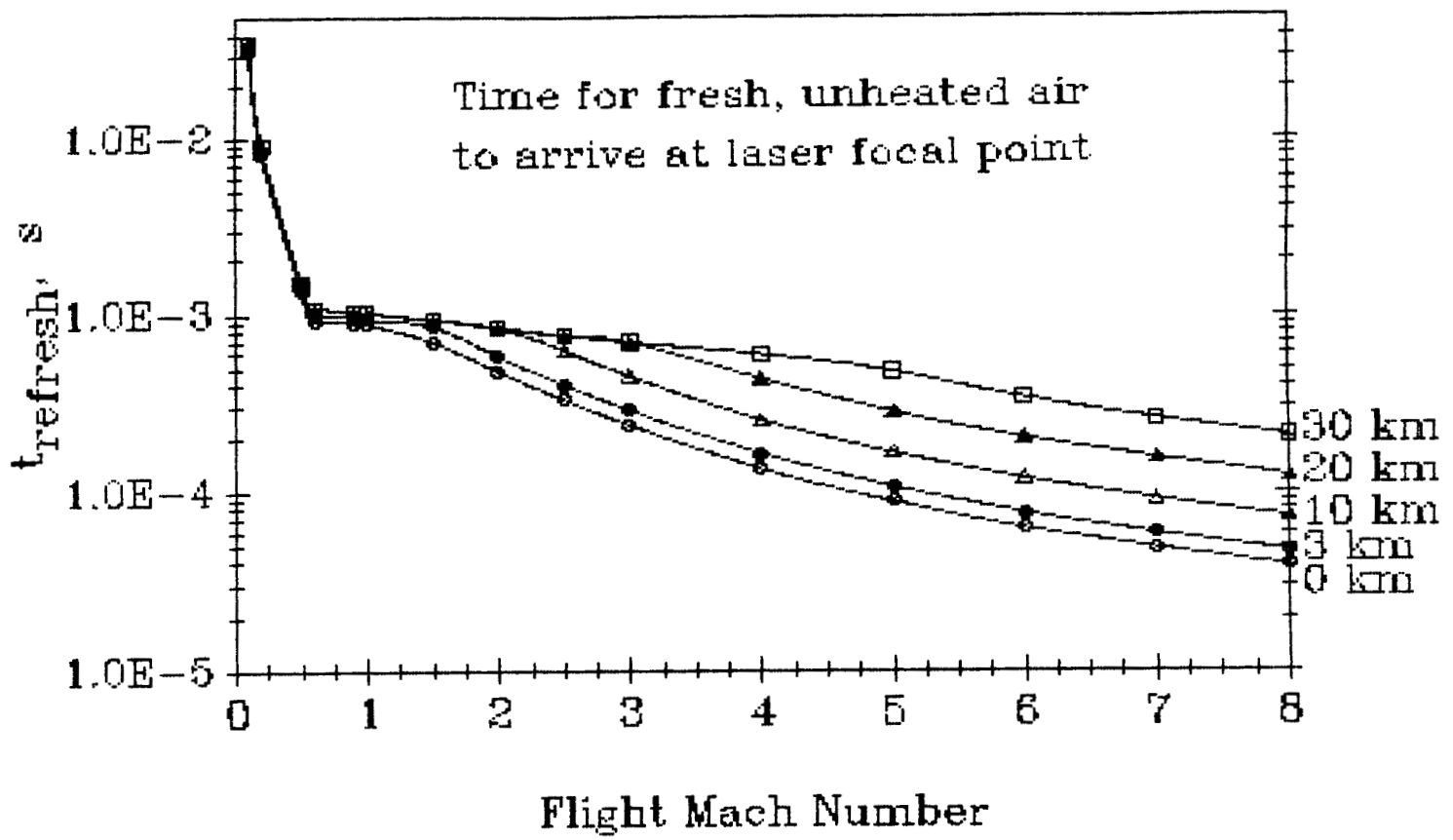
Appendix B

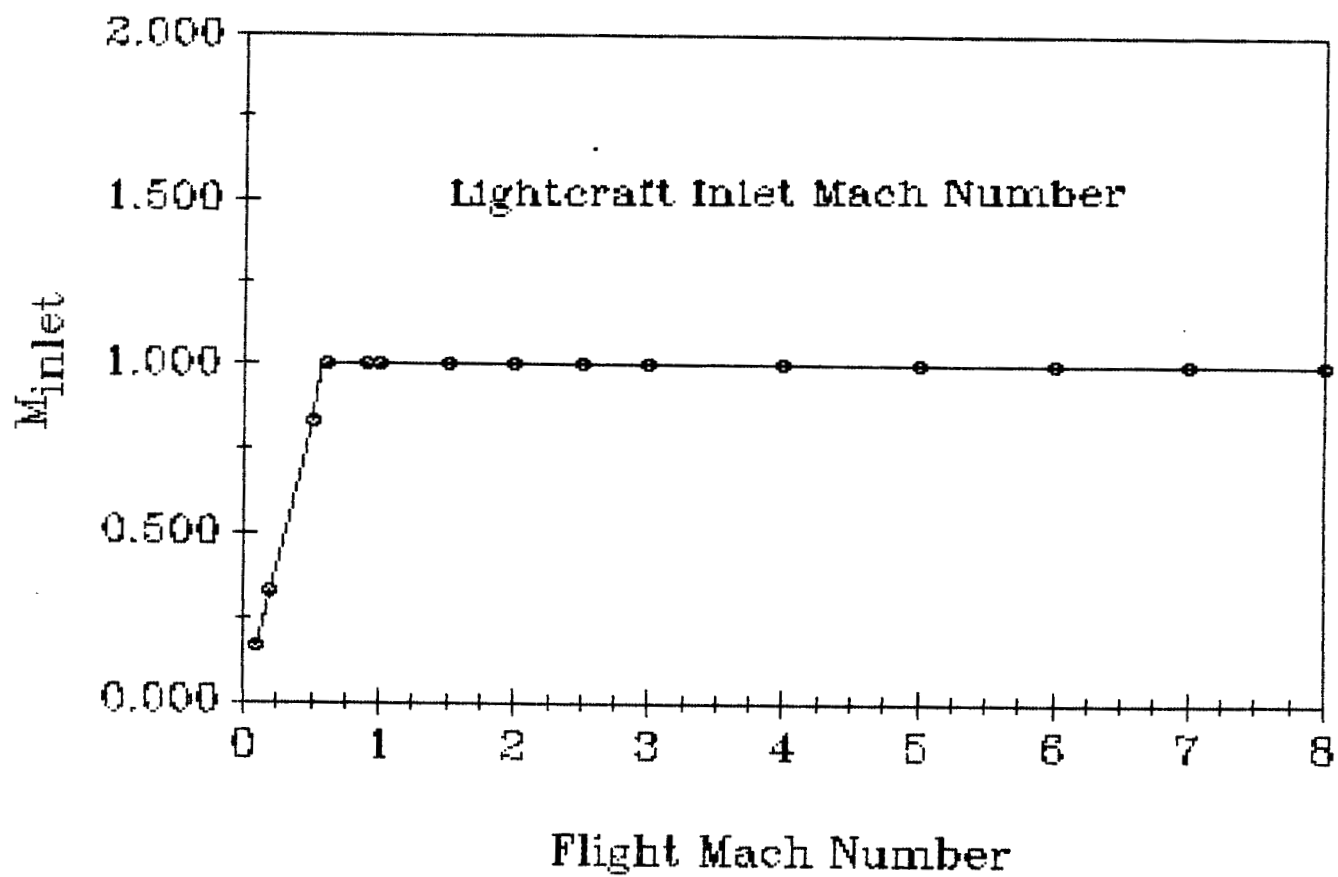
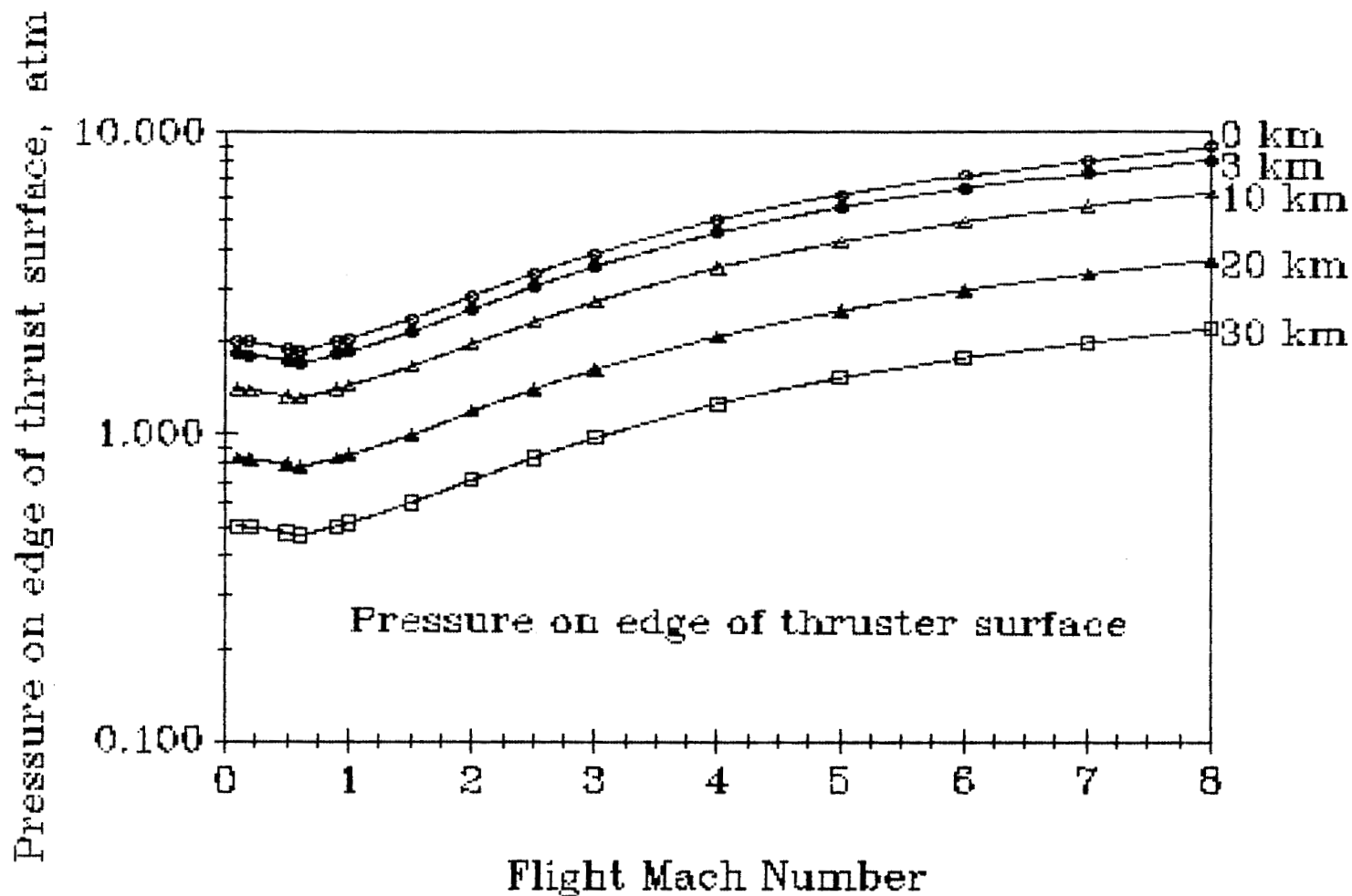
ERH Thruster Performance

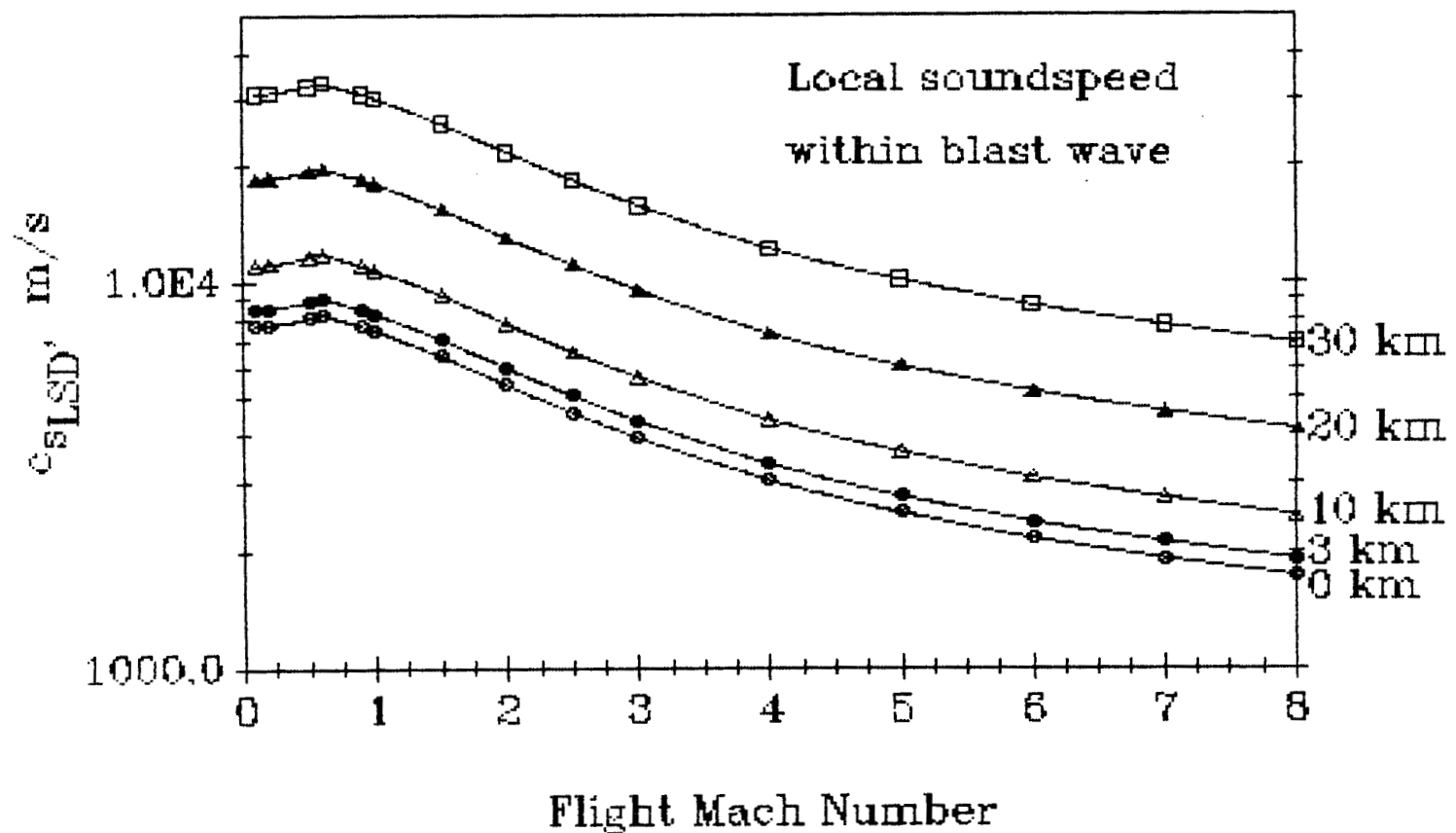
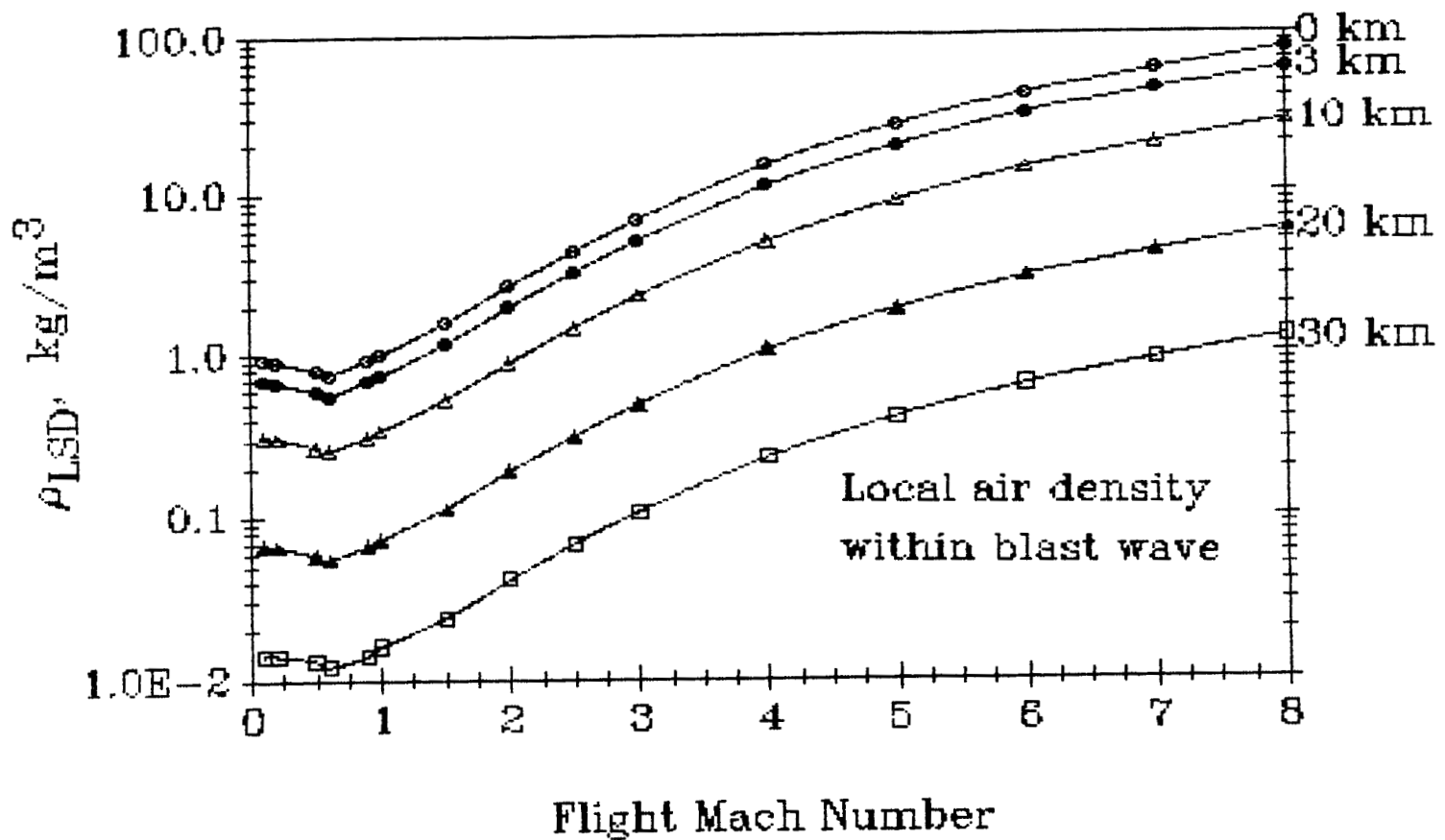


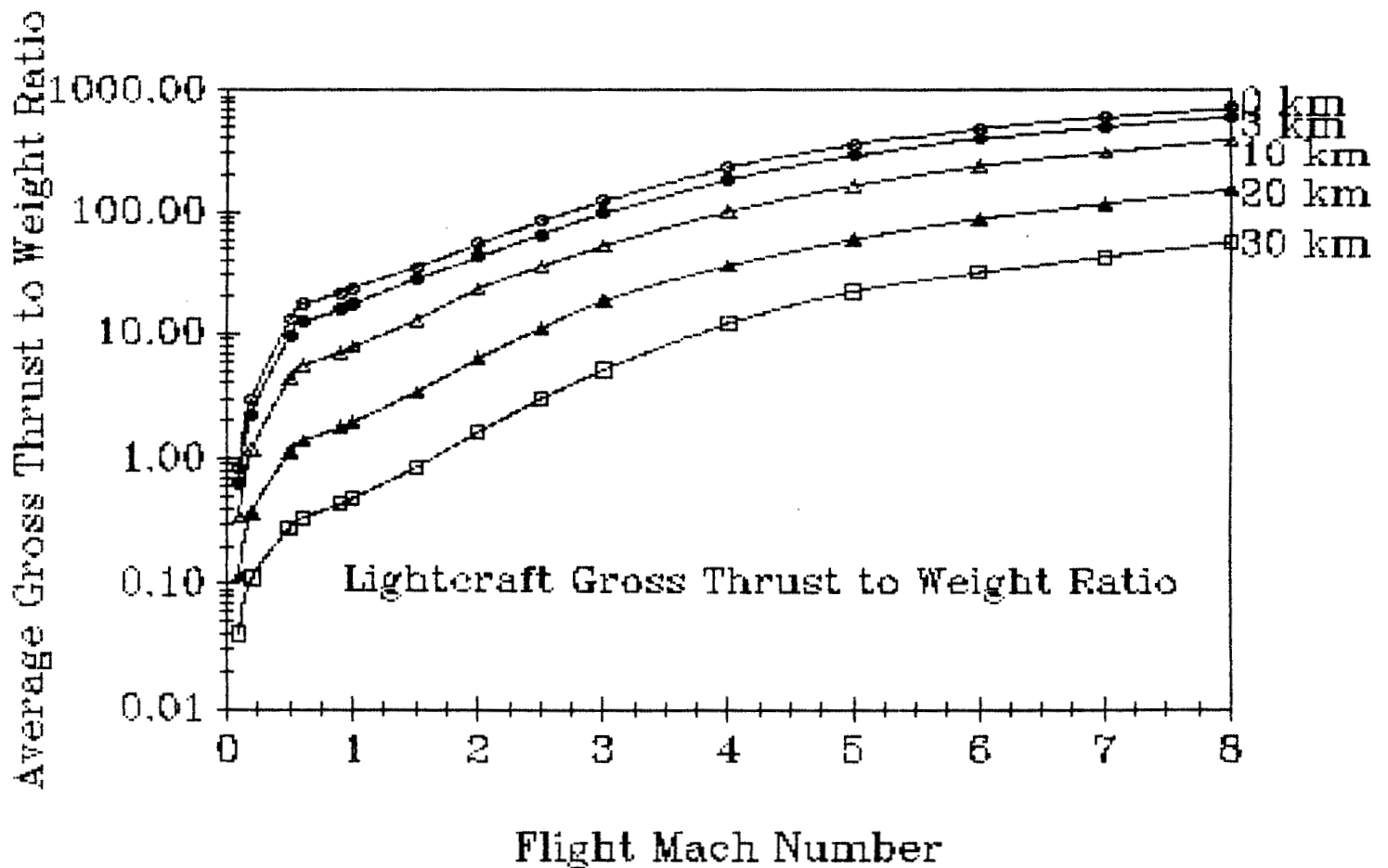
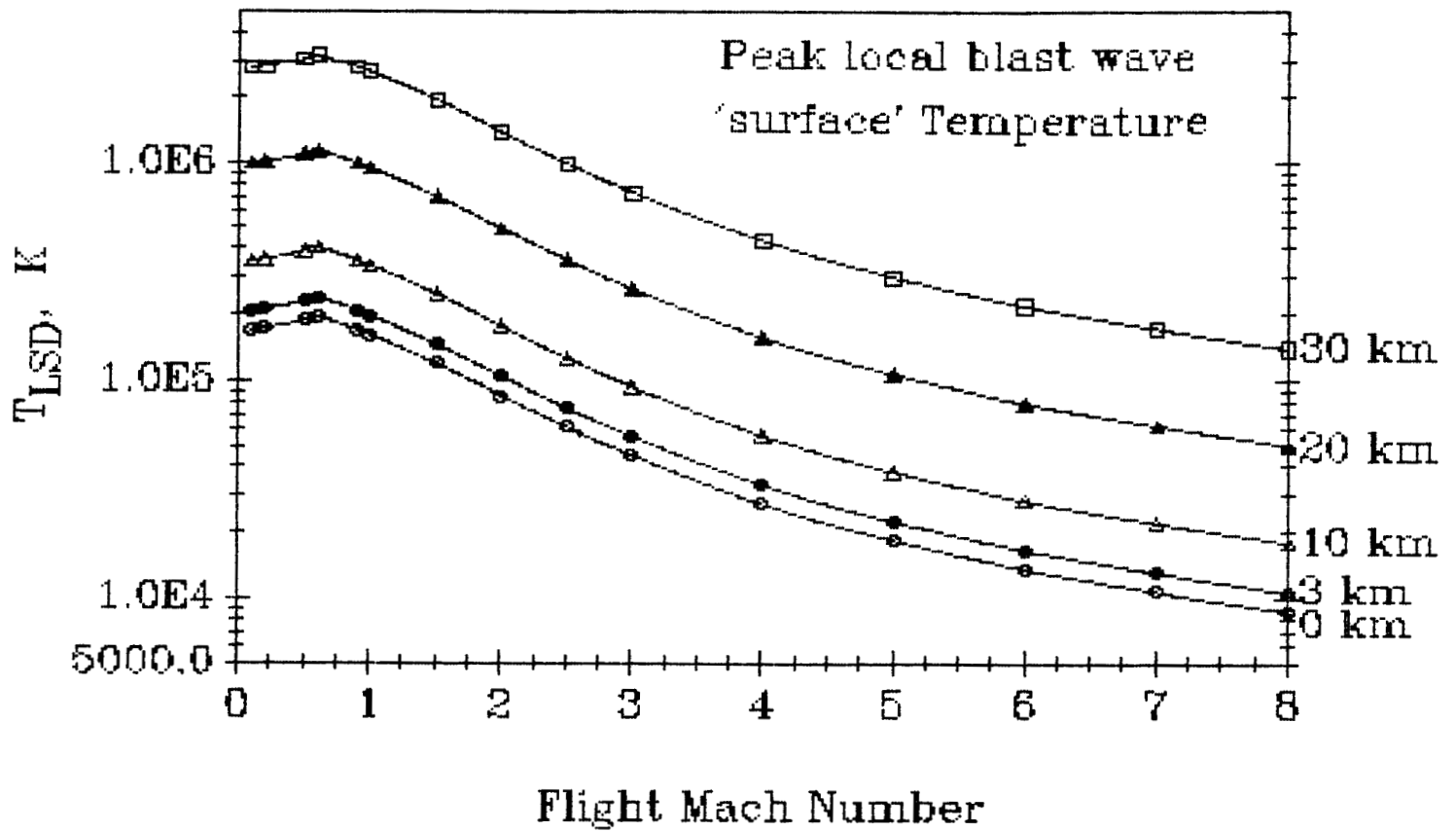


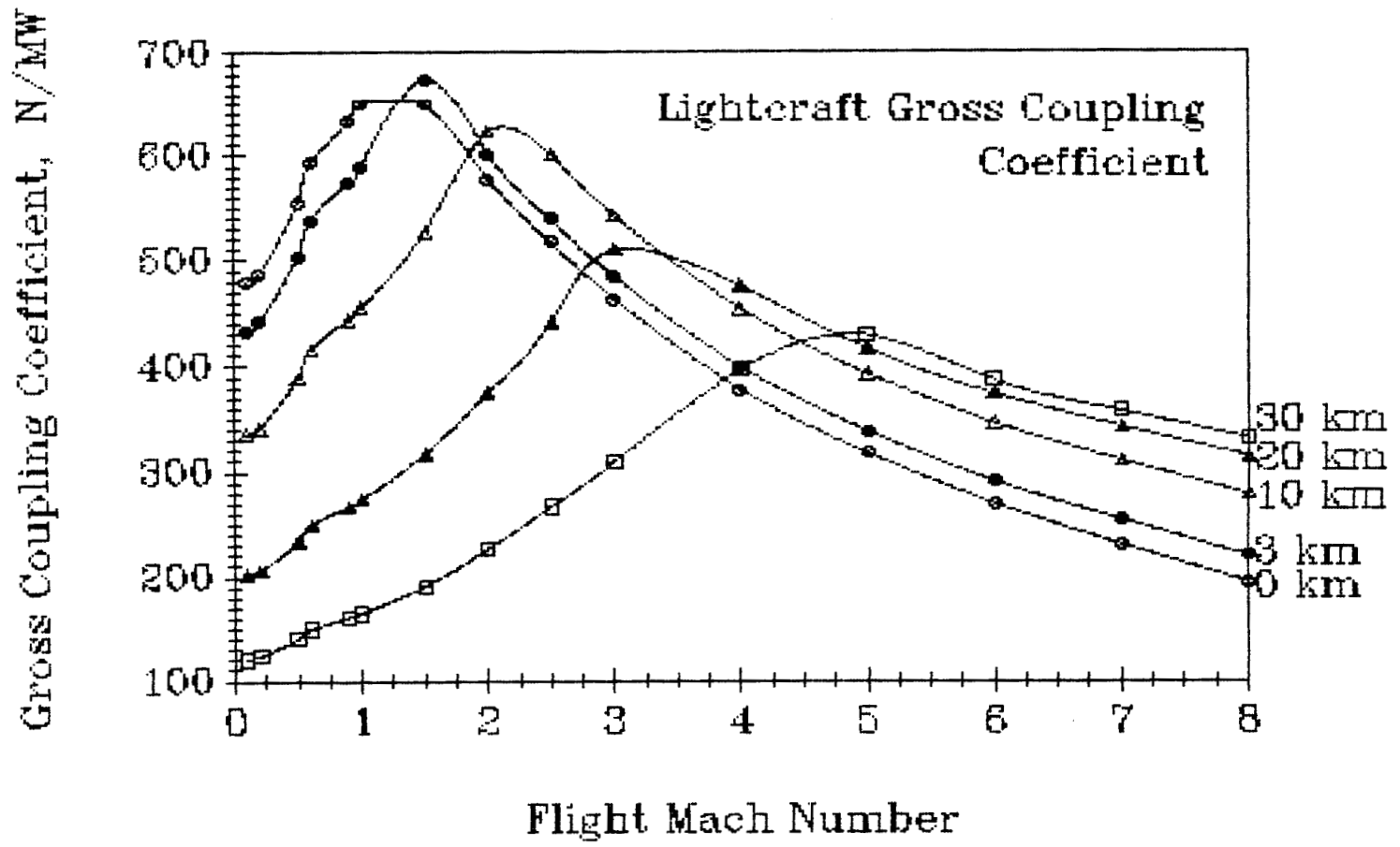
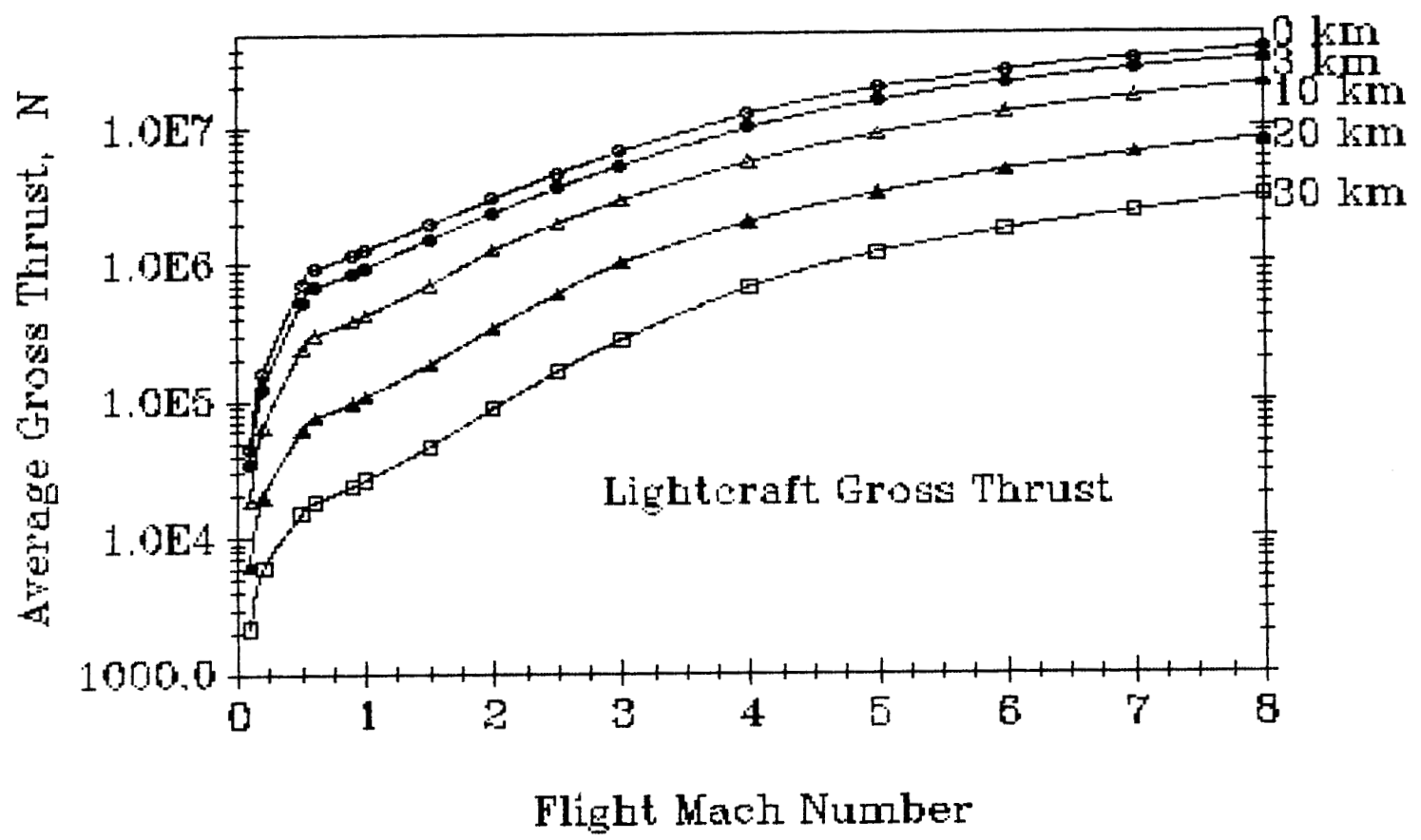






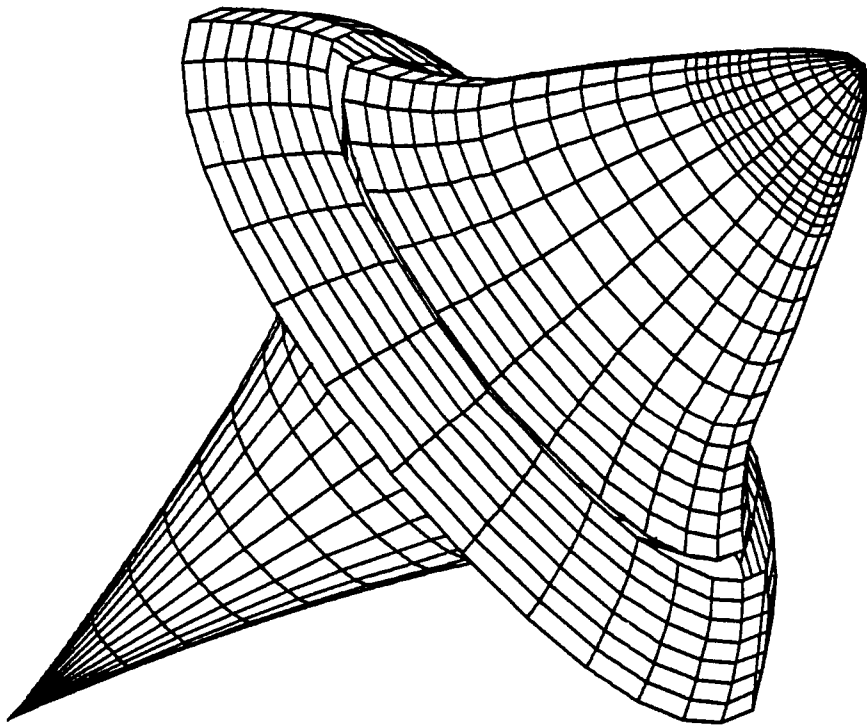


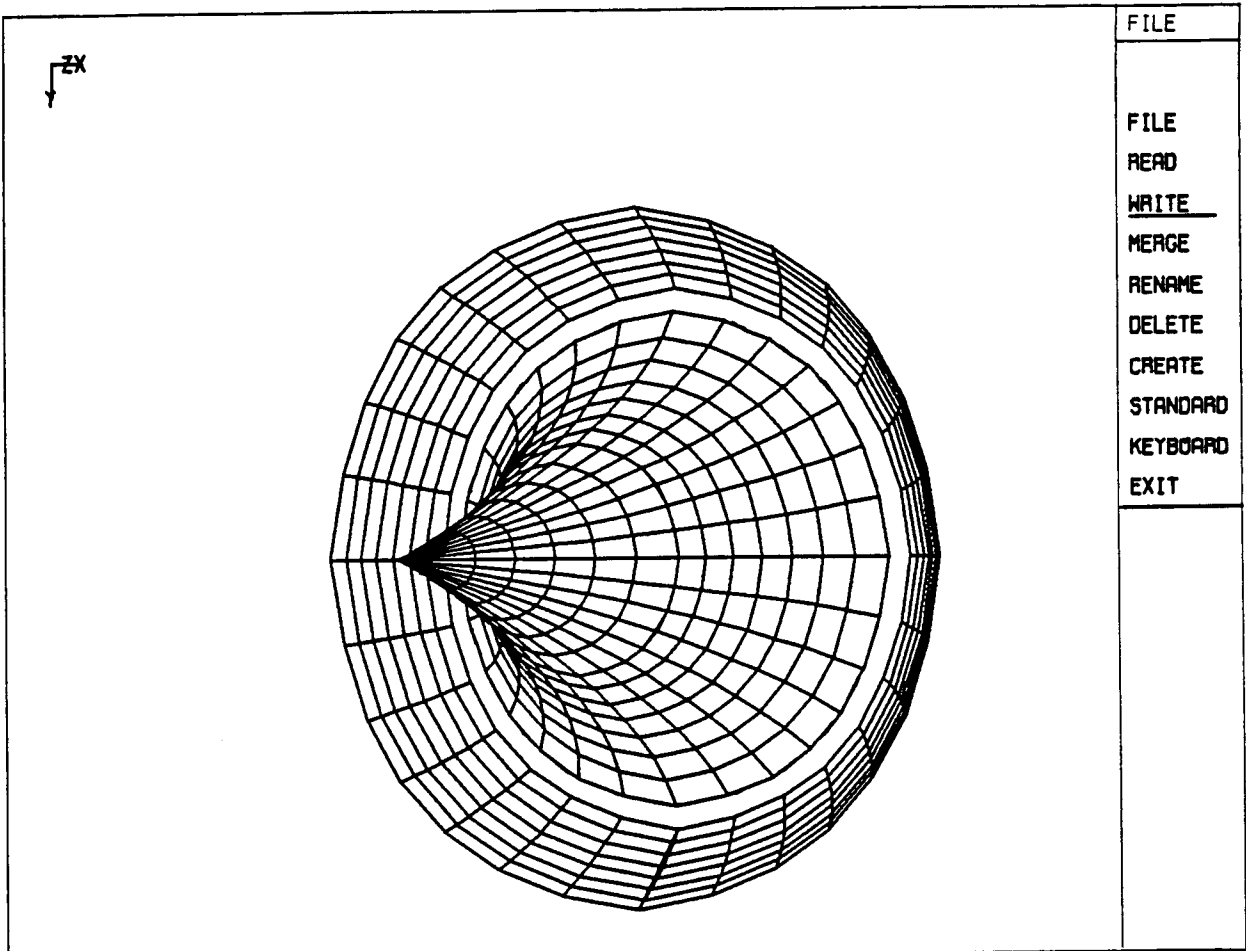




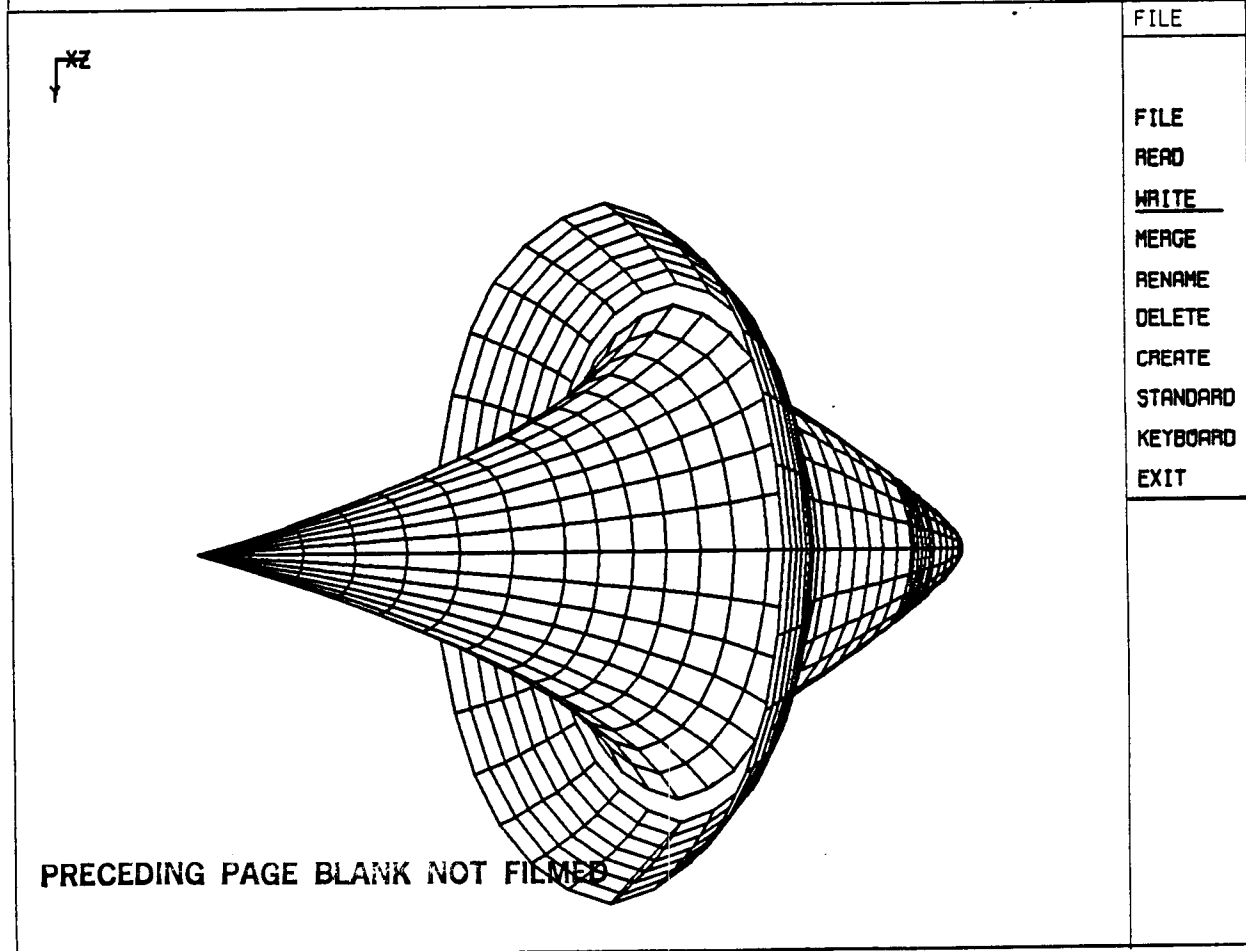
Appendix C

Lightcraft Technology Demonstrator Loft Lines



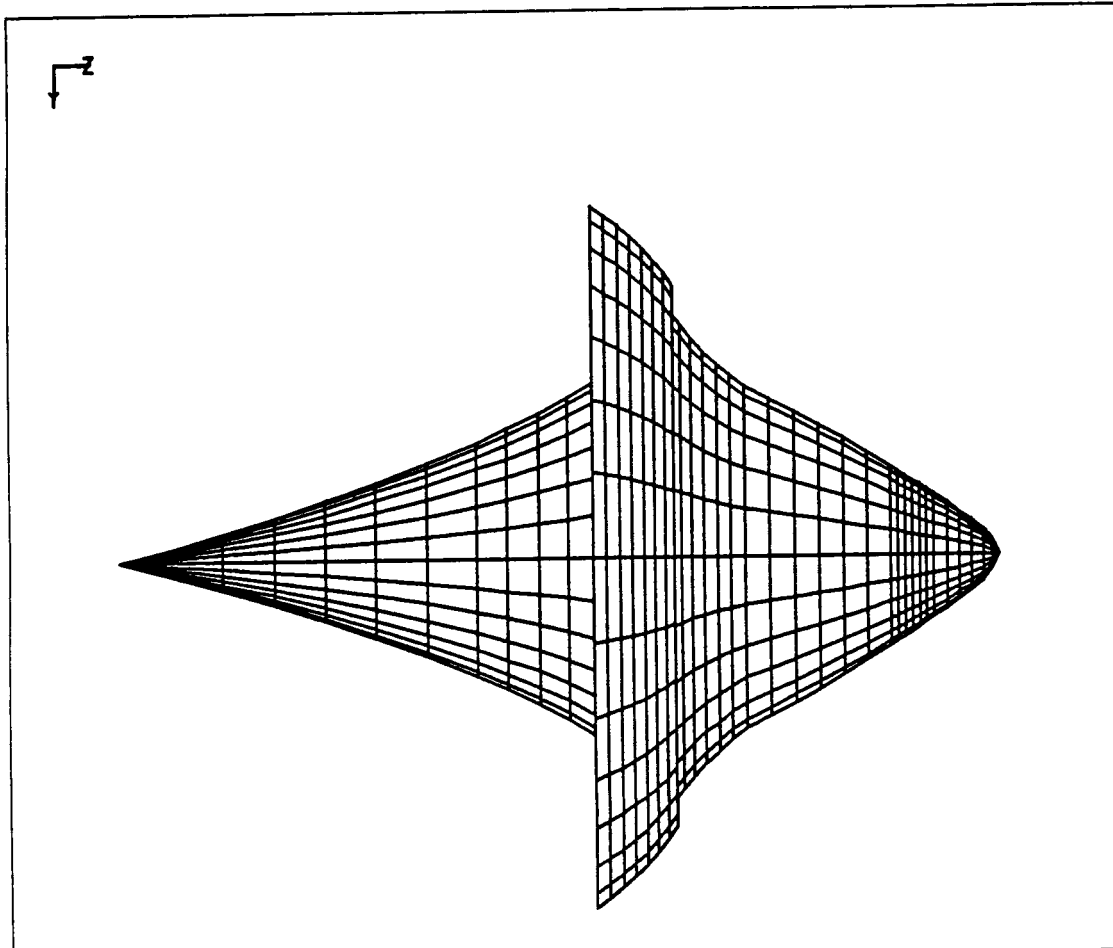


FILE
 FILE
 READ
WRITE
 MERGE
 RENAME
 DELETE
 CREATE
 STANDARD
 KEYBOARD
 EXIT



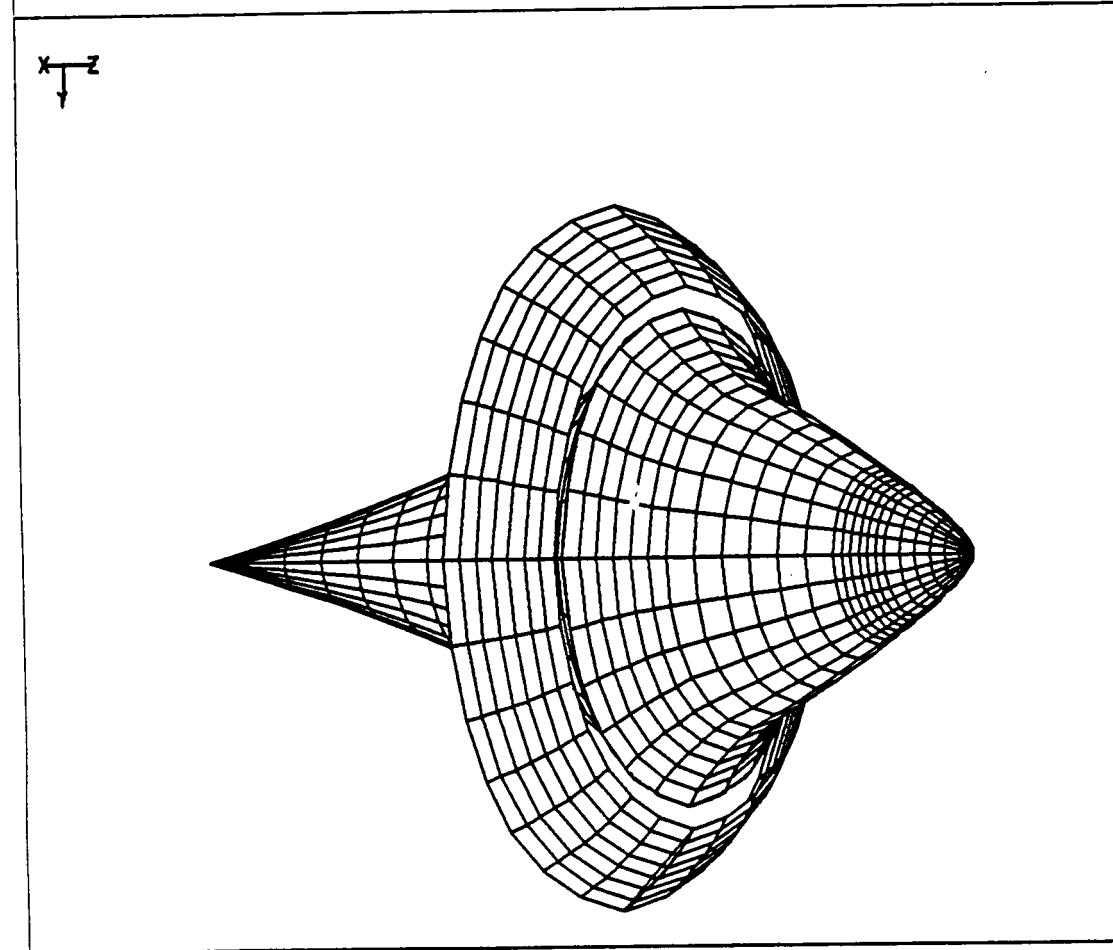
FILE
 FILE
 READ
WRITE
 MERGE
 RENAME
 DELETE
 CREATE
 STANDARD
 KEYBOARD
 EXIT

PRECEDING PAGE BLANK NOT FILMED



FILE

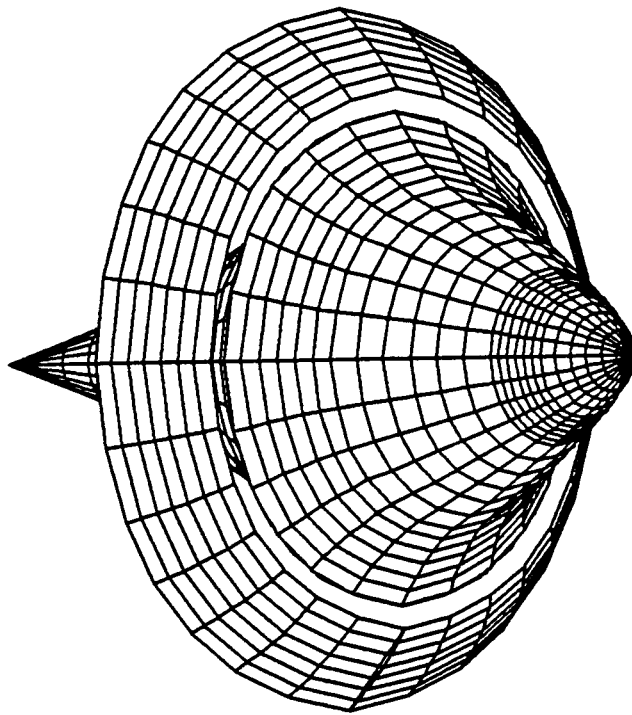
FILE
 READ
WRITE
 MERGE
 RENAME
 DELETE
 CREATE
 STANDARD
 KEYBOARD
 EXIT



FILE

FILE
 READ
WRITE
 MERGE
 RENAME
 DELETE
 CREATE
 STANDARD
 KEYBOARD
 EXIT

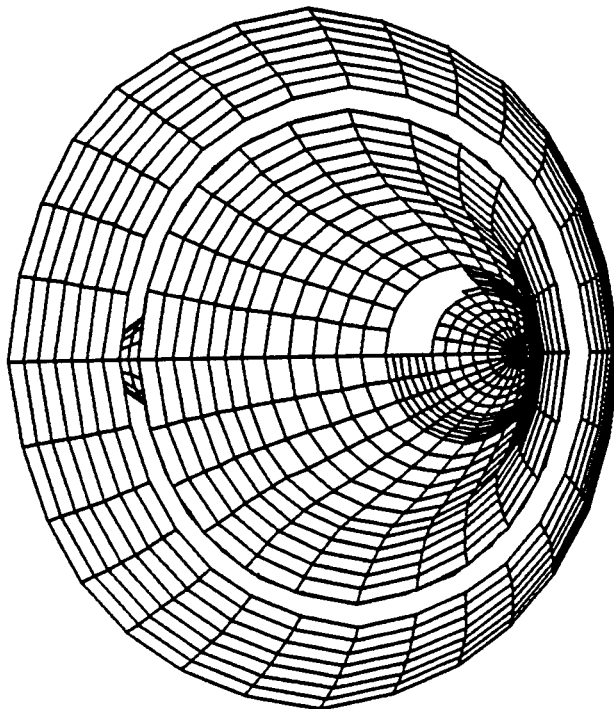
x z
↓



FILE

FILE
READ
WRITE
MERGE
RENAME
DELETE
CREATE
STANDARD
KEYBOARD
EXIT

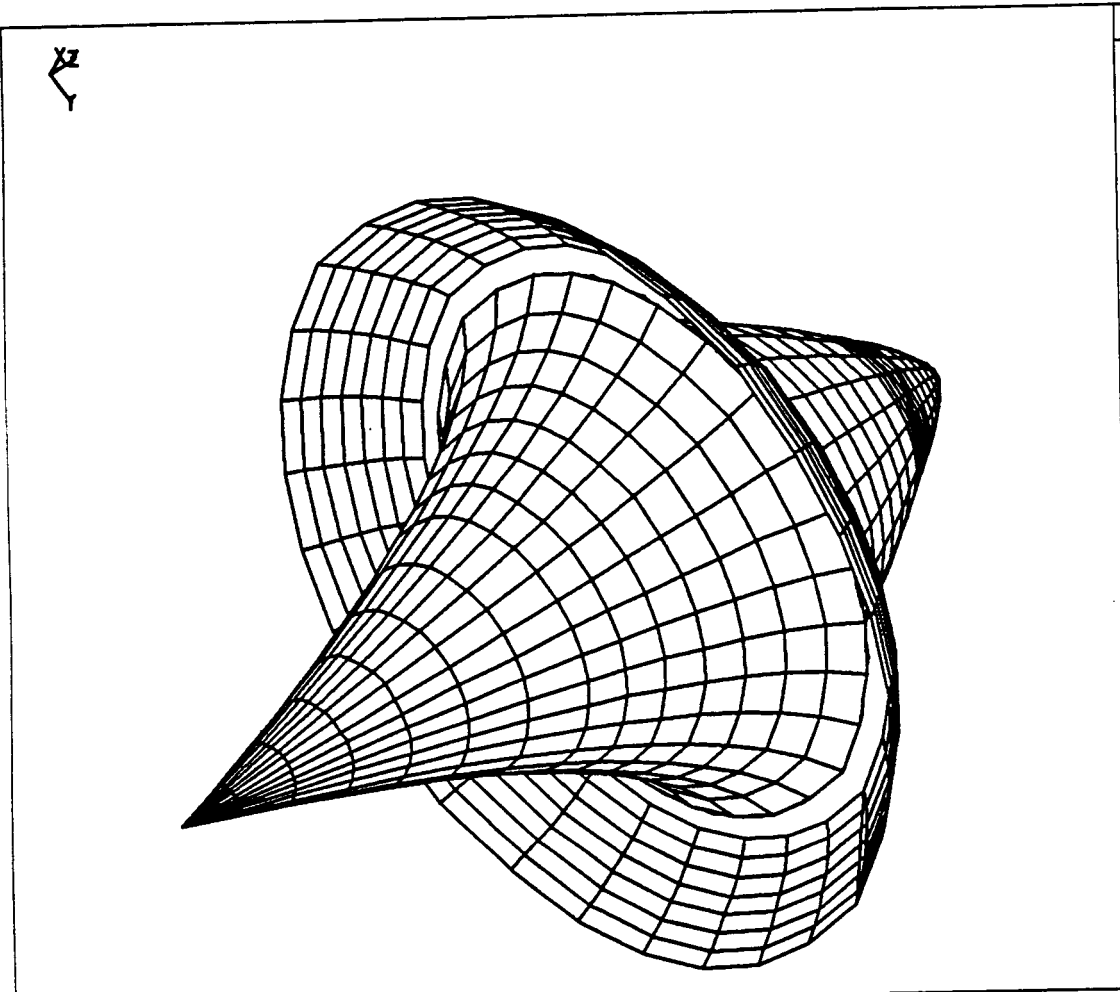
x z
↓



IMAGE

MOD PLN
MOD SPCE
MOD SCR
DEF VIEW
DEF SCR
STORE
RECALL

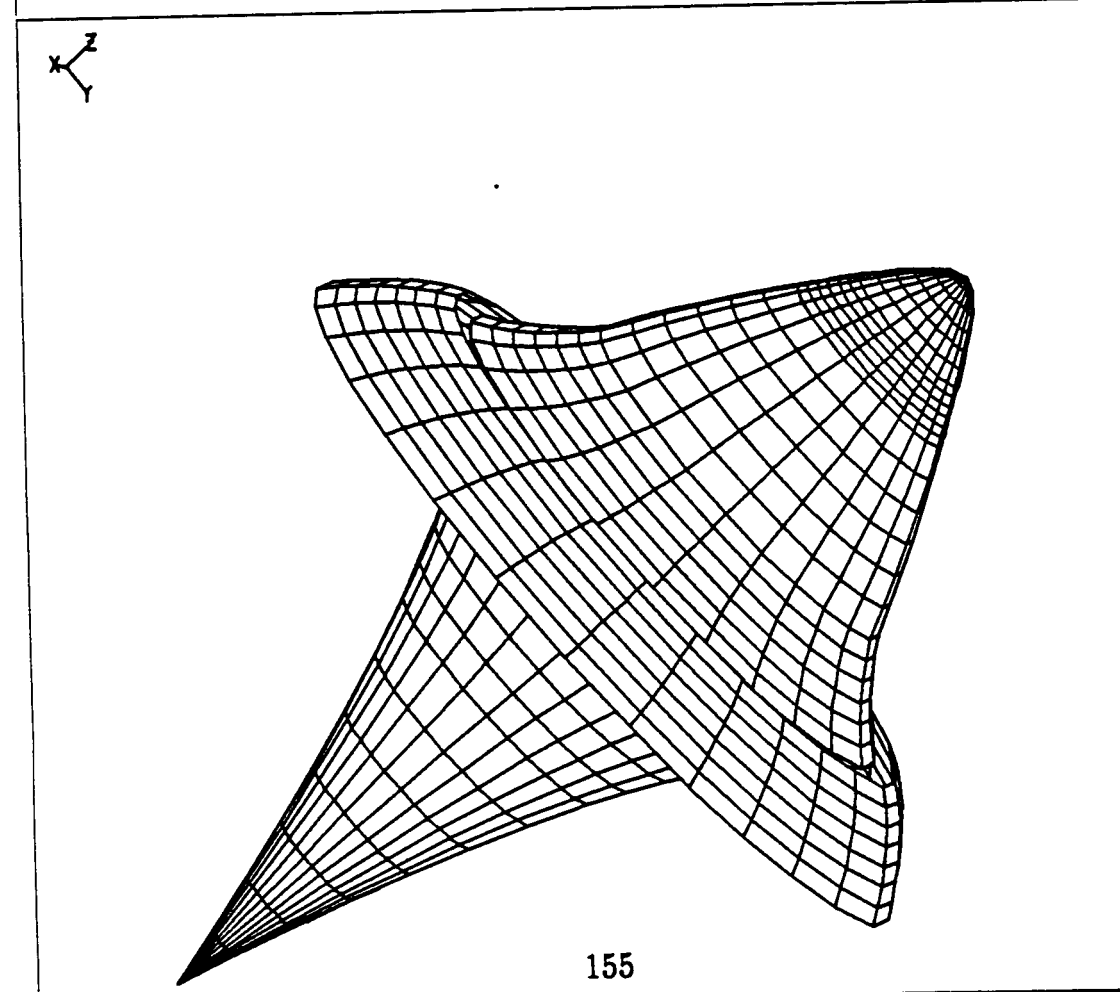
ROTATE
ROT VERT
ROT HOR



ERASE

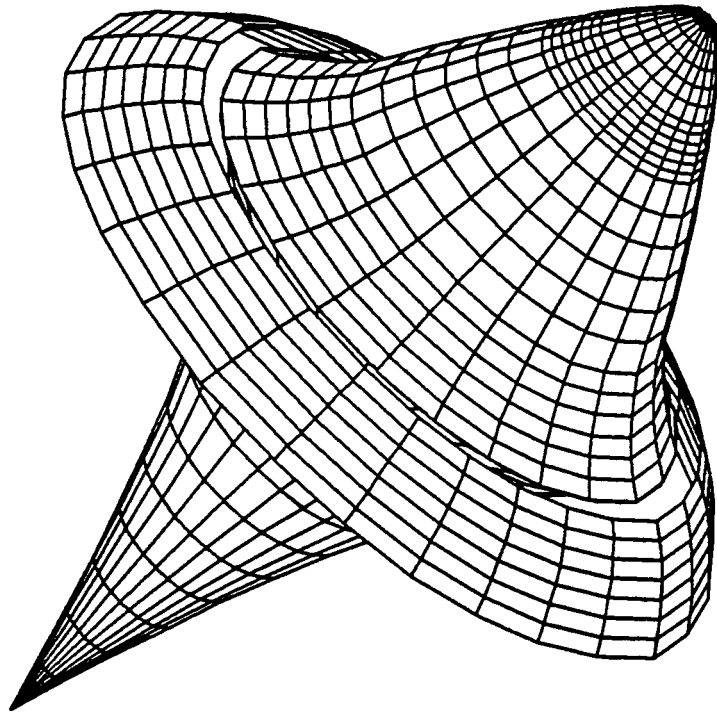
ERASE
PACK
NO SHOW
SHOW
INTENSIT
LINETYPE
BLINK
STEADY

ELEMENT
SET
TYPE



FILE

FILE
READ
WRITE
MERGE
RENAME
DELETE
CREATE
STANDARD
KEYBOARD
EXIT



FILE

FILE

READ

WRITE

MERGE

RENAME

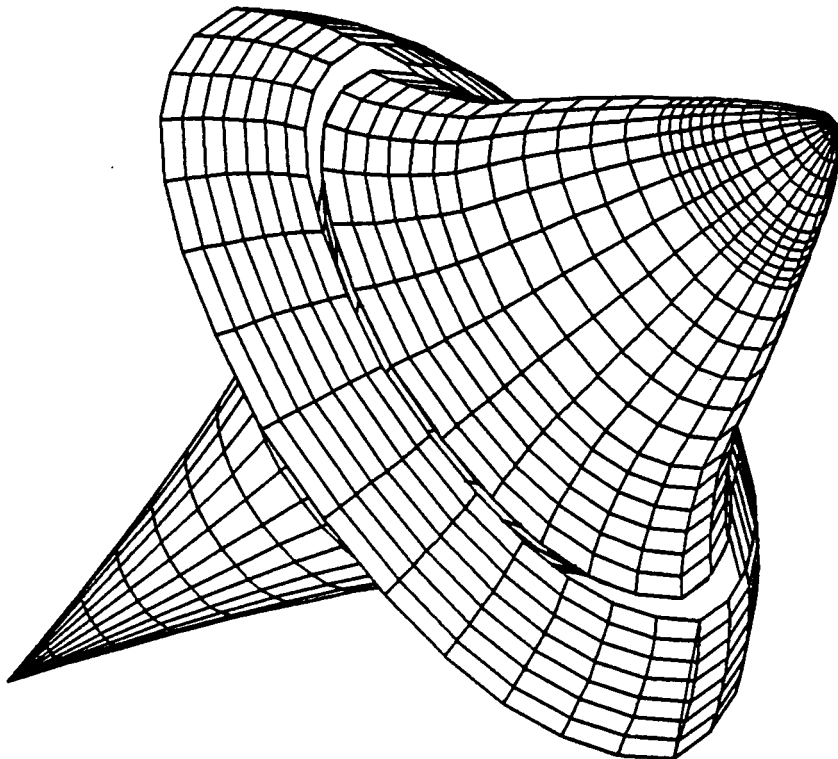
DELETE

CREATE

STANDARD

KEYBOARD

EXIT



ERASE

ERASE

PACK

NO SHOW

SHOW

INTENSIT

LINETYPE

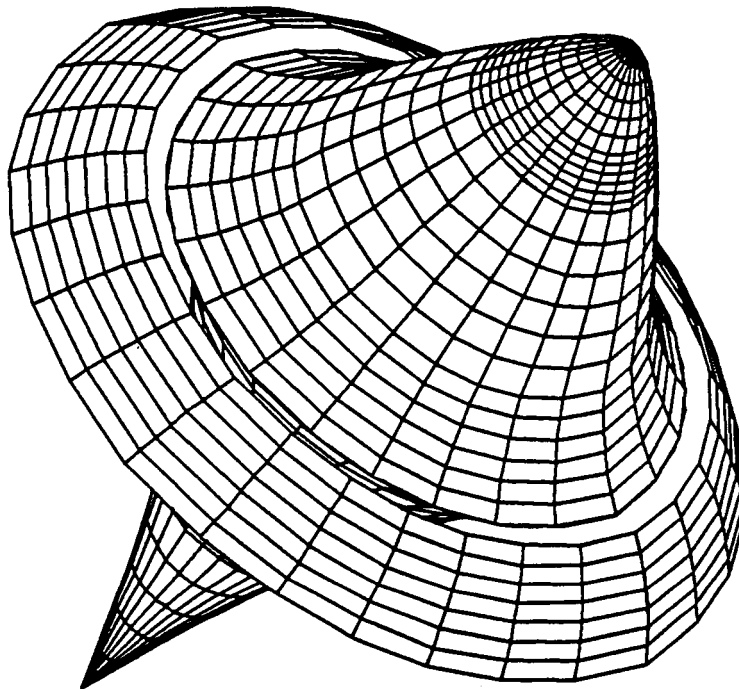
BLINK

STEADY

ELEMENT

SET

TYPE



ERASE

ERASE

PACK

NO SHOW

SHOW

INTENSIT

LINETYPE

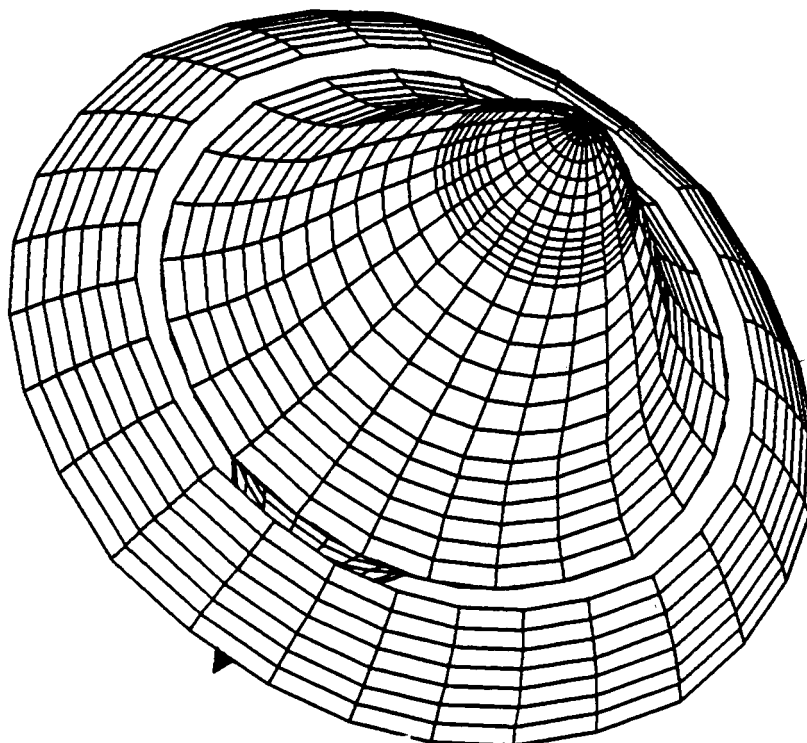
BLINK

STEADY

ELEMENT

SET

TYPE



ERASE

ERASE

PACK

NO SHOW

SHOW

INTENSIT

LINETYPE

BLINK

STEADY

ELEMENT

SET

TYPE